A linear Paul trap for barium tagging of neutrinoless double beta decay in nEXO

by

Yang Lan

M.Sc., The University of British Columbia, 2014
B.Sc., Huazhong University of Science and Technology, 2012

A THESIS SUBMITTED IN PARTIAL FULFILLMENT OF
THE REQUIREMENTS FOR THE DEGREE OF

DOCTOR OF PHILOSOPHY

in

The Faculty of Graduate and Postdoctoral Studies

(Physics)

THE UNIVERSITY OF BRITISH COLUMBIA

(Vancouver)

November 2020

The following individuals certify that they have read, and recommend to the Faculty of Graduate and Postdoctoral Studies for acceptance, the dissertation entitled:

A linear Paul trap for barium tagging of neutrinoless double beta decay in nEXO

submitted by Yang Lan in partial fulfillment of the requirements for

the degree of Doctor of Philosophy
in Physics

Examining Committee:

Jens Dilling, Physics and Astronomy, UBC
Supervisor

Chris Waltham, Physics and Astronomy, UBC
Supervisory Committee Member

Kirk Madison, Physics and Astronomy, UBC
University Examiner

Don Douglas, Chemistry, UBC
University Examiner

Additional Supervisory Committee Members:

Reiner Kruecken, Physics and Astronomy, UBC
Co-supervisor

Jason Holt, TRIUMF
Supervisory Committee Member

Abstract

nEXO is the next-generation Enriched Xenon Observatory searching for neutrinoless double beta decay ($0\nu\beta\beta$) in ^{136}Xe. If observed, $0\nu\beta\beta$ will validate the neutrino to be its own anti-particle and determine the absolute mass scale of the neutrinos. nEXO's sensitivity is limited by the background level. Barium tagging is the ultimate background rejection method using the coincidence detection of ^{136}Ba as the daughter nucleus.

A linear Paul trap (LPT) is needed for the barium tagging concept in nEXO or a future gaseous experiment. The theory of an ideal LPT was studied from first principles to obtain analytical solutions of the trapped ions and to validate a simulation method. Then simulations were done to optimize the design of a realistic final LPT. The final LPT has been manufactured and is being set up. Meanwhile, prototypes of key components of the LPT were built for the experimental developments.

A prototype of the LPT's quadrupole mass filter (QMF) achieved mass resolving power $m/\Delta m$ around 140 and exceeded its requirement. A 3D printed prototype of the novel ion cooler demonstrated successful ion cooling, trapping and ejection.

Based on the progress with the prototypes, improvements were made to the design of the final setup. The final LPT will be installed between an RF funnel and a high precision mass spectrometer for barium tagging of nEXO.

Lay Summary

The nEXO collaboration is studying a rare nuclear reaction (neutrinoless double beta decay) which is much slower than the current age of the universe (1.38 billion years) and in fact has never been observed. The reaction is important because its discovery can reveal some hidden secrets of the neutrino – currently one of the most mysterious fundamental subatomic particles.

In order to help discover this rare nuclear reaction, I studied and built an ion trap which can capture and identify an ion from the reaction. I also developed experiments to test the ion trap and proved it is capable of separating different ions and capturing the ions we need. The ion trap will be combined with other ratus to further test its functionalities and help to reveal the nature of neutrinos.

Preface

The work presented in this dissertation contains contributions from many individuals and groups in the three collaborations I have been a member of: EXO-200 (Enriched Xenon Observatory), nEXO (next-generation Enriched Xenon Observatory) and TITAN (TRIUMF's Ion Trap for Atomic and Nuclear science).

The EXO-200 collaboration is formed by researchers from 26 institutes in 7 countries. The development of the experiment started in the early 2000s; the data-taking was done between 2010 to 2018. I participated in shifts to run the EXO-200 and took data from June 20 to 25 of 2016, August 23 to September 16 of 2017, December 14 to December 23 of 2017 and August 27 to September 11 of 2018. In addition, I was the data quality analyzer from January 2017 to December 2018. I performed routine inspections of events measured by EXO-200 and provided weekly data quality reports. The data quality reports helped to steer the operations of the EXO-200 at a low background level and determine the cut of data with a high level of background or abnormal events.

My shift work and data quality analysis of the EXO-200 contributed to the two publications below. The manuscripts were prepared by C. Licciardi in 2018 and G.S. Li in 2019.

J. B. Albert, et al. (EXO-200 collaboration). Search for neutrinoless double-beta decay with the upgraded EXO-200 detector. *Physical Review Letters* 120, 072701, 2018.

G Anton, et al. (EXO-200 collaboration). Search for neutrinoless double-β decay with the complete EXO-200 dataset. *Physical Review Letters* 123, 161802, 2019.

The key result from the above papers was used in Section 1.3.1 and Figure 1.4 of this dissertation.

The nEXO collaboration was formed around 2014 by most of the researchers from EXO-200 and a few other institutes. I participated in the development of a barium tagging technique for nEXO.

The barium tagging technique was based on the Monte Carlo simulations of an RF funnel by V. Varentsov at FAIR (Facility for Antiproton and Ion Research) and the experimental study of an RF funnel prototype at Stanford University by T. Brunner (now at McGill University) and D. Fudenberg. Figure 4.2 of this dissertation is plotted using simulated results of the RF funnel by V. Varentso and D. Fudenberg (unpublished).

I mainly focused on developing a linear Paul trap (LPT) downstream from the RF funnel for the barium tagging. The development of the LPT was done at the TITAN group at TRIUMF (TRI-University Meson Facility, Canada's particle accelerator centre). Contributions to the development of the LPT from different individuals and groups are listed below:

- In Chapter 2, the theory and analytical solutions of an ideal LPT were derived by me.
- In Chapter 3, the simulations were done by me. I reported the simulations results in regular meetings with the TITAN group and the barium tagging group of nEXO; the feedback from these meetings contributed to the progress of the simulations.
- In Chapter 4, the mechanical design of the LPT was done by me with consultations provided by J. Langrish at TRIUMF's design office and M. Good of the TITAN collaboration.
- In Chapter 5 and Appendix A, the prototypes of the LPT were designed and machined by me. The experimental development of the electronics, control and DAQ (data acquisition) systems was done by me with discussion and advice from members of the TITAN group and the nEXO barium tagging group. The data of all the experimental measurements were taken by me. The machining of the parts for the final LPT setup was done by the Physics department machine shop of the Université de Montréal. The partial assembling of the final LPT was done by X. Shang and H. S. Rasiwala at McGill University.
- In Appendix B, the mechanical drawings of the LPT were made by X. Shang based on the 3D Solidworks models I designed. Many improvements to the design have been contributed by X. Shang.

Based on the material of this dissertation, the following publications are in preparation. The manuscripts were written by me and will be revised based on communications with the co-authors.

- Y Lan and J Dilling. Analytical solutions for the performance of quadrupole mass spectrometers and ion guides. Adapted from Chapter 2.
- Y Lan, T Brunner, A Kwiatkowski and J Dilling. A novel ion cooler and buncher with tapered electrodes. Adapted from Section 4.4.2 and Section 5.3.

Table of Contents

Appendices

List of Tables

List of Figures

List of Abbrevations

$0\nu\beta\beta$ Neutrinoless double beta decay.

CEM Channel Electron Multiplier.

CLB Cooler, Laser spectroscopy and Buncher.

DAQ Data ACquisition.

EXO Enriched Xenon Observatory.

FC Faraday Cup.

LPT Linear Paul Trap.

LSIT Laser Spectroscopy Ion Trap.

MR-TOF Multi-Reflection Time-Of-Flight.

nEXO next-generation Enriched Xenon Observatory.

QMF Quadrupole Mass Filter.

QMS Quadrupole Mass Spectrometer.

RFQ Radio Frequency Quadrupole.

TMP Turbo Molecular Pump.

Acknowledgments

I would like to thank my academic and research supervisor Dr. Jens Dilling for introducing me to the exciting research at EXO and TITAN and for the continued guidance over the years. I am especially grateful for the knowledge and experience he shared with me on how to build an ion trap. I am also grateful for not being laughed at with my usually too optimistic timeline and for not being pressured when I was lagging behind.

I would like to thank my co-supervisor Dr. Reiner Krucken for introducing me to the interdisciplinary field of isotopes and for the financial support through the IsoSiM (Isotope for Science and Medicine) fellowship program.

During my adventure of developing and building an ion trap, I got the most direct and valuable advice from Dr. Thomas Brunner who leads the neutrino physics group at McGill and Dr. Ania Kwiatkowski who leads the TITAN group at TRIUMF. I am also grateful for their efforts in keeping the teams and labs safe, healthy and friendly.

I appreciate the opportunity provided by Dr. Giorgio Gratta for my research stay at Stanford University when I first joined EXO, and I appreciate the lab experience shared with me by Thomas and Dan.

I also appreciate the opportunity provided by Dr. Michael Block for my research stay at GSI in Germany. I am grateful for the hospitality of the SHIPTRAP members and for the trust of Dr. Sebastian Raeder in giving me full control of a quadrupole mass filter setup. The experience and skills I gained there were invaluable later when I developed the experimental setup of the ion trap.

I would like to thank my collaborators Brian and Jon for introducing and accompanying me to the unique underground facility of EXO-200 during my shifts. It was very warm at -2150 ft on those winter days.

I thank all the other 60+ TITAN, EXO-200 and nEXO colleagues and collaborators I worked and chatted with. I cherish those productive and happy experiences with each of them.

The experimental development of the ion trap benefited from the expertise of many people at TRIUMF. Especially, I thank John Langrish for being the ideal consultant when I was doing the mechanical design of the ion trap and I thank Mel Good for keeping the vacuum pumps running.

The simulations presented in this work were made possible by Compute Canada and WestGrid, especially Orcinus. Without these high-performance computing clusters, these simulations would take more than 20 years to run on my quad-core desktop computer.

Finally and most importantly, I would like to thank my wife Meiling for taking care of the family during the months when I was spending all my time with experiments and writing.

Chapter 1

Introduction

The Enriched Xenon Observatory (EXO) is searching for the extremely rare neutrinoless double beta decay ($0\nu\beta\beta$) in ^{136}Xe. Experimental detection of this lepton number violating process would prove the neutrino to be its own antiparticle.

Assuming the neutrino to be a light Majorana neutrino is currently the most favored explanation to $0\nu\beta\beta$ [DPR19, Car18]. Under this theoretical mechanism, the measured half-life time of $0\nu\beta\beta$ would provide critical information for determining the absolute mass scale of the neutrino.

1.1 Neutrino

The neutrino was postulated by Wolfgang Pauli [Pau30] in 1930 in order to explain energy and momentum conservation in beta decay. The elusive nature of the neutrinos, due to lack of electromagnetic and strong interaction with matter, makes them very difficult to detect with current experimental measurements.

The first direct detection of neutrinos (electron antineutrino) was in 1956 by Cowan and Reines [RC56] using two large tanks filled with 200 L of water to react with neutrinos emitted from a nearby nuclear reactor. The reaction used for the neutrino detection was via the inverse beta decay $\bar{\nu}_e + p \rightarrow n + e^+$. The positron e^+ generated in the reaction would annihilate with a nearby electron and emit a pair of gamma rays. The water was also filled with 40 kg of $CdCl_2$ to absorb the neutron generated in the reaction and emit another gamma ray. The gamma rays of expected sequences were detected by photomultiplier tubes inside three tanks filled with liquid scintillator which were arranged beside and between the water tanks. Even though the neutrino flux from the reactor was $5 \times 10^{13}\,\mathrm{s^{-1}cm^{-2}}$, the detected event rate was only 2.88 ± 0.22 counts/hr in the entire volume.

In subsequent experiments, neutrinos were found to have three types (flavors) associated with each of the three leptons: electron neutrino ν_e,

muon neutrino ν_μ [DGG$^+$62] and tau neutrino ν_τ [KUA$^+$01].

The standard model of particle physics constructed in the 1970s assumed the neutrino to have zero mass. However, breakthroughs in neutrino oscillation experiments in the last few decades proved that neutrinos have non-zero mass and they can change flavor when travelling through space [FHI$^+$98a, AAA$^+$02]. Neutrinos are in states of a definite flavor when being produced or when interacting with matter; otherwise they are in states of definite mass when propagating in space. The neutrino flavor states $\begin{bmatrix}\nu_e \, \nu_\mu \, \nu_\tau\end{bmatrix}^{\mathrm{T}}$ and mass states $\begin{bmatrix}\nu_1 \, \nu_2 \, \nu_3\end{bmatrix}^{\mathrm{T}}$ are related via a matrix transformation

$$\begin{bmatrix}\nu_e \\ \nu_\mu \\ \nu_\tau\end{bmatrix} = \begin{bmatrix}U_{e1} & U_{e2} & U_{e3} \\ U_{\mu 1} & U_{\mu 2} & U_{\mu 3} \\ U_{\tau 1} & U_{\tau 2} & U_{\tau 3}\end{bmatrix} \begin{bmatrix}\nu_1 \\ \nu_2 \\ \nu_3\end{bmatrix}, \tag{1.1}$$

where $U_{\alpha i}$ are elements of the Pontecorvo-Maki-Nakagawa-Sakata (PMNS) matrix [Ber14]. Neutrino oscillation experiments such as the Super-Kamiokande [FHI$^+$98b], Sudbury Neutrino Observatory (SNO) [CDDJ$^+$98], KamLAND [EEF$^+$03], MINOS [MAA$^+$06] and T2K [AAA$^+$12] determined most of the parameters in the PMNS matrix and the differences of squared masses among the three mass eigenstates: $\Delta m^2_{21} \approx 7.5 \times 10^{-5}\,\mathrm{eV}^2$ and $|\Delta m^2_{32}| \approx 2.4 \times 10^{-3}\,\mathrm{eV}^2$ [CFL$^+$14], where $\Delta m^2_{ij} = m^2_i - m^2_j$. Since $|\Delta m^2_{32}| \gg \Delta m^2_{21}$ and the sign of Δm_{32} is unknown, there are two possible mass hierarchies:

$$\Delta m^2_{32} > 0 \implies m_1 < m_2 < m_3 \quad \text{“Normal hierarchy”}, \tag{1.2}$$

$$\Delta m^2_{32} < 0 \implies m_3 < m_1 < m_2 \quad \text{“Inverted hierachy”}. \tag{1.3}$$

In order to identify the correct neutrino mass hierarchy and obtain the absolute mass scale of the neutrinos (their masses' offset from zero), there are a few possible approaches [BK18]:

- Beta decay spectrum end point

  A classical and direct way to measure the electron neutrino mass is to measure the beta decay spectrum endpoint of normal beta decays. The Mainz and Troitsk experiments measuring the beta decay of tritium obtained $m_{\nu_e} \leq 2.3\,\mathrm{eV}$ [KBB$^+$05] and $m_{\nu_e} \leq 2.2\,\mathrm{eV}$ [ABB$^+$11]. A combined collaboration from Mainz, Troitsk and other experiments are setting up a large experiment, KATRIN (Karlsruhe Tritium Neutrino Experiment), aiming at lowering the limit by a factor of 10 to

0.2 eV [Cho17]. As of the end of 2019, KATRIN has been operating and obtained the experimental result of $m_e < 1.1\,\mathrm{eV}$ [AAA+19].

- Cosmological observation

  The neutrino is the most abundant matter particle in the universe, so the neutrino mass could have an observable effect on the density of the universe if it are heavy enough. Via measurement of the cosmic wave background, the Planck experiment reported the sum of neutrino mass $\sum_i m_i < 0.12\,\mathrm{eV}$ [AAA+18a].

- Neutrinoless double beta decay ($0\nu\beta\beta$)

  $0\nu\beta\beta$ experiment is an indirect way of measuring the neutrino mass. However, it potentially has the best sensitivity by probing the neutrino mass around 10 meV [DMVV16] or lower; a few next-generation $0\nu\beta\beta$ experiments aiming at such sensitivity are already under development [DPR19].

1.2 Neutrinoless double beta decay

Double beta decay ($\beta\beta$) is a process where a nucleus with proton number Z and mass number A (Z, A) undergoes two beta decays simultaneously and becomes $(Z+2, A)$. For an ordinary double beta decay, two neutrons inside the nucleus turn into two protons; two electrons and two-electron antineutrino are emitted. For ^{136}Xe as an example, the $\beta\beta$ process is

$$^{136}\mathrm{Xe} \rightarrow {}^{136}\mathrm{Ba}^{++} + 2e^- + 2\bar{\nu}_e. \tag{1.4}$$

This ordinary double beta decay is also called a two neutrino double beta decay ($2\nu\beta\beta$) to be distinguished from the neutrinoless double beta decay ($0\nu\beta\beta$) which does not emit any neutrinos:

$$^{136}\mathrm{Xe} \rightarrow {}^{136}\mathrm{Ba}^{++} + 2e^- + 0\bar{\nu}_e, \tag{1.5}$$

which would be possible assuming that the two neutrinos annihilated each other and have violated the conservation of lepton number.

Double beta decay only happens to even-even isotopes [GP12] where the process is kinematically forbidden from the ordinary beta decay due to excessively large binding energy from the nucleon pairs while emitting two

electrons is kinematically allowed. The $\beta\beta$ is extremely rare with a half-life in the order of 10^{20} years. $0\nu\beta\beta$ is even rarer and in fact has never been experimentally observed.

The theoretical $0\nu\beta\beta$ half-life time is related to the effective neutrino mass [AIEE08] via

$$\frac{1}{T_{1/2}^{0\nu\beta\beta}} = G|M|^2\langle m_{\beta\beta}\rangle^2 \approx 10^{28}\left(\frac{0.01\,eV}{\langle m_{\beta\beta}\rangle}\right)^2, \tag{1.6}$$

where G is the phase space factor for emission of the two electrons, M is the theoretically derived nuclear matrix element for this second order process and $\langle m_{\beta\beta}\rangle$ is the effective Majorana mass of the electron neutrino.

The calculated value of $G \approx 10^{-25}\,\mathrm{yr}^{-1}eV^{-2}$ for the $0\nu\beta\beta$ of ^{136}Xe is available from literature [KI12, SM13]. The currently available value of the nuclear matrix element M for the $0\nu\beta\beta$ of ^{136}Xe varies in the range of 1.89 to 4.2 depending on the different nuclear models [ME13]. Inserting these values into Eq. (1.6), the half-life of the $0\nu\beta\beta$ of ^{136}Xe can be approximately expressed as [DPR19]

$$T_{1/2}^{0\nu\beta\beta} \approx 10^{28}\left(\frac{0.01\,\mathrm{eV}}{\langle m_{\beta\beta}\rangle}\right)^2 \mathrm{year}. \tag{1.7}$$

The effective Majorana mass $\langle m_{\beta\beta}\rangle$ of the electron neutrino in Eq. (1.6) and Eq. (1.7)

$$\langle m_{\beta\beta}\rangle = \sum_{i=1}^{3} m_i U_{ei}^2, \tag{1.8}$$

where U_{ei} is the PMNS matrix element with the electron flavor state and m_i is the mass of the neutrinos in their mass eigenstate used in the definition of the neutrino mass hierarchy.

1.2.1 $0\nu\beta\beta$ experiments

In double beta decay, the two neutrinos are practically impossible to be detected due to their small rate of interaction (or interaction cross-section) with any detector material. So the only practical way to identify the $\beta\beta$ or $0\nu\beta\beta$ event is via the energy spectrum of the two electrons from the decay.

For $2\nu\beta\beta$, the $Q_{\beta\beta}$ is the sum of the kinetic energy of all the decay products. The two electrons' summed energy spectrum would be continuous, similar to that of the normal beta decay because the two neutrinos carry away some kinetic energy. The ion always shares 0.003% or less of the kinetic energy as a result of the conservation of momentum. For the special case of $0\nu\beta\beta$ when there is no neutrino, the two electrons carry at least 99.997% of the kinetic energy. So the $0\nu\beta\beta$ spectrum would appear as a narrow peak exactly at the $Q_{\beta\beta}$ value (see Figure 1.1).

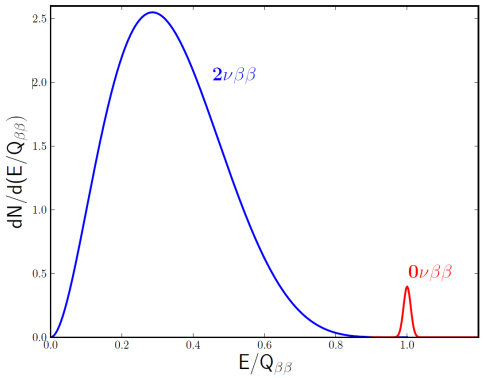

Figure 1.1: Electron energy spectrum for $\beta\beta$ (blue) and $0\nu\beta\beta$ (red). The $0\nu\beta\beta$ spectrum is based on a detector resolution of $2\%Q_{\beta\beta}$ and has been scaled up by at least 10^4 to make it visible in the plot. Figure credit: Walton, 2016 [Wal16].

There are 35 known naturally existing isotopes that could undergo $\beta\beta$ decay. For 12 of them, $2\nu\beta\beta$ has been observed and a few among them can be candidates for a $0\nu\beta\beta$ experiment. ^{136}Xe appears to be a good choice for a $0\nu\beta\beta$ experiment because of the following arguments:

- Xenon is a noble gas element, so it is chemically inert and can be cleaned to high purity in order to remove radioactive contaminants.
- Xenon has ionization and scintillation response to the $\beta\beta$ decay products, so the same source material can also be used as a detector to minimize radioactive contaminants.
- With either liquid or gaseous xenon, a small test detector can be potentially upscaled to a ton-level experiment.

- Last and most importantly, xenon is practically the only $0\nu\beta\beta$ candidate which can have the daughter isotope barium identified (barium tagging) to ultimately eliminate background events.

1.3 EXO

The EXO collaboration has completed the experiment EXO-200 which made use of 175 kg (initially planned to be 200 kg) of liquid xenon enriched to 80.6% of ^{136}Xe. The liquid xenon is in a recirculation system for periodic purification. The next generation of the experiment next-EXO (nEXO) [KAA$^+$18] is in the R&D process and will use 5 tonnes of liquid xenon.

1.3.1 EXO-200

The EXO-200 experiment [AAB$^+$12] was located at the Waste Isolation Pilot Plant (WIPP) in New Mexico. The facility is 655 meters underground, providing $\sim$ 1620 meters of water equivalent shielding against cosmic rays which can cause background for the experiment. The experiment setup and supporting equipment were housed in class 100 clean rooms. An engineering design rendering of the cleanroom containing the EXO-200 detector is shown in Figure 1.2. The central part of the experiment was a Time Projection Chamber (TPC) containing 110 kg of liquid xenon. The TPC was placed in a cryostat filled with cryogenic fluid [1] to keep the xenon at a stable liquid phase under atmospheric pressure as well as to shield the TPC from radioactive backgrounds. The cryostat was further shielded with 25 cm of lead on all sides. Despite being underground, a small number of cosmic muons could still reach the EXO-200 detector. In order to veto events induced by these cosmic muons, scintillator panels (veto panels) were used to cover more than 95% of the cleanroom.

The TPC was a cylinder of $\sim$ 40 cm in diameter and $\sim$ 44 cm in length. An illustration of the TPC is shown in Figure 1.3. When a $\beta\beta$ event occurred inside the TPC, the two electrons from the decay dissipated their kinetic energy to the liquid xenon in the form of ionization electrons and scintillation light. The scintillation light was collected by avalanche photodiodes (APDs); the ionization electrons drift to the charge collection wires in the electric field between the cathode and the wires. The event energy was obtained via the total detected amount of scintillation light and ionization electrons. When the electrons reached the charge collection

[1] 3M Novec 7000 Engineered Fluid

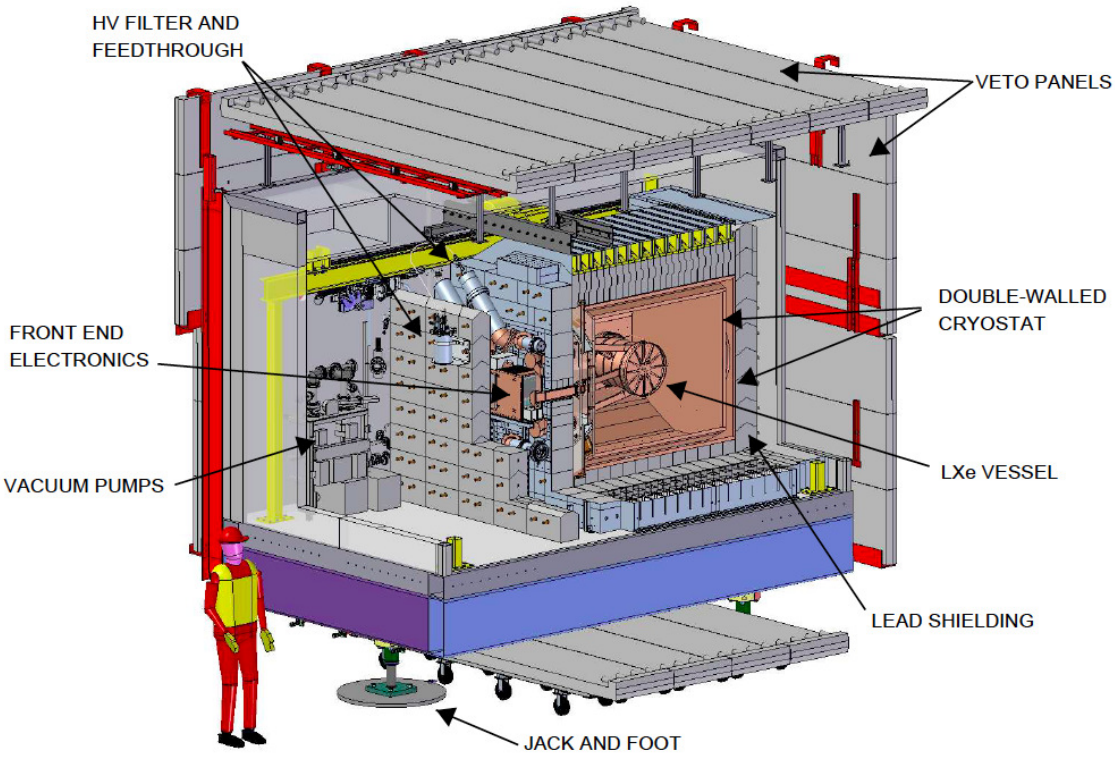

Figure 1.2: Engineering design rendering of the cleanroom containing the EXO-200 detector. The detector is placed in a cryostat shielded by lead on all sides. The detector is covered by veto panels. See text for details. Figure credit: EXO collaboration (2012) [AAB+12].

wires, their transverse positions were recorded. The longitudinal position of these ionization electrons can be calculated by their drift speed in the TPC and the time difference between the scintillation light signal and the charge collection signal. Thus, the 3D topologies of the events were reconstructed. The topology information was used to distinguish the true $\beta\beta$ events from the background; it could also locate the barium ion to facilitate barium tagging in-situ or for extraction of the volume containing the barium ion out of the TPC for barium tagging at a later stage.

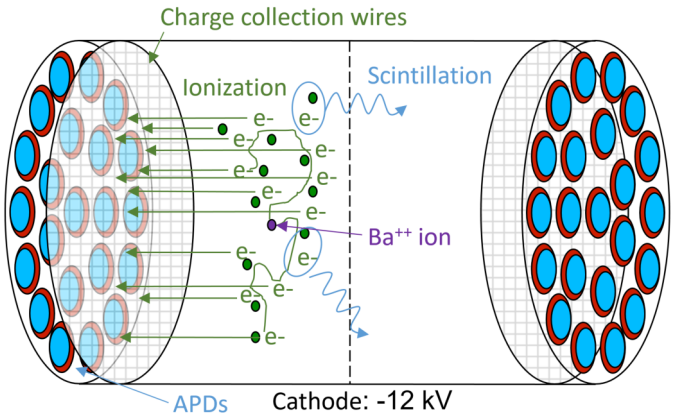

Figure 1.3: Illustration of the EXO-200 TPC. The TPC consisted of two symmetric halves with the cathode in the central plane, charge collection wires and avalanche photodiodes (APDs) on each side. See text for details. Figure credit: EXO-200 collaboration.

EXO-200 started data-taking in May 2011. In August 2011, the first ever measurement of $2\nu\beta\beta$ in ^{136}Xe was made to be $T_{1/2}^{2\nu\beta\beta} = 2.11 \pm 0.04(stat) \pm 0.21(syst) \times 10^{21}$ years [AAA+11]. In 2014, EXO-200 updated the lower limit of $0\nu\beta\beta$ in ^{136}Xe to be $T_{1/2}^{0\nu\beta\beta} > 1.1 \times 10^{25}$ years at 90% confidence level [c+14].

EXO-200 underwent an upgrade of electronics and cathode high-voltage during a shut-down from 2014 to 2016. Data-taking was resumed after the upgrade until the completion of EXO-200 at the end of 2018. The data of the phase I (September 2011 to February 2014) and phase II (May 2016 to December 2018) were analyzed. The energy spectrum of the data with the best fit is shown in Figure 1.4. The combined data with a total live time of 1181.3 days resulted in no statistically significant evidence for $0\nu\beta\beta$ and

the lower limit of $0\nu\beta\beta$ in ^{136}Xe was set to be $T_{1/2}^{0\nu\beta\beta} > 3.5 \times 10^{25}$ years at 90% confidence level.

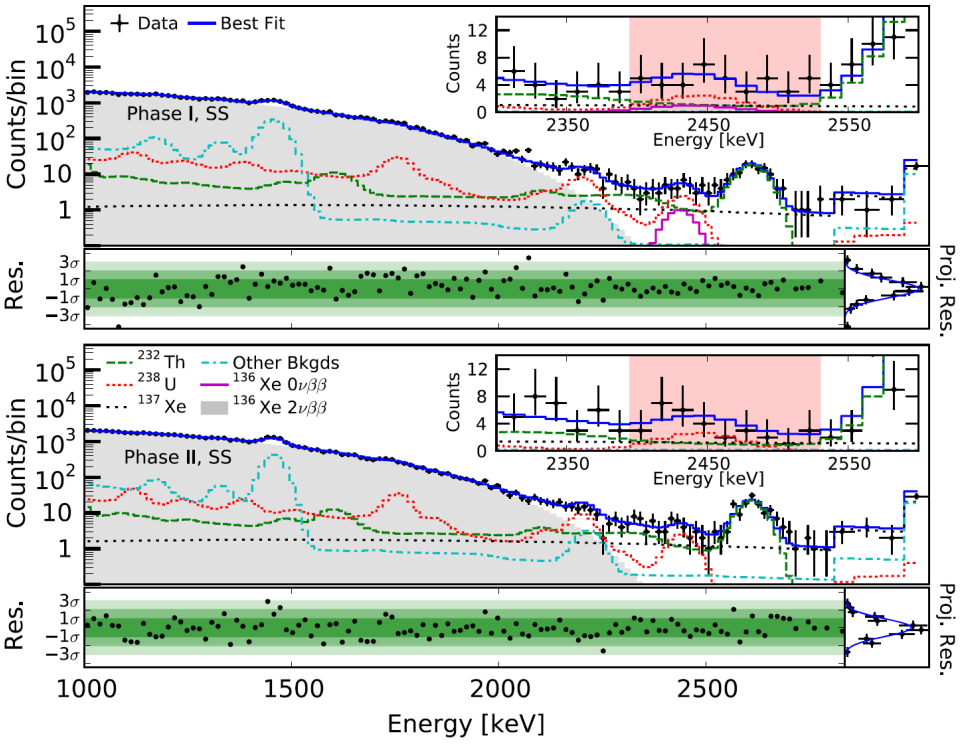

Figure 1.4: Best fit to the energy spectrum for Phase I (top) and Phase II (bottom) data of EXO-200. The insets shows the zoomed in plots for the region-of-interest near $Q_{\beta\beta} = 2458\,\text{keV}$. Figure from [ABB+19].

1.3.2 nEXO

nEXO is being designed with the goal to be as close as possible to the EXO-200 concept but scaled up to 5 tonnes of liquid xenon as illustrated in Figure 1.5. The experiment is planned to be set up in the cryopit of the SNOLAB, where a deeper 2070 m (6010 m water equivalent) underground shielding will provide further reduction of the rate of cosmic ray compared to EXO-200.

In the later stage of the operation of nEXO, a barium tagging setup may be added to the experiment to reject all the backgrounds except $2\nu\beta\beta$ events

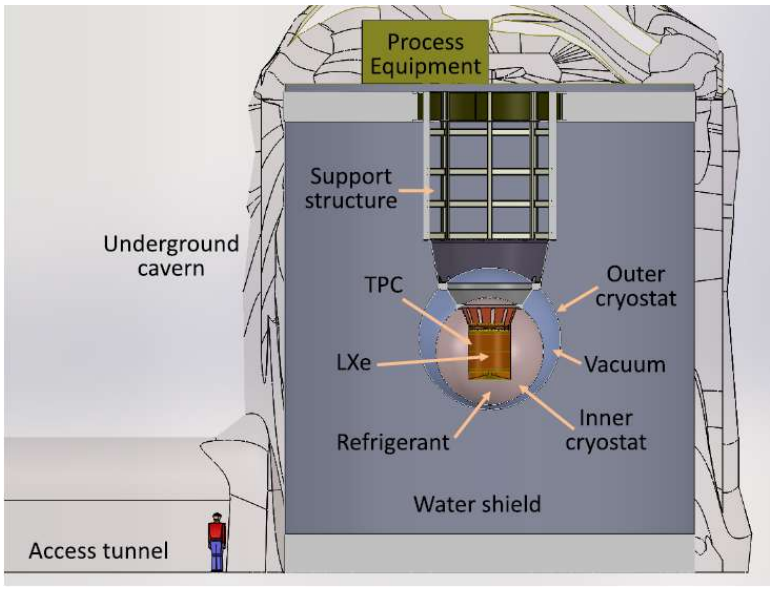

(a)

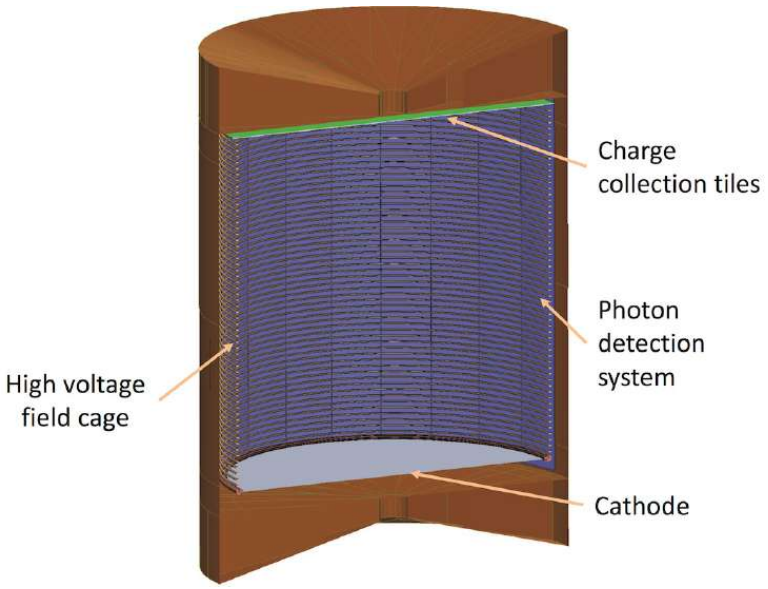

(b)

Figure 1.5: Pre-conceptual design of nEXO. (a) Engineer design rendering of nEXO in the SNOLAB cryopic. (b) Cut view of the nEXO TPC. See text for details. Figures from [AAA+18b].

at the tail of their energy spectrum near $Q_{\beta\beta}$.

1.4 Barium tagging

Due to the very long half-life, the expected event rate of $0\nu\beta\beta$ is extremely low even after considering a large amount of source material. For the current EXO-200 experiment which has 110 kg of enriched liquid xenon in the detector (3.9×10^{26} ^{136}Xe atoms), there is only one $2\nu\beta\beta$ event every 250 seconds. The $0\nu\beta\beta$ event rate is 1/10,000 of that or lower, depending on the effective Majorana electron neutrino mass $\langle m_{\beta\beta} \rangle$. Meanwhile, there are background events from radioactive contaminants and cosmic rays making the $0\nu\beta\beta$ signal more difficult to be distinguished from the background signals. In such cases, it is critical to reduce these background events and ideally eliminate all of them. The EXO experiments have been considered in every possible aspect to reduce background events. The ultimate approach to reject the backgrounds for EXO is via barium tagging.

The idea of barium tagging, i.e. identification of the barium ion as the $0\nu\beta\beta$ daughter of ^{136}Xe, was first proposed by Moe [Moe91]. Moe's proposed barium tagging technique is based on the classic experiment with the successful observation of single Ba^+ ions in ion trap by Neuhauser et al. [NHTD80].

The technique works by illuminating the Ba^+ ions with a blue (493 nm) and red (650 nm) laser; the Ba^+ ions would emit fluorescent light at both wavelengths. The presence of barium ions is then determined by the detection of the signature fluorescent light. In this way, only an event which also produces a barium ion at the event location (reconstructed by the TPC) will be verified as a $2\nu\beta\beta$ or $0\nu\beta\beta$ event; all the other events without coincidence production of a barium ion will be rejected.

Figure 1.6 shows the expected improvement of nEXO's sensitivity after including barium tagging. Assuming 100% barium tagging efficiency (identify all ^{136}Ba ions generated by $0\nu\beta\beta$), running nEXO for 1.1 years can reach the same sensitivity as running it for 10 years without barium tagging (improvement by a factor of 9). Even at 50% of barium tagging efficiency, the sensitivity can be greatly improved such that nEXO could probe the effective Majorana neutrino mass down to 3 meV in the normal mass hierarchy region after running for 10 years. The minimum barium tagging efficiency required to bring improvement to nEXO is 11%.

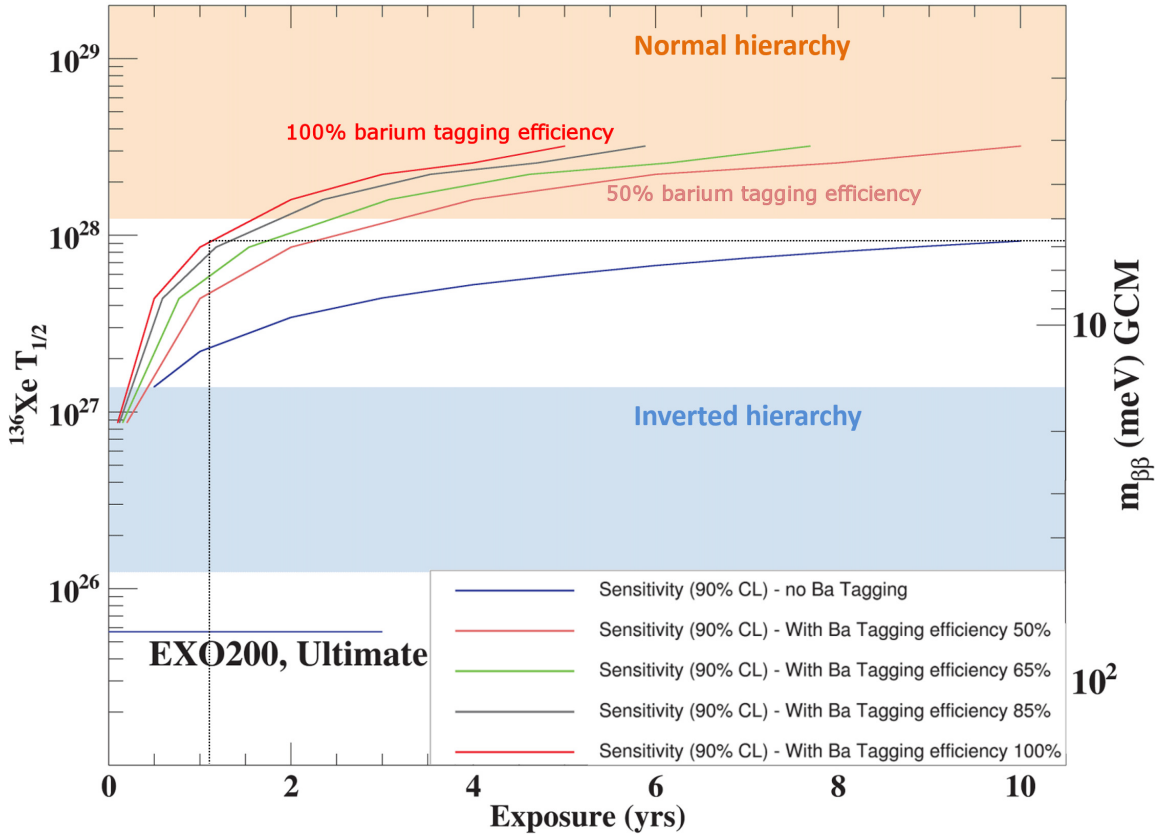

Figure 1.6: Sensitivity of nEXO with and without barium tagging. The left y-axis represents the sensitivity to $0\nu\beta\beta$ half-life time, the right y-axis is the sensitivity of the effective Majorana mass of the electron neutrino. The two color bands are ranges of the normal and inverted mass hierarchies; the ranges are set by the neutrino's absolute mass scale and the uncertainty in the calculation of the nuclear matrix element. Figure credit: nEXO simulation group, 2015.

The research and development of barium tagging started at the early stage of the EXO collaboration. Because of the importance of barium tagging and the challenges in achieving it, multiple techniques have been under development.

Barium tagging techniques

The most direct approach to barium tagging is to shine lasers to where a barium ion is generated during the decay inside the TPC and subsequently detect the fluorescent light [DDD$^+$00]. The mobility of barium ions inside liquid xenon has been measured and found to be small; the small ion mobility leads the barium ions to move slowly and makes a tagging laser easy to follow the ion while producing fluorescent light [Jen04]. However, further development of this technique found that the fluorescent light cannot be reliably identified within the whole detector volume [Hal12].

An alternative approach to barium tagging is to insert a probe into the TPC and attract the barium ion to the tip of the probe with electrostatic force. Then the barium ion identification can possibly be done in-situ using laser spectroscopy through optical fiber to send the lasers and collect the fluorescent light. The probe can also possibly be removed from the TPC along with the barium ion (or atom), then transfer the barium to a dedicated setup for identification.

A cold probe is being developed for barium tagging in xenon ice [Wam07a]. Barium identification in solid xenon ice at an external setup obtained a fluorescence image sensitive to fewer or equal than 10^4 atoms [MCW$^+$15]. Further progress on this has led to imaging of individual barium atoms [CWF$^+$19].

An RSI (laser resonance ionization) probe is also being developed [Die12, TKD$^+$14, Wam07b]. The tip of the RSI probe is a clean semiconducting substrate such as silicon or silicon carbide. The barium ions in liquid xenon would neutralize on the surface of the substrate, then the probe is transferred to an external setup to resonantly ionize the barium atom with lasers. The barium ions were then identified via time-of-flight mass spectrometry.

Following the classic experiment of Neuhauser et al. [NHTD80], an ion trap has been developed for EXO and achieved single barium ion identification [Wal05, FGW$^+$07]. Subsequently, a second generation of the ion trap was developed for the additional purpose of testing ion ejection (loading) to (from) a cold probe [Gre10]. The attempt to recover ions from the cold probe to the ion trap has not been successful yet.

The second generation of the ion trap was transferred to Carleton University and the research on laser spectroscopy continues there. Through improvements of the laser scheme, in particular the inter-modulation of the blue and red lasers, the background photo count of the fluorescent light has been significantly reduced [Kil15].

This work focuses on developing an ion trap for barium tagging in gaseous xenon. At the early R&D stage of EXO, a large ($40\,m^3$) gaseous TPC with barium tagging has been proposed [DDD+00]. Later, both EXO-200 and nEXO were designed with a smaller liquid TPC to reduce the engineering challenges. In the future, an experiment may be built with a gaseous TPC to study the electron correlations in the double beta decay and requires barium tagging in gaseous xenon.

The concept of barium tagging in gaseous xenon will follow these steps:

- Extract the Ba^{++} ions from the high pressure xenon gas.
- Convert the Ba^{++} ions into Ba^{+} [Rol11] if needed.
- Capture and confine the Ba^{+} ions in an ion trap.
- Unambiguously identify the Ba^{+} ions via laser spectroscopy or mass spectrometry.

Extraction of ions from high pressure xenon gas of up to 10 bar to 10^{-6} mbar vacuum environment has been demonstrated [BFV+15] using an RF funnel. The RF funnel is made of 301 thin concentric electrodes with decreasing inner diameters to form the shape of a funnel. The electrodes are connected to an RF potential to confine the ions along the axis, while the neutral xenon gas is vented through gaps between the electrodes.

A linear Paul trap (sometimes also called a linear quadrupole ion trap or a linear radio frequency ion trap) will be used at the downstream end of the RF funnel to capture, cool and store the extracted ions to allow ion identification. This work particularly focuses on the development of such a linear Paul trap.

This linear Paul trap may be used for the barium tagging of the upcoming nEXO if future studies of transferring barium ions from liquid xenon to the trap are successful.

The linear Paul trap and the RF funnel are also planned to be used with a new ion extraction approach under development at Carleton University [Wat19]. The new ion extraction approach aims at extracting barium ions from liquid xenon using a specially designed capillary to vaporize the liquid xenon along with the ions. If successful, the ions extracted by the capillary will be sent to the RF funnel and the linear Paul trap as described

above.

The key features and goals of the linear Paul trap are the following:

- Transmit and trap close to 100% of the ions extracted from gaseous xenon through the RF funnel, or from liquid xenon through an alternative ion extraction method.
- Cool the ions to a temperature close to that of the buffer gas and trap the ions a few seconds for identification via laser spectroscopy.
- Eject the ions as fine bunches to a multi-reflection time-of-flight (MR-TOF) mass spectrometer for additional ion identification via high precision mass spectrometry. The ion bunch needs to have a small energy spread (typically within 2%) and a small time spread (typically tens of nanoseconds).

In order to achieve the above goals, the theory of the linear Paul trap was studied from the first principles to obtain analytical solutions for ions trapped in an ideal linear Paul trap as described in Chapter 2. The analytical solutions were used to validate simulations of the same ideal linear Paul trap, then simulations were done for the design and optimization of a realistic linear Paul trap as described Chapter 3. The mechanical design of the optimized linear Paul trap is described in Chapter 4. Finally, the experimental development and tests with prototypes are described in Chapter 5.

Chapter 2

Theory of the linear Paul trap

The linear Paul trap (LPT) was developed based on the concept leading to winning the Nobel prize by Wolfgang Paul [PS53]. A LPT consists of one or more sets of radio frequency quadrupoles (RFQ) to transmit or trap ions. The theory and principles of the RFQ are studied and presented in Section 2.1 followed by the characterization of its performance in Section 2.2. Such RFQs can also be configured to work as a simple ion guide to transmit all ions without filtering as described in Section 2.3 or a quadrupole mass filter in Section 2.4. The details of ion cooling and trapping in a linear Paul trap are described in Section 2.5.

2.1 Radio frequency quadrupole

A radio frequency quadrupole (RFQ) consists of four electrodes as illustrated in an example in Figure 2.1(a). The two diagonal pairs of the electrodes are supplied with opposite polarities of a DC potential U and an oscillating RF potential $V \cos \Omega t$, where V is the RF amplitude and Ω is the angular frequency. The electrodes create a quadrupole potential

$$\phi_{RF} = (U - V \cos \Omega t) \frac{(y^2 - z^2)}{r_0^2}, \tag{2.1}$$

in the center of the y-z plane as shown in Figure 2.1(b), where r_0 is the distance from the inner surface of the electrodes to the x-axis.

2.1.1 Ion dynamics in an RFQ

The ion dynamics, or in other words, how the ion trajectories are determined in an RFQ, are governed by the time-dependent electric field (the effect of gravity is typically much smaller and can be ignored). At a radial position

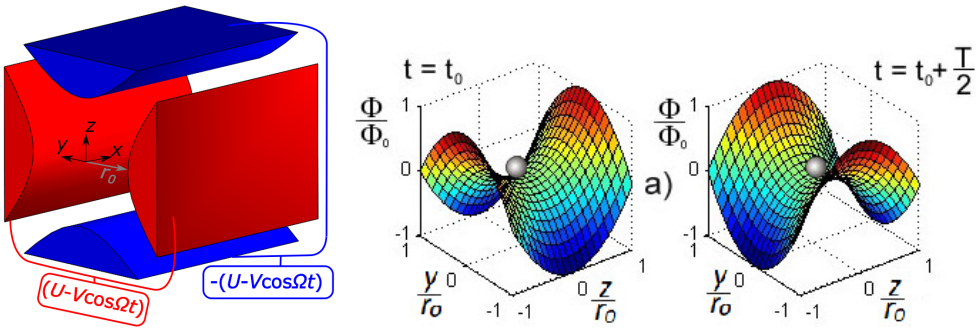

(a) (b)

Figure 2.1: (a) Illustration of an RFQ and the voltage configuration on its electrodes. (b) Quadrupole potential inside the trap for ion confinement in the transverse directions; adapted from [KP15].

(y, z) as shown in Figure 2.1, the electric field at time t is:

$$E(y,t) = (U - V\cos\Omega t)\frac{2y}{r_0^2} \tag{2.2}$$

$$E(z,t) = (U - V\cos\Omega t)\frac{-2z}{r_0^2}, \tag{2.3}$$

so the ion motion can be described independently in the y and z directions.

For a positive singly charged ion of mass m, the equations of motion are:

$$m\frac{d^2y}{dt^2} = \frac{-2ey}{r_0^2}(U - V\cos\Omega t), \tag{2.4}$$

$$m\frac{d^2z}{dt^2} = \frac{2ez}{r_0^2}(U - V\cos\Omega t), \tag{2.5}$$

where $e = 1.6 \times 10^{-19}$ C is the elementary charge. The equations can be rewritten in form of the Mathieu equation:

$$\frac{d^2u}{d\xi^2} + (a - 2q\cos 2\xi)u = 0, \tag{2.6}$$

$$\xi = \frac{\Omega t}{2}. \tag{2.7}$$

The variable u denotes a coordinate of either y or z, while a and q are the

so-called stability parameters:

$$a = a_y = -a_z = \frac{8eU}{m\Omega^2 r_0^2}, \quad q = q_y = -q_z = \frac{4eV}{m\Omega^2 r_0^2}. \tag{2.8}$$

When a and q are small, the ion dynamics can be simplified and approximated by the so-called *pseudopotential well* model developed by Wuerker [WSL59] and extended by Dehmelt [Deh68].

2.1.2 Pseudopotential well model

In this model the ion motion is described by a combination of a micromotion δ with the same frequency as the RF potential, and a lower frequency macromotion $\bar{u}$:

$$u = \bar{u} + \delta. \tag{2.9}$$

Plugging Eq. (2.9) into the Mathieu equation Eq. (2.6) results in the equation

$$\frac{d^2\bar{u}}{d\xi^2} + \frac{d^2\delta}{d\xi^2} = -(a - 2q\cos(2\xi))(\bar{u} + \delta). \tag{2.10}$$

When the following conditions are met:

$$\delta \ll \bar{u}, \frac{d^2\bar{u}}{d\xi^2} \ll \frac{d^2\delta}{d\xi^2}, a \ll q; \tag{2.11}$$

Eq. (2.10) can be simplified as

$$\frac{d^2\delta}{d\xi^2} = 2q\cos(2\xi)\bar{u}. \tag{2.12}$$

The micromotion is then solved as

$$\delta = -\frac{q\bar{u}}{2}\cos(2\xi). \tag{2.13}$$

To solve for the macromotion, plug Eq. (2.13) back into Eq. (2.10):

$$\frac{d^2\bar{u}}{d\xi^2} + \frac{d^2\delta}{d\xi^2} = -a\bar{u} + \frac{aq\bar{u}}{2}\cos 2\xi + 2q\bar{u}\cos 2\xi - q^2\bar{u}\cos^2(2\xi). \tag{2.14}$$

Then average Eq. (2.14) over one RF cycle. The micromotion term $\frac{d^2\delta}{d\xi^2}$ on the left and the two terms on the right containing $\cos 2\xi$ vanish:

$$\int_0^\pi \frac{d^2\delta}{d\xi^2} d\xi = \int_0^\pi 2q\bar{u}\cos 2\xi d\xi = 0, \tag{2.15}$$

$$\int_0^\pi (\frac{aq\bar{u}}{2}\cos 2\xi + 2q\bar{u}\cos 2\xi) d\xi = 0. \tag{2.16}$$

After integrating the remaining terms, Eq. (2.14) becomes

$$\left\langle \frac{d^2\bar{u}}{d\xi^2} \right\rangle = \int_0^\pi \frac{d^2\bar{u}}{d\xi^2} d\xi = -(a + \frac{q^2}{2})\bar{u}. \tag{2.17}$$

When the change of $\bar{u}$ ($d\bar{u}$) is small over one RF cycle,

$$\frac{d^2\bar{u}}{d\xi^2} = -(a + \frac{q^2}{2})\bar{u}. \tag{2.18}$$

Then replace the variable ξ with t using the relationship $d\xi = \frac{\Omega}{2}dt$,

$$\frac{d^2\bar{u}}{dt^2} = -\frac{\Omega^2}{4}(a + \frac{q^2}{2})\bar{u}. \tag{2.19}$$

This Eq. (2.19) describes $\bar{u}$ in a simple harmonic motion

$$\frac{d^2\bar{u}}{dt^2} + \bar{\omega}^2\bar{u} = 0, \tag{2.20}$$

where the secular frequency is

$$\bar{\omega} = \frac{\Omega}{2}\sqrt{a + \frac{q^2}{2}}. \tag{2.21}$$

For a positive singly charged ion with mass m, the potential well can be described as

$$\bar{D}(\bar{u}) = \frac{m\Omega^2}{8e}(a + \frac{q^2}{2})\bar{u}^2. \tag{2.22}$$

The depth of the pseudopotential well is $\bar{D}(\bar{u})$ when $\bar{u} = r_0$:

$$\bar{D} = \frac{m\Omega^2 r_0^2}{8e}(a + \frac{q^2}{2}). \tag{2.23}$$

Substituting a and q from their definition in Eq. (2.8) reveals

$$\bar{D} = U + \frac{qV}{4}. \tag{2.24}$$

Specifically, for the y and z axes

$$\bar{D}_y = U + \frac{q_y V}{4} \tag{2.25}$$

$$\bar{D}_z = -U + \frac{|q_z|V}{4}. \tag{2.26}$$

The pseudopotential well is similar to a simple harmonic well when the conditions in Eq. (2.11) are met. The depth $\bar{D}$ determines the maximum number of ions that can be trapped and the kinetic energies of the ions.

2.1.3 Full solution of Mathieu equation

The full solution of the Mathieu equation (2.6) is known to be an infinite series expansion [MT05]:

$$u(\xi) = \Gamma e^{\mu\xi} \sum_{n=-\infty}^{\infty} C_{2n,u} \exp(2ni\xi) + \Gamma' e^{-\mu\xi} \sum_{n=-\infty}^{\infty} C_{2n,u} \exp(-2ni\xi), \tag{2.27}$$

where Γ and Γ' are constants dependent on the initial values of the position u_0, velocity $\dot{u}_0$ and the RF phase ξ_0; $C_{2n,u}$ are coefficients of these terms and their values only depend on a and q; the value of μ leads to different categories of the solution:

1. μ is a non-zero real number; the solution $u(\xi)$ will be unstable due to exponential growth with ξ in either $e^{\mu\xi}$ or $e^{-\mu\xi}$.

2. μ is a complex number; the solution $u(xi)$ will still be unstable due to the real part of μ.

3. $\mu = im$, where m is an integer number; the solution will be periodic but unstable.

4. $\mu = i\beta$, where β is not an integer number; this is the only situation for the solution $u(\xi)$ to be periodic and stable.

Only solutions described in the last category are stable and suitable for ion confinement within a finite volume. The stable solution can be rewritten as

$$u(\xi) = A \sum_{n=-\infty}^{\infty} C_{2n} \cos[(\beta + 2n)\xi] + B \sum_{n=-\infty}^{\infty} C_{2n} \sin[(\beta + 2n)\xi], \quad (2.28)$$

where $A = \Gamma + \Gamma'$, $B = i(\Gamma - \Gamma')$. The solution describes the ion motion as a Fourier series with frequencies

$$\omega_n = \frac{\Omega}{2}(\beta + 2n). \quad (2.29)$$

Analytical solution for β

The value of β can be obtained by inserting Eq. (2.28) back to the Mathieu equation (2.6). Keep only the cosine terms for now:

$$-A \sum_{n=-\infty}^{\infty} C_{2n,u}(\beta + 2n)^2 \cos[(\beta + 2n)\xi] + (a - 2q\cos 2\xi)A \sum_{n=-\infty}^{\infty} C_{2n,u} \cos[(\beta + 2n)\xi] = 0. \quad (2.30)$$

Applying the trigonometric relationship

$$\cos(2\xi)\cos(\beta + 2n\xi) = \frac{1}{2}(\cos(\beta + 2n + 2)\xi + \cos(\beta + 2n - 2)) \quad (2.31)$$

to Eq. (2.30) and re-arranging the cosine terms:

$$A \sum_{n=-\infty}^{\infty} [\frac{a - (\beta + 2n)^2}{q} C_{2n} - C_{2n+2} - C_{2n-2}] \cos(\beta + 2n)\xi = 0. \quad (2.32)$$

Working on the sine terms would yield the same result as Eq. (2.32).

Eq. (2.32) implies that for every term of n

$$D_{2n}C_{2n} - C_{2n+2} - C_{2n-2} = 0, \quad (2.33)$$

where

$$D_{2n} = \frac{a - (\beta + 2n)^2}{q}. \quad (2.34)$$

For $n = 0$,

$$D_0 = \frac{a - \beta^2}{q} = \frac{C_2}{C_0} + \frac{C_{-2}}{C_0}. \tag{2.35}$$

Re-arranging Eq. (2.33) also leads to two recursive relationships

$$\frac{C_{2n+2}}{C_{2n}} = D_{2n} - \frac{C_{2n-2}}{C_{2n}} = D_{2n} - \frac{1}{D_{2n-2} - \frac{1}{D_{2n-4} - \cdots}} \tag{2.36}$$

$$\frac{C_{2n-2}}{C_{2n}} = D_{2n} - \frac{C_{2n+2}}{C_{2n}} = D_{2n} - \frac{1}{D_{2n+2} - \frac{1}{D_{2n+4} - \cdots}} \tag{2.37}$$

which can be inserted into Eq. (2.35) to solve for β:

$$\frac{a - \beta^2}{q} = \frac{1}{D_{-2} - \frac{1}{D_{-4} - \cdots}} + \frac{1}{D_2 - \frac{1}{D_4 - \cdots}}. \tag{2.38}$$

Finally, using the definition of D_{2n} from Eq. (2.34) and re-arranging it to write β in a recursive form:

$$\beta = \sqrt{a - \frac{q^2}{a - (\beta - 2)^2 - \frac{q^2}{a - (\beta - 4)^2 - \cdots}} - \frac{q^2}{a - (\beta + 2)^2 - \frac{q^2}{a - (\beta + 4)^2 - \cdots}}}. \tag{2.39}$$

An equivalent expression of β is given by Eq. (2.94) of [MT05].

For small a, q and hence small β values ($\beta \ll 4$), Eq. (2.39) can be approximated as

$$\beta \approx \sqrt{(a + \frac{1}{2}q^2)}. \tag{2.40}$$

Then the fundamental frequency of the ion motion described by Eq. (2.28) is

$$\omega_0 = \frac{\Omega}{2}\beta = \frac{\Omega}{2}\sqrt{a + \frac{q^2}{2}}, \tag{2.41}$$

which is exactly the secular frequency of the macromotion derived in the pseudopotential well model in Section 2.1.2.

Stability diagram

For larger q and a values, the approximation in Eq. (2.40) is no longer valid because $\beta \ll 4$ is no longer true. As an original method proposed in this study, β can be calculated by numerical iteration of Eq. (2.39) using some

initial guesses. Such a numerical calculation was carried out with n up to 20 in D_{2n} and the recursive formula of Eq. (2.39). The initial guess for β was empirically set to be $\beta_0 = 1$ for every q and a coordinate.[1] After 1000 iterations, the results in the range of $|q| < 10$ and $|a| < 5$ converged to changes smaller than 1×10^{-15} (which is the limit of the double-precision floating-point number) except around and outside the stable-unstable boundaries.[2] In this way, the value of β is effectively solved analytically. The precise value of β around the stable-unstable boundaries is obtained after more iterations.

The values of β at the end of the iterative calculation are plotted in Figure 2.2, showing a stability diagram in the (q, a) parameter space. The value of β in the color-coded stable region is a real number and non-integral, making the Mathieu equation's solution Eq. (2.28) stable. The stability diagram is found to be symmetric along the line $q = 0$ as predicted by Eq. (2.39).

Most RF quadrupoles work in the region of $0 < \beta < 1$. A detailed stability diagram of this region is shown in Figure 2.3.

For the ion described at the beginning of this section, it would have stable motion in the y coordinate for $q_y = q$ and $a_y = a$ within those stability diagrams. For the z coordinate $q_z = -q_y$ and $a_z = -a_y$. Therefore, the stability diagram for the z coordinate only needs to be flipped along the line $a = 0$ due to the symmetry in the q axis, see Figure 2.4(a). In the overlapped stable region shown in Figure 2.4(b), the ion would be confined in both y and z axis.

There are two noticeable characteristics of the stability diagram in this region.

- For $a = 0$, the maximum q is found to be

$$q_m = 0.90804633. \tag{2.42}$$

- The upper tip of the stable region is found to be

$$q_t = 0.7059961,\ a_t = 0.2369940. \tag{2.43}$$

[1] I found complex numbers needed for these numerical iterations so in fact $\beta_0 = 1 + 0i$ was used; at the end of the calculation, only the real part of β was kept.

[2] This numerical iterative method doesn't converge in some regions of large q and a values. But the range of $|q| < 10$ and $|a| < 5$ already fully cover their values used for ion confinement in RFQs and Paul traps.

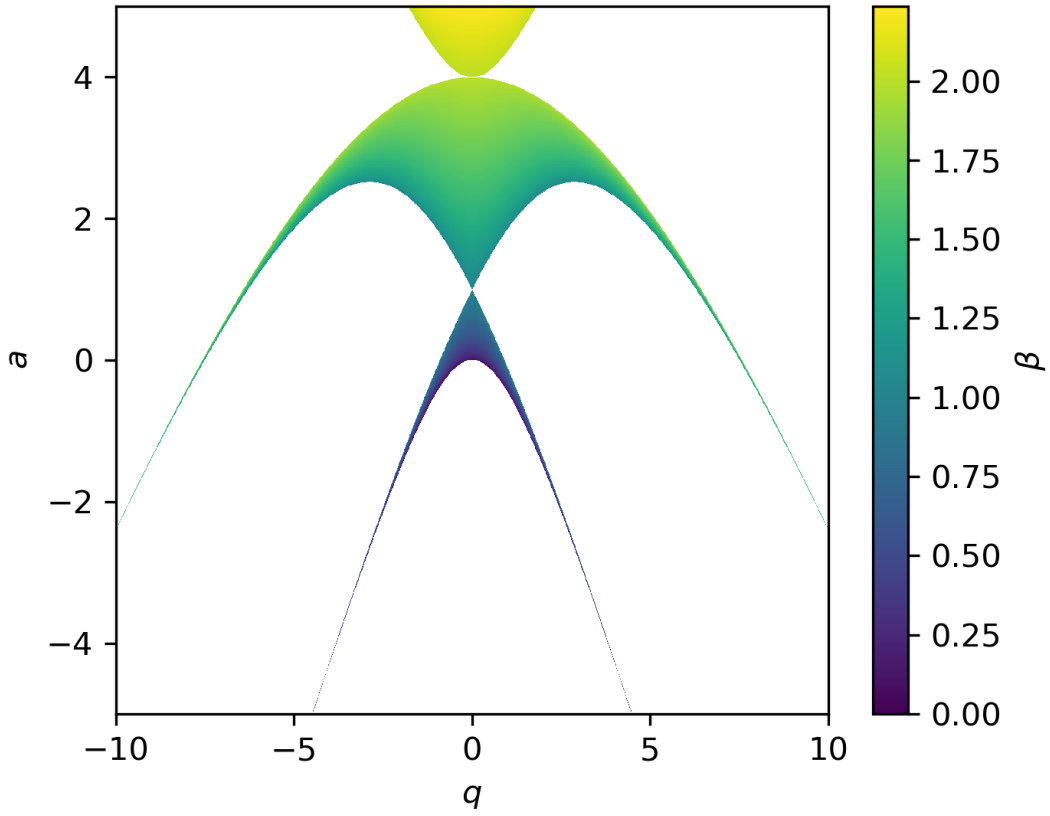

Figure 2.2: Calculated stability diagram of the Mathieu equation. The value of β is calculated by numerical iterations. The solution of the Mathieu equation is stable in the colored region.

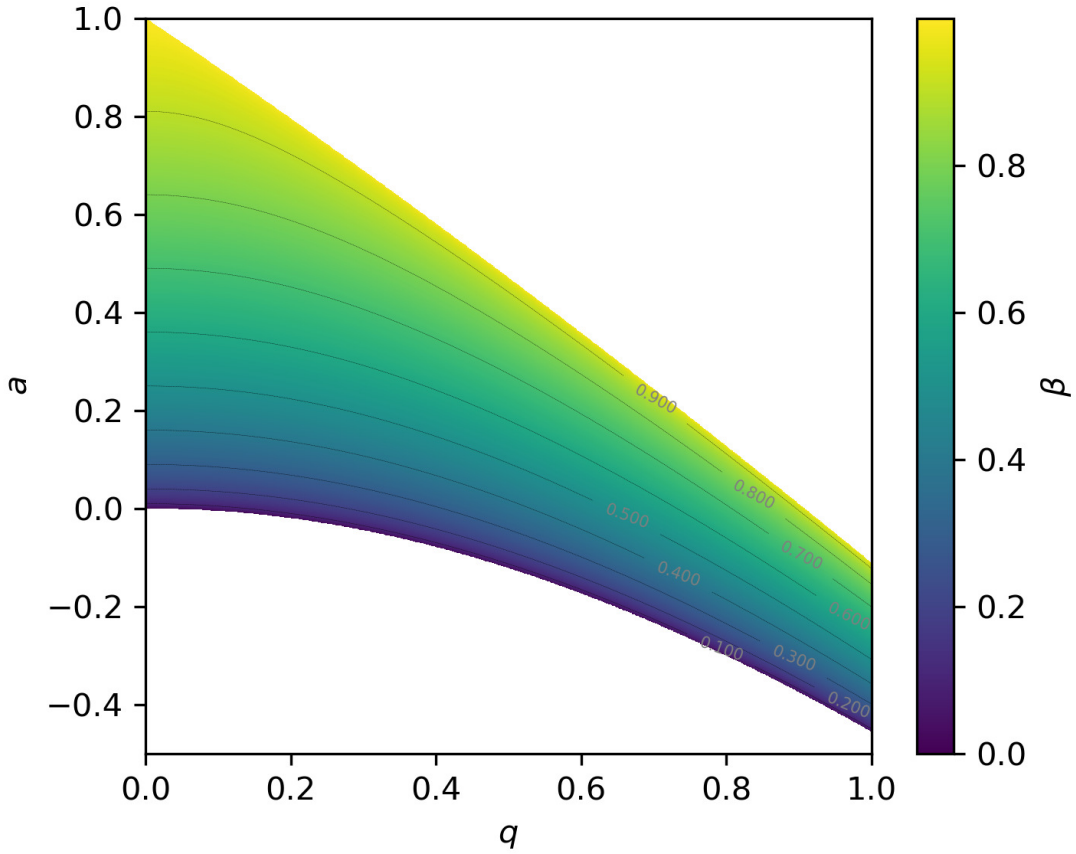

Figure 2.3: Calculated stability diagram for $0 < \beta < 1$. Equal-β lines from 0.1 to 0.9 are plotted on top.

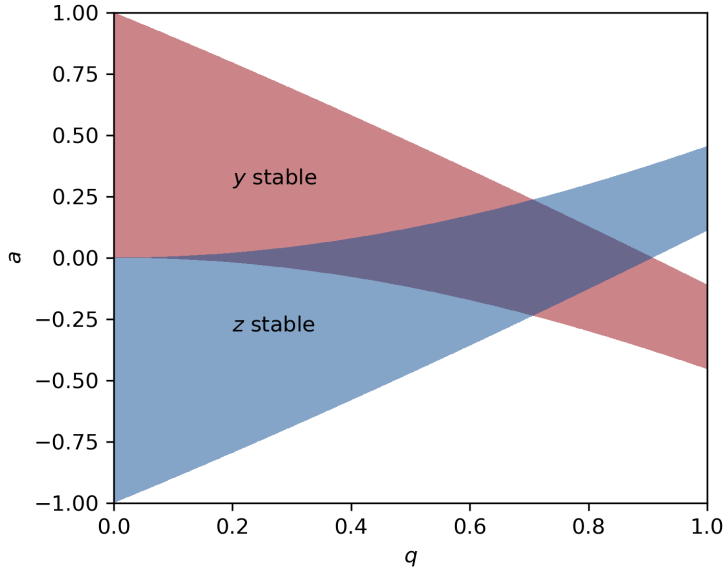

(a)

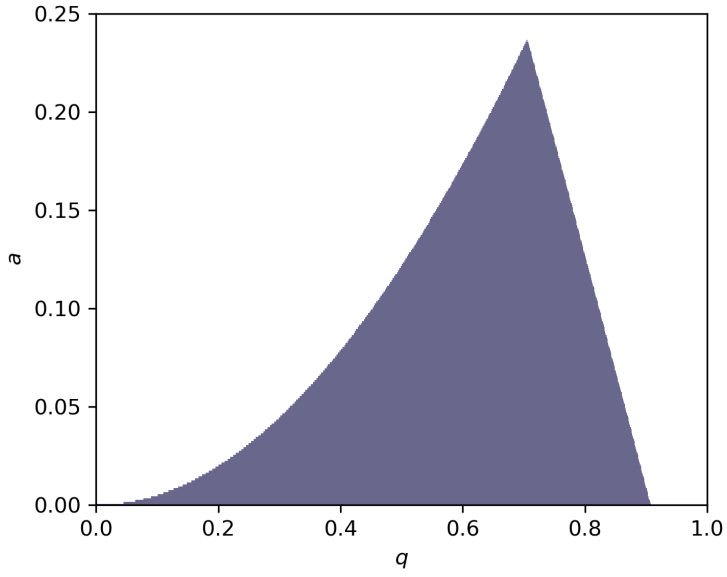

(b)

Figure 2.4: (a) Stability diagram for the y and z axes of an RFQ. (b) combined stable region where the solution is stable in both axes. See text for details.

These values are obtained after 100,000 iterative calculations. The precise values are useful for validating and benchmarking alternative approaches such as numerical integration in Section 2.1.4 and simulations in Chapter 3.

2.1.4 Ion motion

Now, the exact ion motion described by the Mathieu equation's solution can be obtained both analytically and numerically.

Analytical solutions

For an ion with initial position u_0 and velocity $\dot{u}_0$ at $\xi_0 = 0$, the following two relationships can be obtained from Eq. (2.28):

$$u_0 = u(0) = A \sum_{n=-\infty}^{\infty} C_{2n}, \tag{2.44}$$

$$\dot{u}_0 = \frac{du}{d\xi}\Big|_{\xi=0} = B \sum_{n=-\infty}^{\infty} C_{2n}. \tag{2.45}$$

For the convenience of calculation, set the amplitude of the fundamental frequency term $C_0 = 1$, then the other C_{2n} values can be obtained via the recursive relations of Eq. (2.36) and Eq. (2.37).

As an example of the calculation, Table 2.1 shows values of the C_{2n} ($-10 \leq n \leq 10$) terms for $q = 0.1$, 0.5 and 0.908 with $a = 0$.[1] The sum of C_{2n} shown in the last row of the table can be used to relate the initial conditions u_0 and $\dot{u}_0$ to A and B in Eq. (2.44) and Eq. (2.45). Then for any given value of (q, a) within the stable region, and with initial condition (u_0, $\dot{u}_0$), the full solution can be explicitly expressed in the form of Eq. (2.28).

In this way, for the (q , a) values listed in Table 2.1 and initial condition

$$u_0 = 1,\ \dot{u}_0 = 0; \tag{2.46}$$

the evaluations of u over ξ are shown in Figure 2.5 as the curves labeled "Analytical". The horizontal axes are also labeled as time t which is related to ξ as

$$t = \frac{2\xi}{\Omega}, \tag{2.47}$$

[1]For each corresponding negative q value, their C_{2n} has the same absolute values but are all positive.

Table 2.1: Calculated C_{2n} for a few typical values of q when $a = 0$.

q	0.1	0.5	0.908
β	0.07085	0.37374	0.99362
C_{-20}	8.9319e-30	2.2625e-22	9.5528e-19
C_{-18}	-3.5475e-26	-1.743e-19	-3.8005e-16
C_{-16}	1.1404e-22	1.083e-16	1.2105e-13
C_{-14}	-2.8935e-19	-5.289e-14	-3.0022e-11
C_{-12}	5.614e-16	1.9641e-11	5.5931e-09
C_{-10}	-7.989e-13	-5.3096e-09	-7.4617e-07
C_{-8}	7.8762e-10	9.8401e-07	6.6652e-05
C_{-6}	-4.9519e-07	-0.00011445	-0.0036027
C_{-4}	0.00017408	0.0072451	0.09938
C_{-2}	-0.026875	-0.19043	-0.98563
C_0	1.0	1.0	1.0
C_2	-0.023322	-0.088943	-0.10169
C_4	0.00014073	0.0023255	0.0037055
C_6	-3.8186e-07	-2.8624e-05	-6.8805e-05
C_8	5.8623e-10	2.0412e-07	7.7245e-07
C_{10}	-5.7801e-13	-9.4838e-10	-5.8035e-09
C_{12}	3.967e-16	3.0971e-12	3.1212e-11
C_{14}	-2.0036e-19	-7.4953e-15	-1.2607e-13
C_{16}	7.7578e-23	1.3979e-17	3.9639e-16
C_{18}	-2.3757e-26	-2.0703e-20	-9.9769e-19
C_{20}	5.8973e-30	2.493e-23	2.0554e-21
$\sum C_{2n}$	0.95012	0.73006	0.012157

with the unit of $2T_{RF}$ where T_{RF} is the RF period

$$T_{RF} = \frac{2\pi}{\Omega}. \tag{2.48}$$

Numerical integration

For each set of given (q, a) and (u_0, $\dot{u}_0$), the solution $u(\xi)$ can also be obtained by applying numerical integration to the Mathieu equation (2.6). The Runge-Kutta method to the 4^{th} order is used to calculate $u(\xi)$ for the same parameters and also shown in Figure 2.5 with label "RK4". The analytical and RK4 results agree well.

For $q = 0.909$ which is outside of the stable region, the value of β is not a real number and cannot be obtained in the method described above. So only the result of the numerical integration is shown. The envelope formed by the maxima of u increases exponentially along with ξ and therefore the solution $u(\xi)$ is indeed unstable.

In order to validate the numerical integration approach, more calculations were run with $a = 0$ and q around 0.908 to obtain the boundary between stable and unstable solutions. When the integration step width h is set to be

$$h = \frac{T_{RF}}{200} \tag{2.49}$$

or smaller, the maximum q allowing a stable solution was found to be

$$0.90804633 < q_m < 0.90804634 \tag{2.50}$$

(see Figure 2.6). The value of q_m agrees with the result obtained in the previous analytical approach in Eq. (2.42).

For (q, a) far away from the stability boundaries, a larger integration step width up to $h = \frac{T_{RF}}{20}$ can be good enough to correctly obtain the numerical solutions.

2.2 Ion acceptance and emittance

The ion motions in an RFQ can be better understood and characterized in the position-velocity phase space (u, $\dot{u}$) with the concept of acceptance and emittance.

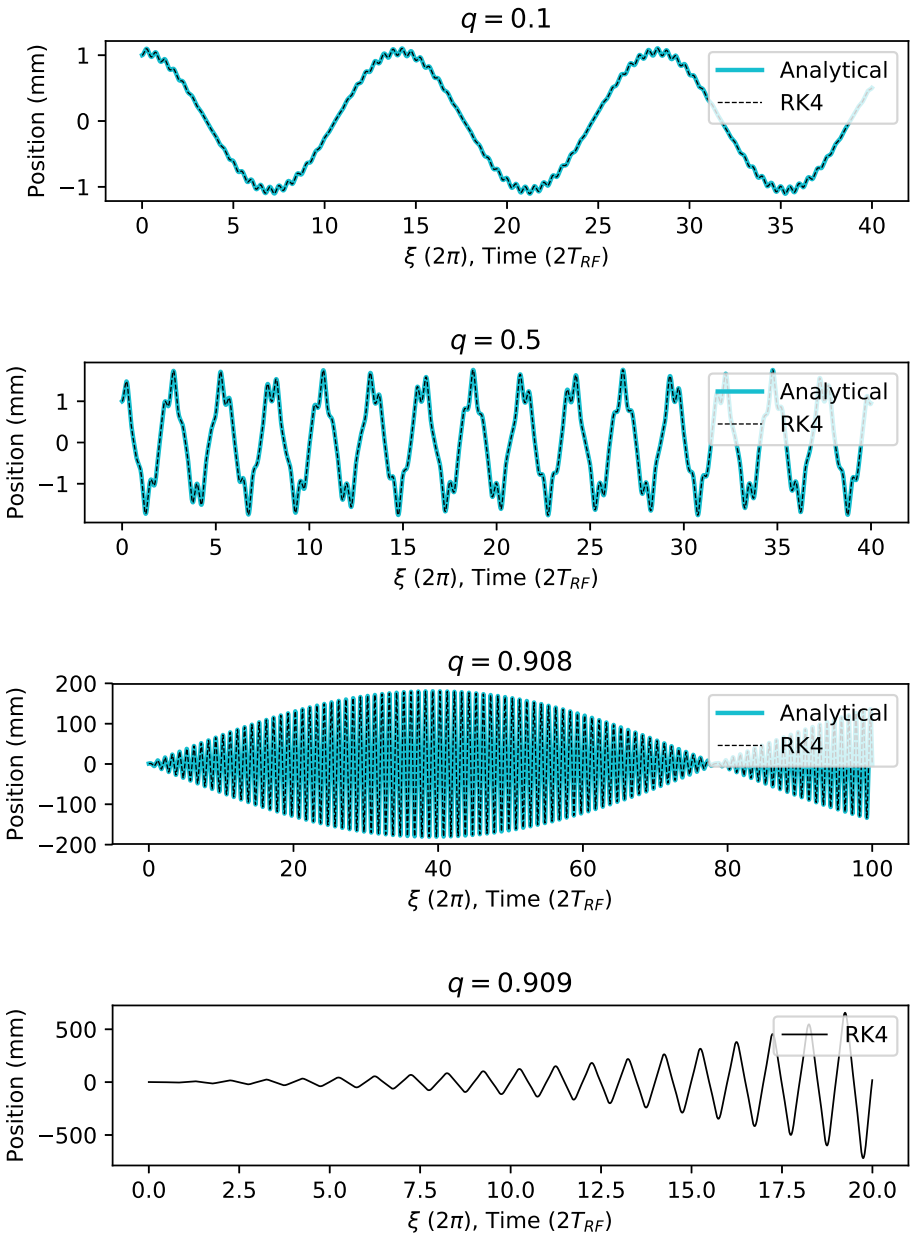

Figure 2.5: Solutions of the Mathieu equation for a few q values annotated in each plot when $a = 0$. The solutions are stable for $|q| < 0.90804633$; for $q = 0.909$ shown in the last plot, the solution is unstable.

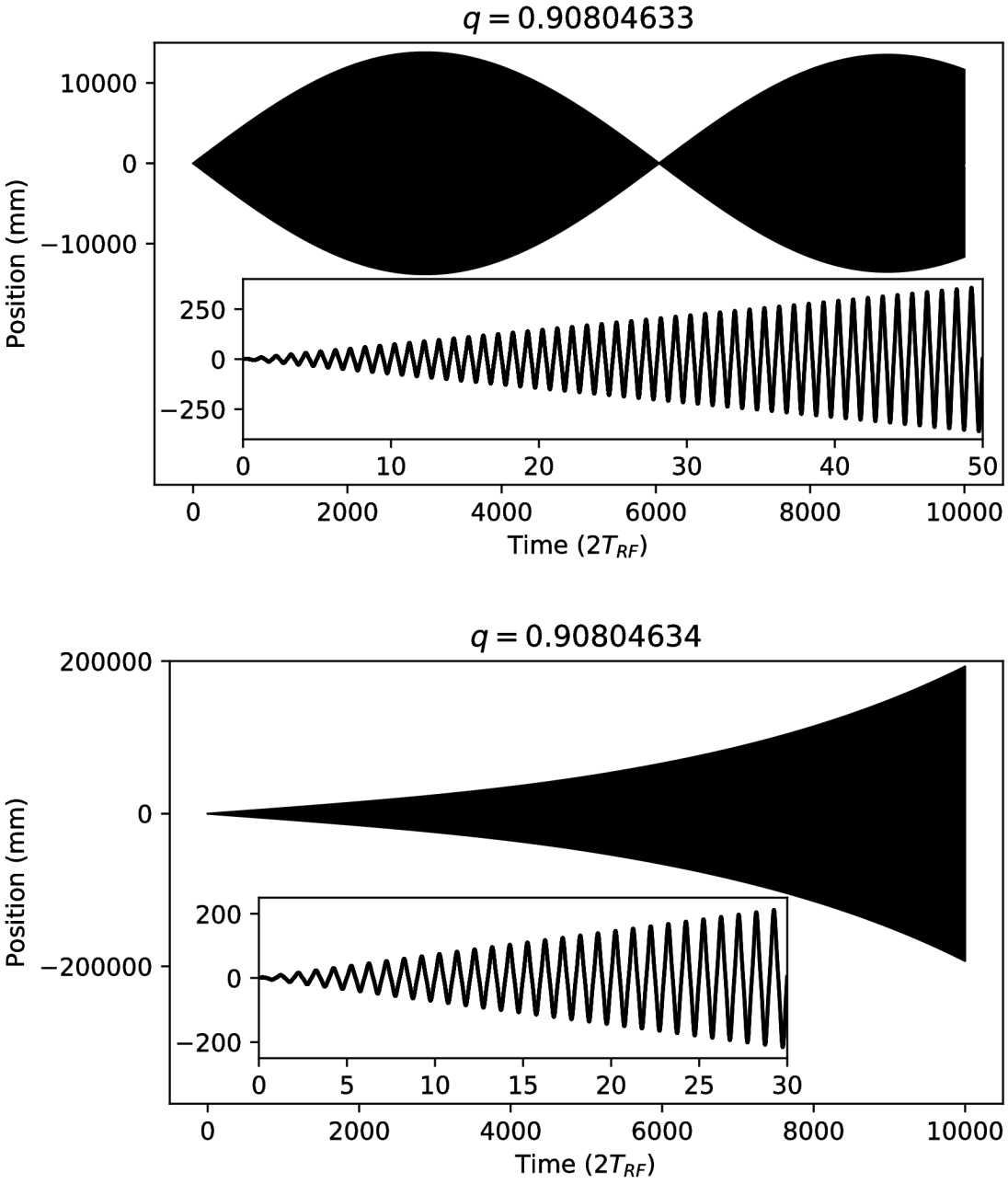

Figure 2.6: Stable and unstable solutions of Mathieu equation obtained by numerical integrations. The filled regions are actually dense curves with an oscillation period T_{RF} as shown in the zoomed-in plots in the insets.

The acceptance of an RFQ ϵ_a is the region of (u, $\dot{u}$) that allows ions to be stably confined or transmitted, while the emittance ϵ_e is the phase space area occupied by the ions existing in the RFQ. Usually

$$\epsilon_a = \epsilon_e \tag{2.51}$$

when there is a sufficient amount of ions in the system.

Acceptance ellipses

As an example, for an ion with ($q = 0.1$, $a = 0$) and initial condition ($u_0 = 1$, $\dot{u}_0 = 0$), Figure 2.7(a) shows its position and velocity in the phase space corresponding to the y axis. An interesting fact is, if plotting only these specific (u, $\dot{u}$) exactly one RF cycle apart, then they land perfectly on ellipses [Daw75] as shown in Figure 2.7(b). The fact is true for any other initial condition (u_0, $\dot{u}_0$) and any other (q, a) values within the stable region.

The RF phase labeled for each ellipse in Figure 2.7 is the initial phase φ_0 in the RF potential

$$\phi_{RF} = (U - V\cos(\Omega t + \varphi_0))\frac{(y^2 - z^2)}{r_0^2}. \tag{2.52}$$

The requirement for an ion to be accepted in the RFQ is that its maximum displacement from the x axis must be within r_0, which is the physical boundary defined by the electrodes as shown in Figure 2.1. In Figure 2.7, the maximum displacement of the ion is the semi-major of the ellipse with initial RF phase $\varphi_0 = \pi$. Thus the ions which can be accepted are the ones with initial condition (u_0, $\dot{u}_0$) within this ellipse. For any other initial RF phase φ_0, the acceptance is the corresponding ellipse.

It is noteworthy that, in the z axis, an ion's maximum displacement is the semi-major of the ellipse with initial RF phase $\varphi_0 = 0$. The difference comes from the sign of q and hence the resulting C_{2n} coefficients in Eq. (2.28). C_{2n} are all positive when $a - 2q > 0$. For $a - 2q < 0$, C_{2n} is negative when n is an odd number.

The equation of these ellipses can be derived analytically as below.

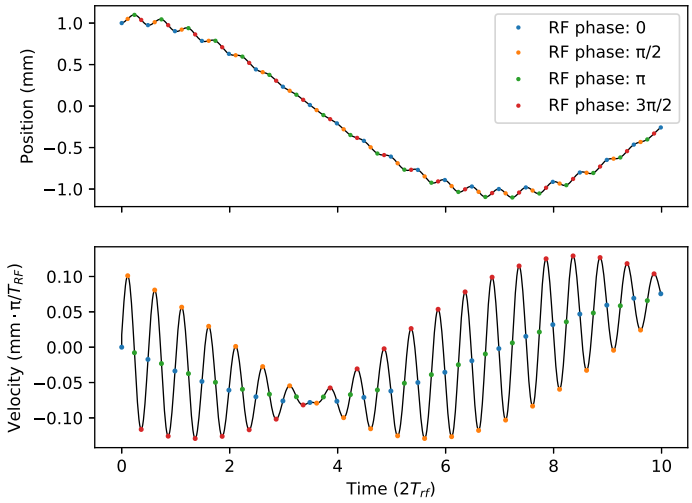

(a)

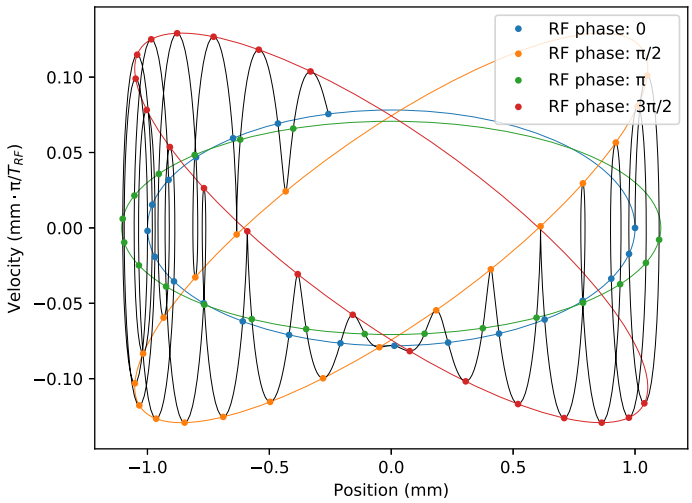

(b)

Figure 2.7: (a) Position and velocity of an ion from the solution of the Mathieu equation. (b) The same position and velocity plotted in phase space $(u, \dot{u})$, showing ellipses corresponding to each initial phase.

Derivation of ellipses from Mathieu equation solutions

The non-zero initial phase φ_0 in the RF potential adds a variable in the Mathieu equation

$$\frac{d^2u}{d\xi^2} + [a - 2q\cos(2\xi + \varphi_0)]u = 0. \tag{2.53}$$

Then the solution of Eq. (2.53) is

$$u_{\varphi_0}(\xi) = A\sum_{n=-\infty}^{\infty} C_{2n}\cos[(\beta+2n)(\xi+\frac{\varphi_0}{2})]+B\sum_{n=-\infty}^{\infty} C_{2n}\sin[(\beta+2n)(\xi+\frac{\varphi_0}{2})]. \tag{2.54}$$

The above expression can be expanded using the trigonometric relations to separate the terms for ξ and φ_0

$$\begin{aligned} u_{\varphi_0}(\xi) =& A\sum_{n=-\infty}^{\infty} C_{2n}\cos[(\beta+2n)\xi]\cos[(\beta+2n)\frac{\varphi_0}{2}]- \\ & A\sum_{n=-\infty}^{\infty} C_{2n}\sin[(\beta+2n)\xi]\sin[(\beta+2n)\frac{\varphi_0}{2}]+ \\ & B\sum_{n=-\infty}^{\infty} C_{2n}\sin[(\beta+2n)\xi]\cos[(\beta+2n)\frac{\varphi_0}{2}]+ \\ & B\sum_{n=-\infty}^{\infty} C_{2n}\cos[(\beta+2n)\xi]\sin[(\beta+2n)\frac{\varphi_0}{2}]. \end{aligned} \tag{2.55}$$

For $\xi_k = k\pi$ $(k = 0, 1, 2, \dots)$ corresponding to the successive points $(u_{\varphi_0}(\xi_k), \dot{u}_{\varphi_0}(\xi_k))$ on each ellipse,

$$\cos(\beta+2n)\xi_k = \cos\beta\xi_k,\ \sin(\beta+2n)\xi_k = \sin\beta\xi_k \tag{2.56}$$

Then the solution Eq. (2.55) can be simplified as

$$u_{\varphi_0}(\xi_k) = u_{\varphi_0}(0)\cos\beta\xi_k + u_{\varphi_0}(\xi_K)\sin\beta\xi_k, \tag{2.57}$$

where

$$u_{\varphi_0}(0) = A\sum_{n=-\infty}^{\infty} C_{2n}\cos\frac{\varphi_0}{2}(\beta+2n) + B\sum_{n=-\infty}^{\infty} C_{2n}\sin\frac{\varphi_0}{2}(\beta+2n). \tag{2.58}$$

and

$$u_{\varphi_0}(\xi_K) = -A \sum_{n=-\infty}^{\infty} C_{2n} \sin \frac{\varphi_0}{2}(\beta + 2n) + B \sum_{n=-\infty}^{\infty} C_{2n} \cos \frac{\varphi_0}{2}(\beta + 2n); \tag{2.59}$$

$$\xi_K = K\pi = \frac{2m\pi + \frac{\pi}{2}}{\beta}, \tag{2.60}$$

where m is an integer.

In a similar way,

$$\dot{u}_{\varphi_0}(\xi_k) = \dot{u}_{\varphi_0}(0) \cos \beta\xi_k + \dot{u}_{\varphi_0}(\xi_K) \sin \beta\xi_k, \tag{2.61}$$

where

$$\dot{u}_{\varphi_0}(0) = -A \sum_{n=-\infty}^{\infty} (\beta{+}2n) C_{2n} \sin \frac{\varphi_0}{2}(\beta{+}2n) + B \sum_{n=-\infty}^{\infty} (\beta{+}2n) C_{2n} \cos \frac{\varphi_0}{2}(\beta{+}2n) \tag{2.62}$$

and

$$\dot{u}_{\varphi_0}(\xi_K) = -A \sum_{n=-\infty}^{\infty} (\beta{+}2n) C_{2n} \cos \frac{\varphi_0}{2}(\beta{+}2n) - B \sum_{n=-\infty}^{\infty} (\beta{+}2n) C_{2n} \sin \frac{\varphi_0}{2}(\beta{+}2n). \tag{2.63}$$

Now $u_{\varphi_0}(\xi)$ and $\dot{u}_{\varphi_0}(\xi)$ can be written in the form of an ellipse's standard parametric equations

$$u_{\phi_0}(\xi) = u_M \cos(\beta\xi_k + \theta_1) \tag{2.64}$$

$$\dot{u}_{\phi_0}(\xi) = \dot{u}_M \sin(\beta\xi_k + \theta_2), \tag{2.65}$$

where

$$u_M = \sqrt{u_{\varphi_0}(0)^2 + u_{\varphi_0}(\xi_K)^2} \tag{2.66}$$

$$\dot{u}_M = \sqrt{\dot{u}_{\varphi_0}(0)^2 + \dot{u}_{\varphi_0}(\xi_K)^2} \tag{2.67}$$

and

$$\theta_1 = \arctan2(-u_{\varphi_0}(\xi_K), u_{\varphi_0}(0)) \tag{2.68}$$

$$\theta_2 = \arctan2(\dot{u}_{\varphi_0}(0), \dot{u}_{\varphi_0}(\xi_K)). \tag{2.69}$$

The area of the ellipse A_e is

$$A_e = \pi u_M \dot{U}_M \cos(\theta_2 - \theta_1) = \pi[-u(0)\dot{u}(\xi_K) + u(\xi_K)\dot{u}(0)]. \tag{2.70}$$

Twiss parameters

The ellipses can also be expressed in the so-called Twiss parameters which are often used in accelerator physics to describe the transverse beam dynamics of charged particles:

$$C_T u^2 + 2A_T u\dot{u} + B_T \dot{u}^2 = \epsilon, \tag{2.71}$$

with the constraint of

$$C_T B_T - A_T^2 = 1. \tag{2.72}$$

Then

$$\epsilon = \frac{A_e}{\pi}, \tag{2.73}$$

where A_e is the area of the ellipse. The angle θ between the ellipse's major-axis to the horizontal coordinate is

$$\theta = \frac{1}{2} \arctan \frac{2A_T}{C_T - B_T}. \tag{2.74}$$

A few characteristic points on the ellipse are calculated and shown in Figure 2.8. The intercepts of the ellipse with the horizontal or vertical axis are obtained by setting $\dot{u} = 0$ or $u = 0$. The coordinates of the maximum u or $\dot{u}$ on the ellipse are obtained by finding $\frac{du}{d\dot{u}} = 0$ or $\frac{d\dot{u}}{du} = 0$.

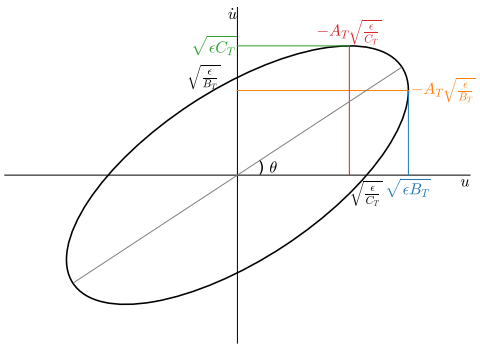

Figure 2.8: An ellipse corresponding to the Twiss parameters.

The Twiss parameters are then related to the parameters in Eq. (2.66) – Eq. (2.70) in the following way:

$$u_M = \sqrt{\epsilon B_T} \tag{2.75}$$

$$\dot{u}_M = \sqrt{\epsilon C_T} \tag{2.76}$$

$$\tan(\theta_2 - \theta_1) = -\frac{1}{A_T} \tag{2.77}$$

$$-u(0)\dot{u}(\xi_K) + u(\xi_K)\dot{u}(0) = \epsilon. \tag{2.78}$$

Analytical calculation of acceptance

The acceptance of the RFQ in the y axis can be calculated with the special case of initial phase $\phi_0 = 0$ and $B = 0$ in Eq. (2.54). Then

$$\epsilon = -u(0)\dot{u}(\xi_K) \tag{2.79}$$

and

$$u(0) = A \sum_{n=-\infty}^{\infty} C_{2n}, \tag{2.80}$$

$$\dot{u}(\xi_K) = -A \sum_{n=-\infty}^{\infty} (\beta + 2n) C_{2n}. \tag{2.81}$$

In order to account for the physical dimensions of the RFQ, the acceptance ϵ needs be normalized to the maximum ion position r_0 limited by the quadrupole electrodes

$$r_0 = A \sum_{n=-\infty}^{\infty} |C_{2n}|. \tag{2.82}$$

Acceptance of the RFQ in the y axis analytically calculated in this way is shown in Figure 2.9.

For the z axis, the acceptance is Figure 2.9 flipped vertically along $a = 0$. The combined acceptance ϵ_{yz} of an RFQ for transmitting ions is the product of its acceptances in the y and z axes

$$\epsilon_{yz} = \epsilon_y \epsilon_z. \tag{2.83}$$

The calculated values of ϵ_{yz} are shown in Figure 2.10.

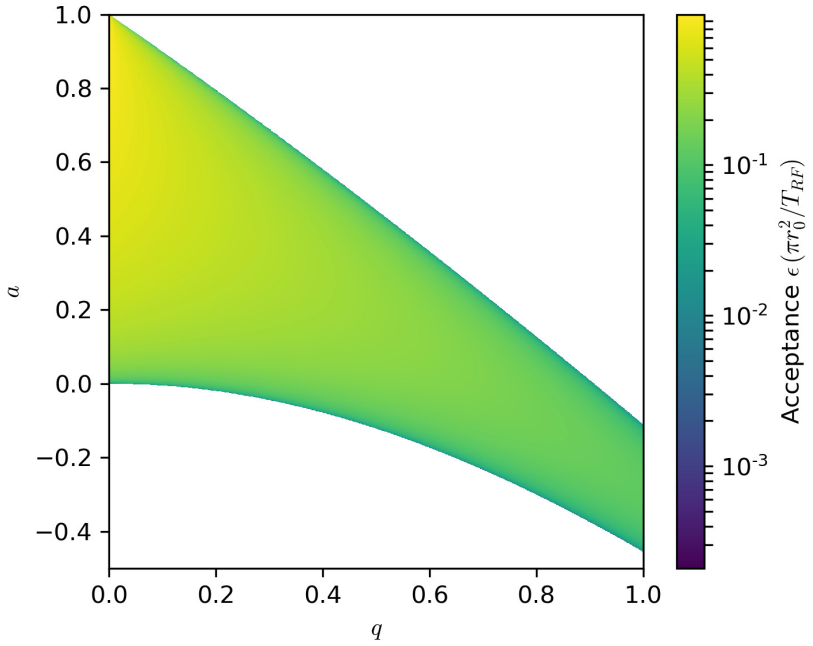

Figure 2.9: Acceptance of the RFQ in one of the transverse directions y calculated analytically from the Mathieu equation's solution.

2.3 RFQ ion guide

An RFQ ion guide is a straightforward application of the RFQ. Usually the DC voltage U of the ion guide is set to 0 to obtain larger acceptance (see Figure 2.10 along $a = 0$) and consequently higher ion transmission efficiency.

Acceptance of the ion guide ϵ_{yz} as a function of q (proportional to the RF voltage V) when $U = 0$ is shown in Figure 2.11. The results are from both analytical calculation and the area of a fitted ellipse using the relationship

$$\epsilon_{yz} = \frac{A_{e,y}}{\pi}\frac{A_{e,z}}{\pi}. \tag{2.84}$$

Values of the two sets of results agree well as shown in the figure.

The acceptance is maximum when $q = 0.577$. To have better than half of the maximum acceptance, q needs to be between 0.271 to 0.817.

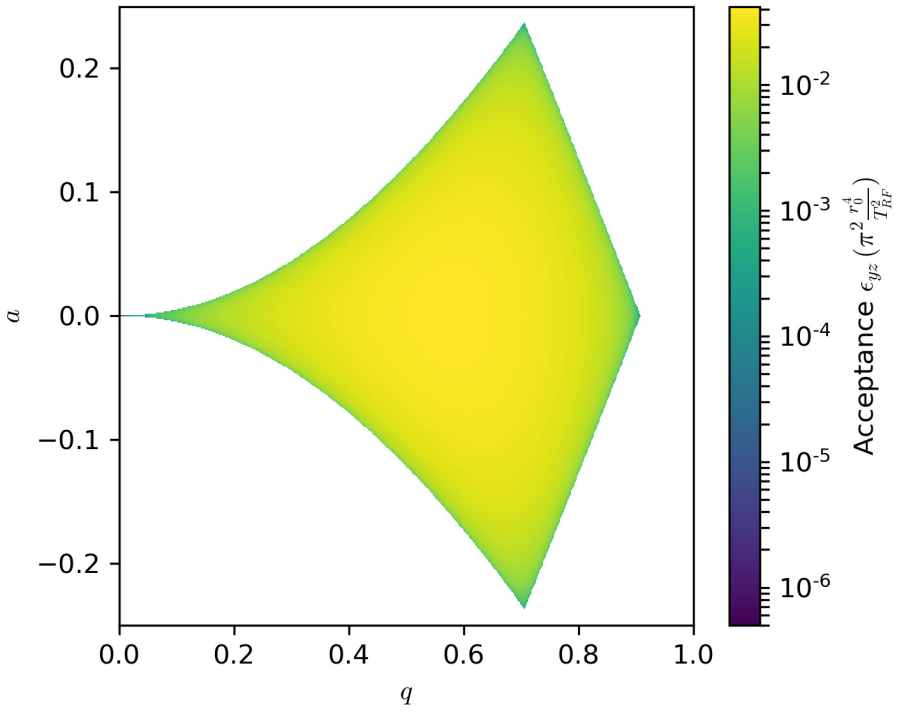

Figure 2.10: Acceptance of the RFQ in both the y and z axes.

2.4 Quadrupole mass filter

A quadrupole mass filter (QMF) uses the stability parameters near the upper tip of the stability diagram in Figure 2.4 with $q \approx 0.706$ and $a \approx 0.237$. In this case, only the ions within a narrow range of mass can pass through the QMF.

The QMF can also work as a quadrupole mass spectrometer (QMS) by scanning the operating parameters while the ions are continuously injected into the system. The ions of different mass will subsequently pass through the QMS and produce a measured mass spectrum.

2.4.1 Mass scan of QMS

The mass scan of a QMS can be done with two different approaches as below.

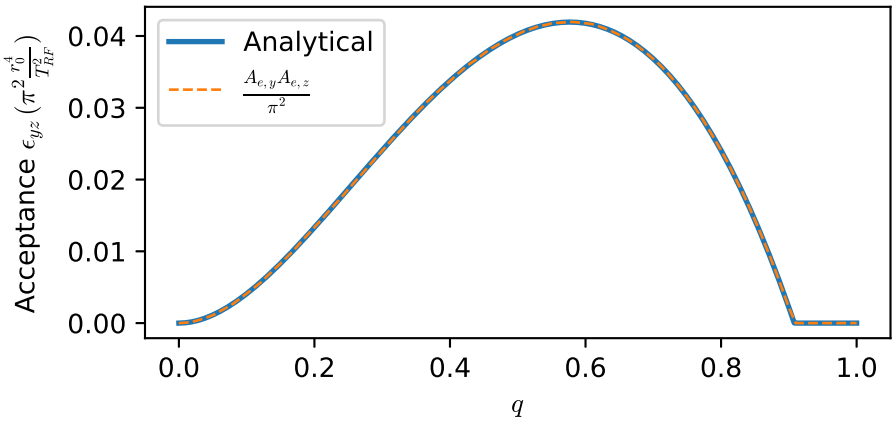

Figure 2.11: Acceptance of the RF ion guide when $a = 0$ from two sets of calculations.

Approach 1: QMS with voltage sweep

The approach to operating the RFQ as a QMS with voltage sweep is often used when the RF voltage of the QMS is provided by a resonant circuit that performs best at a fixed frequency. The mass scan is done by sweeping both the DC and RF voltages to let the ions of different mass pass through the tip of their stable region one after another, see Figure 2.12.

The voltages V and U are normalized with units shown in the labels of Figure 2.12 q_{m_1} and a_{m_1} which are the stability parameters of the ion with mass m_1. According to Eq. (2.43), the mass scan for this ion reaches the tip of its stable region when

$$q_{m_1} = q_t = 0.7059961, \tag{2.85}$$
$$a_{m_1} = a_t = 0.2369940. \tag{2.86}$$

The mass m is related to the RF voltage V at the tip of its stable region via

$$m = V \cdot \frac{4e}{\Omega^2 r_0^2 q_t}, \tag{2.87}$$

as labeled on the top axis of Figure 2.12.

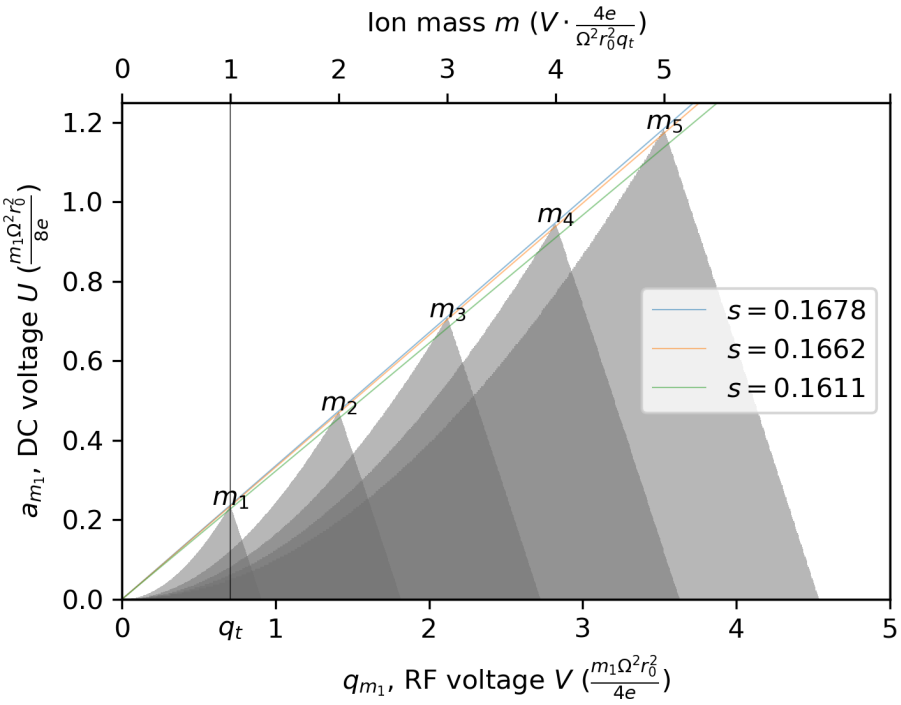

Figure 2.12: Mass scan of the QMS by sweeping both RF and DC voltages V and U. The overlapping shaded regions are stable regions of ions with different masses m_1 – m_5. The slope of the scan lines is $s = \frac{U}{V}$. The values on horizontal and vertical axes are dimensionless for the stability parameters q_{m_1} and a_{m_1} corresponding to an ion of mass m_1. The mass of ions corresponding to each tip of the stable region is given as the top axis.

The DC voltage is set to be

$$U = sV, \tag{2.88}$$

where the slope $s = \frac{U}{V}$ as the mass scan line is related to the mass resolving power R of the QMS:

$$R = \frac{m}{\Delta m}. \tag{2.89}$$

Details of the mass resolving power of the QMS will be discussed in Section 2.4.2.

Approach 2: QMS with frequency sweep

This approach is possible when a wide frequency band of the RF voltage can be provided by the hardware. Then both the RF and DC voltages can be fixed and only sweep the RF frequency Ω (see Figure 2.13). The mass of ions m is related to Ω as

$$m = \frac{1}{\Omega^2} \cdot \frac{4eV}{r_0^2 q_t}. \tag{2.90}$$

For different mass resolving power R, the DC voltage U is set at different values of s or a

$$U = sV = \frac{a}{2q_t}V. \tag{2.91}$$

2.4.2 QMS mass resolving power and transmission efficiency

The number of ions which can be transmitted by a QMS is related to the acceptance ϵ_{yz}. For the special case when there are a large number of ions randomly distributed uniformly in the phase space $(u_y, \dot{u}_y)$ and $(u_z, \dot{u}_z)$, the ion transmission efficiency T is proportional to the acceptance ϵ_{yz}

$$T \propto \epsilon_{yz}. \tag{2.92}$$

Then Δm_{FWHM}, defined as the full-width at half-maximum (FWHM) of the acceptance ϵ_{yz}, can be used to calculate the mass resolving power R via $R = m/\Delta m_{FWHM}$. Analytically calculated acceptance of an RFQ shown in Figure 2.10 is used to derive the mass resolving power (see Figure 2.14).

The mass resolving power R as a function of the stability parameter a (or the DC to RF ratio s) shown in Figure 2.14 is only true for a theoretically

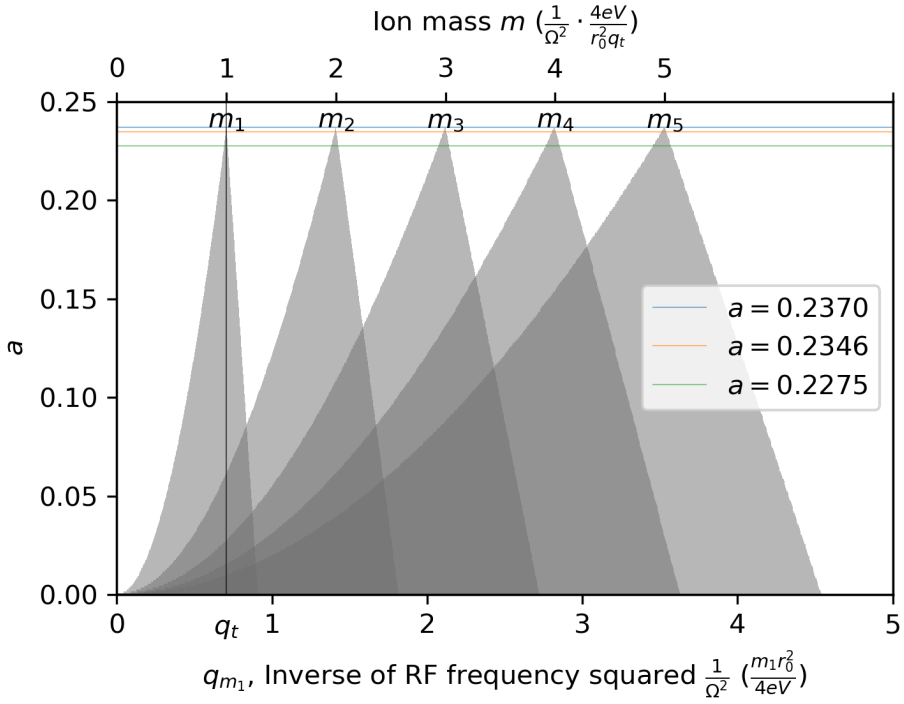

Figure 2.13: Mass scan of the QMS by sweeping the RF frequency. For more details see Figure 2.12 and text.

idealized QMF with infinite length to allow the ions to experience an infinite number of RF cycles. The mass resolving power R of a realistic QMF is also limited by the length of the quadrupole electrodes.

Limitation of mass resolving power from RF cycles

An ion of mass m_i in the unstable region of a QMF will have an exponentially increasing amplitude of its oscillatory motion (similar to the bottom plot shown in Figure 2.5). Depending on the stability parameters (q_i, a_i) and the ion's initial position and velocity, the ion takes a certain number of RF cycles $n_{RF,i}$ to have its amplitude reach r_0 and hit the electrodes to be filtered. If the number of RF cycles experienced by the ion in the QMF is smaller than $n_{RF,i}$, the ion can fly through the QMF even though its stability parameters (q_i, a_i) are outside of the theoretical stable region. In such cases, the transmission of the unwanted ions reduces the mass resolving

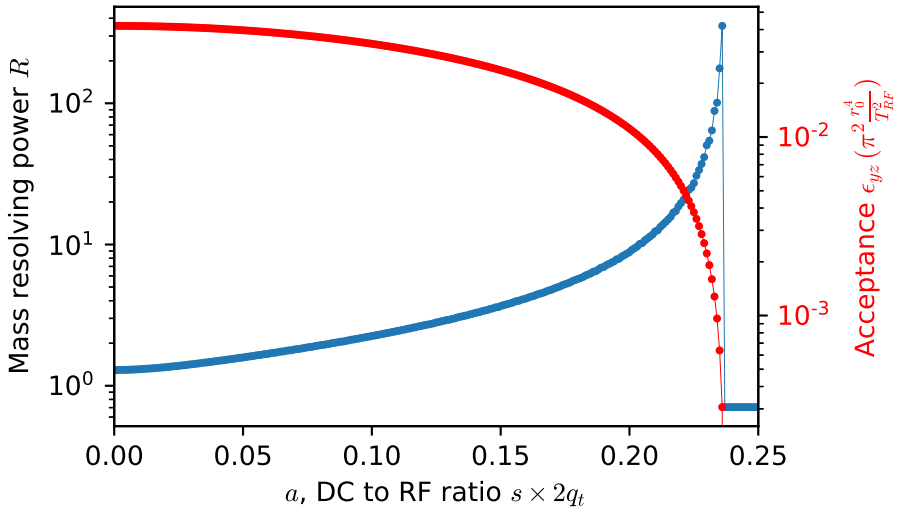

Figure 2.14: Mass resolving power of a QMS and its acceptance corresponding to ion transmission efficiency.

power of a QMF.

The limitation of mass resolving power by the number of RF cycles can be empirically expressed as [Dou09]

$$R_n = \frac{n_{RF}^2}{h}, \tag{2.93}$$

where $h \approx 12.25$ was obtained by Paul et al. [PRVZ58]. Later, $h \approx 20$ was found by Austin et al. based on more experimental results [AHL76]. The exact value of h is also dependent on the QMF such as the detailed electrode geometry.

Note that these experimentally obtained values of h are based on mass scans with RF amplitude (shown in Figure 2.12). The value of h would be smaller for mass scans with RF frequency as shown in Figure 2.13.

2.5 Linear Paul trap

A linear Paul trap (LPT) uses RFQs to confine ions in the transverse directions y and z. The DC potential U of an LPT is usually set to 0 to have

larger ion acceptance, similar to an RF ion guide described in Section 2.3.

To confine ions in the longitudinal direction, a DC trapping potential along the x axis is needed. One way of forming the longitudinal potential is to use a segmented RFQ with configurable DC voltage for each segment (see Figure 2.15(a)). The DC voltage U_n is the same for the two diagonal pairs of electrodes, as shown in Figure 2.15(b). Note that in this case, the DC voltage U_n doesn't contribute to the quadrupole potential, hence the stability parameter $a = 0$.

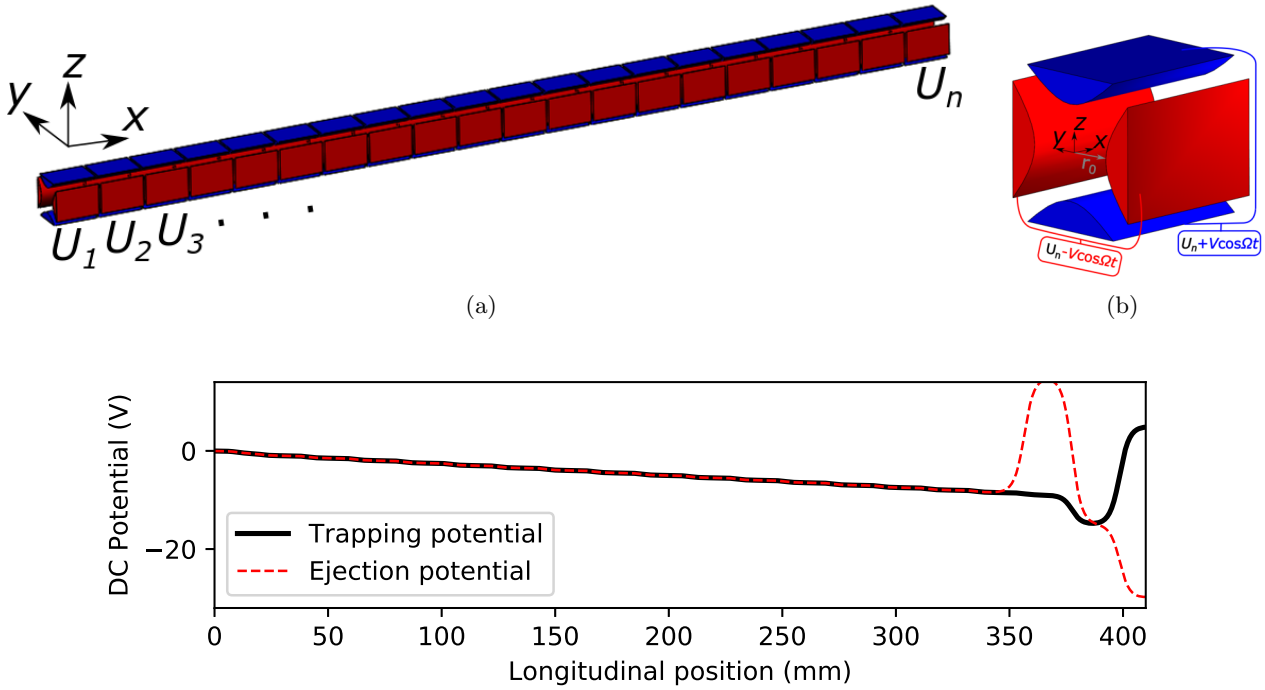

(a) (b)

(c)

Figure 2.15: (a) Illustration of a linear Paul trap consisting of segmented quadrupole electrodes. (b) Electric connection for each set of quadrupole electrodes. (c) DC potential of the LPT along the x axis. See text for details.

The LPT for this study also needs to provide a cooling effect to trap and store the ions. The ion cooling can be achieved by filling the LPT with buffer gas to damp the ions via ion-gas collisions [Kim97]. The collisions

were found to be cooling down the ions when the gas molecules are lighter than the ions [MD68]. Helium is a good choice as the buffer gas due to its light atomic mass. In addition, helium is a noble gas so it is chemically inert and can reach high purity to reduce ion loss due to charge exchange from other contaminate gas molecules.

A typical configuration of the DC potential for the LPT along the x axis is shown in Figure 2.15(c). The majority of the segments' purpose is to form an electric field (drag field) to guide the cooled ions to the location of the lowest potential near the exit. After enough ion cooling and accumulation, the DC voltages of the last three segments are switched to form an ejection potential, and the ions will be ejected as an ion bunch out of the LPT with small emittance, time spread and energy spread.

2.5.1 Ion cooling with buffer gas

Ion mobility

The motion of ions in a buffer gas can be quantitatively described using the concept of ion mobility K, which describes a constant drift velocity of ions v_d in the buffer gas with the presence of an electric field E

$$v_d = KE. \tag{2.94}$$

For a singly charged positive ion, the electric force experienced by the ion is balanced by a frictional force from the buffer gas from the averaged effect of ion-gas collisions:

$$F_f = -eE = -\frac{ev_d}{K}. \tag{2.95}$$

For an ion of mass m with initial velocity v_i, the ion's equation of motion is

$$m\frac{dv}{dt} = -\frac{ev}{K} + eE = -\frac{e(v - v_d)}{K}, \tag{2.96}$$

then the ion's velocity as a function of time is

$$v(t) = v_d + (v_i - v_d)e^{-\frac{t}{\tau_v}}, \tag{2.97}$$

where

$$\tau_v = \frac{mK}{e} \tag{2.98}$$

is the time constant of the ion slowing down from v_i to v_d.[1].

For $^{136}Ba^+$ ions in helium gas, when the ion drift velocity $v_d < 0.268$ mm/µs (kinetic energy $K_e < 0.05$ eV) the experimentally measured ion standard mobility is found to be [VM95].

$$K_0 = \frac{N}{N_0} K = 1.66 \times 10^{-3} \text{ m}^2\text{V}^{-1}\text{s}^{-1}, \tag{2.99}$$

where $N_0 = 2.687 \times 10^{25}$ m^{-3} is the standard number density of ideal gas at 0°C and 1 bar. The ion mobility is smaller at larger ion velocities. At temperature 313 K (the temperature used in the literature [VM95]) and buffer gas pressure of 0.01 mbar, the ions' slowing down time constant for small initial and final drift velocity is calculated to be $\tau_v = 272$ µs, which is inversely proportional to the buffer gas pressure.

2.5.2 Ion cooling in LPT

The ion cooling in an LPT can be approximately described by including a damping term in the ion's equation of motion

$$m\frac{d^2u}{dt^2} = \frac{-2eu}{r_0^2}(U - V\cos\Omega t) - \frac{e}{K}\frac{du}{dt}. \tag{2.100}$$

Using the same parameters q, a and ξ in Section 2.1, the equation becomes

$$\frac{d^2u}{d\xi^2} + 2k\frac{du}{d\xi} + (a - 2q\cos 2\xi)u = 0, \tag{2.101}$$

where the damping coefficient $k = \frac{e}{mK\Omega}$ comes from the ion cooling effect of the buffer gas.

Following McLachlan [McL51], Whetten [Whe74] and Kim [Kim97], Eq. (2.101) can be solved by defining

$$u = u_1 e^{-k\xi}, \tag{2.102}$$

then Eq. (2.101) will come to a similar form as the Mathieu equation:

$$\frac{d^2u_1}{d\xi^2} + (a - k^2 - 2q\cos 2\xi)u_1 = 0. \tag{2.103}$$

[1]Note that Eq. (2.97) and Eq. (2.98) are no longer valid when K is dependent on the ion velocity.

After further using the substitution of an adjusted stability parameter

$$\bar{a}_u = a - k^2, \tag{2.104}$$

u_1 will have the same solutions as described in Section 2.1.1 in the stable region of ($\bar{a}_u$, q).

In this way, for any initial position u and velocity $\dot{u}$, the evolution of u as a function of ξ or t with any initial condition $(u_0, \dot{u}_0)$ is obtained as Eq. (2.102). The $e^{-k\xi}$ term in the solution of u leads to the exponential decay of the u with a time constant

$$\tau_u = \frac{2mK}{e}. \tag{2.105}$$

Such calculations were done using the standard mobility in Eq. (2.99) for $^{136}Ba^+$ in helium buffer gas. The derived parameters for helium pressure from 0.01 mbar to 10 mbar are shown in Table 2.2.

Table 2.2: Parameters of $^{136}Ba^+$ ion cooling in helium buffer gas at different pressures.

pressure (mbar)	0.01	0.1	1	10
Ion mobility K ($m^2V^{-1}s^{-1}$)	192.7	19.27	1.927	0.1927
Damping coefficient k	5.86×10^{-4}	5.86×10^{-3}	5.86×10^{-2}	0.586
Adjusted stabi. param. $\bar{a}_u$	-3.4×10^{-7}	-3.4×10^{-5}	-3.4×10^{-3}	-0.34
Cooling time const. τ_u (µs)	544	54.4	5.44	0.544

Using the values of k and $\bar{a}_u$ from Table 2.2, solutions of u were obtained for ($q = 0.1$, $a = 0$) in the form of Eq. (2.102). The coordinate z was used as u so that the initial condition of ($u_0 = 1$, $\dot{u}_0 = 0$) at $t = 0$ has the maximum position, this is equivalent to having initial RF phase $\varphi_0 = \pi$ in Figure 2.7. The results are plotted in Figure 2.16 with label Analytical.

The analytical result was not obtained at 10 mbar pressure because ($q = 0.1$, $\bar{a}_u = -0.34$) leads to an imaginary number of β and hence the solution u_1 is outside of the stable region of the Mathieu equation's solution. Due to the $e^{-k\xi}$ term in Eq. (2.102), the solution $u = u_1 e^{-k\xi}$ will still be stable but needs to be solved differently than Section 2.1.1. In fact u will have stable solution in an extended stable region up to $\Re(\mu) < k$ [Whe74], where $\mu = i\beta$ is introduced in the previous Eq. (2.27).

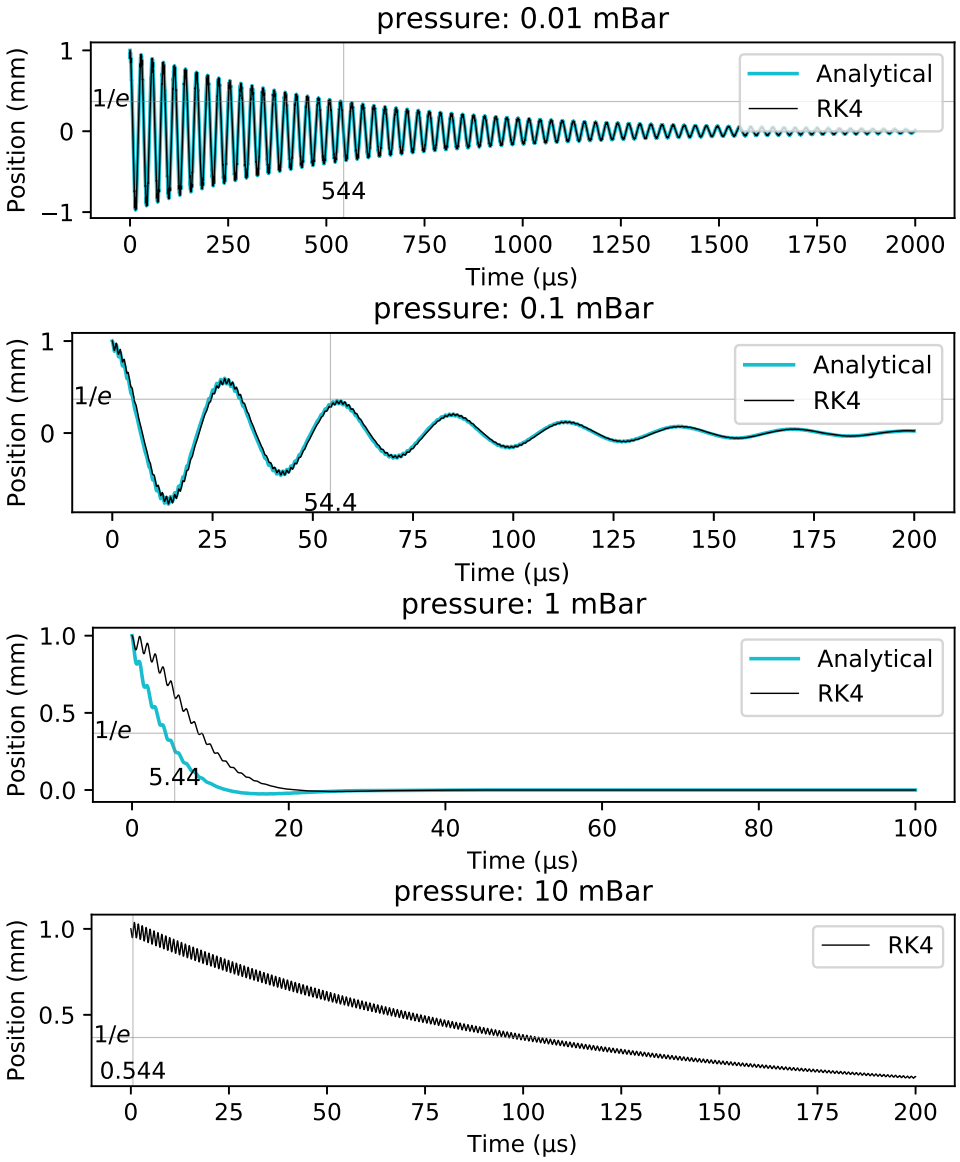

Figure 2.16: Analytical and numerical calculation of ion cooling with buffer gas using the ion mobility at different gas pressures as annotated in each plot. The stability parameters are ($q = 0.1$, $a = 0$). See text for details.

Numerical solutions

The damped Mathieu Eq. (2.101) can also be solved numerically using the Runge-Kutta method similarly as described in Section 2.1.4. The results are plotted in Figure 2.16 with label RK4 and overlaid with the analytical solutions for buffer gas pressures of 0.01 mbar to 1 mbar.

The analytical and numerical solutions are almost the same for the gas pressure of 0.01 and 0.1 mbar when the damping coefficient k is small. For gas pressure of 1 mbar, there is a noticeable discrepancy as shown in Figure 2.16. In this case, the analytical solution is found to be incorrect because the $e^{-k\xi}$ term leads to a large decrease of the amplitude from the beginning, when the velocity $\dot{u}$ is still small. In these cases, the RK4 numerical solution obtained the correct evolution of $u(t)$.

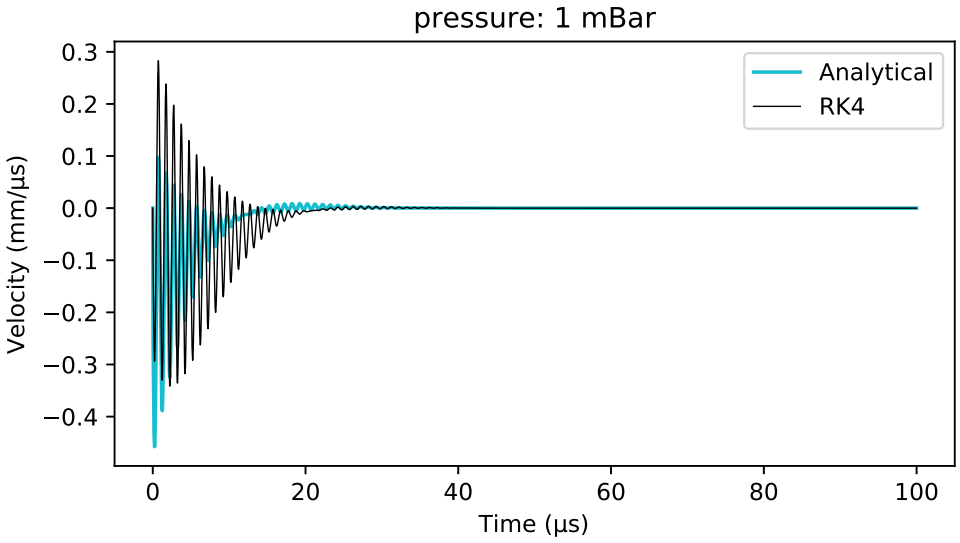

Figure 2.17: Ion velocity of analytical and numerical solutions shown in Figure 2.16.

2.5.3 Optimum gas pressure for ion cooling

The ion cooling time constant τ_u is inversely proportional to the buffer gas pressure in Eq. (2.105) and Table 2.2. The values of τ_u annotated in the plots of Figure 2.16 correctly indicate when the envelope of the waveform decreases to $1/e$ ($e = 2.71828\ldots$) for the gas pressure of 0.01 and 0.1 mbar.

However, at a higher pressure of 1 mbar and 10 mbar, the actual ion cooling time constant is significantly larger. In fact, the ions are cooled more slowly at 10 mbar than at 0.1 mbar.

Macromotion as damped oscillation

The unexpected slower ion cooling rate at higher gas pressure was explained by Kim in Section 4.2 of his dissertation [Kim97], where the macromotion of the ions is described as a damped oscillation with the presence of buffer gas:

$$\frac{d^2\bar{u}}{dt^2} + 2\bar{k}\frac{d\bar{u}}{dt} + \bar{\omega}^2 = 0, \tag{2.106}$$

where

$$\bar{k} = \frac{e}{2mK} \tag{2.107}$$

and the other variables $\bar{u}$ and $\bar{\omega}$ are the same as in Eq. (2.9) to Eq. (2.21). The fastest ion cooling occurs at the critical damping when $\bar{k} = \bar{\omega}$. For $q = 0.1$ and RF frequency $f_{RF} = 1$ MHz, this corresponds to a helium gas pressure of 1.2 mbar. The slower ion cooling rate at 10 mbar is caused by over-damping.

For a larger value of $q = 0.5$, around which is used commonly in RFQ ion coolers, the critical damping occurs at a higher helium pressure gas pressure of 6.0 mbar. Calculations of ion cooling were done for this q value and shown in Figure 2.18. As expected, the actual ion cooling rate at 10 mbar is shorter than when $q = 0.1$ in Figure 2.16.

For the lower helium gas pressure, the macromotion is under-damped and the time constant

$$\tau_{\bar{u}} = \frac{1}{\bar{k}} = \frac{2mK}{e} \tag{2.108}$$

is the same as τ_u obtained earlier in Eq. (2.105).

The buffer gas pressure in RFQ coolers is usually limited to be lower than 0.1 mbar by the vacuum system. At this range, higher gas pressure is more optimum in achieving a faster ion cooling rate.

Ion cooling in the axial direction

In the axial direction x, the ions experience only a DC trapping potential as shown in Figure 2.15. At the final stage of ion cooling, the axial DC

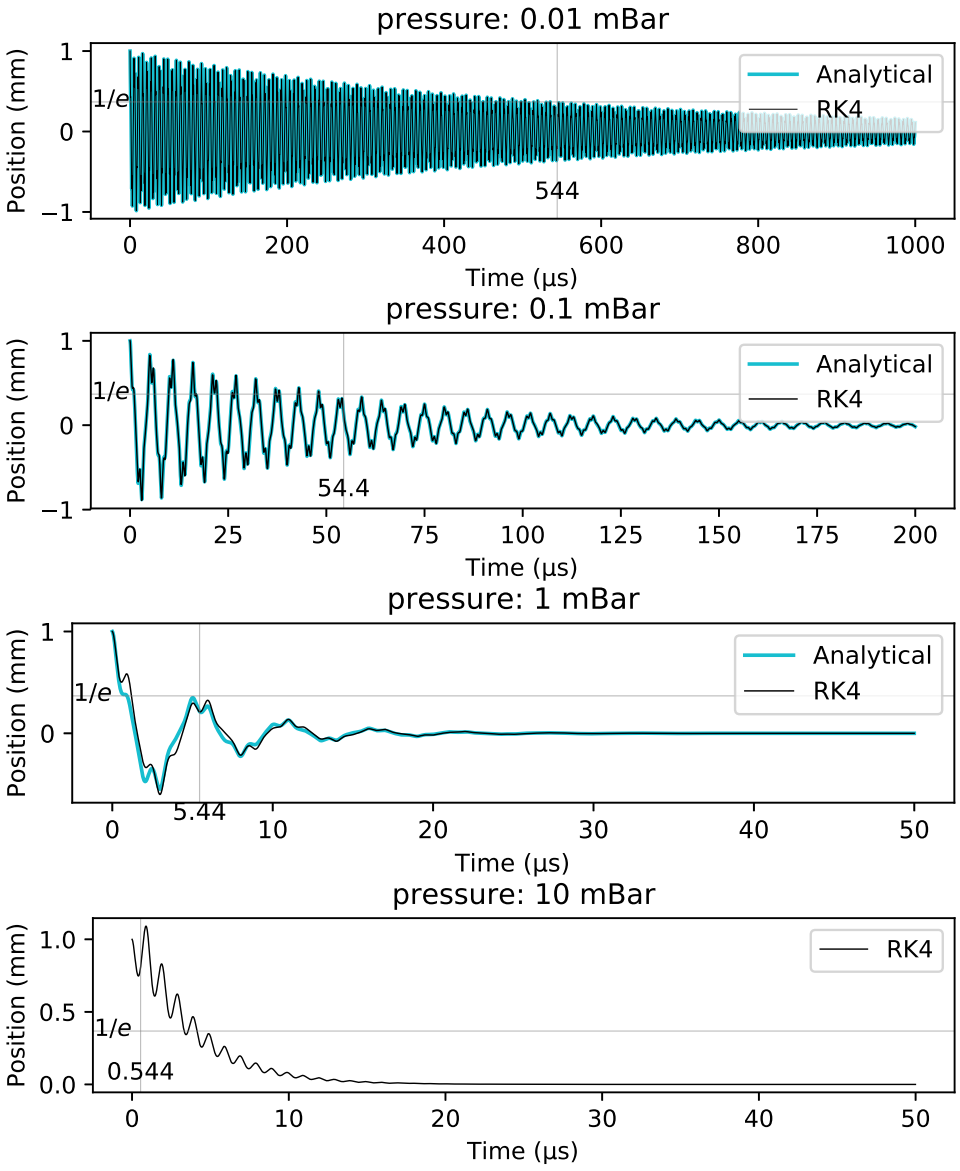

Figure 2.18: Analytical and numerical calculation of ion cooling using the ion mobility at different gas pressures as annotated in each plot. The stability parameters are ($q = 0.5$, $a = 0$). See text for details.

potential is close to a quadrupole potential, hence the ion motion can be described as

$$\frac{d^2x}{dt^2} + 2\bar{k}\frac{d\bar{x}}{dt} + \omega_x^2 = 0, \tag{2.109}$$

where ω_x is the axial oscillation frequency corresponding to the shape of the axial DC potential. Usually the axial DC potential is flatter than the pseudopotential in the radial direction, hence the axial oscillation frequency ω_x will be smaller, resulting in a lower gas pressure at critical damping.

The optimum gas pressure for ion cooling in the axial direction needs to be considered according to the actual configuration of DC trapping potential and will be discussed in more details in Chapter 3.

2.5.4 Equilibrium ion temperature

The equilibrium temperature is an important characteristic of the ion cooling and needs to be considered in addition to the analytical and numerical calculations in Section 2.5.2. Because the ions cannot be cooled to a temperature lower than that of the buffer gas, the ions will be cooled to an ion cloud of a size corresponding to the equilibrium temperature instead of infinitely approaching the zero position as shown in Figure 2.16 and Figure 2.18. A lower ion temperature corresponds to a smaller ion cloud size and smaller emittance for the extracted ions.

The equilibrium temperature of ion cooling has been extensively studied in a 3D Paul trap [Lun92, LBM92, Gha96] and LPTs [Kim97, Smi05]. The ion temperature was found to be higher than the buffer gas temperature and depends on the stability parameter q of the ion trap. The more detailed study of the ion temperature via simulation will be discussed in Section 3.5.3.

Chapter 3

Simulations of the linear Paul trap

Contemporary computational hardware and software have enabled simulation of many scientific apparatus before they were built. Such simulations can usually significantly cut down the time and resources needed for experiments and improve their design and performance.

For the linear Paul trap (LPT), electrostatic simulations are needed to determine the electrodes' geometry and voltage settings as described in Section 3.1. The characteristic of ion transmission in an RFQ was simulated in terms of ion acceptance as described in Section 3.2. Then the specific simulations and optimizations were done for an RFQ ion guide (Section 3.2) and a QMF (Section 3.4). Finally, simulations of ion cooling with buffer gas in an LPT is described in Section 3.5.

3.1 Electric potential in an LPT

Electric potential in any charge-free space, such as the center of an ion trap, follows the simple form of Laplace equation

$$\nabla^2 \phi = 0. \tag{3.1}$$

In polar coordinates, the general solution is

$$\phi(r,\theta) = A_0 \ln r + B_0 + \sum_{n=1}^{\infty} (A_n \cos(n\theta) + B_n \sin(n\theta))(C_n r^n + D_n r^{-n}). \tag{3.2}$$

For ideal quadrupole electrodes, the solution can be reduced to keep only the spatial harmonic terms ϕ_n[DGKS99]

$$\phi(r,\theta) = \sum_{n=0}^{\infty} A_n \phi_n, \tag{3.3}$$

$$\phi_n = \cos(n\theta)(\frac{r}{r_0})^n, \tag{3.4}$$

where r_0 is the distance from an electrode's inner surface to the central axis of the electrodes as illustrated in Figure 2.1. In 2D Cartesian coordinates of the $y - z$ plane,

$$\phi_n = \Re[(\frac{y + iz}{r_0})^n]. \tag{3.5}$$

For four ideally positioned quadrupole electrodes with rotational symmetry, the first non-zero terms are

$$\phi_0 = A_0 \tag{3.6}$$

$$\phi_2 = A_2 \frac{y^2 - z^2}{r_0} \tag{3.7}$$

$$\phi_6 = A_6 \frac{x^6 - 15x^4y^2 + 15x^2y^4 - y^6}{r_0^6} \tag{3.8}$$

$$\phi_{10} = A_{10} \frac{x^{10} - 45x^8y^2 + 210x^6y^4 - 210x^4y^6 + 45x^2y^8 - 7^{10}}{r_0^{10}}. \tag{3.9}$$

3.1.1 Quadrupole electrode geometries

The coefficients A_n in Eq. (3.3) depend on the geometry of electrodes as the boundary condition, and the pure electric potential of each term can be created by having electrodes follow the equipotential lines $\phi_n(y, z) = V$.

For example, to produce an ideal quadrupole potential

$$\phi(y, z) = V \frac{y^2 - z^2}{r_0^2}, \tag{3.10}$$

the electrodes needs to have hyperbolic shape defined by the equipotential lines of $\phi(y, z) = V$:

$$y^2 - z^2 = r_0^2. \tag{3.11}$$

These equipotential lines are infinitely long, while in the real world, the electrodes need to be at least truncated.

Electric potential in real-world quadrupole electrodes are simulated using commercially available software SIMION [D10]. In a SIMION simulation, electric potential in a 3D or 2D space is defined by a potential array (PA).

The PA corresponding to electrodes is given fixed voltage values, then the potential in the space between electrodes is solved by the Finite Boundary Method (FBM). Effects of the electrodes' shape are described below.

Hyperbolic electrodes

A set of hyperbolic electrodes placed inside a grounded metal tube of radius $4r_0$ is simulated. The two pairs of electrodes are set at +1 V and -1 V. Results within $|y| < r_0$ and $|z| < r_0$ are used for least-square fitting to determine the coefficients of the spatial harmonics terms in Eq. (3.3). Simulations were done for electrodes of different truncation. Results of different truncations in units of r_0 are shown in Figure 3.1. The higher-order terms A_6, A_{10}, A_{14} and A_{18} are found to be smaller than 1×10^{-5} for truncation $T > 1.6r_0$.

These results also validate the reliability of using SIMION for electrostatic simulations of the quadrupole electrodes.

Round electrodes

Hyperbolic electrodes are difficult to manufacture and assemble to high precision. As an alternative, round electrodes have been explored as the quadrupole electrodes and are currently used in most cases.

The configuration of round electrodes has only one independent variable

$$\eta = r_e/r_0, \tag{3.12}$$

where r_e is radius of the electrode. To best approximate a pure quadrupole potential, a "magic" value of

$$\eta = r_e/r_0 \approx 1.14511 \tag{3.13}$$

is known to make the first higher-order term $A_6 = 0$ [LWY71, RSM$^+$96, DGKS99].

This "magic" value is double checked in this study by running simulations of η from 0.5 to 1.5 and in fine steps from 1.144 to 1.146. The results are shown in Figure 3.2. The zero-crossing of A_6 is found to be between 1.1451 and 1.1452. The fine agreement was made possible with the surface enhancement feature for electrode geometry introduced in the 8.1 version of SIMION.

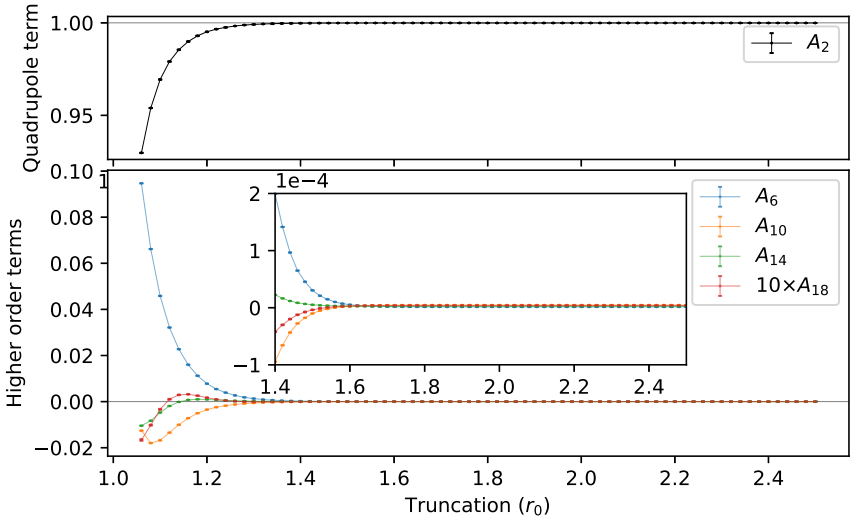

(a)

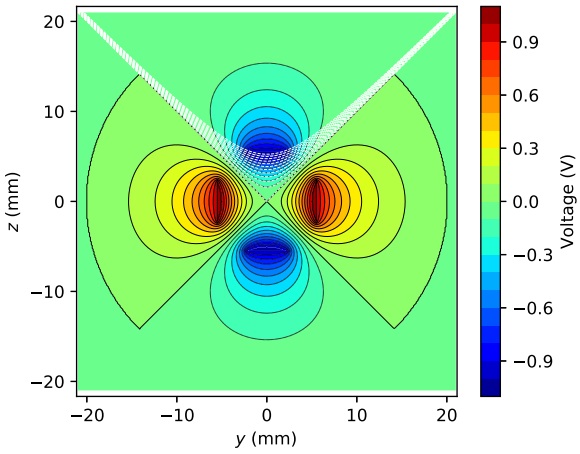

(b) Truncation = $1.1r_0$

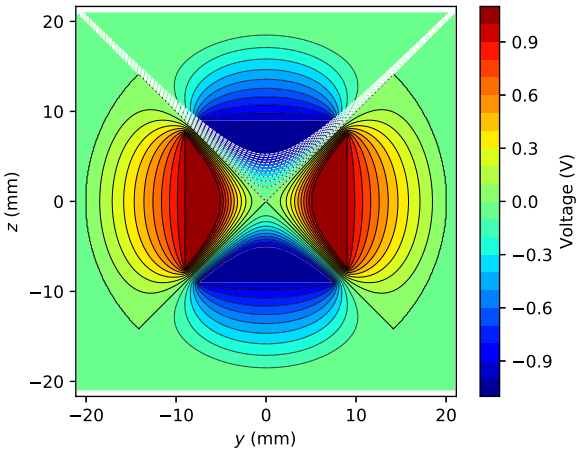

(c) Truncation =$1.8r_0$

Figure 3.1: (a) Spatial harmonic terms of electric potential in hyperbolic electrodes with different truncations. (b) Electrodes truncated close to r_0, causing deviations of the potential from a pure quadrupole. The deviations are more obvious at large radial positions (close to r_0). (c) Electrodes truncated at a larger distance ($1.8r_0$), forming almost a pure quadrupole potential. The white dashed lines are equipotential lines of a pure quadrupole potential at the given values in the color bar.

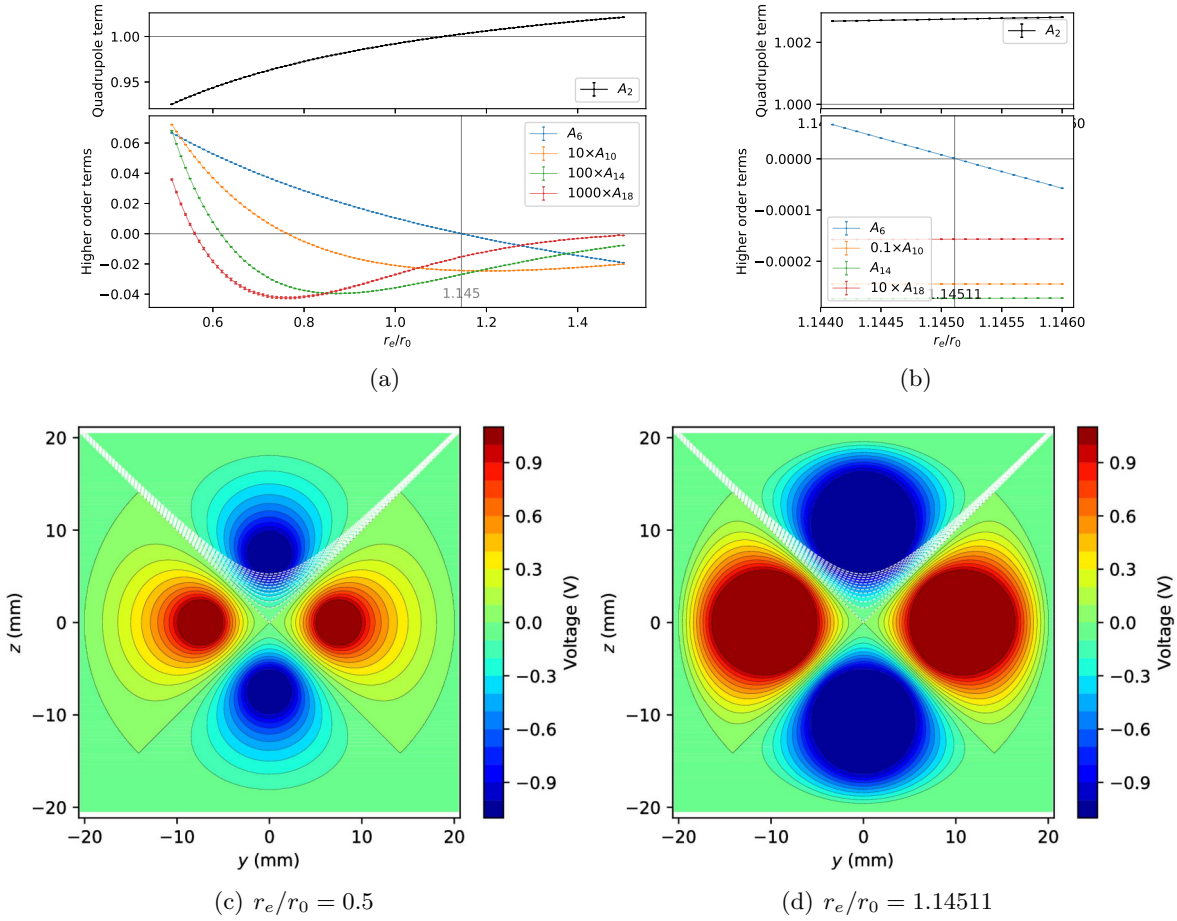

Figure 3.2: (a) Spatial harmonic terms of round electrodes with different radius r_e. (b) Detailed simulation around the "magic" value of $r_e/r_0 = 1.14511$. (c) Non-ideal potential formed by round electrodes with small radius $r_e = 0.5r_0$. (d) Electrodes with radius $r_e = 1.14511r_0$ to best approximate a pure quadrupole potential in the inner area.

3.2 Ion transmission simulations in an RFQ

SIMION also allows simulation of ion trajectories in a time-dependent electric potential such as the case of a Radio Frequency Quadrupole (RFQ). Such simulations were done to characterize the ion transmission performance of an RFQ.

In a SIMION simulation, the electrodes were represented by a potential array file such as electrode.PA#; each set of electrodes with the same voltage is solved independently and saved as a potential array (electrode.PAn). Then the electrical potential inside the RFQ is the superposition of the potential from each electrode set at each time step of the simulation, and the effect of alternating voltages on electrodes at radio-frequency is created.

The simulations in this section were done with an RFQ wth the following parameters:

- $r_0 = 5$ mm
- RF frequency $f_{RF} = 1$ MHz
- RFQ length $L = 350$ mm
- Initial RF phase $\varphi_0 = 0°$.

An example of the simulation is shown in Figure 3.3. The round electrodes are for demonstration only and do not represent the exact electrode geometries used in the simulations. The four electrodes are shielded by a grounded metal tube to ensure a well defined electric boundary condition.

Ions with given initial position and velocities start near the entrance of the RFQ in the left of Figure 3.3, then SIMIION calculates the ions' trajectories for each time step using a modified Runge-Kutta method to the 4th order. Ions with initial conditions that meet the ion acceptance are transmitted to the exit of RFQ while the other ions get lost by hitting the electrodes or the shielding tube.

3.2.1 Ion acceptance simulations in a pure quadrupole potential

To validate the reliability of SIMION, ion transmission simulations were done for an ideal RFQ with pure quadrupole potential so that the results

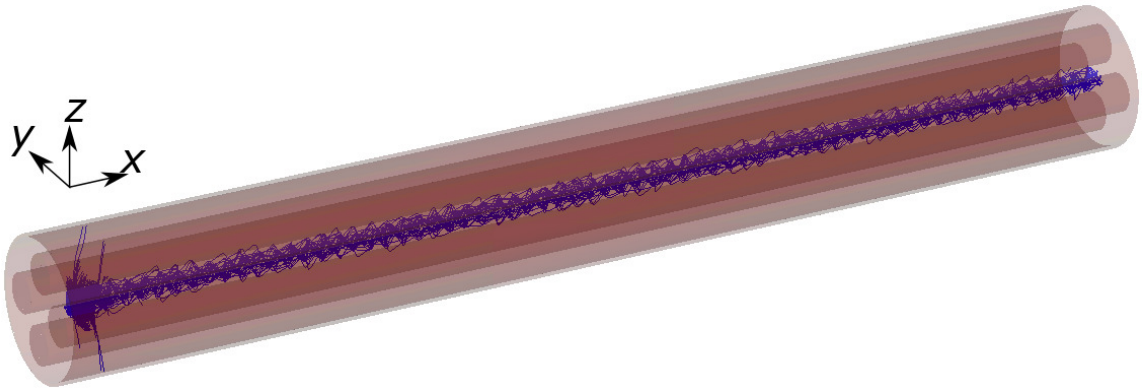

Figure 3.3: Ion transmission simulation through an RFQ in SIMION. The trajectories of the ions are shown as the blue curves.

can be compared to the theory in the previous chapter.

The virtual ions were initiated at $x = 10$ mm. The ion's velocity component along the x axis is $v_x = 5\,\mathrm{mm/\mu s}$, hence the number of RF cycles the ions take to travel through the RFQ is

$$n_{RF} = \frac{L}{v_x} = 70. \tag{3.14}$$

In the transverse directions y and z, the ions' position and velocity are represented in the phase space (y, v_y) and (z, v_z). The voltages on the electrodes determine the ion transmission characteristics of the RFQ as the ion acceptance discussed in Section 2.2.

Figure 3.4(a) shows $N_{total} = 10,000$ randomly generated ions with uniform distribution in (y, v_y) and (z, v_z). For the DC voltage $U = 0$ V ($a = 0$) and RF voltage $V = 34.8$ V ($q = 0.1$), the transmitted ions are shown in Figure 3.4(b).

The ion acceptance in units of $\pi r_0^2/\mu s$ is shown in the figure's legend. The theoretical acceptance was obtained using the analytical method described in Section 2.2. For N transmitted ions, assuming the ion acceptance is an elliptical area, then the simulated acceptance is calculated as

$$\epsilon = 4\sigma_u\sigma_v\sqrt{1 - r_{uv}^2}, \tag{3.15}$$

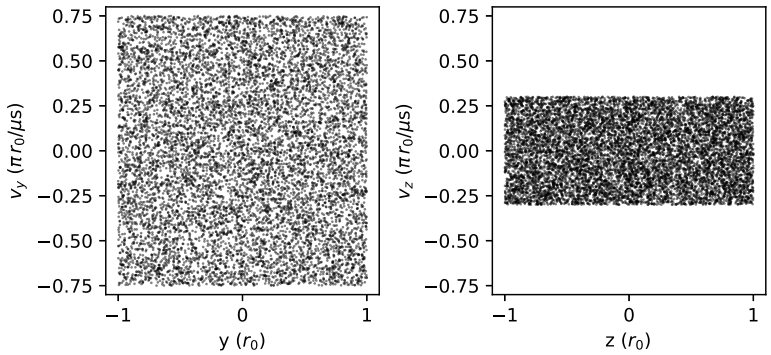

(a) 10,000 ions uniformly distributed in (y, v_y) and (z, v_z)

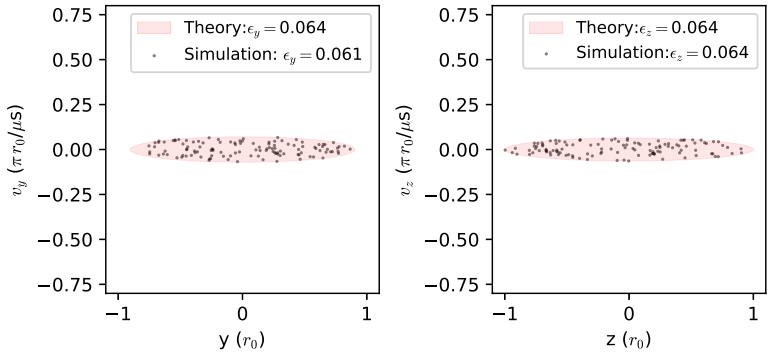

(b) $q = 0.1$, $a = 0$: 117 ions transmitted.

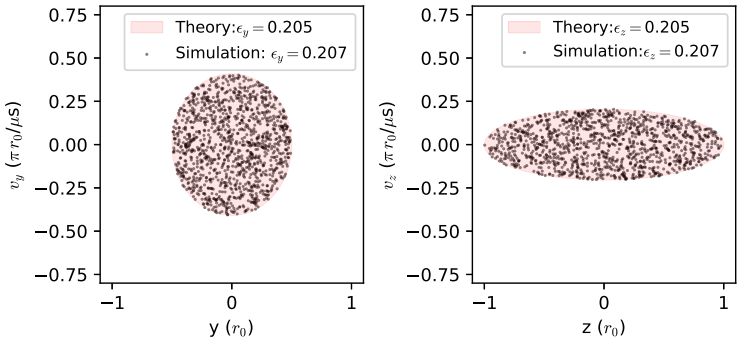

(c) $q = 0.577$, $a = 0$: 1198 ions transmitted.

Figure 3.4: Distribution of initial (a) and transmitted (b, c) ions in the RFQ simulation.

where u represents the ion positions y or z, and v represents the ion velocities v_y or v_z; σ_u and σ_v are the standard distribution of the ions' position and velocity; r_{uv} is the Pearson correlation coefficient

$$r_{uv} = \frac{\sigma_{uv}}{\sigma_u \sigma_v} = \frac{\sum_{i=1}^{N}(u_i - \bar{u})(v_i - \bar{v})}{\sqrt{\sum_{i=1}^{N}(u_i - \bar{u})^2}\sqrt{\sum_{i=1}^{N}(v_i - \bar{v})^2}}. \tag{3.16}$$

Due to the elliptical shape of the simulated acceptance, the uncertainty of the acceptance ϵ is

$$\sigma_\epsilon = \epsilon \frac{\sqrt{\pi}}{\sqrt{N}}. \tag{3.17}$$

Figure 3.4(c) shows the maximum ion acceptance for the given r_0 and f_{RF} when $a = 0$ and $q = 0.577$ (RF voltage $V = 200$ V). Correspondingly, more ions were able to be transmitted compared to the smaller ion acceptance of Figure 3.4(b).

Ion acceptance and transmission efficiency

The ion transmission efficiency T as defined previously in Eq. (2.92) is related to the acceptance ϵ_{yz}. For ions uniformly distributed in both (y, v_y) and (z, v_z), the ion transmission efficiency

$$T = \frac{N}{N_{total}} \tag{3.18}$$

is proportional to the combined ion acceptance ϵ_{yz}

$$\epsilon_{yz} = \epsilon_y \times \epsilon_z. \tag{3.19}$$

The uncertainty of ϵ_{yz} is

$$\sigma_{\epsilon_{yz}} = \sqrt{(\epsilon_y \sigma_{\epsilon_z})^2 + (\epsilon_z \sigma_{\epsilon_y})^2} = \epsilon_{yz} \frac{\sqrt{2\pi}}{\sqrt{N}}. \tag{3.20}$$

Results of the combined acceptance ϵ_{yz} from the simulation of $a = 0$ and q from 0 to 1 are compared to theoretical results as shown in Figure 3.5. The ion counts which represent the transmission efficiency are plotted in red dots and appear proportional to the acceptances as expected.

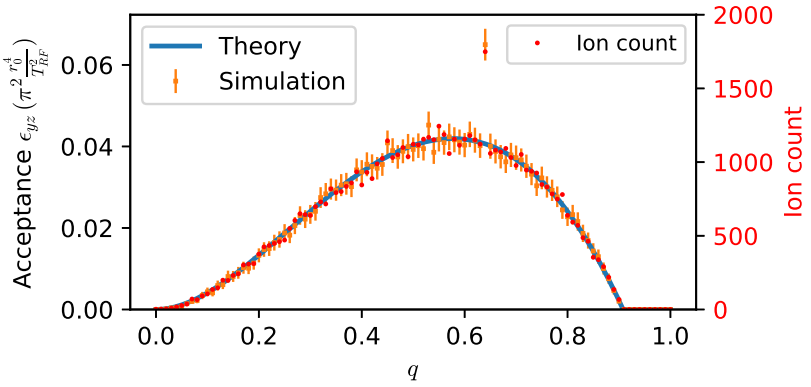

Figure 3.5: Simulated ion acceptance compared to theoretical values. The error bars are the uncertainties calculated using Eq. (3.20). The abnormality around $q = 0.64$ is explained in text.

Ion acceptance abnormality around $q = 0.64$

The ion acceptances obtained from simulations agree well with theory except for an abnormality around $q = 0.64$ in Figure 3.5. Figure 3.6(a) shows the transmitted ions at $q = 0.64$. The unexpected large ion acceptance results from the transmitted ions outside of the elliptical acceptance area. To rule out possible issues of SIMION or the simulation settings, the simulations were also done through a custom-written Python script and the same abnormality was observed.

Further detailed study and simulations were done to understand the abnormal acceptance around $q = 0.64$. The first thing to check is the number of RF cycles in the ion transmission simulation because the theoretical acceptance assumes the ions travel down an RF ion guide of infinite length and experience infinite RF cycles. When the longitudinal velocity of the ions is set to $v_x = 0.5\,\mathrm{mm/\mu s}$ so that the ions experience 700 RF cycles, the abnormality disappears as shown in Figure 3.6(b).

The abnormally large ion acceptance around $a = 0$ and $q = 0.64$ may be used as a benefit in RF ion guides to improve ion transmission efficiency. For ions experiencing 70 RF cycles or less, operating the ion guide at this setting should increase its ion transmission efficiency by 50%.

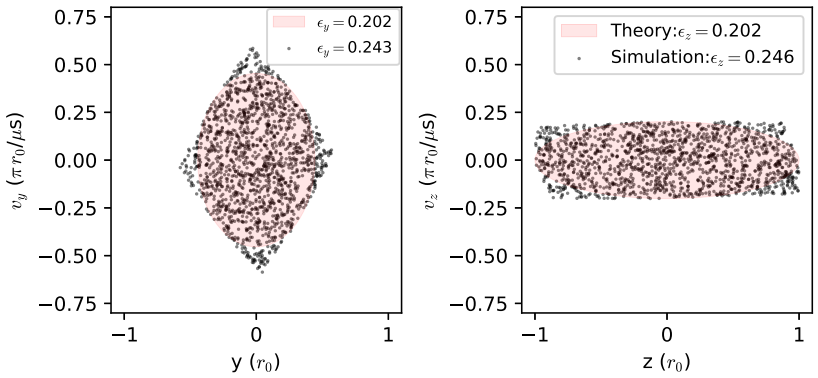

(a) $v_x = 5\,\mathrm{mm/\mu s}$: 70 RF cycles

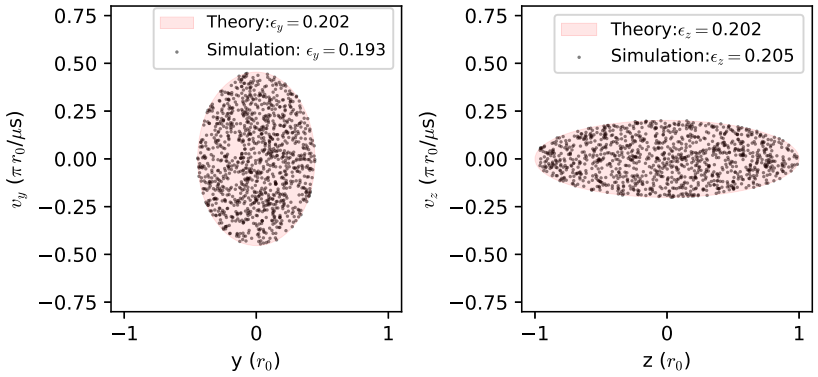

(b) $v_x = 0.5\,\mathrm{mm/\mu s}$: 700 RF cycles

Figure 3.6: Simulated ion transmission and acceptance at $q = 0.64$ and $a = 0$ with different RF cycles.

3.2.2 Ion acceptance in non-perfect quadrupole potentials

A realistic RFQ with non-hyperbolically shaped electrodes have higher-order spatial harmonics in the electric potential as described in Section 3.1.1. In this case, there is no known analytical solution to ion motion, hence numerical simulations are the only approaches.

Simulations similar to those shown in Figure 3.4 were done for quadrupole potentials with added higher-order spatial harmonics terms. For $a = 0$ and $q = 0.577$, ion transmission simulations with the presence of the higher-order spatial harmonics in the electric potential are shown in Figure 3.7 to Figure 3.10. The effect of these spatial harmonic terms is negligible when

they are smaller than 0.001. With larger higher-order spatial harmonics, the boundary of the ellipse becomes blurred and the amount of transmitted ions decreases.

With the presence of higher-order spatial harmonics in the electric potential, the ions transmitting through an RFQ no longer follow an elliptical acceptance. So, the acceptance can not be calculated from Eq. (3.38) and Eq. (3.20). Instead, the acceptances shown in the legends of Figure 3.7 to Figure 3.10 are calculated from the count of transmitted ions

$$\epsilon_{yz} = \frac{N}{N_{total}} \epsilon_{total}, \tag{3.21}$$

where ϵ_{total} is the acceptance that gets all the initial ions transmitted. For the ions used for these simulations in phase space range shown in Figure 3.4(a), $\epsilon_{total} = 0.365\pi^2 \frac{r_0^4}{T_{RF}^2}$.

3.3 RFQ ion guide simulation and optimization

The theory of the RFQ ion guide is introduced in Section 2.3. For an ideal RFQ ion guide with pure quadrupole potential, the theoretical and simulated ion acceptance is shown in Figure 3.5.

For practical applications of RFQ, the influence of higher-order spatial harmonics in the electric potential needs to be considered as discussed in Section 3.2.2, and in more detail in Section 3.3.1.

3.3.1 Influence of higher-order spatial harmonics in electric potential

Simulations were done for an RFQ ion guide with the presence of the 6th spatial harmonic term for q values between 0 and 1. Acceptances calculated using Eq. (3.21) from the simulations are shown in Figure 3.11. The abnormally large ion acceptance around $q = 0.64$ as discussed near the end of Section 3.2.1 is still visible for $|A_6| < 0.01$.

Similar simulations were done for an RFQ ion guide with the 10th and above higher-order spatial harmonics in the electric potential. Acceptances derived from the simulations are shown in Figure 3.12.

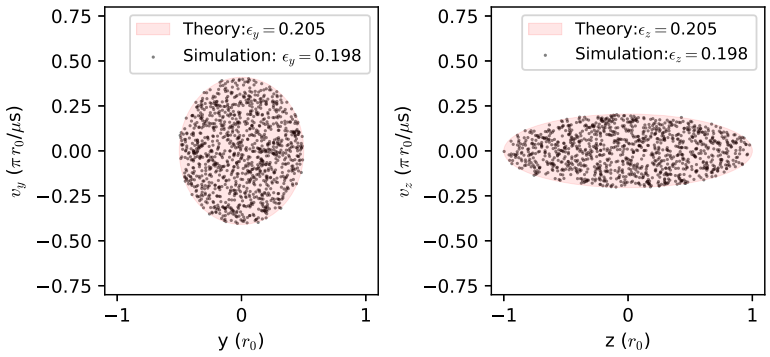

(a) $A_6 = 0.001$: 1121 ions transmitted

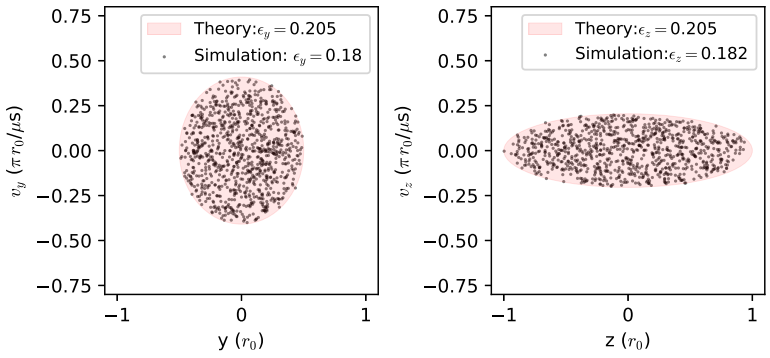

(b) $A_6 = 0.01$: 936 ions transmitted

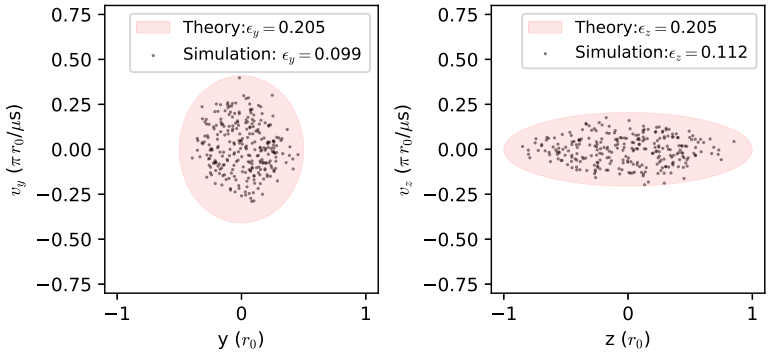

(c) $A_6 = 0.1$: 273 ions transmitted

Figure 3.7: Ion transmission simulation for an RF ion guide with added 6th spatial harmonics in electric potential for $a = 0$ and $q = 0.577$.

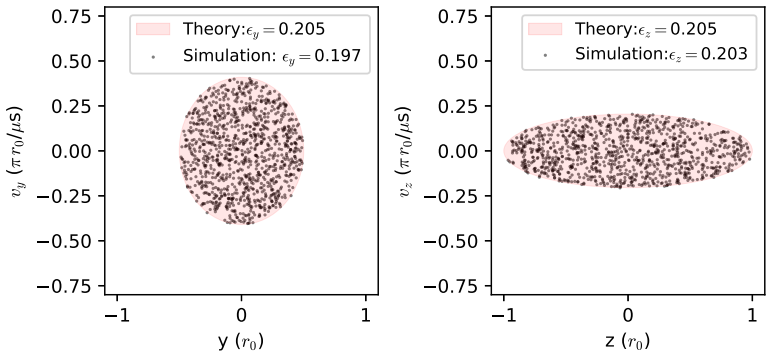

(a) $A_{10} = -0.001$: 1048 ions transmitted

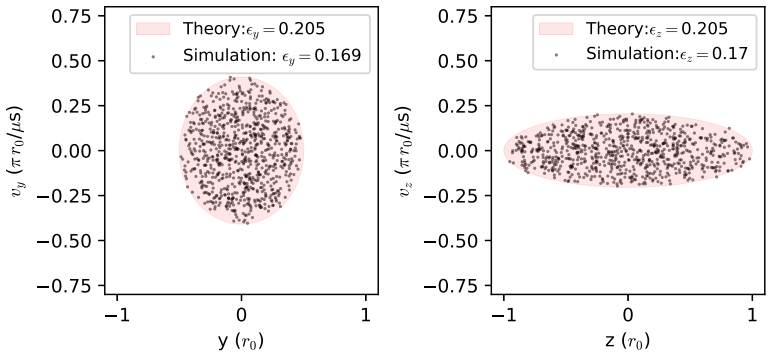

(b) $A_{10} = -0.01$: 791 ions transmitted

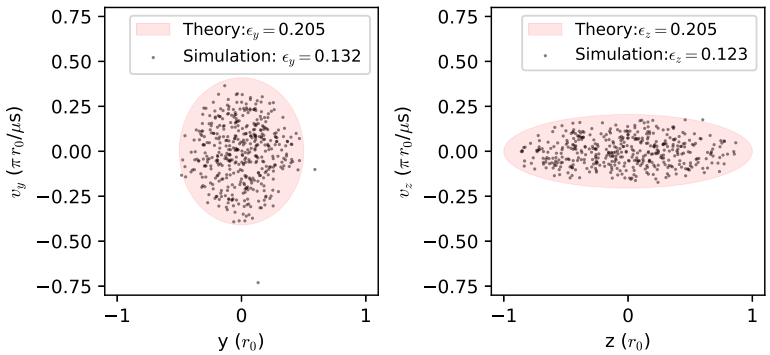

(c) $A_{10} = -0.1$: 437 ions transmitted

Figure 3.8: Ion transmission simulation for an RF ion guide with added 10th spatial harmonics in electric potential for $a = 0$ and $q = 0.577$.

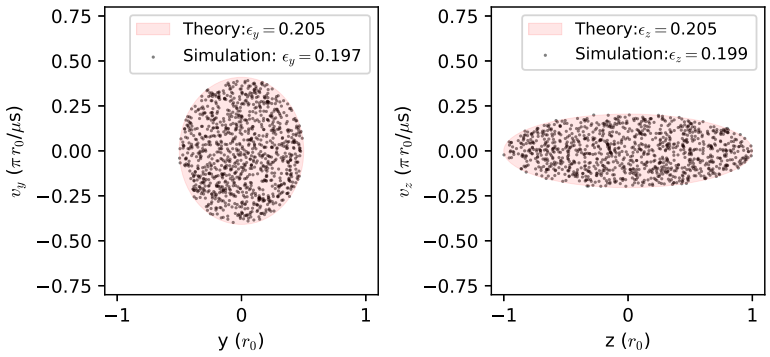

(a) $A_{14} = 0.001$: 1048 ions transmitted

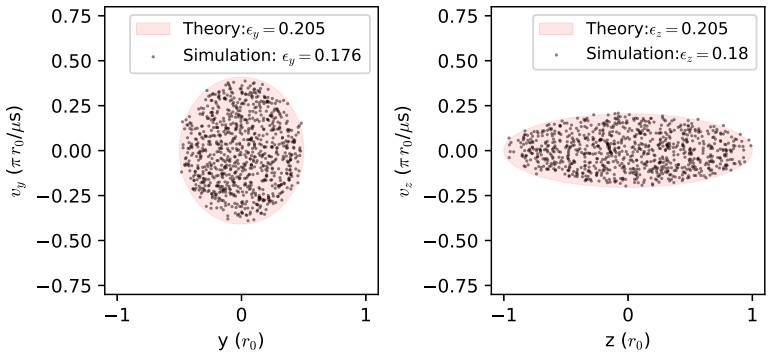

(b) $A_{14} = 0.01$: 871 ions transmitted

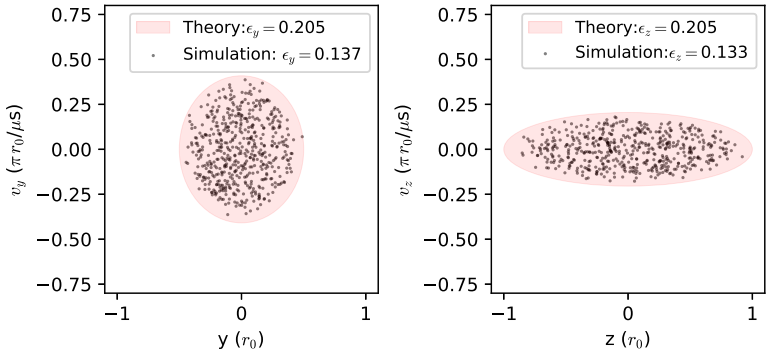

(c) $A_{14} = 0.1$: 518 ions transmitted

Figure 3.9: Ion transmission simulation for an RF ion guide with added 14th spatial harmonics in electric potential for $a = 0$ and $q = 0.577$.

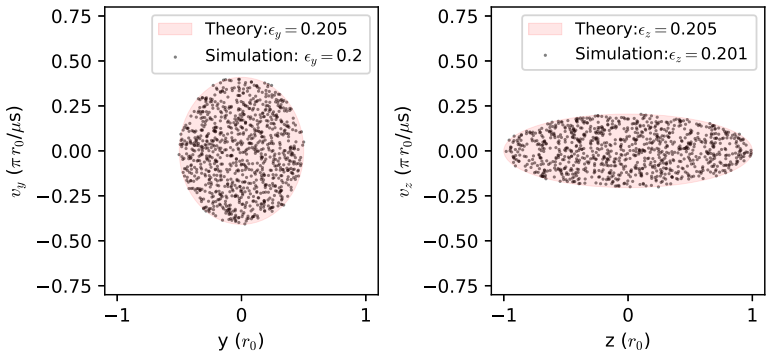

(a) $A_{18} = 0.001$: 961 ions transmitted

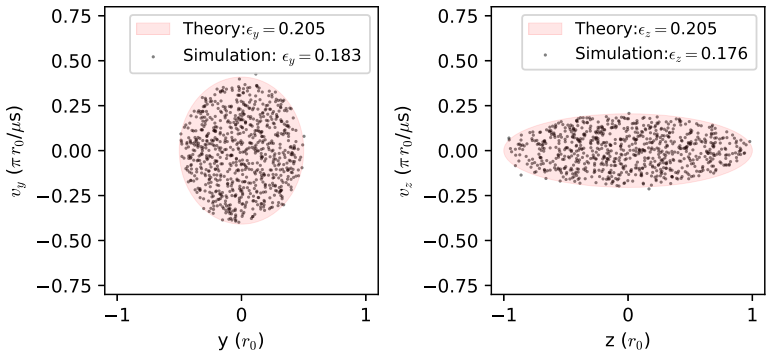

(b) $A_{18} = 0.01$: 784 ions transmitted

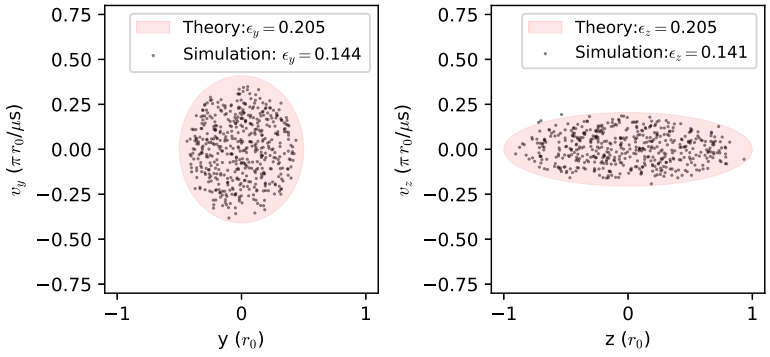

(c) $A_{18} = 0.1$: 496 ions transmitted

Figure 3.10: Ion transmission simulation for an RF ion guide with added 18th spatial harmonics in electric potential for $a = 0$ and $q = 0.577$.

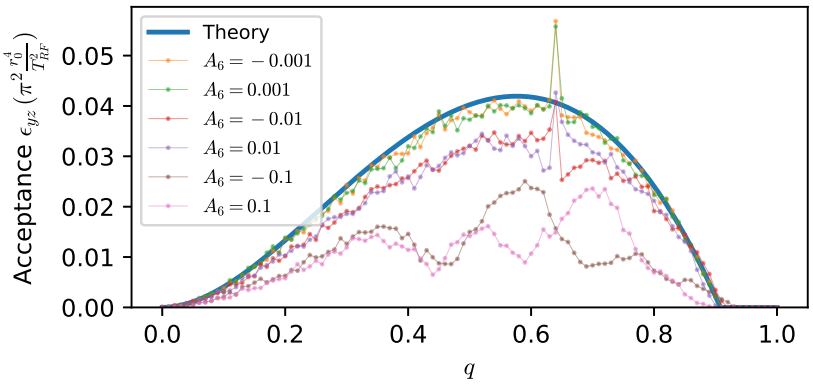

Figure 3.11: Simulated ion acceptance for the electric potential with the presence of the 6th spatial harmonic component. The abnormality around $q = 0.64$ is discussed in text.

From these simulation results, an RFQ ion guide needs to have higher-order spatial harmonics close to 0.001 or smaller to avoid any noticeable loss of ion transmission efficiency due to decreased ion acceptance. Such requirements can be met by an ion guide with either truncated hyperbolic electrodes or round electrodes as discussed in Section 3.1.1, and in more detail in Section 3.3.2.

3.3.2 Electrode geometries for RFQ ion guide

Hyperbolic electrode

The ideal choice of the electrode geometry to ensure minimum higher-order spatial harmonic terms is the hyperbolic shape as shown in Figure 3.1. Ion transmission simulations were done for an RFQ ion guide with such truncated hyperbolic electrodes to determine the influence of the truncation on ion acceptance. Acceptances derived from the simulations are shown in Figure 3.13.

For electrodes truncated closer to r_0, less of the hyperbolic profile is left hence larger spatial harmonic terms exist in the electric potential. Figure 3.13 shows the RFQ ion guide with electrode truncated at $1.04r_0$ and $1.1r_0$ has much lower ion acceptance than the ideal case.

Electrodes truncated at $1.4r_0$ or larger were found to have optimum ion

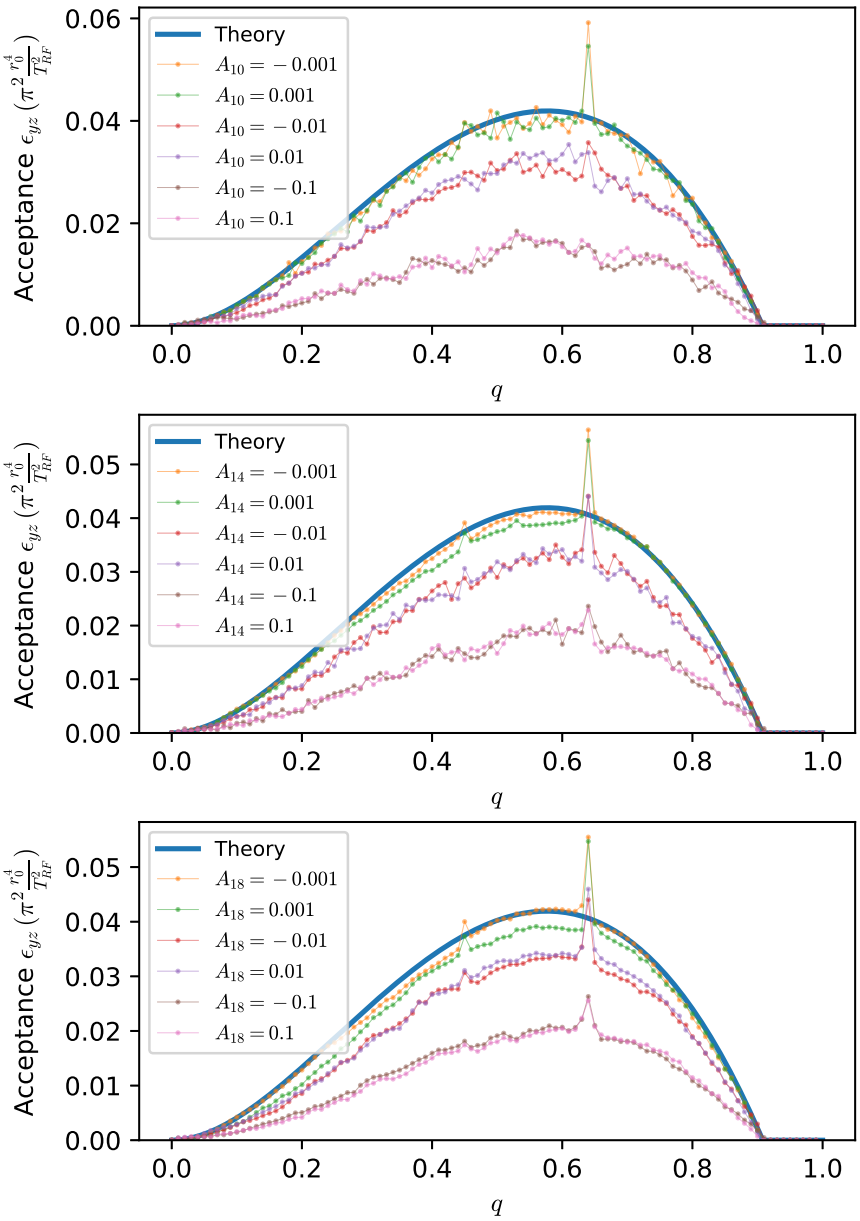

Figure 3.12: Simulated ion acceptance for the electric potential with the presence of the 10th (top) 14th (middle) and the 18th (bottom) spatial harmonic component.

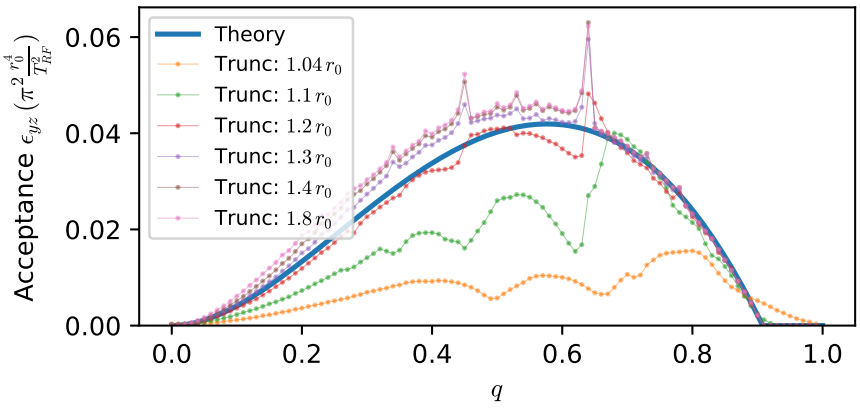

Figure 3.13: Simulated acceptance of an RF ion guide with hyperbolic electrodes of different truncation. See text for details.

acceptance, because the higher-order spatial harmonics terms are all smaller than 2×10^{-4} as shown in Figure 3.1. The optimum ion acceptances are larger than the theory in some q values because the larger hyperbolic shaped surface of electrodes was used as the boundary for ions instead of a square of r_0 used in the theory.

Round electrode

Round rods are used as quadrupole electrodes in many RFQ ion guides because of the easier manufacturing and assembly processes. Simulations were done for an RFQ with round electrodes of different radius. Acceptances derived from the simulations are shown in Figure 3.14.

For electrodes with radius $r_e = 1.0r_0$ and $r_e = 1.2r_0$, the higher-order spatial harmonic terms are in the order of 0.01 and caused the RFQ to have noticeably lower acceptance for some regions of the q value. However, it is noteworthy that the "magic" value of $r_e = 1.14511r_0$ which enables the RFQ to have $A_6 = 0$ didn't produce the optimum ion acceptances. Instead, r_e between $1.1r_0$ and $1.3r_0$ leads to the optimum ion acceptances of the RFQ ion guide.

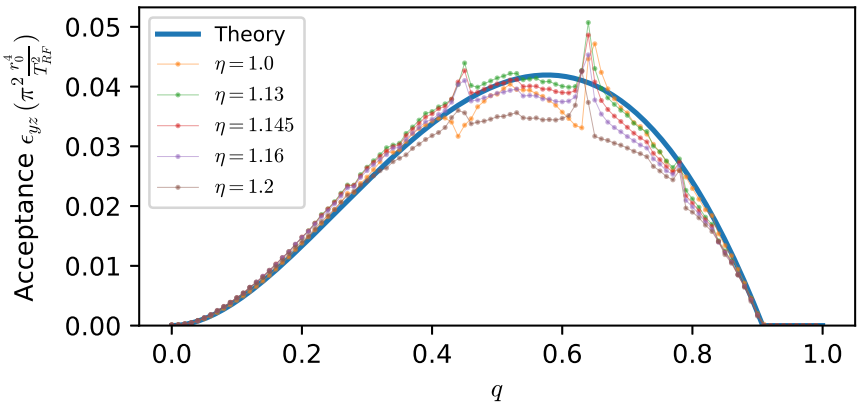

Figure 3.14: Simulated acceptance of an RF ion guide with round electrodes of different radius $r_e = \eta r_0$. See text for details.

3.4 QMS simulation and optimization

The theory of QMS is introduced in Section 2.4. An ideal QMS with pure quadrupole potential has the optimum performance in mass spectrometry. Ion acceptance of such an ideal QMS is shown in Figure 3.15 for the upper tip of the stable region used for mass spectrometry.

Figure 3.15 also shows the performance of the QMS in terms of mass resolving power R and the acceptance ϵ_{yz} as a function of the a value. As a approaches $a_t = 0.2369940$ when $q = q_t = 0.7059961$, the mass resolving power R becomes infinitely large while the ion acceptance becomes infinitely small. So a trade-off needs to be made between these two. Usually, a mass resolving power of a few hundred is achievable in a realistic QMS.

For the real world applications of QMS, the influence of higher-order spatial harmonics in the electric potential needs to be considered as discussed in Section 3.4.1.

3.4.1 Influence of higher-order spatial harmonics

Simulations similar to Section 3.2.2 were done for $q = 0.706$ and $a = 0.23$ to investigate the influence of higher-order spatial harmonics on ion acceptance of the QMS. Due to the smaller ion acceptance at a larger a value, 100,000 ions were simulated for the QMS. The ions were randomly generated with normal distribution in the same phase space range as Figure 3.4(a).

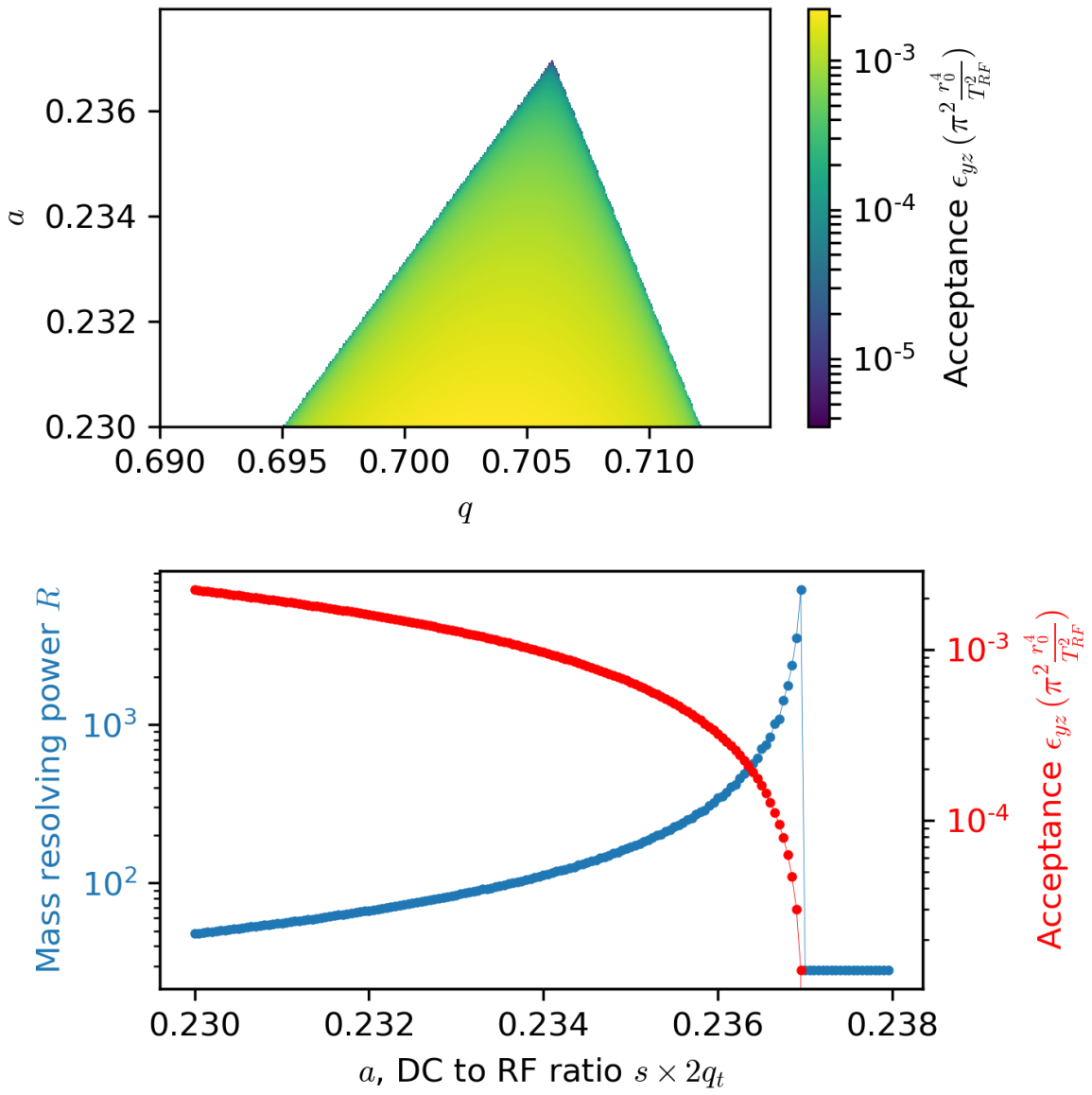

Figure 3.15: (Top) Ion acceptance of an ideal QMS with pure quadrupole potential. (Bottom) The mass resolving power is derived from the ion acceptance and shown as a function of a.

The simulation results of ion transmission and acceptance are shown in Figure 3.16. The ion acceptance is affected more obviously compared to the case of an RF ion guide in Figure 3.7 when $q = 0.577$ and $a = 0$.

The affected ion acceptances change the peak shape of the mass spectrometry measurement of the QMS, and are related to the performance of the QMS such as mass resolving power R and ion transmission efficiency T. For $a = 0.23$, the theoretical peak shape of an ideal QMS with pure quadrupole potential is shown in Figure 3.17 as the blue solid line. Simulated peak shape for a QMS with and without the presence of the 6th spatial harmonic is also shown in the figure.

For $a = 0.23$, the ideal QMS has theoretical mass resolving power

$$R_{a=0.23} = \frac{q_t}{\Delta q} = 50.5, \tag{3.22}$$

where $q_t \approx 0.706$ and Δq is the peak's full-width at half-maximum (FWHM). The simulation of the ideal QMS ($A_6 = 0$) agrees well with the theory.

With the presence of the 6th spatial harmonic in the electric potential, the peak shape changes. When $A_6 = \pm 0.001$, the mass resolving power is close to the ideal QMS; the ion transmission efficiency at the peak decreases about 10% and the peak is deformed. For larger A_6, both the mass resolving power and the ion transmission efficiency is significantly affected. Also, the position of the peak is shifted and would lead to a mass shift in the mass spectrometry.

The influence of the 10th and higher spatial harmonics on the peak shape is shown in Figure 3.18.

The presence of these higher-order spatial harmonic terms is dependent on the geometry of the electrodes as discussed in Section 3.1.1.

3.4.2 Electrode geometries for QMS

Hyperbolic electrode for QMS

The ideal choice of electrode geometry for the QMS is the hyperbolic shape to minimize the higher-order spatial harmonic terms. The influence of

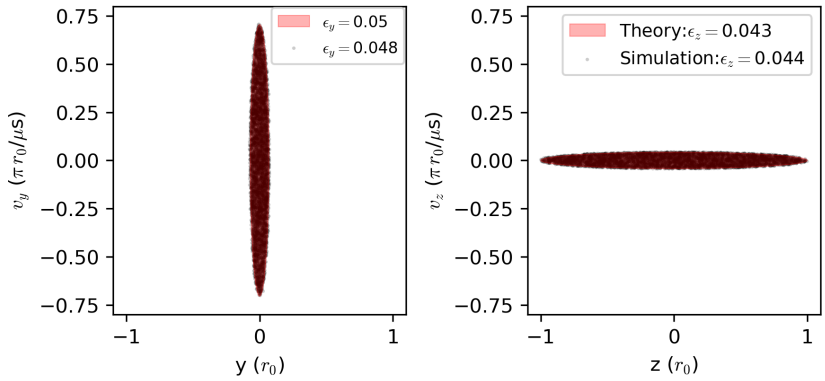

(a) $A_6 = 0.001$: 5904 ions transmitted

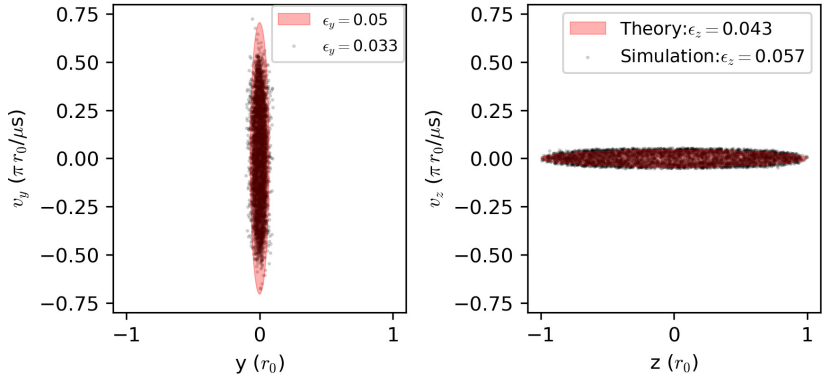

(b) $A_6 = 0.01$: 4418 ions transmitted

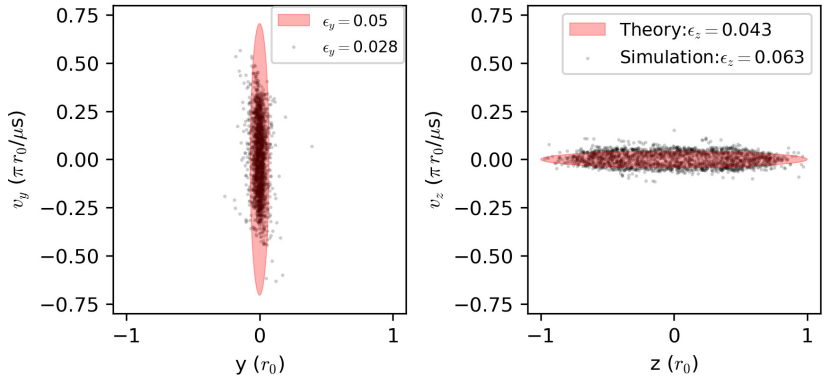

(c) $A_6 = 0.1$: 2076 ions transmitted

Figure 3.16: Ion transmission simulation in a QMS with added 6th spatial harmonics in electric potential for $a = 0.23$ and $q = 0.706$. The three sets of plot show the effect of the 6th spatial harmonics of different amplitude.

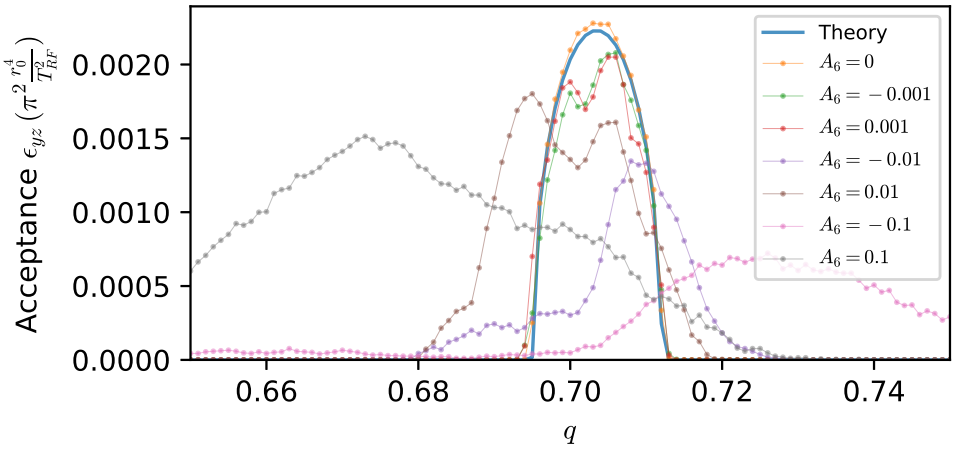

Figure 3.17: Peak shape of a QMS with pure quadrupole potential (theory) and added 6th order spatial harmonic (simulations).

truncation of electrodes on a QMS's performance was studied in the simulation when $a = 0.236$; corresponding to a theoretical mass resolving power $R = 345.1$.

To have the simulations correctly represent this large mass resolving power, the ions need to go through enough RF cycles to filter out the ions with unstable trajectories as discussed in Section 2.4.2.

The longitudinal ion velocity of $v_x = 5\,\text{mm/µs}$ used in the previous simulations corresponds to $n_{RF} = 70$ and $R_n \approx 245 < 345.1$. So, a slower longitudinal velocity $v_x = 2\,\text{mm/µs}$ was also used in simulations to have more RF cycles ($n_{RF} = 175$). The simulation results shown as acceptances and peak shapes are shown in Figure 3.19.

The simulations show that when the electrodes are truncated close to r_0 and hence have only a small surface area, the peak shape is broad due to the influence of the higher-order spatial harmonics. For electrodes truncated at $1.4r_0$ or larger, the peak shape is the same as the theory.

More detailed simulations were done for a QMS with hyperbolic electrodes truncated at $2r_0$ so that the higher-order spatial harmonic terms are all smaller than 1×10^{-5} and negligible. Results of the simulations are shown in Figure 3.20.

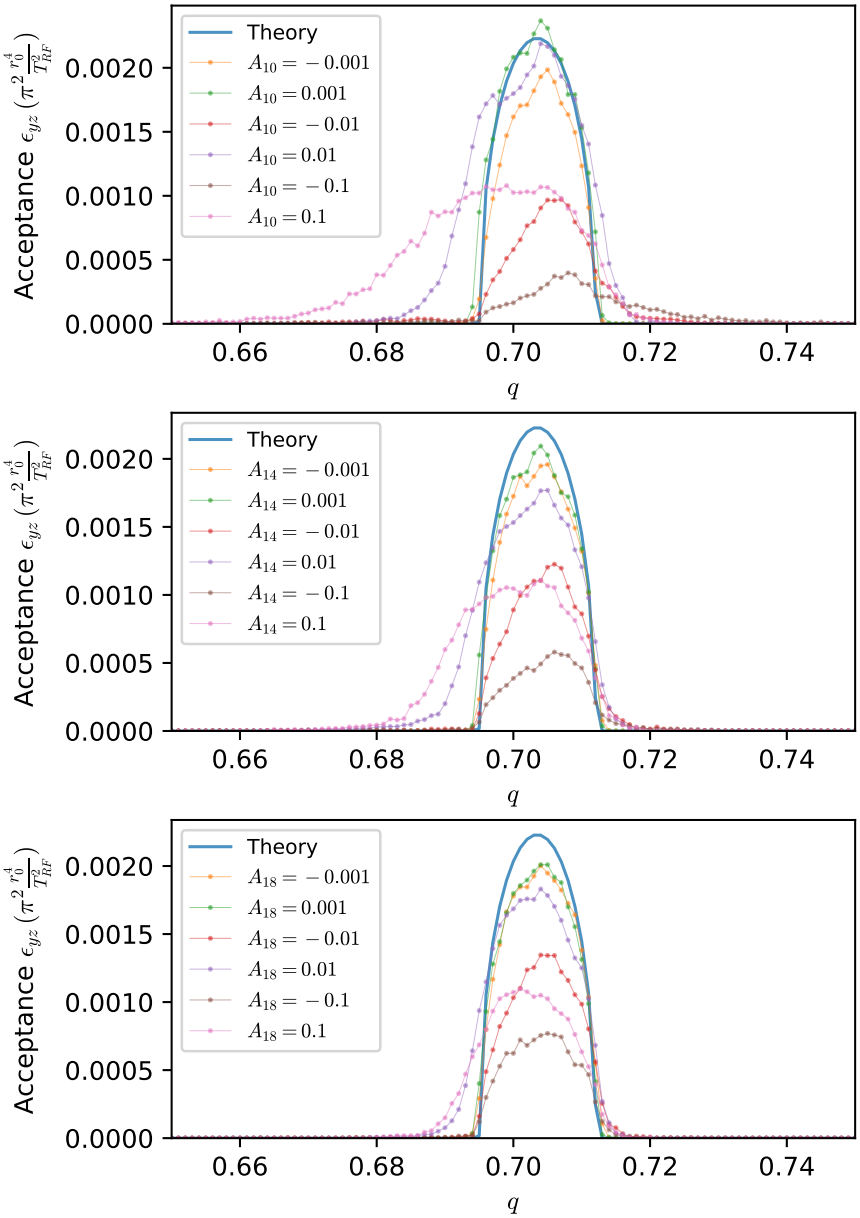

Figure 3.18: Peak shape of a QMS with pure quadrupole potential (theory) and the added 10th (top), 14th (middle) and 18th (bottom) higher-order spatial harmonic (simulations).

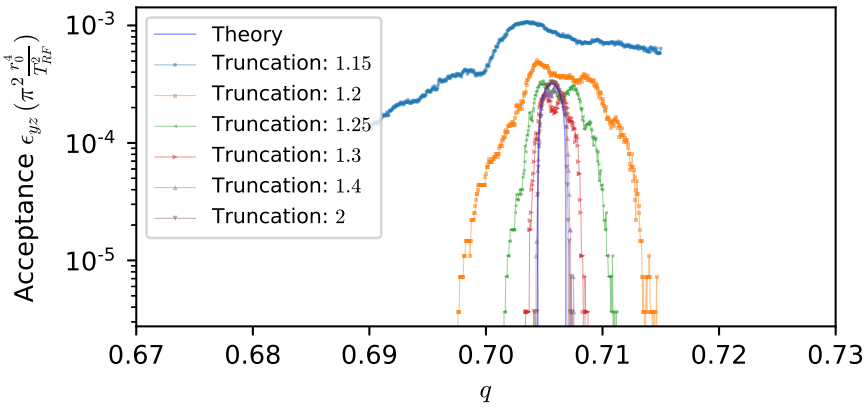

Figure 3.19: Peak shapes of QMS with hyperbolic electrodes of different truncation at $a = 0.236$.

For ions with longitudinal velocity $v_x = 2\,\mathrm{mm/\mu s}$, Figure 3.20 shows the QMS's performance of both mass resolving power R and ion acceptance ϵ_{yz} are close to theory. For ions with $v_x = 5\,\mathrm{mm/\mu s}$, R and ϵ_{yz} starts to deviate from theory from $a = 0.236$. In this case, the QMS's mass resolving power R is limited up to 1000 by the RF cycle $n_{RF} = 70$.

Round electrode for QMS

In practice, hyperbolic shaped electrodes are difficult to machine and assemble to high precision in a QMS, so round electrodes are often used. A "magic" value of $\eta = r_e/r_0 = 1.14511$ is known to have the first higher-order spatial harmonic $A_6^m = 0$ [LWY71, RSM+96, DGKS99]. This configuration was believed to enable the best mass spectrometry performance in the early days of QMS research. However, at this configuration the next higher-order spatial harmonic terms are not all negligible:

$$A_{10}^m = -2.44 \times 10^{-3} \tag{3.23}$$

$$A_{14}^m = -2.73 \times 10^{-4} \tag{3.24}$$

$$A_{18}^m = -1.57 \times 10^{-5}. \tag{3.25}$$

A QMS with round electrodes of $r_e = 1.14511 r_0$ were simulated and the results shown in Figure 3.21 reveal some issues:

- ion transmissions still occur outside of the QMS's theoretical stable region,

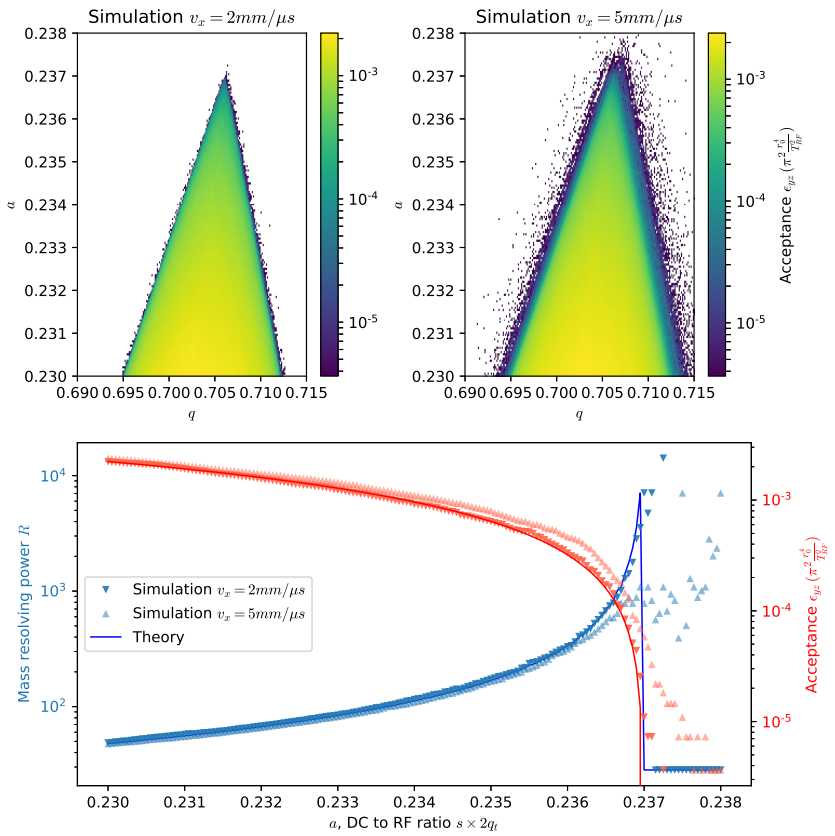

Figure 3.20: Simulation of a QMS with hyperbolic electrodes.

- the boundary of the original stable region becomes unclear,
- ion transmissions inside the original stable region decrease.

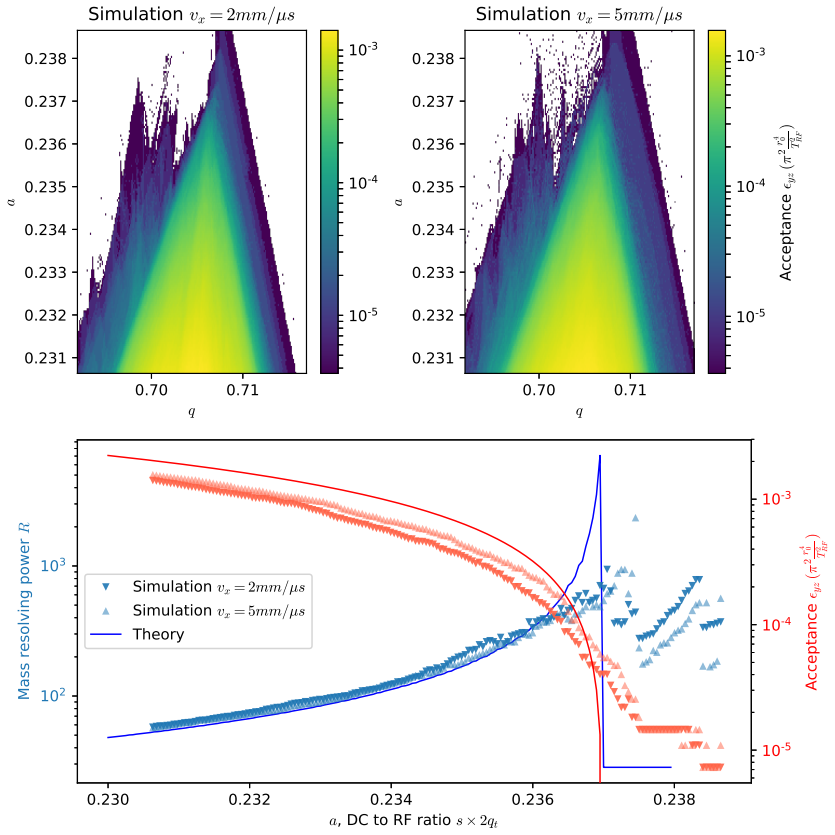

Figure 3.21: QMS with round electrodes with radius $r_e = 1.14511 r_0$.

These issues lead to a decrease in the performance of the QMS. The ion acceptance is about 60% of the theoretical value for most of the a value. The mass resolving power R starts to deviate from the theory around $a = 0.2362$ when $R \approx 400$. The maximum mass resolving power achievable is $R \approx 700$ around $a = 0.2372$.

In later QMS research, it was found that a slightly smaller ratio of $\eta = r_e/r_0$ leads to better QMS performance [GT01, DK02]. Following these findings, simulations were also done for a QMS with round electrodes of

$r_e = 1.13r_0$ and the results are shown in Figure 3.22.

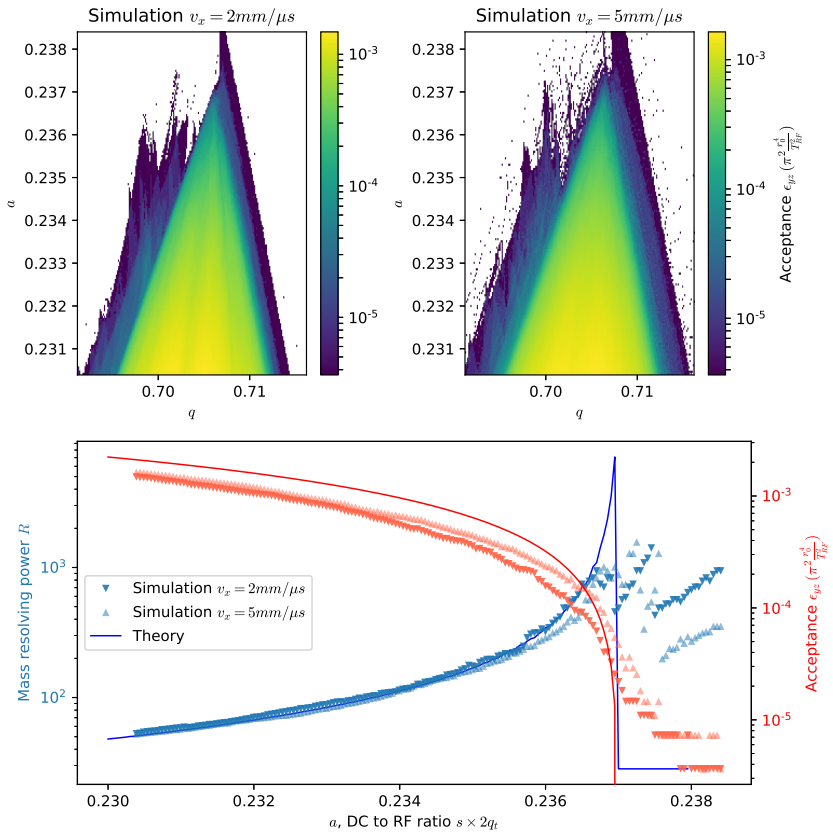

Figure 3.22: QMS with round electrodes with radius $r_e = 1.13r_0$.

In comparison to Figure 3.21, there is less ion transmission outside of the theoretical stable region. The simulation with $v_x = 2\,\text{mm/µs}$ only starts to deviate from theory from $a = 0.2367$ when $R \approx 1000$. Thus the QMS with round electrodes of $r_e = 1.13r_0$ indeed has better performance than the one with electrodes of $r_e = 1.14511r_0$. The QMF for this study will be designed with round electrodes with $r_e = 1.13r_0$.

3.5 RFQ ion cooler

The physics of ion cooling with buffer gas has been described with the concept of ion mobility in Section 2.5. Simulation of the ion cooling is done by including randomized ion-gas collision in the numerical calculation of the ion trajectories. In this way, the simulations can obtain some more detailed ion cooling characteristics, such as the coolng time for the ions to reach thermal equilibrium and the equilibrium ion temperature.

Simulation of the ion cooling process is done using SIMION with a user-customizable hard-sphere model HS1 [Man07]. In the simulations, the helium buffer gas is treated as an ideal gas at room temperature with randomized Maxwell-Boltzmann distribution. The occurrence of the collisions is related to the mean-free path

$$l = \frac{v_{ion}}{\bar{v}\sigma n} \tag{3.26}$$

of the ions in the gas. In Eq. (3.26) $\bar{v}$ is the mean relative velocity between the ion and gas, n is the number density of the helium gas, and

$$\sigma = \pi(r_{ion} + r_{gas})^2 \tag{3.27}$$

is the combined cross-section of the collisions.

3.5.1 Ion drift velocity and mobility

To get started with the ion-neutral simulations and to benchmark the SIMION HS1 model for $^{136}Ba^+$ ions in the helium buffer gas, simulations were done for 1000 randomly generated ions in a constant electric field E with the presence of 0.1 mbar helium gas. The velocities of the ions stabilize after flying 1000 µs and were obtained after the drift velocity v_d.

At first, the Van Der Waals radius of helium $r_{helium} = 143$ pm [Web20a] and the Pauling ionic radius of Ba^+ $r_{Ba^+} = 153$ pm [Web20b] were used for the cross-section calculation in Eq. (3.27). But the simulated ion drift velocities were found to be significantly larger than the previously experimentally measured values [VM95]. The drift velocity was also found to be inversely proportional to the collision cross-section σ, so later an empirical value of Ba^+ $r^e_{Ba^+} = 220$ pm was used. The results of the simulations are

shown in Figure 3.23. The ion mobility is derived as

$$K = \frac{v_d}{E}, \tag{3.28}$$

and the standard ion mobility is

$$K_0 = \frac{N}{N_0} K = \frac{p_{gas}}{p_{atm}} \frac{T}{273.15} K, \tag{3.29}$$

where $p_{gas} = 0.1$ mbar is the helium gas pressure and $p_{atm} = 1013.25$ mbar is the standard atmospheric pressure.

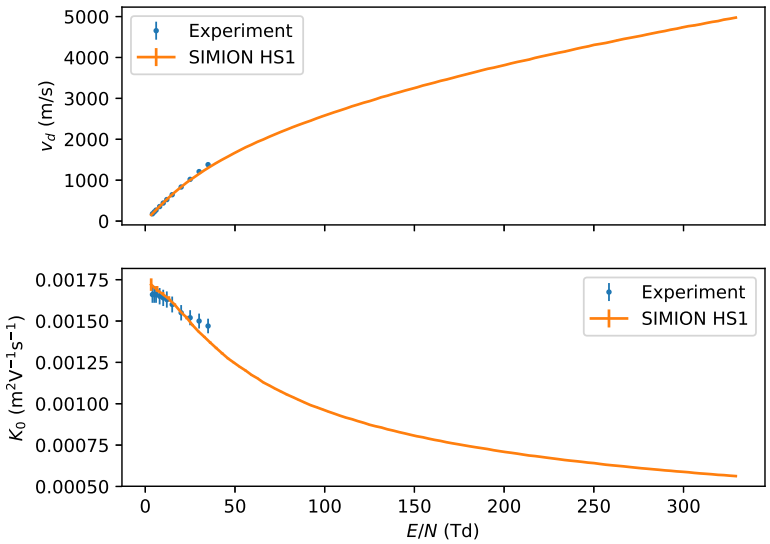

Figure 3.23: Simulation of ion drift velocity v_d in 0.1 mbar helium gas with different electric field strength. The unit of the horizontal axis is Townsend (1 Td = 10^{-21} Vm^2). The standard ion mobility K_0 is derived from Eq. (3.29). Previously published experimental results [VM95] are also plotted for comparison.

The results from simulation agree well with experimental data when the ion velocity is small, e.g. $v_d < 1000$ m/s. At larger ion velocity, the discrepancy is likely a result of the simplification of the hard sphere collision model HS1. An alternative model using the realistic potential [Kim97, Smi05, Sch06] between the ion and gas molecules to calculate the collisional parameters ha better agreement with experimental data.

3.5.2 Ion cooling rate

Ion cooling simulations in SIMION were done for ions in an LPT with RF frequency $f_{RF} = 1$ MHz. The initial RF phase is $\varphi_0 = 0$; the initial ion position is $(x = y = 0, z = 10)$ and the initial velocity is ($v_x = 0.1$ mm/µs, $v_y = v_z = 0$). For the stability parameter ($q = 0.1$, $a = 0$), the results are plotted in Figure 3.24. The results are compared to numerical solutions obtained using ion mobility as described in Section 2.5.2.

For helium gas pressure of 0.01 mbar and 0.1 mbar, the ion trajectories shown in the top and middle plot of Figure 3.24 are found slowing down faster than the calculated time constant from the ion mobility. This is because at larger ion velocity the ion mobility is smaller, as shown in Figure 3.23. The smaller ion mobility corresponds to a larger damping effect for the ion.

For a larger helium gas pressure of 1 mbar, the ion cooling is found to be taking longer than the RK4 solution. This is also expected because the ion is being over-damped as discussed in Section 2.5.3.

Simulations were also done for the stability parameter ($q = 0.5$, $a = 0$) with the same RF frequency and initial RF phase. The initial ion position is $(x = y = 0, z = 1)$ and the initial velocity is ($v_x = 0.1$ mm/µs, $v_y = v_z = 0$). The results are shown in Figure 3.25.

The ion velocity of an ion being cooled at 1 mbar is shown in Figure 3.26 and compared with the RK4 solution from ion mobility. The ion-neutral collisions can be seen as the abrupt changes in ion velocity, in contrast to the smooth decrease in the RK4 solution.

Figure 3.24 to Figure 3.26 also reveal that the ion position and velocity doesn't keep decreasing to infinitesimal. Instead, both the position and velocity reach thermal equilibrium with the helium gas.

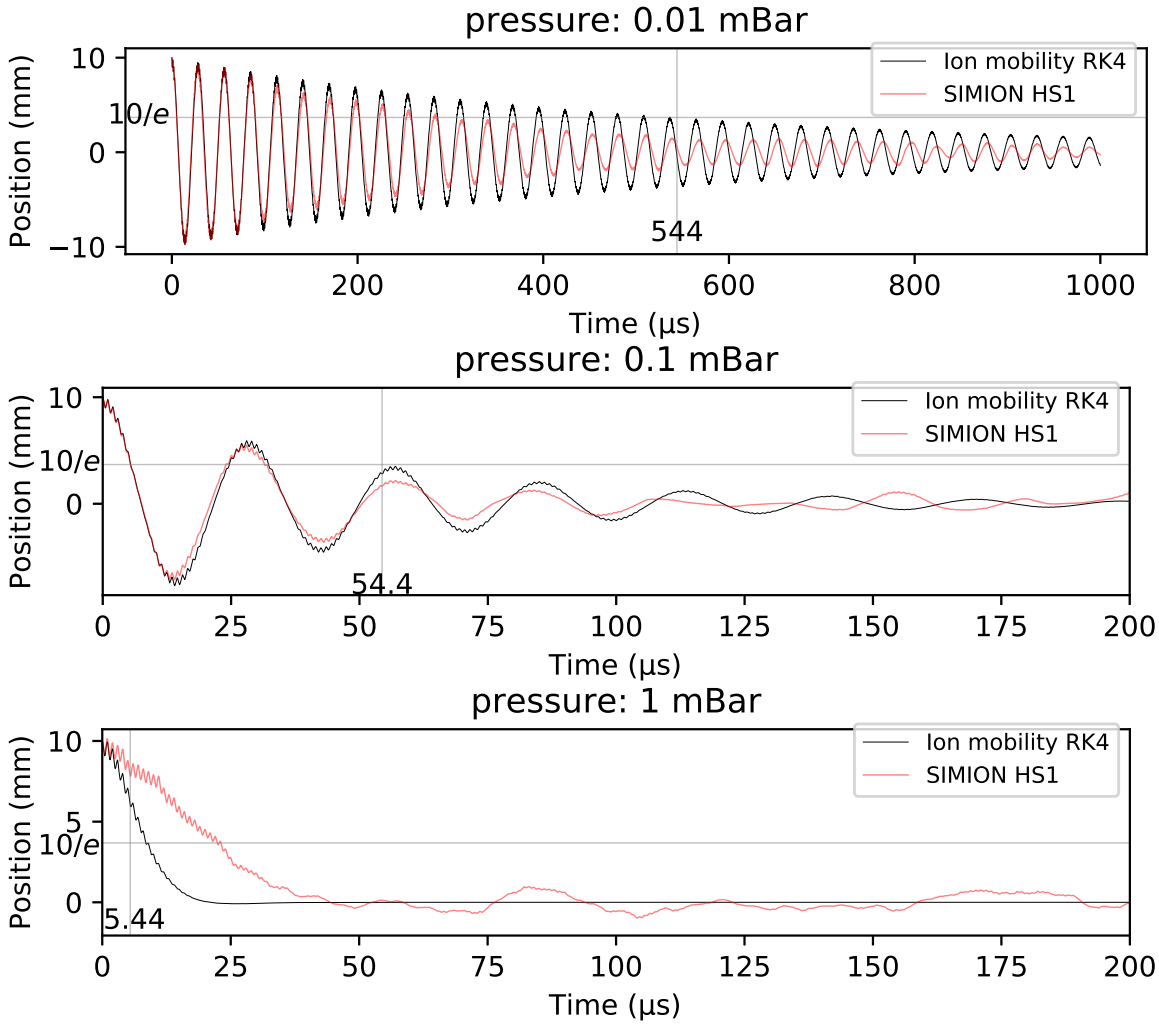

Figure 3.24: Ion cooling simulation in an LPT with stability parameter ($q = 0.1$, $a = 0$) at helium gas pressure of 0.01 mbar (top), 0.1 mbar (middle) and 1 mbar (bottom).

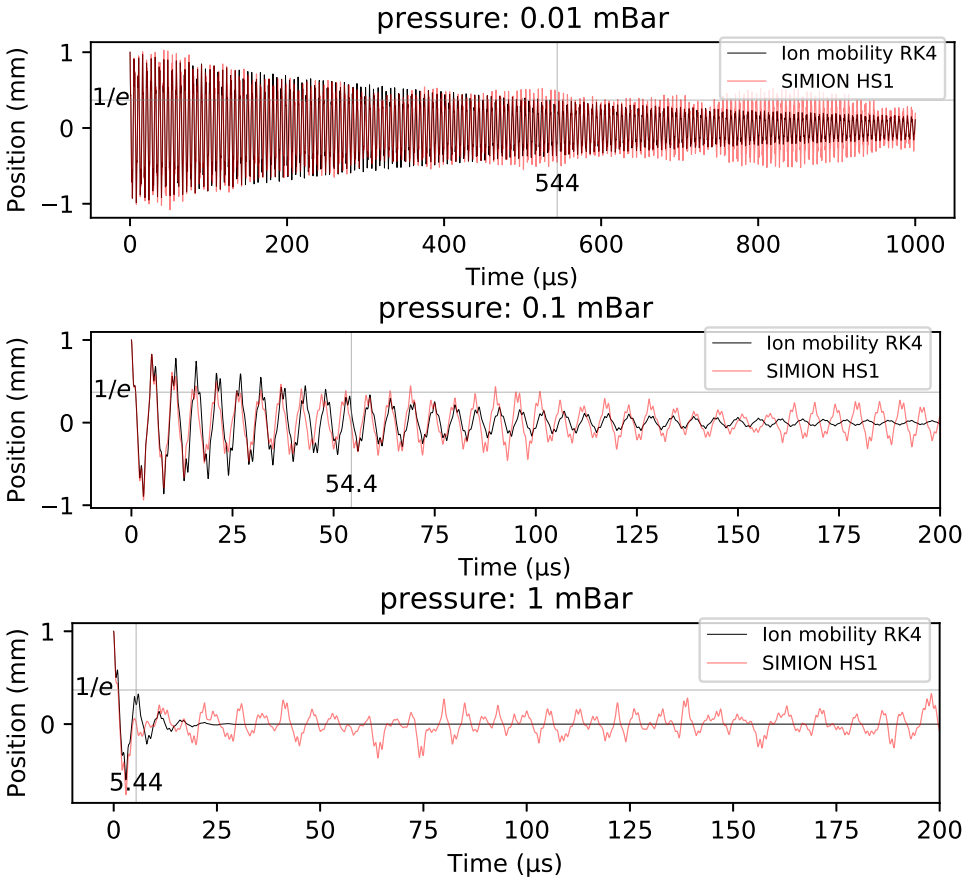

Figure 3.25: Ion cooling simulation in an LPT with stability parameter ($q = 0.5$, $a = 0$) at helium gas pressure of 0.01 mbar (top), 0.1 mbar and 1 mbar (bottom).

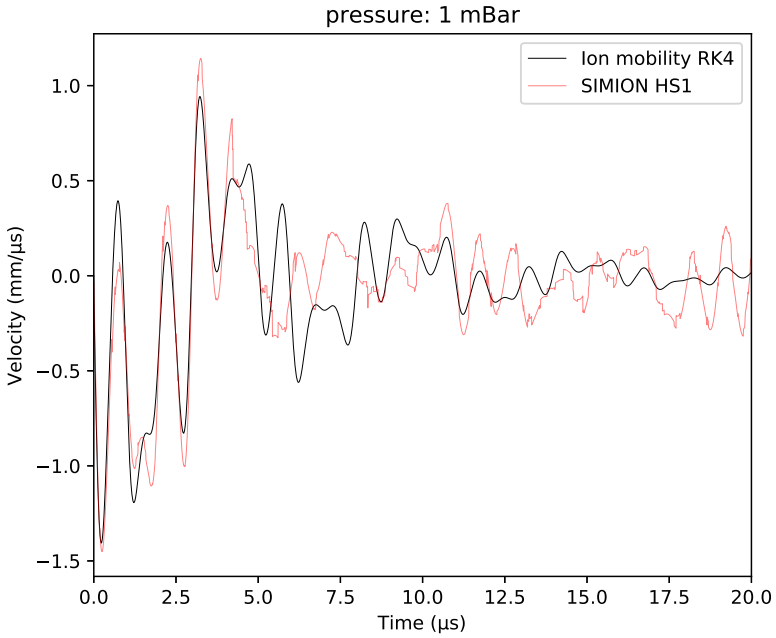

Figure 3.26: Velocity as a function of time for an ion cooled in an LPT with 1 mbar of helium gas.

3.5.3 Ion temperature

The temperature of ions in a linear Paul trap has been extensively studied by Kim [Kim97]. Some notations and derivations below are borrowed from there.

The distribution of ions after reaching thermal equilibrium with the buffer gas can be generically described using the Boltzmann distribution

$$\frac{dN}{dE} = \frac{N_0}{k_B T} e^{-\frac{E}{k_B T}}, \tag{3.30}$$

where dN is the number of ions in the energy interval dE, N_0 is the total ion number, k_B is the Boltzmann constant and T is the ion temperature.

Temperature of ions in a simple harmonic well potential

For ions trapped in a simple harmonic well, the phase space distribution of the ions follows the Gibbs distribution

$$\frac{\partial^6 N}{\partial S} = A e^{-\frac{E}{k_B T}}, \tag{3.31}$$

where A is a normalization constant. When the ion motion is independent in the coordinates, the Gibbs distribution in one of the coordinates u is

$$\frac{\partial^2 N}{\partial u \partial p_u} = A \exp(-\frac{E}{k_B T}). \tag{3.32}$$

For a singly charged positive ion of mass m, the ions experience a restoring force F from the electric field E_u. The electric field and the resulting restoring force are proportional to the displacement u in the harmonic well

$$F = -eE_u = -ku. \tag{3.33}$$

The energy of the ion in the harmonic well is

$$E = \frac{p_u^2}{2m} + \frac{ku^2}{2} = \frac{p_u^2}{2m} + \frac{m\omega^2 u^2}{2}, \tag{3.34}$$

where ω is the harmonic oscillation frequency of the ion in the well. In the phase space, the oscillation of the ions is represented by ellipses as shown in Figure 3.27. The area of the ellipses is proportional to the ion energy.

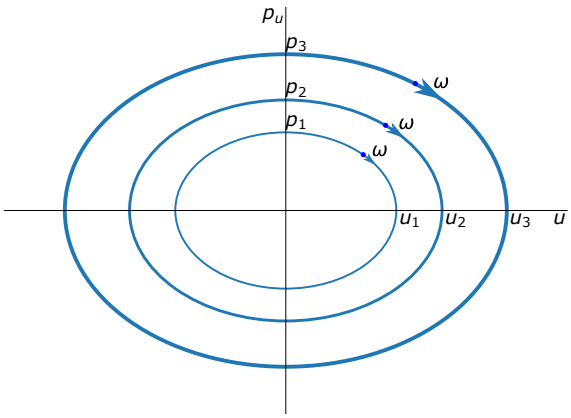

Figure 3.27: Motion of ions trapped in a simple harmonic potential well shown in the position-momentum $(u - p)$ phase space.

Inserting Eq. (3.34) back to Eq. (3.32) reveals that the ions have Gaussian distribution of both their position u and momentum p_u. The standard deviation of u and p_u is

$$\sigma_u = \sqrt{\frac{k_B T}{m\omega^2}}, \tag{3.35}$$

$$\sigma_{p_u} = \sqrt{m k_B T}. \tag{3.36}$$

The ion temperature can be derived from either σ_u or σ_{p_u}. Note that the ion temperature can be different in the three coordinates.

Temperature of ions in an LPT

The ion trapping in the longitudinal direction x of an LPT is similar to the case of a harmonic potential well. According to Eq. (3.36) and $p_u = mv_u$, the ion temperature T_x is derived from σ_{v_u}:

$$T_x = \frac{m\sigma_{v_u}^2}{2k_B}. \tag{3.37}$$

In the transverse directions y and z of an LPT, the ions are confined by a pseudopotential formed by the RF potential. The ions undergo a macromotion and a micromotion as discussed in Section 2.1.2 and Section 2.1.3. In the phase space, the ion motions evolved along ellipses with the secular frequency $\bar{\omega}$ as the macromotion. In each RF cycle, the ellipse tilts to different angles depending on the RF phase as a result of the micromotion as shown in Figure 2.7(b). As a result, both σ_u and σ_{p_u} varies along the RF phase. However, the ion emittance is independent of the RF phase

$$\epsilon = 4\sigma_u\sigma_v\sqrt{1 - r_{uv}^2}, \tag{3.38}$$

where r_{uv} is the Pearson correlation coefficient defined in Eq. (3.16). According to Eq. (3.35), Eq. (3.36) and $p_u = mv_u$, the ion temperature is derived as

$$T_u = \frac{m\bar{\omega}^2\sigma_u\sigma_v\sqrt{1 - r_{uv}^2}}{k_B}, \tag{3.39}$$

where $\bar{\omega} = \omega_0 = \frac{\beta\Omega}{2}$, and β is obtained from Eq. (2.39).

Simulations were done for 4000 ^{136}Ba ions in an LPT filled with 0.1 mbar of helium buffer gas. To first study the effect of the RF confinement, no DC potential was applied in the longitudinal direction. The ions were set to have a small initial longitudinal velocity $v_x = 0.1\,\mathrm{mm/\mu s}$ to make sure they do not fly out of the simulation volume.

The RF frequency of the simulation was set at 1 MHz, the RF amplitude was set within $24.7\,\mathrm{V} < V < 221.9\,\mathrm{V}$ corresponding to the stability parameter $0.1 < q < 0.9$ for an LPT with $r_0 = 4.21\,\mathrm{mm}$. For each time step, the ions' standard deviation of the position σ_u and velocity σ_{v_u} for each

coordinate was recorded, the Pearson correlation coefficient r_{uv} between the ion positions and the velocities was recorded for each coordinates as well. The ions reached thermal equilibrium with the buffer gas after a few hundred microseconds. The value of σ_u, σ_{v_u} and r_{uv} recorded during 800 to 1000 µs was used to calculate the ion temperatures according to Eq. (3.37) and Eq. (3.49) and shown in Figure 3.28.

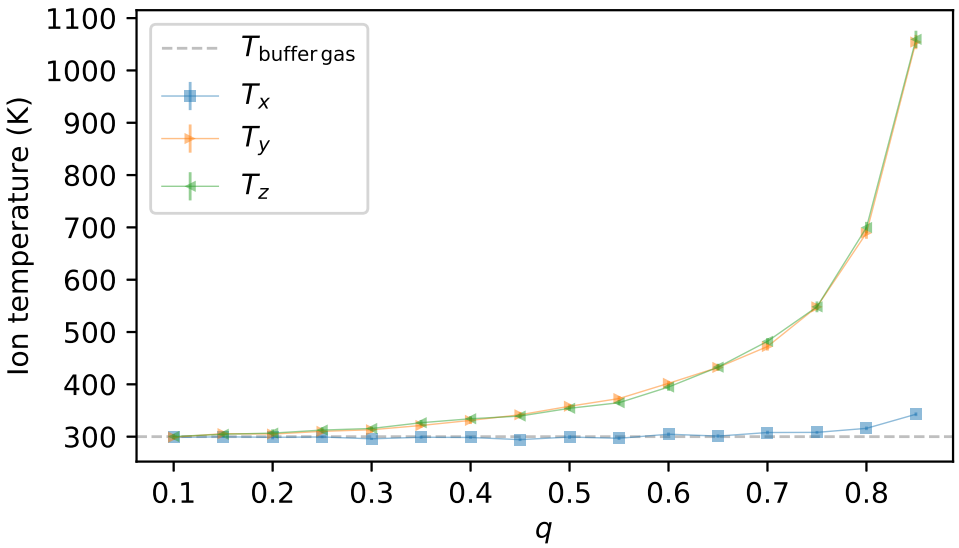

Figure 3.28: Temperature of ions in the LPT with 0.1 mbar helium buffer gas at different stability parameter q. The ions were confined only in the radial direction. See text for details.

The ion temperature in the radial directions y and z were found to be dependent on the q value. The ion temperature is close to the buffer gas temperature of 300 K for a small q value. For larger q values, the ions are driven by the larger micromotion and have more intensive collisions with the buffer gas. The excess micromotions and collisions heat up the ions known as the RF heating [BKQW89, PWM+91, RZS05]. The ion temperature T_y and T_z in the radial directions were found to be below 400 K when $q < 0.6$.

The ion temperature in the longitudinal direction x is mostly the same as the buffer gas temperature at 300 K. The slight effect of RF heating is only noticeable for large q values.

3.5.4 Ion trapping in the longitudinal direction

The trapping of ions in the longitudinal direction in an LPT was studied in a simplified LPT with three sets of short quadrupole electrodes as illustrated in Figure 3.29(a). In the longitudinal direction x, the length of each set of quadrupole electrodes is 4.5 mm; the gap between each set of quadrupole electrodes is 0.5 mm. The DC potential of the first and third set of quadrupole electrodes was set to be $U_1 = U_3 = 0$ V; U_2 was set to a negative voltage to form a longitudinal trapping potential.

Electric potential along the LPT's central axis obtained from SIMION simulation is shown in Figure 3.29(b). The potential is proportional to the applied voltage of U_2. For every -1 V of U_2, the minimum potential at the longitudinal center $x_c = 7.25$ mm is -0.59 V. The simulation result from U_2 =-10 V within the range of the second (central) set of the quadrupole electrode $5 < x < 9.5$ was used for a least-square fitting with the formula

$$U_A = B_0 + B_2 (x - x_0)^2. \tag{3.40}$$

The fitted result are

$$B_0 = -5.897 \pm 0.002(\mathrm{V}), \tag{3.41}$$

$$B_2 = 0.253 \pm 0.001(\mathrm{V/mm^2}), \tag{3.42}$$

$$x_0 = 7.248 \pm 0.002(\mathrm{mm}). \tag{3.43}$$

$$\tag{3.44}$$

The Chi-square of the fitting is $\chi^2 = \sum(U_{simulation} - U_A) = 6.8 \times 10^{-3}$. The small value of χ^2 indicates axial potential in the region of the central set of quadrupole electrodes is close to a pure quadratic potential well. Therefore, the ions will do damped harmonic oscillations in the longitudinal direction

$$m\frac{d^2x'}{dt^2} + \frac{e}{K}\frac{dx'}{dt} + 2eB_2x' = 0, \tag{3.45}$$

where $x' = x - 7.25$, K is the ion mobility and e is the elementary charge.

The ion's equation of motion in Eq. (3.45) can be rewritten as

$$\frac{d^2x'}{dt^2} + 2\zeta\omega_{x0}\frac{dx'}{dt} + \omega_{x0}^2 = 0, \tag{3.46}$$

where $\omega_{x0} = \sqrt{\frac{2eB_2}{m}}$ is the natural resonance frequency of the ions in the x direction when there is no damping, and $\zeta = \frac{e}{mK\omega_{x0}}$ is the damping ratio.

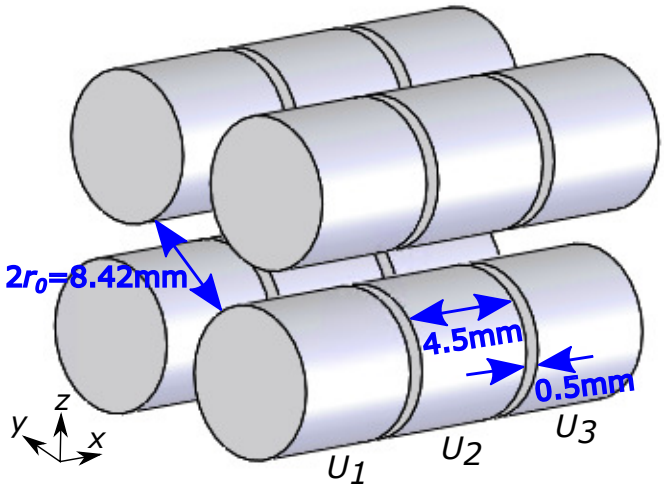

(a) Illustration of a simplified LPT

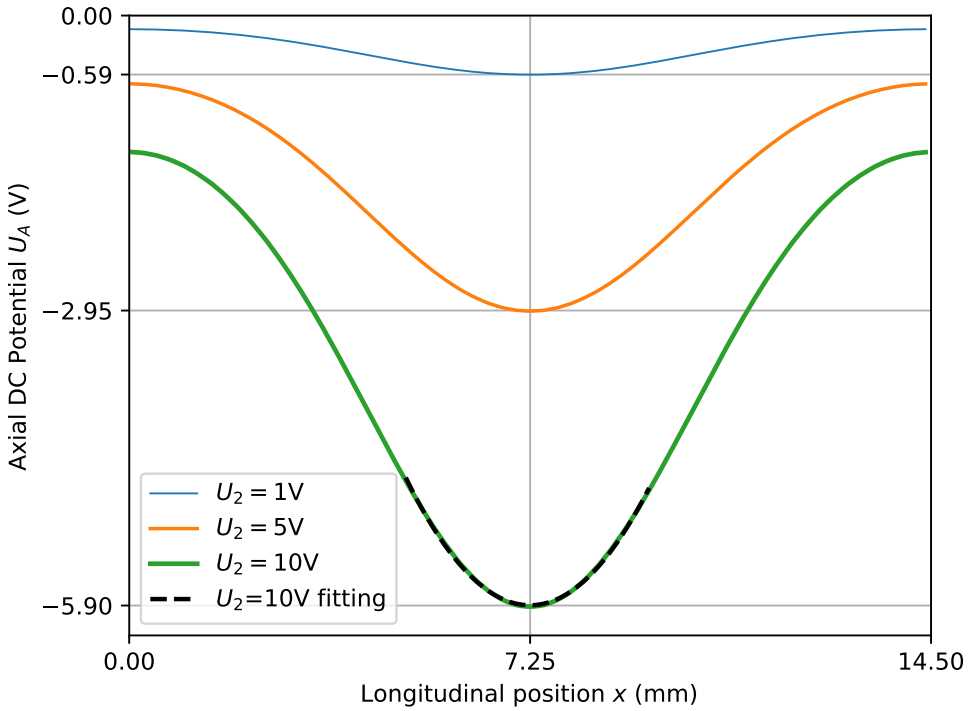

(b) Electric potential along the central axis

Figure 3.29: A simplified LPT for the simulation of ion trapping in the longitudinal direction.

When U_2 =-1 V, $B_2 = 2.53 \times 10^4 \mathrm{V/m^2}$. The natural resonance frequency of the barium ions in the longitudinal direction is $\omega_0 = 3.02 \times 10^4 \cdot 2\pi\mathrm{Hz}$. In this case, $\zeta = 0.23 < 1$ hence the ions are under-damped with actual oscillation frequency $\omega_{x1} = \omega_{x0}\sqrt{1-\zeta^2} = 0.95\omega_{x0}$.

For a deeper trapping potential U_2, the natural oscillation frequency ω_0 of the ions will be larger, hence the damping ratio ζ will be smaller and the actual oscillation frequency of the ions will be closer to ω_{x0}.

Expelling potential in the radial direction

According to the solution of the Laplace equation $\nabla^2\phi = 0$, the trapping potential along the longitudinal direction x expressed by Eq. (3.40) would cause an expelling potential in the radial direction that expels the ions:

$$U_r = B_0 - B_2 r^2, \tag{3.47}$$

where $r = \sqrt{y^2 + z^2}$.

The expelling electric potential causes a decrease in the effective pseudopotential for ion trapping in the radial direction. When the pseudopotential is weaker than the expelling electric potential, the LPT can no longer confine ions.

The reduced pseudopotential corresponds to a reduced secular frequency $\bar{\omega}'$ of the ion motion which can be theoretically expressed as

$$\bar{\omega}' = \sqrt{\bar{\omega}^2 - \omega_{x0}^2/2}. \tag{3.48}$$

For comparison, SIMION simulations were done for 10 ions in the simplified LPT with different trapping voltage U_2. The ion trajectories were recorded and the secular frequency of the ions' motion was obtained from the FFT (fast fourier transform) of the ions' motion and velocity. The results are shown in Figure 3.30.

The good agreement between the theoretical and simulated reduced secular frequency $\bar{\omega}'$ of the ion motion validates the effect of the expelling potential in the radial direction. Note that for the trapping depth $U_2 = -10\,\mathrm{V}$, the pseudopotential of $q < 0.2$ is smaller than the expelling potential hence the ions cannot be trapped in the LPT and the theoretical reduced secular frequency is invalid.

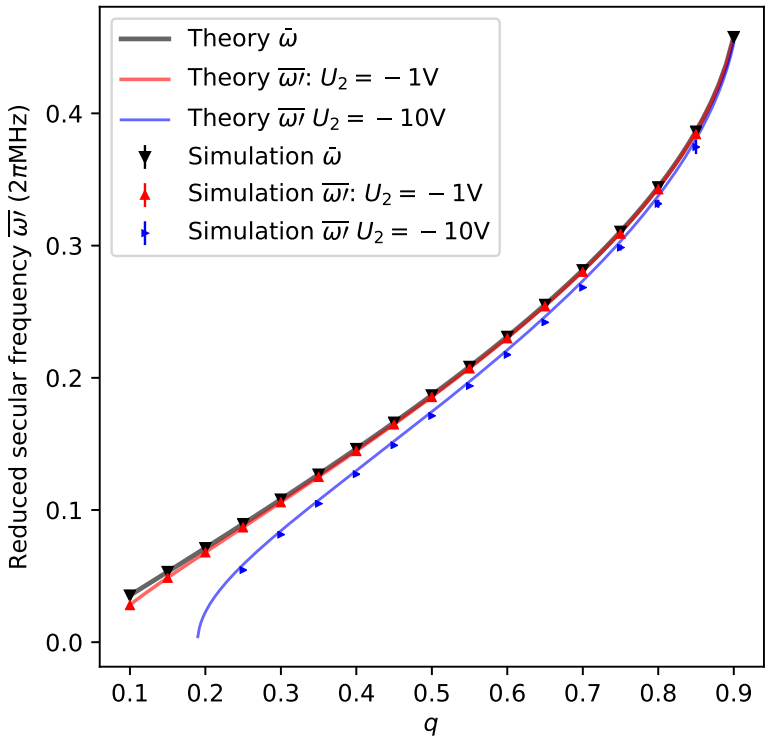

Figure 3.30: Secular frequency $\bar{\omega}$ and reduced secular frequency $\bar{\omega}'$ of ion motion in an LPT. Most of the error bars are too small to be seen.

Effect of longitudinal trapping depth on ion temperature

The ion temperature in an LPT with longitudinal trapping was studied via SIMION simulations of the simplified LPT cooler. The simulations were done with the same RF frequency and voltages as in Figure 3.28. .

For each simulated longitudinal trapping voltage, the ion temperature in the longitudinal direction was obtained using Eq. (3.37). In the radial directions y and z, the ion temperature was calculated from

$$T_u = \frac{m\bar{\omega}'^2\sigma_u\sigma_v\sqrt{1-r_{uv}^2}}{k_B}. \tag{3.49}$$

The results are shown in Figure 3.31.

For both longitudinal trapping depths $U_2 = -1\,\mathrm{V}$ and $U_2 = -10\,\mathrm{V}$, the ion temperature is similar to Figure 3.28 when there is no longitudinal

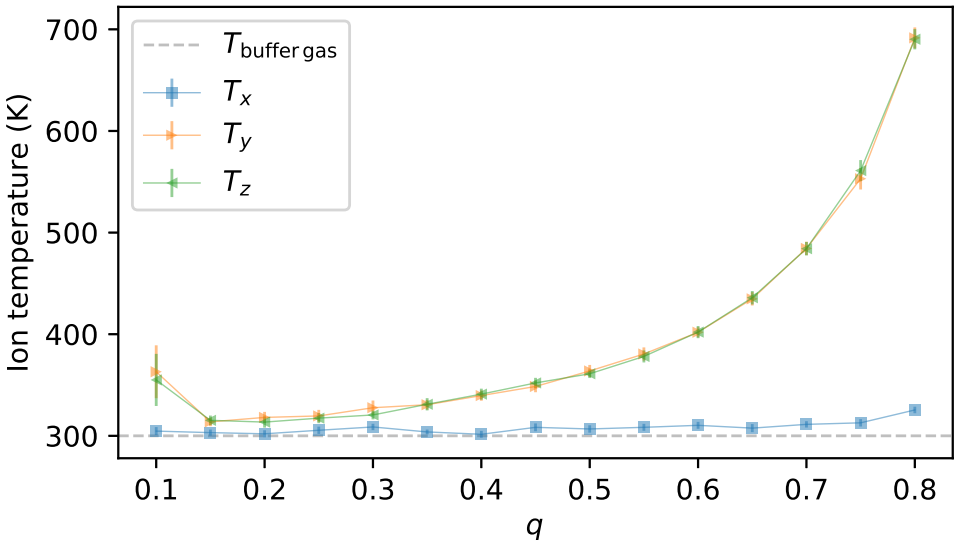

(a) Longitudinal trapping depth $U_2 = -1\,\text{V}$.

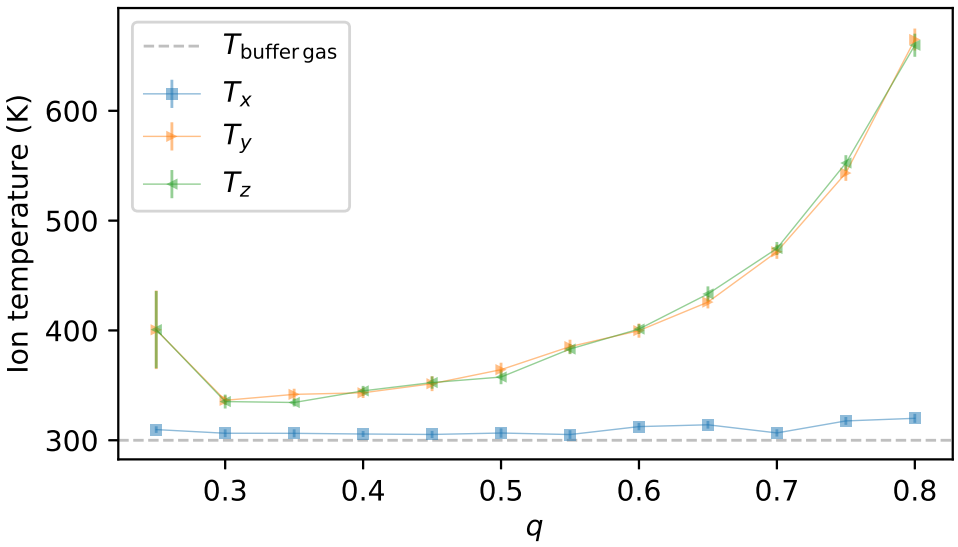

(b) Longitudinal trapping depth $U_2 = -10\,\text{V}$

Figure 3.31: Temperature of ions in an LPT with different longitudinal trapping potential depth U_2.

trapping potential. In the longitudinal direction, the ion temperature is always close to the buffer gas temperature. In the longitudinal direction, the RF heating is more obvious at a larger q value. At the smallest q value that still allows the LPT to trap ions, the ion temperature appeared to be unexpectedly higher but with a larger uncertainty.

Emittance of cooled ions in LPT

Simulations were done to study the emittance of cooled ions in the simplified LPT. In the simulation, 1000 barium ions were cooled for 1000 µs in the LPT with 0.1 mbar of helium buffer gas. The standard deviation of the ion position σ_u and velocity σ_{v_u} were recorded for each time step for each coordinate. The Pearson correlation coefficient r_{uv} (defined in Eq. (3.16)) was also recorded. The ions were cooled to thermal equilibrium after around 300 microseconds. The values of σ_u, σ_{v_u} and r_{uv} from 800 to 1000 microseconds were used to calculate the ion emittance for each coordinate u

$$\epsilon_u = 4\sigma_u\sigma_v\sqrt{1 - r_{uv}^2}. \tag{3.50}$$

At this point, the LPT was studied with a fixed q value of $q = 0.5$. Simulations were done for the longitudinal trap depth U_2 from -1 V to -30 V at the RF frequencies f_{RF} of 0.5 MHz, 1 MHz and 2 MHz. The longitudinal emittance ϵ_x and the transverse emittance $\epsilon_{y,z}$ were calculated using Eq. (3.50) and are shown in Figure 3.32.

For all RF frequencies, the longitudinal ion emittance ϵ_x was found to be smaller with deeper longitudinal trapping potential.

In the transverse direction, a larger RF frequency f_{RF} corresponds to a higher RF amplitude hence a deeper pseudopotential. The transverse ion emittance $\epsilon_{y,z}$ was also found to be smaller at a deeper pseudopotential.

For the lowest RF frequency $f_{RF} = 0.5$ MHz, the transverse emittance was found to be larger at a deeper U_2. This is a result of the decreased effective pseudopotential depth as described above. When $|U_2| > 12$ V, the LPT can no longer trap ions at 0.5 MHz.

At $f_{RF} = 1$ MHz and above, the LPT's pseudopotential is strong enough to trap ions in the whole range of simulated range of U_2 from -1 V to -30 V. The transverse ion emittance $\epsilon_{y,z}$ is slightly larger at a deeper U_2 as expected.

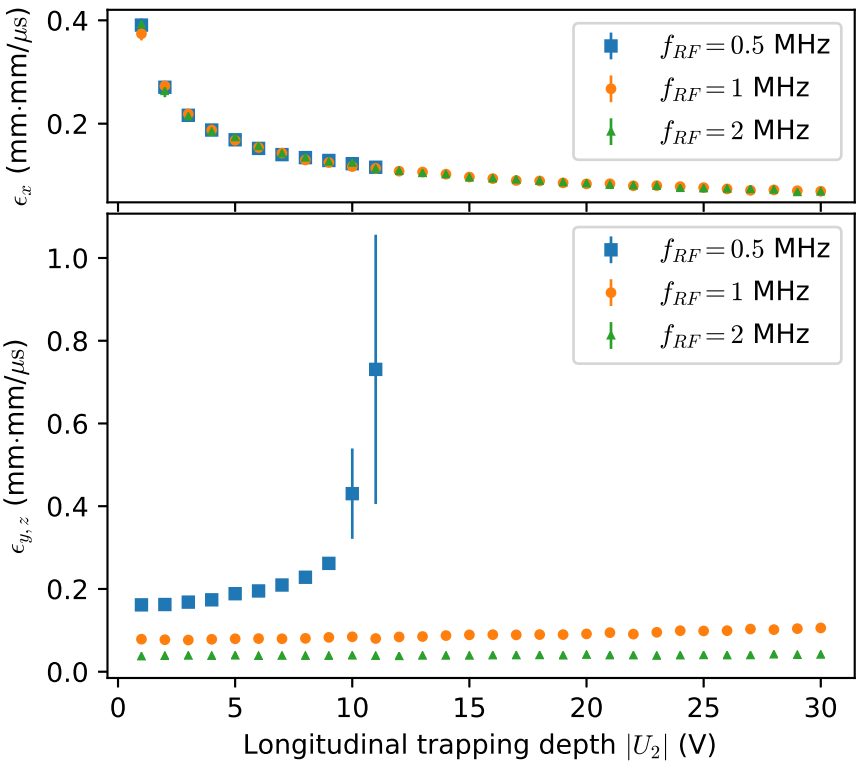

Figure 3.32: Longitudinal emittance ϵ_x and transverse $\epsilon_{y,z}$ of cooled ions in the LPT at different longitudinal trapping potential U_2 and RF frequency f_{RF}.

3.6 RFQ ion buncher

The RFQ ion buncher is needed to eject the cooled ion cloud in the LPT as an ion bunch to an ion detector or downstream experiments. An ion buncher shown in Figure 3.33(a) is studied in this section.

The geometry of the ion buncher is the same as the simplified LPT in Figure 3.29(a) except two additional aperture plates are needed. The electric potential gradient (electric field strength E_x) used to eject the ions is formed by the different DC potentials applied on the three sets of the quadrupole electrode and the aperture plates. The potential along the central axis of the buncher is obtained via electrostatic simulation using SIMION and shown in Figure 3.33(b).

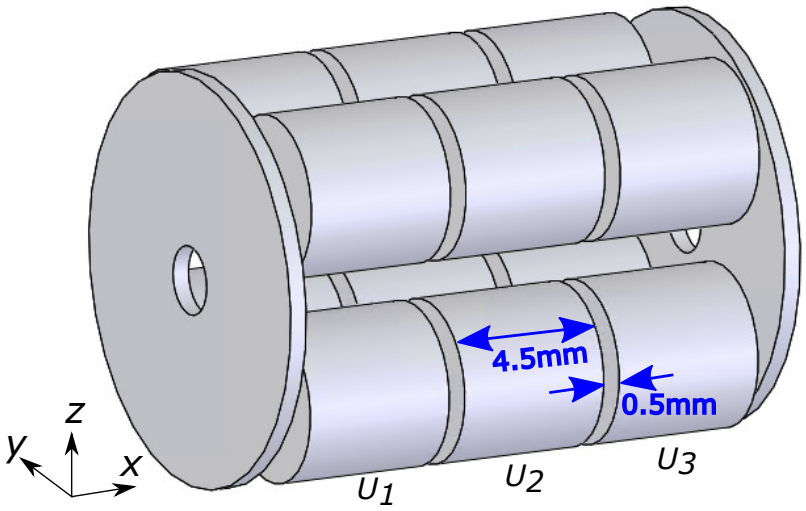

(a) Illustration of an RFQ ion buncher

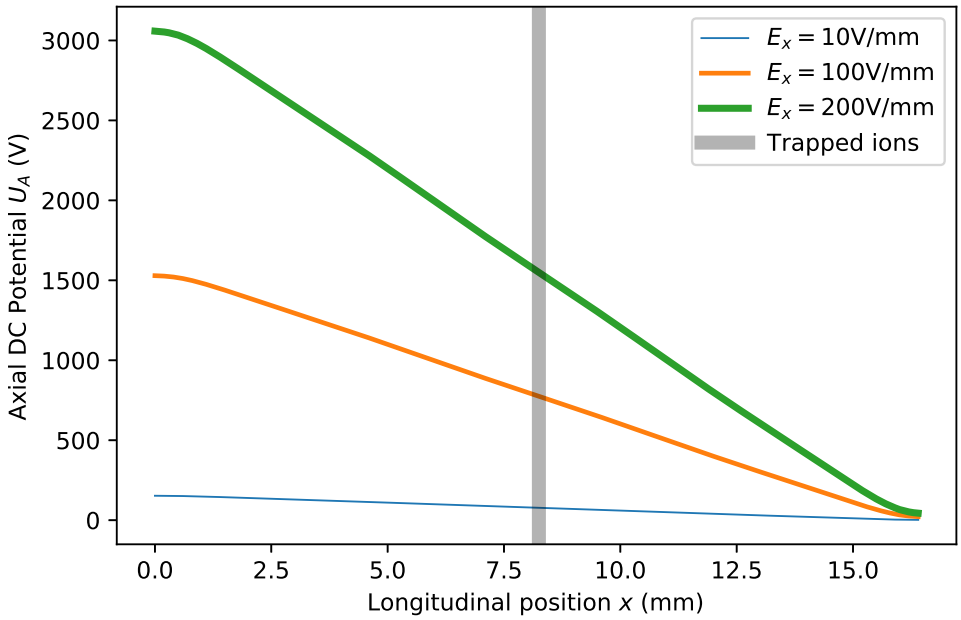

(b) Electric potential along the central axis

Figure 3.33: An RFQ ion buncher for the simulation of ion ejection.

The purpose of the ion buncher in this study is to form fine ion bunches for a downstream MR-TOF mass spectrometer. The MR-TOF requires the ion bunch to have a small energy spread (typically around 2%) and a small time spread (typically tens of nanoseconds).

Energy spread of bunched ions

The kinetic energy K_E of the ejected ions is determined by the DC potential U_T at the position of the trapped ion cloud. Consequently, K_e is proportional to E_x as the simulated results shown in Figure 3.34. The results come from ion ejection simulation of 1000 ions which has been cooled for 1000 µs and trapped as an ion cloud in the center of the ion buncher. The key parameters of the simulation are: $q = 0.5$, $f_{RF} = 1\,\text{MHz}$ and $U_2 = -10\,\text{V}$. The ions stop at the exit of the ion buncher in the simulation, the ions' kinetic energy K_E and time-of-flight (ToF) is recorded for analysis.

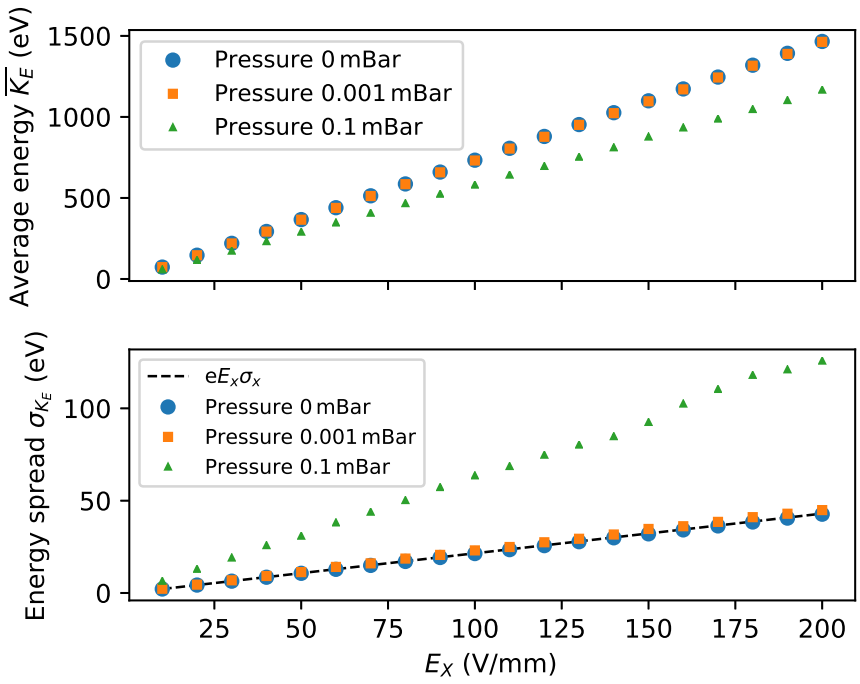

Figure 3.34: Kinetic energy $\bar{K_E}$ (top plot) and energy spread σ_{K_E} (bottom plot) of ions ejected from the buncher at different electric field strength E_x and helium buffer gas pressure.

The kinetic energy spread σ_{K_E} originates from the positional spread σ_x of the ion cloud before the ion ejection (the initial kinetic energy spread from velocity is around 0.01 eV and can be ignored). In the ideal case,

$$\sigma_{K_E} = eE_x\sigma_x, \tag{3.51}$$

where $\sigma_x = 0.215\,\text{mm}$ when $U_2 = -10\,\text{V}$. The ion energy spread calculated in this way is also plotted in Figure 3.34 and agrees well with the simulation when the ion buncher has ideal vacuum with 0 mbar pressure.

Similar simulations were then done for an ion buncher with realistic helium buffer gas pressure. The results are also shown in Figure 3.34. At the pressure 0.1 mbar, the ejected ions have noticeably decreased kinetic energy and increase energy spread as a result of excessive collisions with the helium gas. At 0.001 mbar, the collisional effect of the gas on the ion energy is almost negligible.

Time spread of bunched ions

The time spread of bunched ions comes from both the velocity spread σ_{v_x} and positional spread σ_x of the ion cloud before the bunching.

When the ions are initially accelerated in the electric field, the initial time spread is

$$\sigma_{t_0} = \sigma_{v_x} / \frac{eE_x}{m}, \tag{3.52}$$

where σ_{v_x} is the initial velocity spread of the trapped ion cloud before the ion ejection.

When the ions reach the exit of the ion buncher, there is an additional time spread as a result of the ions' initial position

$$\sigma_{t_1} = \frac{\sigma_x}{v_x}, \tag{3.53}$$

where v_x is the longitudinal velocity of the ions after reaching the exit of the ion buncher.

Finally, the spread of the ions' time-of-flight (ToF) is

$$\sigma_{t_{ToF}} = \sqrt{\sigma_{t_0}^2 + \sigma_{t_1}^2}. \tag{3.54}$$

The average and spread of the ions' time-of-flight t_{ToF} were obtained from the same simulations described above and shown in Figure 3.35. The time spread calculated from theory using Eq. (3.54) is also plotted and agrees reasonably well with the simulation when the helium gas pressure is 0.001 mbar or lower.

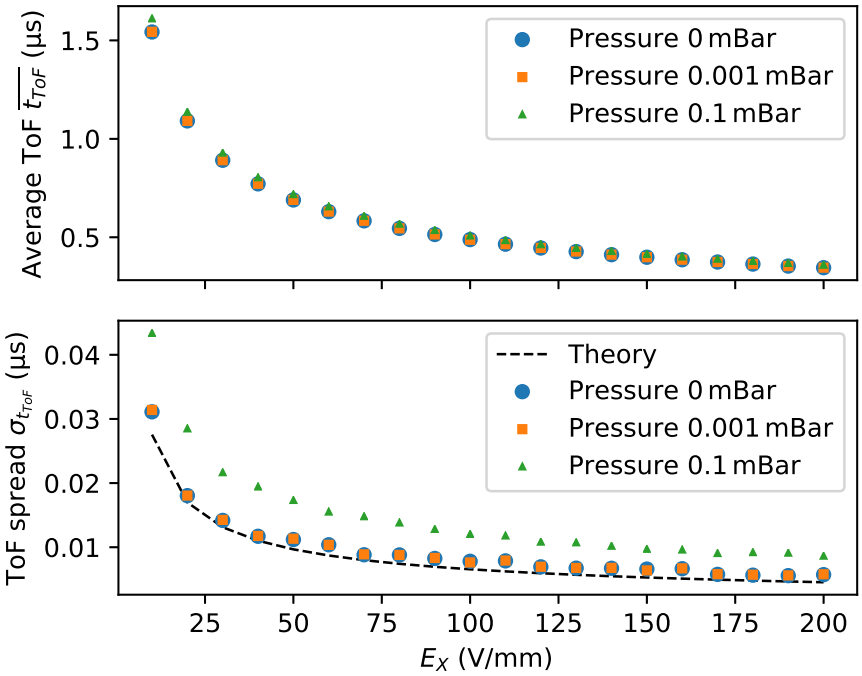

Figure 3.35: Simulated time of flight (ToF) of the ejected ions to reach the exit of the ion buncher as a function of the longitudinal electric field strength E_x. The simulations were done at ideal vacuum (0 mbar), 0.001 mbar and 0.1 mbar. Theoretical values of the ToF spread were calculated according to Eq. (3.54).

For a higher helium gas pressure of 0.1 mbar, the simulated ion time spread is noticeably larger than the theory as a result of excessive collisions with the helium gas during the ion ejection.

Effect of helium gas pressure on ion bunching

The effect of helium gas on the bunched ions' energy spread and time spread was studied in more detail for the electric field strength $E_x = 100$ V/mm. Ion ejection simulations were done for the ion buncher with helium gas pressure from 10^{-5} mbar to 0.6 mbar. The ions' kinetic energy K_E and time-of-flight t_{ToF} obtained from the simulations are shown in Figure 3.36. The energy spread σ_{K_E} and time spread $\sigma_{t_{ToF}}$ are shown as the error bars.

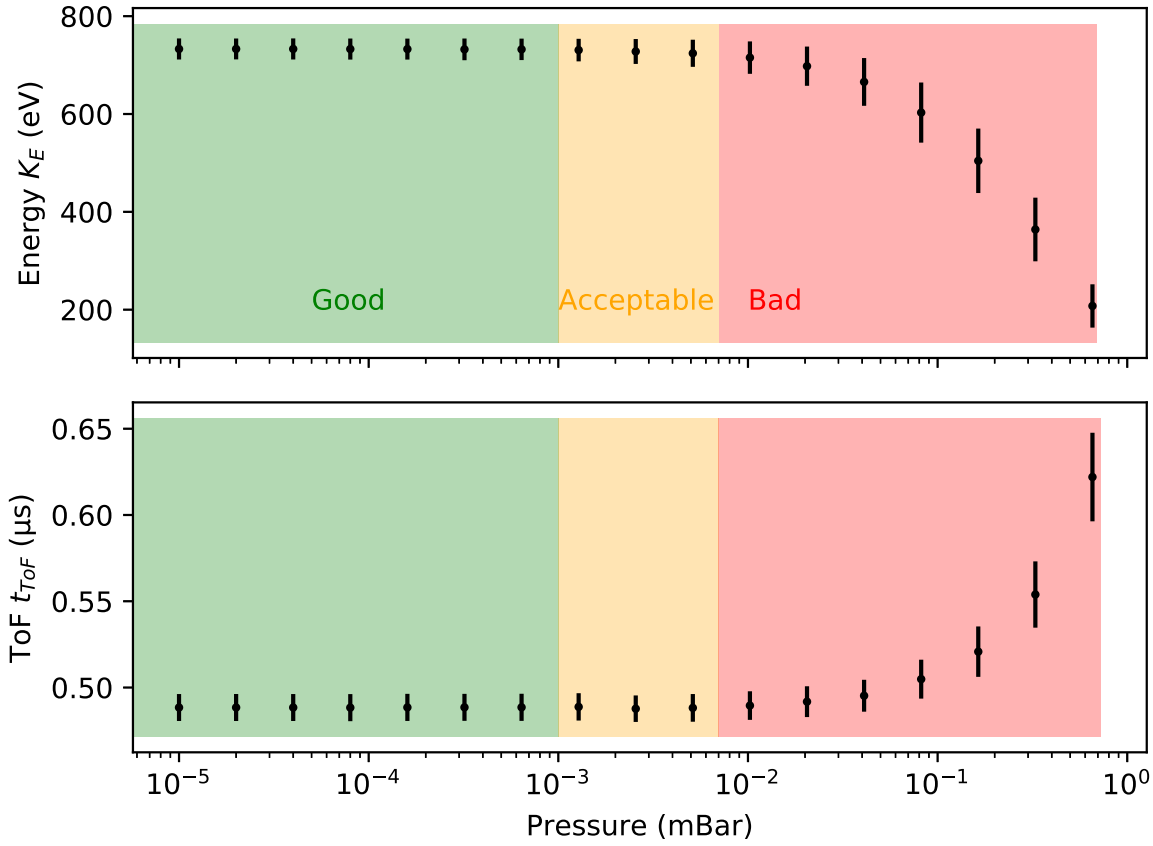

Figure 3.36: Ion energy K_E and time-of-flight t_{ToF} of bunched ions as a function of helium gas pressure in the ion buncher. See text for the details of the different labeled pressure regions.

The effect of the helium gas on the ion energy and ToF was found to be negligible when the gas pressure is lower than 10^{-3} mbar (labeled as

"Good"). At higher gas pressure, both the ion energy spread σ_{K_e} and time spread $\sigma_{t_{ToF}}$ increase significantly.

For the simulated ion cloud cooled in the longitudinal trap depth $U_2 = -10\,\mathrm{V}$, the relative energy spread $\sigma_{K_E}/K_E = 2.9\%$ is already higher than the requirement of the MR-TOF. In theory, the ion energy spread scales linearly with $1/\sqrt{|U_2|}$. Even though a deeper longitudinal trapping depth can reduce the ion energy spread, it is still critical to limit the increase of σ_{K_E} due to helium gas during ion ejection. For the ion buncher of this study, the helium gas pressure in the buncher is required to be lower than $7 \times 10^{-3}\,\mathrm{mbar}$ in order to limit the increase of ion energy spread to within 50% (labeled as "Acceptable"). When the helium gas pressure is higher than $7 \times 10^{-3}\,\mathrm{mbar}$ (labeled as "Bad"), the increase of the bunched ion's time spread and energy spread are more significant.

Chapter 4

A linear Paul trap system for barium tagging

In the following the design of a linear Paul trap (LPT) system based on the theory and simulations in the previous chapters is described. The system is to be installed downstream from an RF funnel to capture the extracted ions. Together they will be useful to carry out detailed studies of ion trapping and identification from xenon gas.

4.1 LPT system requirements

The LPT system is required to capture ideally 100% of the ions from the RF funnel. The ions need to be first cooled by the helium buffer gas, then trapped sufficiently long to allow barium ion identification via laser spectroscopy.

In previous experiments of ion extraction from high pressure xenon gas with a prototype of the RF funnel, significant amounts of ion contaminant were found [Fud18]. Therefore, a multi-reflection time-of-flight (MR-TOF) mass spectrometer is being designed and will be installed downstream from the LPT to systematically study the extracted ion species using high precision mass spectrometry.

For the MR-TOF to work at high precision, the ions from the LPT need to be ejected as fine ion bunches with small energy spread (typically within 2% of the kinetic energy of the ions) and small time spread (typically a few tens of nanoseconds).

The rate of ions that can be cooled in the RFQ cooler is limited. The total number of ions that can be stored in the laser spectroscopy ion trap and ion buncher is limited as well. Therefore, too many contaminant ions may reduce the trapping efficiency of the barium ions. Too many contaminant

ions can also overwhelm the downstream MR-TOF mass spectrometer.

In order to ensure the required conditions, a pre-filter system is needed. This can be realized by including a quadrupole mass filter (QMF) to remove many of the contaminant ions. The mass resolving power required for the QMF is $R = m/\Delta m > 80$ as this allows us to filter out most of the possible contaminant ions other than the isobar $^{136}Xe^{+}$.

According to these requirements, a conceptual design of the LPT system was completed in 2017 as shown in Figure 4.1 [Lan18b]. The design separates the major components of the LPT system into two vacuum chambers: a QMF chamber contains the quadrupole mass filter; a CLB chamber contains the cooler, laser spectroscopy ion trap and the buncher. A pulse drift tube is designed to be placed at the exit of the CLB chamber for adjusting the energy of the ions transferred into the MR-TOF mass spectrometer.

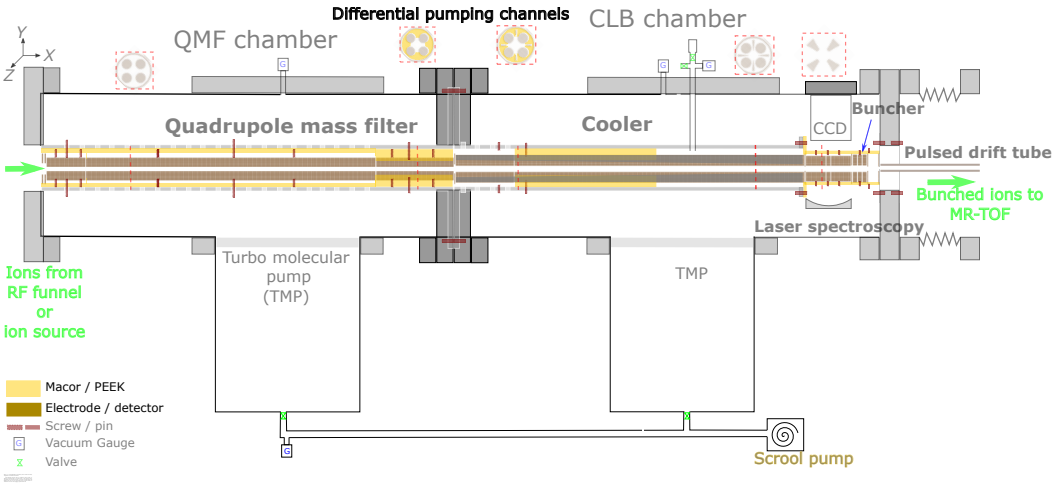

4.1.1 Ion acceptance requirement

The characteristics of ions coming from the RF funnel are shown in Figure 4.2 in one simulated example of 910 ions [Fud15]. The ion bunch has transverse emittance of

$$\epsilon^y_{rms} \approx \epsilon^z_{rms} = 0.16\text{mm} \cdot \text{mm}/\mu\text{s} \tag{4.1}$$

calculated from

$$\epsilon_{rms} = \sigma_u \sigma_v \sqrt{1 - r^2_{uv}}, \tag{4.2}$$

where u is y or z and v is v_y or v_z; r_{uv} is the Pearson correlation coefficient defined in Eq. (3.16).

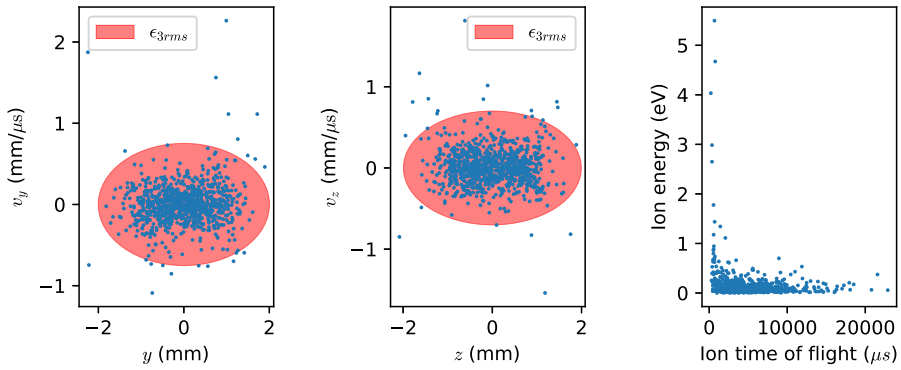

(a) (b) (c)

Figure 4.2: Phase space distribution in the transverse directions y (a) z (b) and the longitudinal direction x (c) of ions extracted from the RF funnel. The ion acceptance ϵ_{3rms} is defined in Eq. (4.4).

For ions with 2D Gaussian distribution of position u and velocity v_u in each coordinate, the probability of ions being captured with an acceptance corresponding to $n_{rms} \cdot \sigma_u$ and $n_{rms} \cdot \sigma_{v_u}$ is

$$P_{n\,rms} = 1 - \exp(-n^2_{rms}/2). \tag{4.3}$$

In order to capture 98% or more of the ions in both y and z axis, $n_{rms} \geq 3$ is needed. The corresponding ion acceptance required is

$$\epsilon_{3rms} = 9\epsilon_{rms} = 1.44\,\text{mm} \cdot \text{mm}/\mu\text{s}, \tag{4.4}$$

which is represented by the ellipses also shown in Figure 4.2.

The ion acceptance ellipse of an RFQ depends on the RF phase (see Section 2.2). The continuous ions coming from the RF funnel can enter the LPT system at any RF phase. To meet the required close to 100% ion transmission efficiency, the ion emittance needs to be within the ion acceptance ellipse of any RF phase [Daw75]. So the overlap of the ion acceptance at different RF phases referred to as phase independent acceptance needs to be considered.

Phase independent acceptance

Practically, 36 equally spaced phases were used to obtain the phase independent acceptance as illustrated in Figure 4.3 for the stability parameters ($q = 0.5$, $a = 0$).

The phase independent acceptance for other q values when $a = 0$ was obtained in the same way as shown in Figure 4.3 and shown in Figure 4.4.

The maximum phase independent acceptance is obtained at $q = 0.45$:

$$\epsilon_{PI,max} = 0.063\ r_0^2\Omega/2. \tag{4.5}$$

At f_{RF} =1 MHz and the stability parameters ($q = 0.45$, $a = 0$), the acceptance ϵ and the phase independent acceptance ϵ_{PI} are calculated for an RFQ with realistic mechanical properties. A few choices of commercially available high precision stainless steel rod as the quadrupole electrodes were considered. The calculated values are shown in Table 4.1. The configuration of $r_0 = r_e/1.13$ is used for each size of rod.

The phase independence acceptance for all three sizes of QMS shown in Table 4.1 meets the requirement of ϵ_{3rms} in Eq. (4.4). The larger acceptance enables more than 99% of ions from the RF funnel to be captured and transmitted.

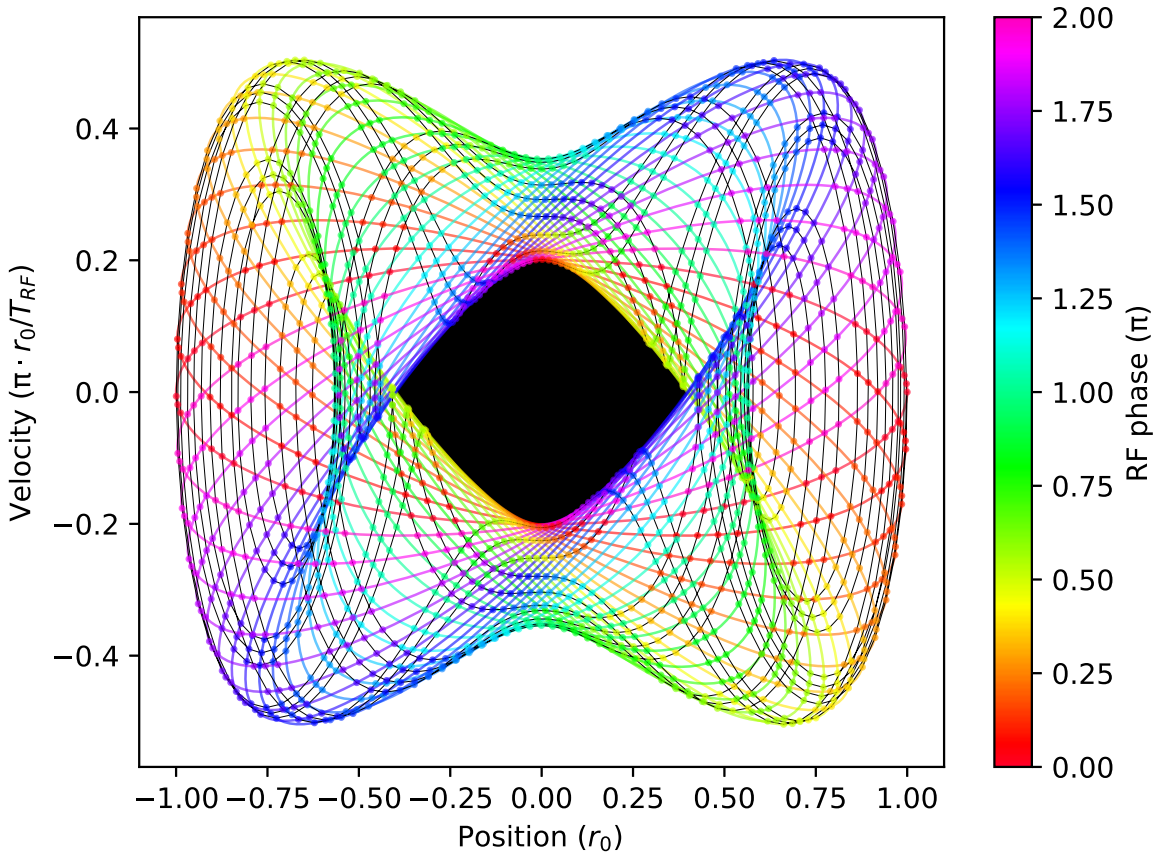

Figure 4.3: The phase independent acceptance ϵ_{PI} obtained as the overlap (plotted in black) of acceptance ellipses at 36 RF phases. The ion motion in the phase space is plotted in the thin black line. At each time step corresponding to each RF phase, the ion is represented by a different color as shown in the colorbar. An ellipse is obtained for each phase by least-square fitting to these points and shown in the same color.

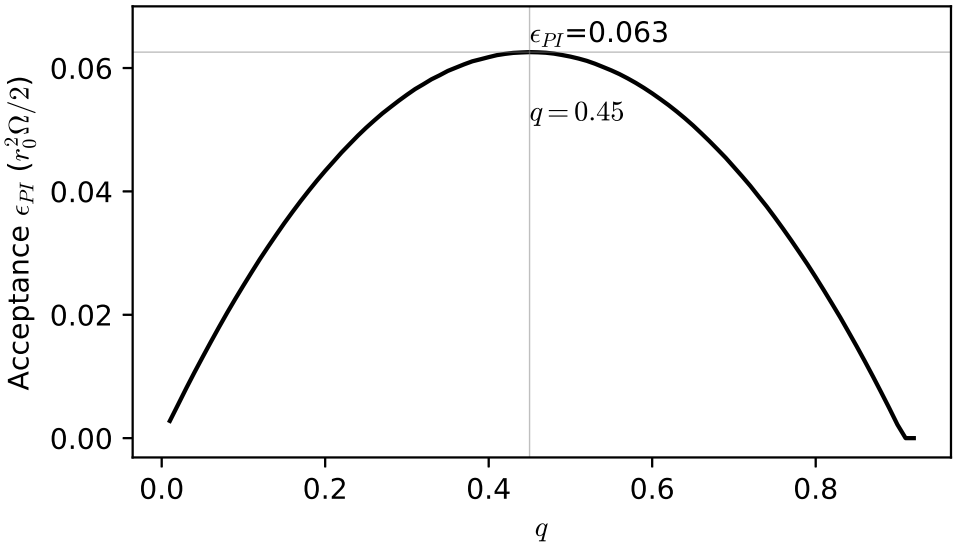

Figure 4.4: The phase independent acceptance ϵ_{PI} at different q value.

4.1.2 Vacuum requirements

The LPT system requires different vacuum levels for the different components. The ion cooler requires ∼0.1 mbar of helium as a buffer gas to effectively trap and cool the $^{136}Ba^{+}$ ions as discussed in Section 3.5. The ion buncher required a pressure lower than 7×10^{-3} mbar to avoid heating the bunched ions as discussed in Section 3.6. The laser spectroscopy ion trap requires a gas pressure smaller than 1×10^{-3} mbar to avoid the scattering of laser lights. The QMF requires the gas pressure to be around 1×10^{-5} mbar

Table 4.1: The acceptance ϵ and phase independent acceptance ϵ_{PI} for a few sizes of RFQ operating at 1 MHz and ($q = 0.45$, $a = 0$). The RF voltage needed is shown in the last row of the table.

r_e (inch)	1/8	5/32	3/16
r_e (mm)	3.18	3.97	4.76
r_0 (mm)	2.81	3.51	4.21
ϵ (mm mm/µs)	4.81	7.51	10.80
ϵ_{PI} (mm mm/µs)	1.56	2.44	3.51
V (V)	49.4	77.1	111.0

or lower so that the ion-neutral collisions will be negligible when the ions traverse through the QMF.

4.1.3 Mechanical tolerance requirements

In all the previous analyses and simulations of the RFQ, the quadrupole electrodes are assumed to be perfectly machined and positioned. However, in a realistic RFQ, the electrodes could have displacement from their designed positions due to mechanical tolerance.

The manufacturing imperfection and displacement of the quadrupole electrodes cause changes to the electric potential in the RFQ. Noticeably, the electrodes will no longer have a four-fold rotational symmetry along the x-axis, hence any order of spatial harmonics described by Eq. (3.5) can exist.

The QMS requires the higher-order spatial harmonics to be small in order to maintain a high mass resolving power R and a large ion acceptance. As discussed in Section 3.4.1, in order for a QMS to have mass resolving power $R = 50.5$ without significantly reduced acceptance, the higher-order spatial harmonic terms A_6, A_{10}, A_{14} and A_{18} need to be 0.01 or smaller. Similar simulations can be done to study the effect of additional higher-order spatial harmonics such as A_3, A_4, A_5, A_7 and so on.

Such simulations were not systematically performed during this study due to the limited time and computing power. Instead, preliminary simulations were done by displacing one of the quadrupole electrodes in the model [Lan18a]. The simulation reveals that in order for the QMS to have mass resolving power $R \geq 60$, the displacement of the electrode needs to be within $0.014r_0$. For reference, past experiments revealed that a relative mechanical tolerance of around 0.01 is necessary to achieve mass resolving power $R \geq 100$ [AHL76].

For QMS with round electrodes, stainless steel rods are commercially available (such as from McMaster-Carr) with a relative precision of the radius better than 0.001. So the mechanical tolerance from the manufacturing imperfection of the quadrupole electrodes can be ignored in comparison to the possible displacement of the electrodes in the assembly.

The cooler, the laser spectroscopy ion trap and the ion buncher were found to require a less strict mechanical tolerance at around $0.05r_0$.

4.2 Mechanical design

The mechanical design of the LPT system was done following the conceptual design as shown in Figure 4.1. The main outer mechanical structures consist of two ConFlat (CF) 6-way crosses, one CF 6-way cube and various flanges for electrical and gas feedthrough as shown in Figure 4.5 (a). On the bottom of each 6-way cross, a turbo molecular pump (TMP) will be installed.

The electrodes and holders are installed on the custom machined flanges as shown in Figure 4.5 (b) and (c). The mechanical and ion optics design of the QMF, ion cooler and the laser spectroscopy ion trap (and ion buncher) are described in the following sections.

4.3 QMF design

The design of the QMF is shown in Figure 4.6. The QMF has three sets of quadrupole electrodes. The two sets of short quadrupole electrodes at the entrance and exit are commonly called the Brubaker filters [Bru68] which have only RF voltage applied to mitigate the fringing field at the end of the long quadrupole electrodes during mass filtering.

The mechanical precision of the quadrupole electrodes is the most critical consideration for the design of the QMF. There are high precision stainless steel rods with a diameter tolerance of 0.0002" (5 µm) from McMaster-Carr which are suitable for the quadrupole electrodes of the QMF. For the QMF of this design, the rod diameter is chosen to be 5/16" (9.74 mm) using the #1255T15 stainless steel rod from McMaster-Carr. The ratio of $r_e/r_0 = 1.13$ was used as discussed in Section 3.4.2. The ion emittance ϵ and phase independent emittance ϵ_{PI} at this dimension and $f_{RF} = 1\,\text{MHz}$ as shown in Table 4.1 allow an ion transmission efficiency larger than 99% when the RFQ is operated as an ion guide with maximum ion acceptance at $q = 0.45$.

The positional precision of the rods is also critically important to achieving an overall tight mechanical tolerance for the QMF. A monolithic electrode holder was specially designed so that the positioning of all the electrodes is fully defined by the holder and human error during the assembly can be minimized. The holder can be machined in a computer numerical controlled (CNC) milling machine.

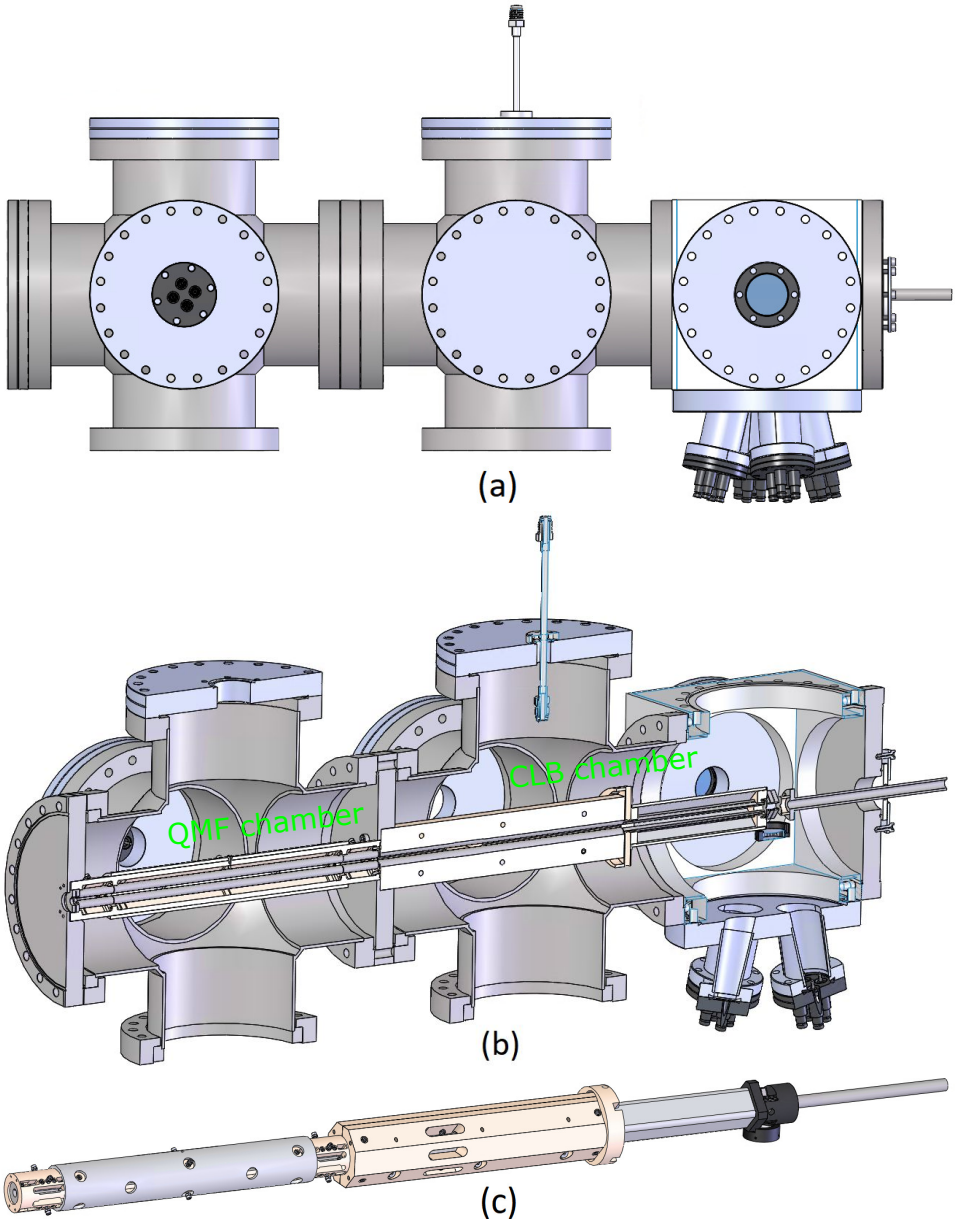

Figure 4.5: Rendered drawings of the mechanical design of the LPT system. See text for details.

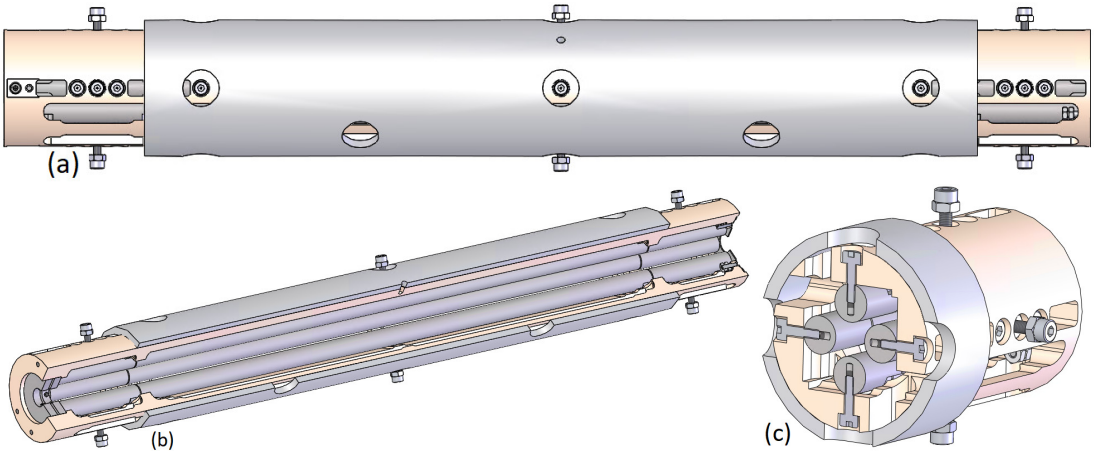

Figure 4.6: Rendered drawings of the finalized design of QMF. (a) side view. (b) cut view showing the electrodes of the QMF and structure of the holder. (c) cut view of the QMF showing the positioning and mounting of the quadrupole electrodes.

The QMF is designed to have two aperture lenses at the entrance and one at the exit. The aperture lenses are used for both creating a well defined electric potential boundary and for adjusting the ion energy.

Additional details and dimensions of the QMF are shown as mechanical drawings in Appendix B (drawing number LPT2Q).

4.4 Ion cooler design

The ion cooler downstream from the QMF needs to be filled with approximately 0.1 mbar of helium gas to effectively capture and cool the barium ions. Between the QMF and the cooler, the gas pressure is different by a factor of around 10^4. The different gas pressures required in the vacuum system can be achieved via differential pumping. However, a single-stage differential pumping is not practical to achieve the 10^4 pressure difference in this case. Therefore, a pre-cooler is needed as a second stage for the differential pumping and for transmitting the ions.

4.4.1 Pre-cooler as the differential pumping channels

An RFQ ion guide is designed to function as the pre-cooler. The pre-cooler transmits the ions while allowing the excess helium gas from the cooler to escape from the space between the quadrupole electrodes. The gas conductance C_{C2Q} from the cooler to the QMF through the pre-cooler needs to be as small as possible to enable effective differential pumping. Considering the vacuum pumps to be used for the vacuum system, $C_{C2Q} < 5\,\mathrm{L/s}$ is required.

A small gas conductance is commonly achieved through a small aperture. However, the size of the aperture has to be large enough for the flight path of the ions to fall within. Depending on the RF phase, the ions coming from the upstream QMF can have positional spread as large as $r_0^{QMF} = 3.51\,\mathrm{mm}$. From Eq. (3.25) of [MDCG09], the conductance of an aperture at the molecular flow region is

$$C_a = 3.7\sqrt{\frac{T}{M}}A\,\mathrm{L/s}, \tag{4.6}$$

where T is the gas temperature in units of Kelvin, M is the mass of the gas molecule in units of Dalton and A is the area of the aperture in cm^2 (conventionally centimeter is the unit used more commonly in the calculation of the conductance). For an aperture with radius 3.51 mm, the calculated conductance $C_a = 12.4\,\mathrm{L/s}$ is larger than the required $5\,\mathrm{L/s}$.

An alternative approach to achieving a small conductance is using a long tube. From Eq. (3.20) of [MDCG09], the conductance of a tube with diameter D and length L in cm in the molecular flow region is

$$C_t = 2.6 \times 10^{-4}\bar{v}\frac{D^3}{L}\mathrm{L/s}, \tag{4.7}$$

where $\bar{v}$ is the average molecular velocity of the gas in cm/s.

The idea of using an RFQ ion guide with partially filled cross-sectional area between the electrodes as a long differential pumping channel originates from the BECOLA (BEam COoler and LAser spectroscopy) ion cooler[Bar14]. The channel is formed along the center of the ion guide after filling the outer space between the quadrupole electrodes with an insulating material like MACOR (Machinable Glass Ceramic) or PEEK (Polyether ether ketone). The design of the original differential pumping channel has been modified for this study to simplify the mechanical design as shown in

Figure 4.7. The concept of simplification stems from the author's experience with designing a flute as a musical instrument made of two halves allowing the inner geometry of the flute to be custom machined [LW16].

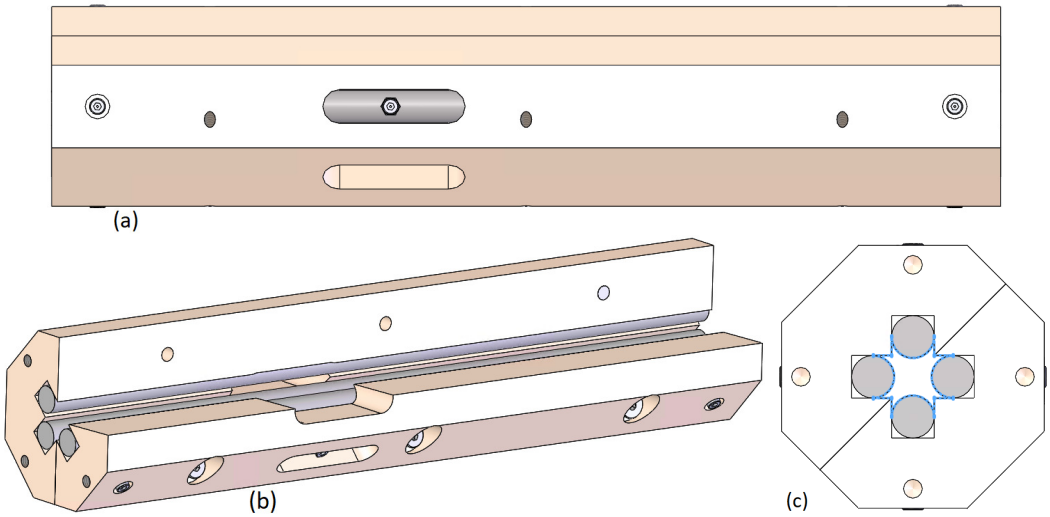

Figure 4.7: Rendered drawings of the design of the pre-cooler. (a) side view. (b) cut view showing the quadrupole electrodes of the pre-cooler. (c) front view of the precooler showing the holder as two halves assembled together; the cross-section of the differential pumping channel is highlighted as blue sketches.

In this design, the electrode holder of the pre-cooler is made of two halves. The channel for differential pumping is formed between the four quadrupole electrodes and the straight inner walls of the electrode holders. The helium gas from the cooler is mainly pumped out through 6 venting holes on the side of the pre-cooler because the venting holes are much larger compared to the cross-section of the channel. The cross-section of the channel is highlighted in Figure 4.7 (c). According to its geometry, the cross-sectional area of the channel is calculated as

$$A_C = (2r_e + 2r_0))^2 - 2\pi r_e^2 - (2r_e^2) = 5.02r_0^2 \tag{4.8}$$

for the fixed ratio of $r_e = 1.13r_0$. In this case, the cross-sectional area of the differential pumping channel is equivalent to a tube of diameter $D_C = 2.53r_0$.

The pre-cooler was designed to have r_e = 3/16" (4.76 mm) and r_0 = 4.21 mm using commercially available stainless steel rods. The larger stainless steel rod is used for the quadrupole electrodes of the pre-cooler than the QMF for the following reasons:

1. When the RF voltage is shared with the QMF, a larger trap size of r_0=4.21 mm leads to a smaller stability parameter q =0.55 and enables the RFQ to work at a more preferable region for ion cooling and lower ion temperature as discussed in Section 3.5.3.

2. The ion acceptance is larger because of the larger r_0 and the value of q as discussed in Section 2.3 and Section 4.1.1.

3. A larger differential pumping channel can be formed to allow ions from the RFQ with larger initial positional spread to be accepted into the pre-cooler and the cooler.

The area of the differential pumping channel of the designed pre-cooler is equivalent to a tube with a diameter $D_C = 10.7$ mm. The conductance of the channel for the side connecting to the QMF with length $L_Q = 80$ mm is

$$C_Q = 3.1\text{L/s}. \tag{4.9}$$

The conductance of the channel for the side connecting to the cooler with length $L_C = 158$ mm is

$$C_C = 1.6\text{L/s}. \tag{4.10}$$

The other details and dimensions of the pre-cooler are shown as mechanical drawings in Appendix B (drawing number LPT2CP).

4.4.2 Ion cooler

The ion cooler is filled with around 0.1 mbar of helium buffer gas to capture and cool the ions as studied in theory in Section 2.5.2 and simulation Section 3.5. The ion cooler needs to have a drag field (electric potential gradient) to guide the ions and accumulate them in the expected longitudinal position with the lowest DC potential as illustrated in Figure 2.15.

The pre-cooler is designed to operate without such a drag field because the ions will have sufficient kinetic energy to be only slowed down to still in the ion cooler region.

DC drag field

The original approach of creating the drag field was to use segmented quadrupole electrodes with different DC voltages. Such a segmented RFQ design has been used as ion coolers of ISOLTRAP [HDK+01], JYFLTRAP (EXOTRAPS) [NHJ+01] and TITAN [BSB+12]. This approach requires tens of segments of the RFQ to create a smooth enough drag field.

To reduce the complexity of electrical configurations, alternative approaches to forming the drag field have been devised and used such as in the second generation of the ion cooler for ISOLTRAP [AFG+04], and the ion cooler in LEBIT [SBR+16]. A new way of creating a drag field using only the variation of the quadrupole electrode geometry is proposed in this study.

Flat quadrupole electrodes

Quadrupole electrodes with a flat inner surface and different widths were studied via electrostatic simulation and the results are shown in Figure 4.8. The electrodes were placed inside a square- shaped metal tube with a biased voltage $V_{tube} = 1$ V while the electrodes were held at 0 V. The electrostatic potential penetration at the central axis of the quadrupole electrodes was found to be dependent on the width of the electrodes.

In this way, a set of flat quadrupole electrodes with gradual width change can create a DC drag field. For the electrodes with $r_0 = 4.21$ mm and widths of 2 mm and 4 mm from one end to the other, every 100 V of biasing voltage on the metal tube creates a DC potential difference of 3.6 V.

The electric potential from the RF voltage for ion confinement in the transverse direction at the center of the flat quadrupole electrodes was simulated and fitted as described in Section 3.1. The coefficient of the quadrupole potential A_2 and the higher-order spatial harmonics are shown in Figure 4.9.

The higher-order spatial harmonic terms A_6 and above are larger than the case of an RFQ with hyperbolic or round electrodes. As a result, the cooler will have reduced acceptance as discussed in Section 3.2.2. However, it can be assumed that the ions have already been cooled to some extent after traveling through the pre-cooler. The reduced acceptance of the cooler can be considered to be enough to trap all the incoming ions using the

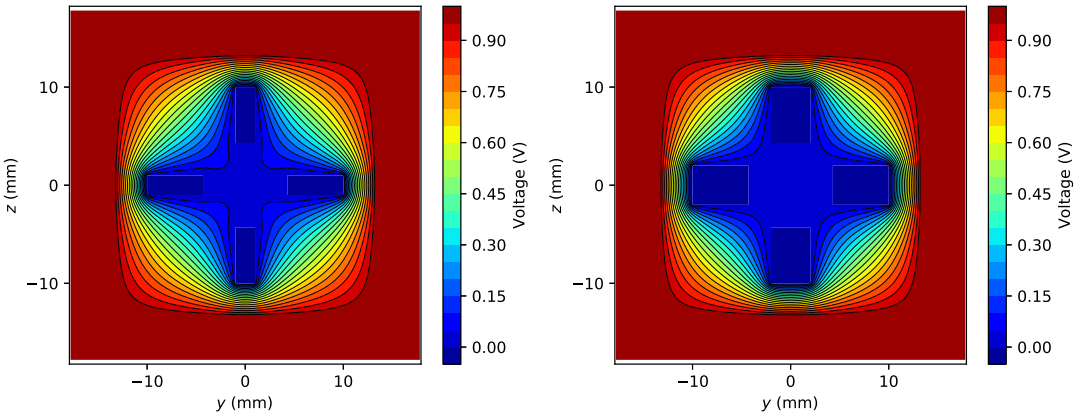

(a) Electrode width $w = 2\,\mathrm{mm}$

(b) Electrode width $w = 4\,\mathrm{mm}$

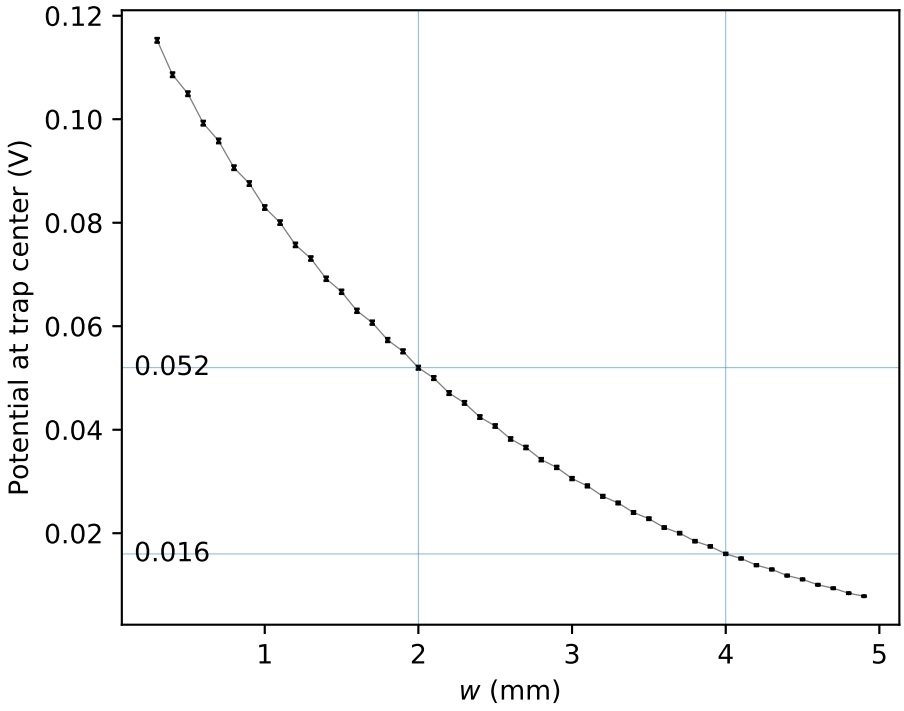

(c) Electric potential along the central axis

Figure 4.8: Electric field penetration for quadrupole electrodes of different width. (a) and (b) show the simulated electric potential distribution for the electrode width 2 mm and 4 mm. (c) shows the potential at the center of the quadrupole electrodes as a function of the electrode width w.

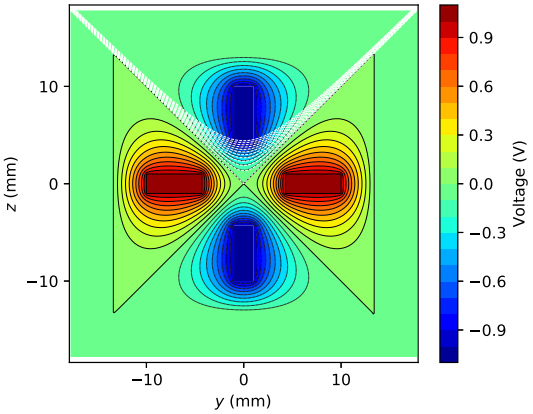

(a) Electrode width $w = 2\,\mathrm{mm}$

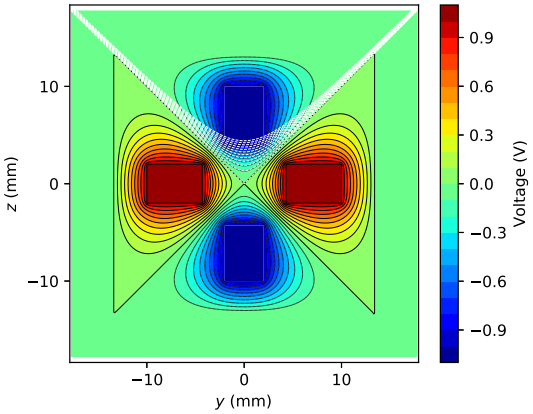

(b) Electrode width $w = 4\,\mathrm{mm}$

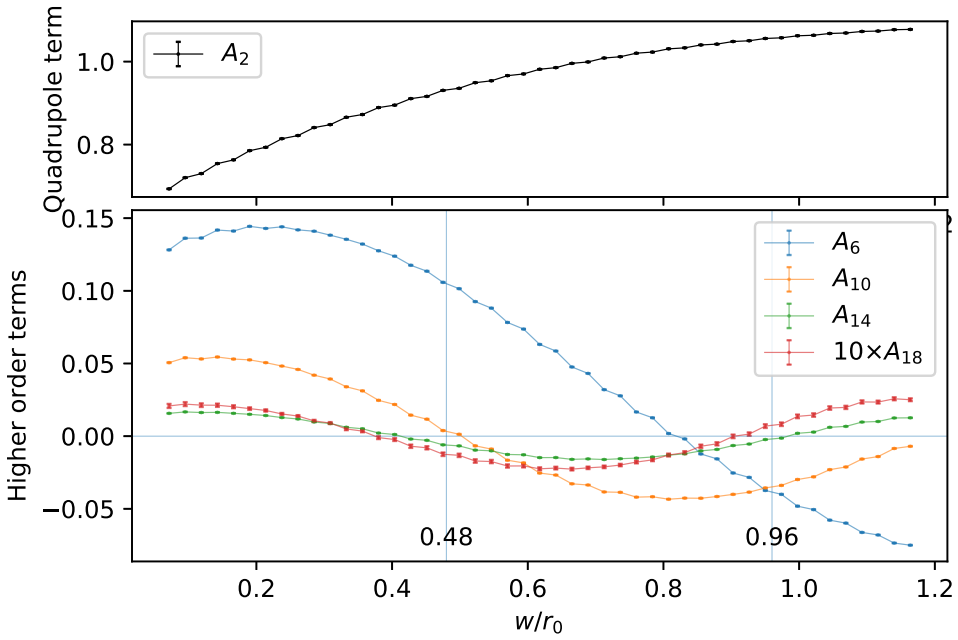

(c) Electric potential along the central axis

Figure 4.9: Multipole expansion of potential inside the cooler. (a) and (b) show the simulated electric potential distribution for the electrode width 2 mm and 4 mm. (c) shows the coefficient of the spatial harmonics as a function of the electrode width w.

optimum settings for the helium buffer gas pressure.

The cooler is designed with flat electrodes as described above. The width of the flat electrodes tapers from 4 mm where the ions enter to 2 mm where the ions exit. The mechanical design of the cooler is shown in Figure 4.10. An aperture plate is located at the exit of the cooler. The 2 mm diameter hole is both relevant for the ions to exit the cooler and for the differential pumping of the helium buffer gas to be achieved.

Additional mechanical details and dimensions of the cooler are shown as mechanical drawings in Appendix B (drawing number LPT2CC).

4.5 Laser spectroscopy ion trap (LSIT) design

The laser spectroscopy identification of the trapped barium ion requires a blue (493 nm) and a red (650 nm) laser to shine precisely on the trapped ions. The fluorescent light emitted by the ions is collected by a CCD (charge coupled device) or PMT (photomultiplier tube) detector through the gap between the quadrupole electrodes. The previous generation of ion trap developed for the barium tagging of EXO [Gre10] suffered background noise from the laser light scattered by the quadrupole electrodes. The amount of fluorescent light that can be collected by the detector is limited by the opening angle $\theta_{fluo} = 25.5°$ between the quadrupole electrode as illustrated in Figure 4.11.

In this study, the quadrupole electrodes for the laser spectroscopy ion trap were designed using a blade-shape following the ion trap at Innsbruck used for quantum computing [SKHG$^+$03]. The blade-shaped electrodes have a much larger angle between the electrode $\theta_{fluo} = 75°$ for the fluorescent light detection; the smaller surface area of the electrode around the laser beam also reduces the scattering of the laser light. The electrode holder will be manufactured from black insulating material to reduce the reflection of scattered laser light. The mechanical design of the laser spectroscopy ion trap is shown in Figure 4.12.

4.6 Ion buncher design

During the study of the laser spectroscopy ion trap (LSIT), it was found that the same trapping region may be employed to work as an ion buncher.

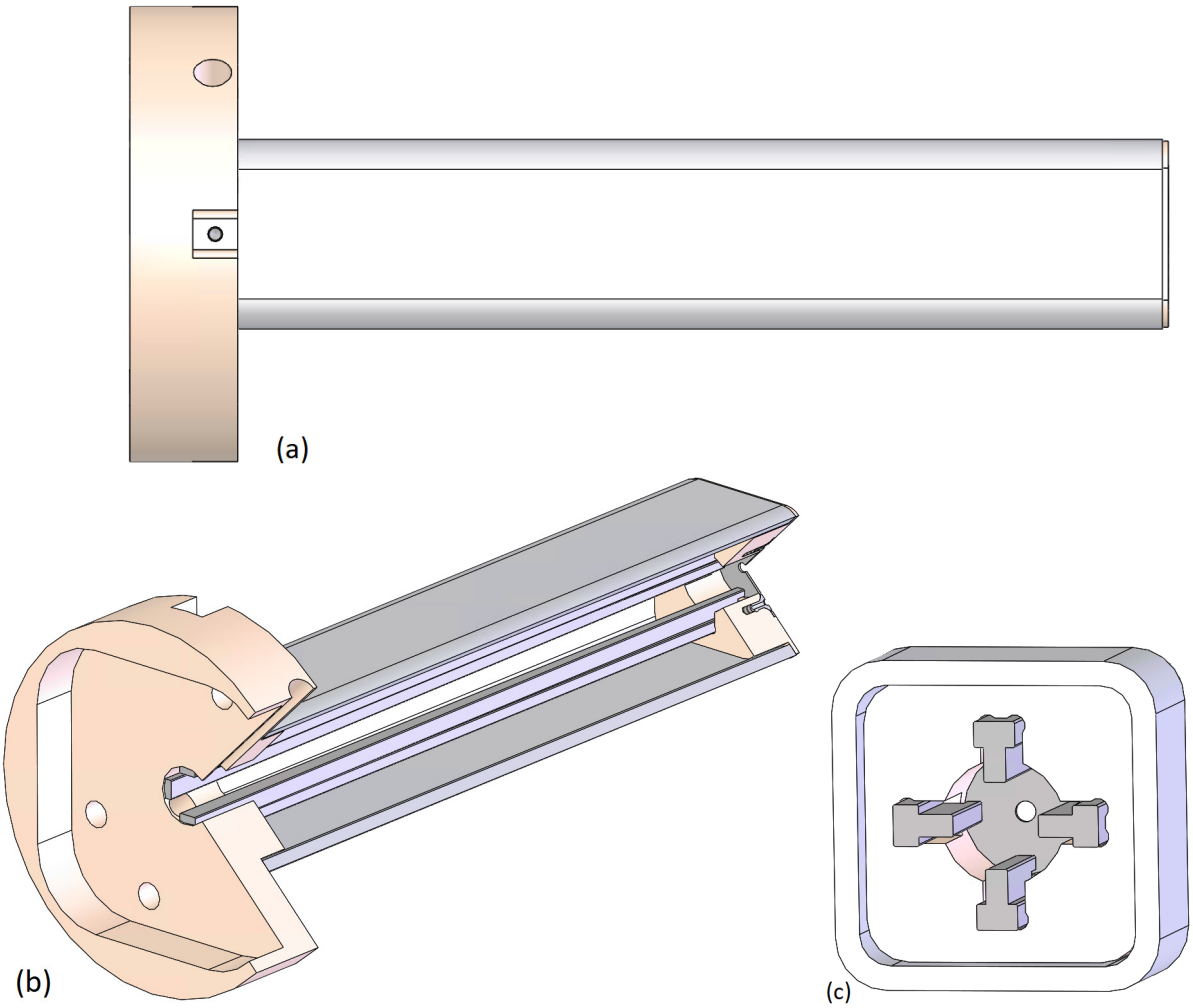

Figure 4.10: Rendered drawings of the mechanical design of the cooler. (a) side view. (b) cut view showing the tapered flat quadrupole electrodes. (c) cross-sectional view of the cooler near the ion exit.

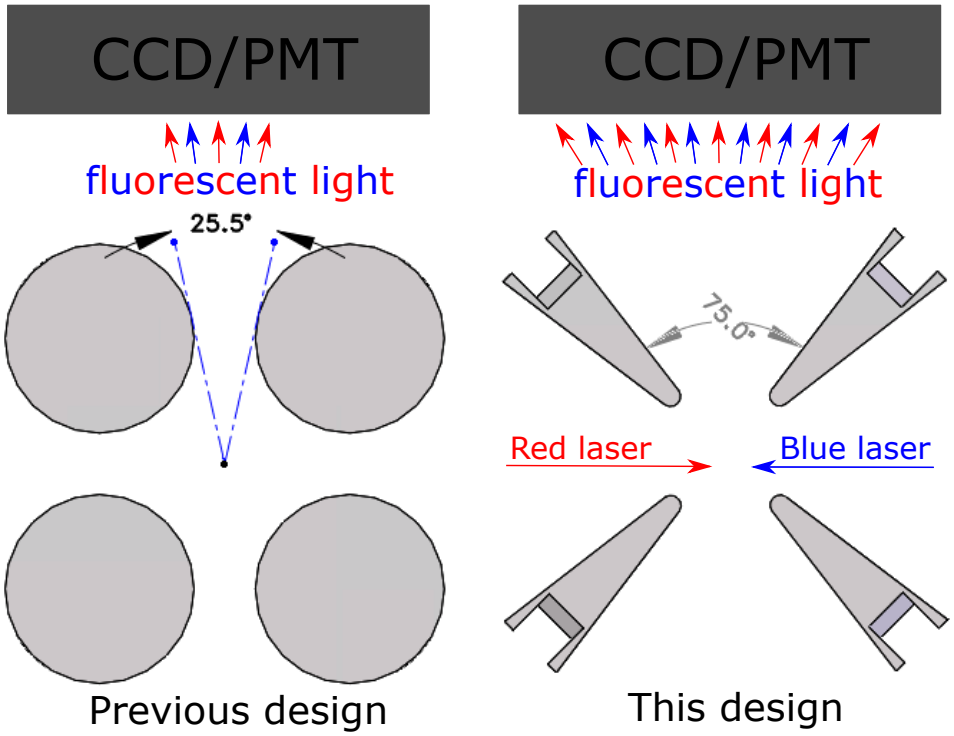

Figure 4.11: Comparison between the previous design (left) of the ion trap for barium tagging and the new design (right) in this study.

At the current design, the only difference between the LSIT and the ion buncher described in Section 3.6 is the shape of the quadrupole electrodes.

Simulations were done to the LSIT with the voltage configuration for ion ejection. The axial potential along the center of the LSIT was found to be the same as for the ion buncher as shown in Figure 3.33(b). Therefore, we decided to also use the LSIT as an ion buncher.

A pulse drift tube (PDT) is added to the exit position of the ion buncher (LSIT) as shown in Figure 4.13. The voltage of the PDT can be quickly switched during the time the ion bunch flies inside the tube, thus allowing the ions to be ejected at different ion energies.

Additional mechanical details and dimensions of the laser spectroscopy ion trap and the ion buncher are shown as mechanical drawings in Ap-

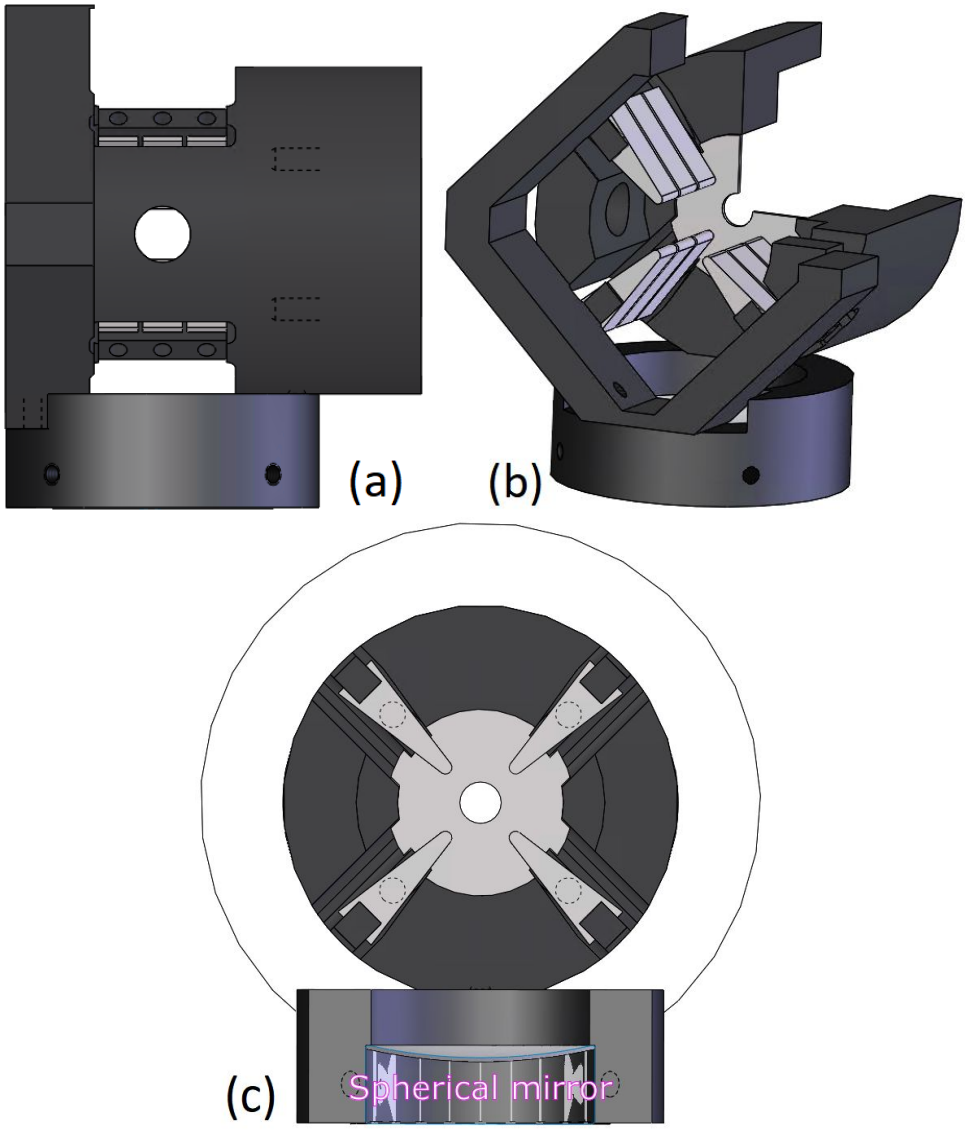

Figure 4.12: Rendered drawings of the mechanical design of the laser spectroscopy ion trap. (a) Side view facing the through hole for the entrance of lasers to the trap center. (b) Cut view showing the blade-shaped quadrupole electrodes and an aperture plate where the ions exit. (c) cross-sectional view from the ion entrance direction; the bottom shows a spherical mirror for reflecting the fluorescent light to the light detector above the ion trap. The electrode holder will be manufactured from black insulating material to reduce the scattering of laser light.

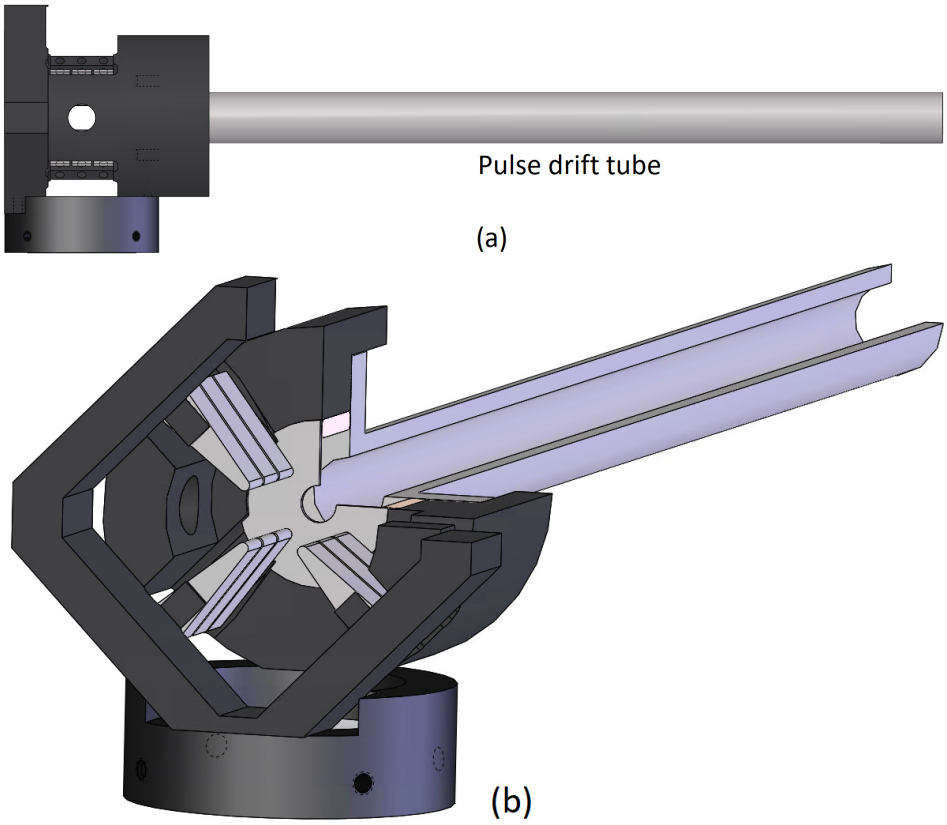

Figure 4.13: Rendered drawings of the laser spectroscopy ion trap as an ion buncher with a pulse drift tube (indicated).

pendix B (drawing number LPT2CL).

4.7 Vacuum system of the LPT

The vacuum system of the LPT is designed to consists of two vacuum chambers with differential pumping through the pre-cooler. The QMF chamber houses the quadrupole mass filter; while the CLB chamber houses the cooler and laser spectroscopy ion trap which also works as an ion buncher. Each of the chambers is pumped by two 500 L/s turbo molecular pumps (TMP).

The mechanical design of each component of the LPT had been done with considerations for the vacuum system as well. The gas pressure and

flow through the LPT were calculated and the results are shown in Figure 4.14.

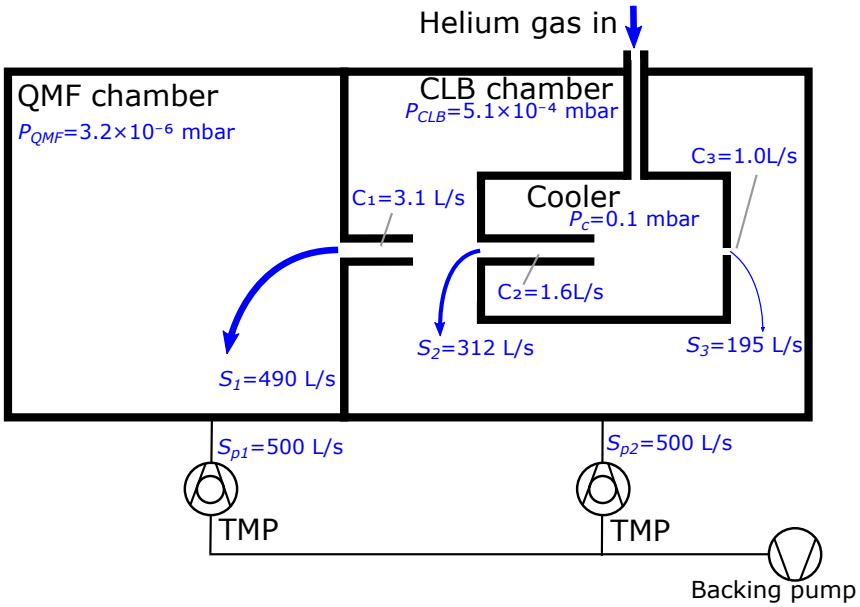

Figure 4.14: Schematics of the vacuum system of the LPT. The gas pressure P and flow S are calculated as described in the text.

The calculation of the gas pressure starts from the required pressure $P_C = 0.1\,\text{mbar}$ inside the cooler. The conductance of the differential pumping channel is $C_1 = 3.1\,\text{L/s}$ and $C_2 = 1.6\,\text{L/s}$ as calculated in Eq. (4.9) and Eq. (4.10). The conductance of the 2 mm diameter aperture lens at the exit of the cooler is $C_3 = 1.0\,\text{L/s}$ calculated using Eq. (4.6).

The total gas flow from the cooler to the CLB chamber is

$$Q_C = (P_C - P_{CLB})C_2 + (P_C - P_{CLB})C_3. \tag{4.11}$$

The total gas flow exiting the CLB is the same

$$Q_C = P_{QMF}\,S_{P1} + P_{CLB}\,S_{P2}, \tag{4.12}$$

where $S_{P1} = S_{P2} = 500\,\text{L/s}$ is the pump speed of the two TMPs. The pressure between the QMF chamber and the CLB chamber is determined through the differential pumping of the pre-cooler:

$$P_{QMF}S_{P1} = (P_{CLB} - P_{QMF})C_1. \tag{4.13}$$

By solving the equations from Eq. (4.11) to Eq. (4.13), the pressures are obtained as $P_{CLB} = 5.1 \times 10^{-4}$ mbar and $P_{QMF} = 3.2 \times 10^{-6}$ mbar. These pressures meets the vacuum requirement of the LPT in Section 4.1.2.

Note that the xenon gas coming from the RF funnel upstream of the LPT is ignored in the above calculations because the estimated xenon partial pressure in the QMF chamber is smaller than 1×10^{-6} mbar when the RF funnel is coupled to the LPT with a sextupole ion guide [BFV+15].

4.8 Manufacturing of the LPT

The mechanical design of the LPT system and its components passed a design review at TRIUMF to make sure the requirements in Section 4.1 were satisfied. The mechanical drawings of the LPT as shown in Appendix B were sent for manufacturing at the Physics department machine shop of the Université de Montréal. The commercially available vacuum chambers, flanges and feedthrough were ordered.

Chapter 5

Experiments and results

The machining of the parts for the LPT took a few months. In the meantime, prototypes of the QMF and the RFQ cooler were built to validate the feasibility of their mechanical design and to facilitate the experimental development of the LPT's electronics, control and DAQ (data acquisition) systems. Some measurements and studies were carried out along with these experimental developments. The remaining components of the LPT, including the laser spectroscopy ion trap (which also functions as a buncher) and the pulse drift tube were not experimented in the duration of this study. The final LPT will be set up later based on the prototypes and the experimental developments.

5.1 Test stand setup

A test stand shown in Figure 5.1 was set up in the ISAC-1 experiment area of TRIUMF, Canada's particle accelerator center.

The main vacuum chamber is a ConFlat (CF) 6-way cross with 8 inch flanges. A Varian TV 551 turbomolecular pump (TMP) was installed on the bottom of the 6-way cross. The TMP is backed by a scroll pump. The vacuum level inside the chamber is measured by a MKS Convectron Pirani gauge and an Agilent IMG-100 inverted magnetron gauge. When nothing was put into the vacuum chamber, the pressure reached a stable value of 2.4×10^{-7} mbar after pumping for a few hours. The pressure level is limited by the Viton O-rings used for sealing CF flanges. In the final setup of the LPT system, copper gaskets will be used and a better vacuum level is expected.

The other apparatus was later added for the development of the LPT system. The key components are annotated in Figure 5.1. The background belonging to other experiments is set to black and white in the photo.

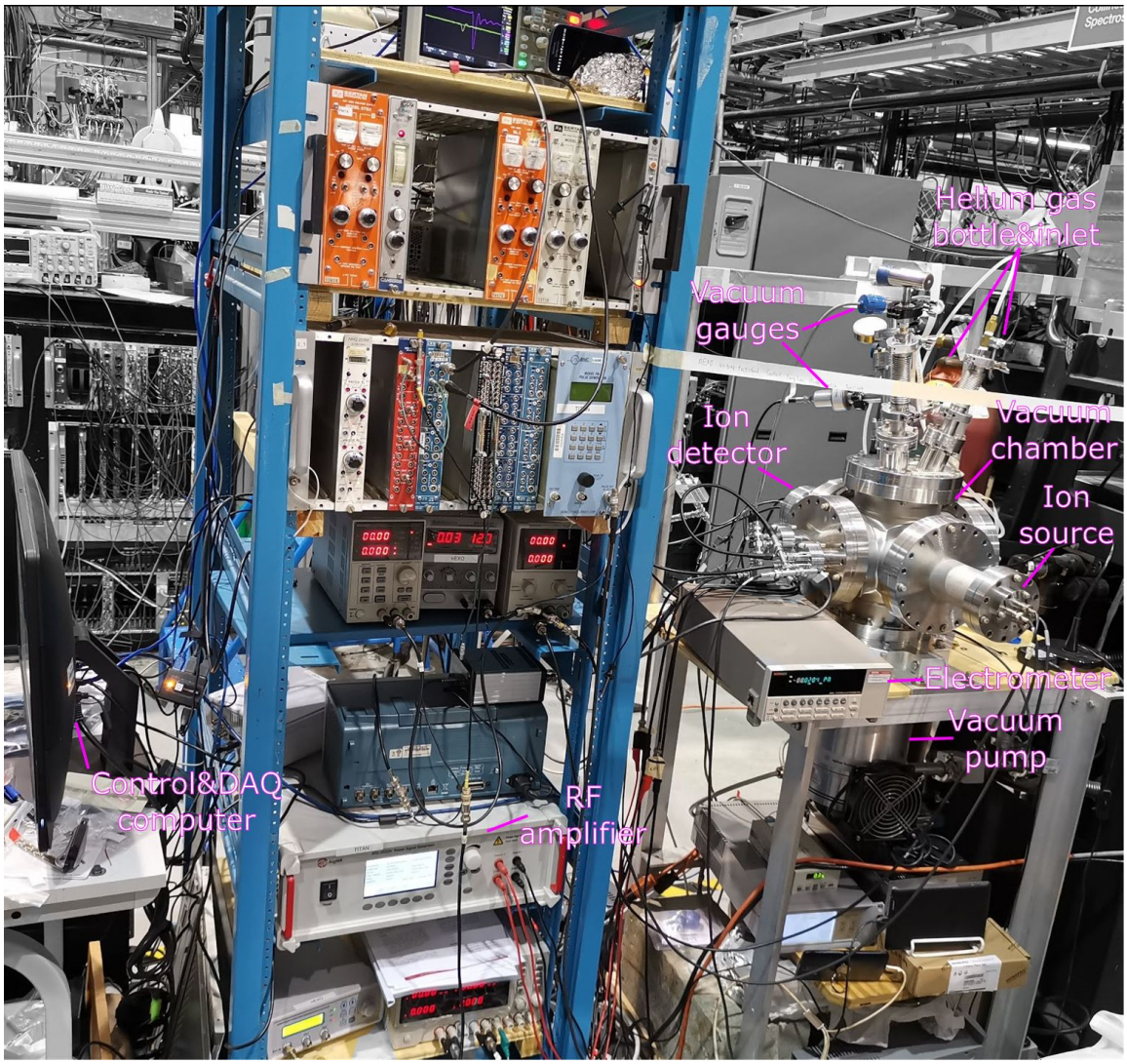

Figure 5.1: The test stand for the experimental development of the LPT system.

5.1.1 Ion source

A test ion source (TIS) assembly on loan from the TITAN group as shown in Figure 5.2(a) was used throughout this work. The TIS was designed to use the HeatWave Model 101139 aluminosilicate ion source as shown in Figure 5.2(b) and 5.2(c). The aluminosilicate as the ion emitting material is fused into a porous tungsten disk (some aluminosilicate is left on the surface of the disk as shown in Figure 5.2(b) and (c)). The tungsten disk as the ion emitter is isolated from the metallic ion source body by a heater cavity, which is filled with non-conductive alumina. A molybdenum wire coil passes through the alumina and heats up the ion source when an electrical current is applied. When the ion source is heated to 950 °C or higher, ions are produced through thermionic emission.

(a) TIS assembly (b) Ion source #1 (c) IS#2 (SN358)

Figure 5.2: (a) Photo of the test ion source (TIS) assembly installed on a 4.62 inch ConFlat (CF) flange. (b) and (c) are two HeatWave Model 101139 ion sources, compatible to be installed in the TIS assembly. The outer diameter of the ion sources is 1/4 inch (6.35 mm).

The ions are emitted from the surface of the ion emitter more effectively when there is a positive electric field gradient. The TIS can have the body of the ion source floated to a positive voltage, and an aperture plate is in front of the ion emitting surface as an anode. The anode can be biased to a

negative voltage. Both voltages can be used to control the number of ions coming out of the 4 mm diameter aperture.

Initially, an alkali ion source (#1, shown in Figure 5.2(b)) which comes with the TIS with unknown properties was used. Later on, an almost purely Cs^+ ion source (#2, shown in Figure 5.2(c)) was used.

5.1.2 Ion detector

Two types of ion detectors were used throughout this work as below.

Faraday cup (FC)

A Faraday cup (FC) is a metal container used to directly measure the current of ions or any other charged particles by depositing them in the inner wall of the container.

An FC has been designed and machined by the author for this work as shown in Figure 5.3. The FC is made from aluminum for ease of machining. The inner diameter of the cup is 1 inch (25.4 mm), except the opening for ion entrance is tapered to 3/4 inch. The inward tapering is designed to mitigate the leakage of secondary electrons generated when the ions hit the cup's inner surface. An electron suppressor lid is added at the ion entrance with the same 3/4 inch opening.

The bottom of the FC is made to be interchangeable so that adapters with various apertures can be installed to allow a small percentage of ions to pass through and be detected by a second ion detector as described below. The purpose of these adapters is for ion detector calibration, and for absolute ion transmission efficiency measurement by placing the FC with the aperture in front of a QMS or an RFQ ion cooler.

The FC is connected to an electrometer (Keithley 6514) via a BNC cable. Since the BNC cable doesn't have electromagnetic shielding as good as a tri-axial cable, the electrometer is placed close to the vacuum chamber to allow a 6 inch (152 mm) short cable to be used. Compared to a 2 meter BNC cable used previously, the short cable led to a reduced noise level by a factor of 10 measured by the electrometer. Ion current from the FC can be measured to the 10^{-14} A level.

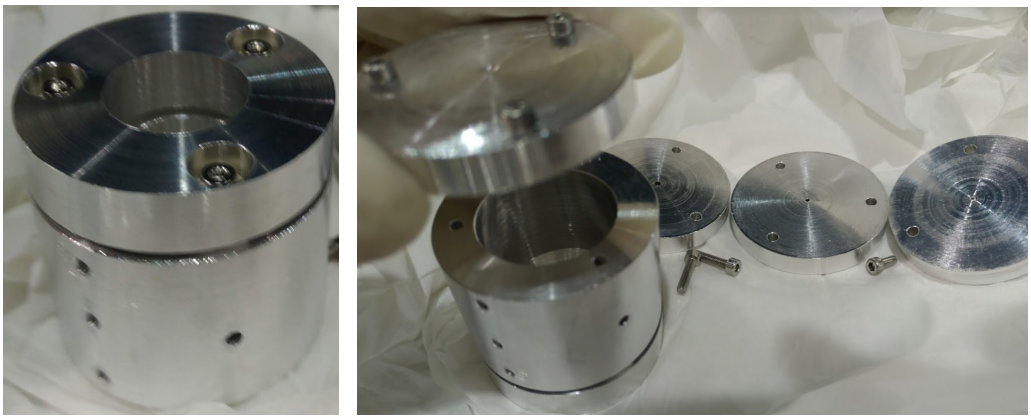

(a) FC with ion entrance on top (b) FC with different adapters for the bottom

Figure 5.3: Photo of a custom made Faraday cup (FC) used in the experiment. In (b), the three aperture adapters have diameters from left to right: 1.6 mm, 1.1 mm and 0.6 mm.

Channel electron multiplier (CEM)

A channel electron multiplier (CEM) can amplify a signal by typically a factor of 10^7 with a few stages of amplification via secondary electron emission along a channel-shaped dynode with high voltage applied across. In this way, each individual ion hitting the entrance of the CEM can generate a large enough pulse shaped signal to be detected. In this work, an Adaptas (previously DeTech) Model 2403 CEM is used. Figure 5.4(a) shows the CEM installed on a 4.5 inch CF flange. The CEM without holder (available separately as Model 2125) is shown in Figure 5.4(b))).

The output signal from the CEM for single ions is typically in the millivolt range. In order for the signal to be detected by a counter (SainSmart MHS-5200A [1]) which requires input signal at TTL (transistor-transistor logic) level, the signal is further amplified by an Ortec VT120 fast timing preamplifier.

[1]This a low-cost signal generator which also comes with the counter function to measure count rate up to 60 MHz.

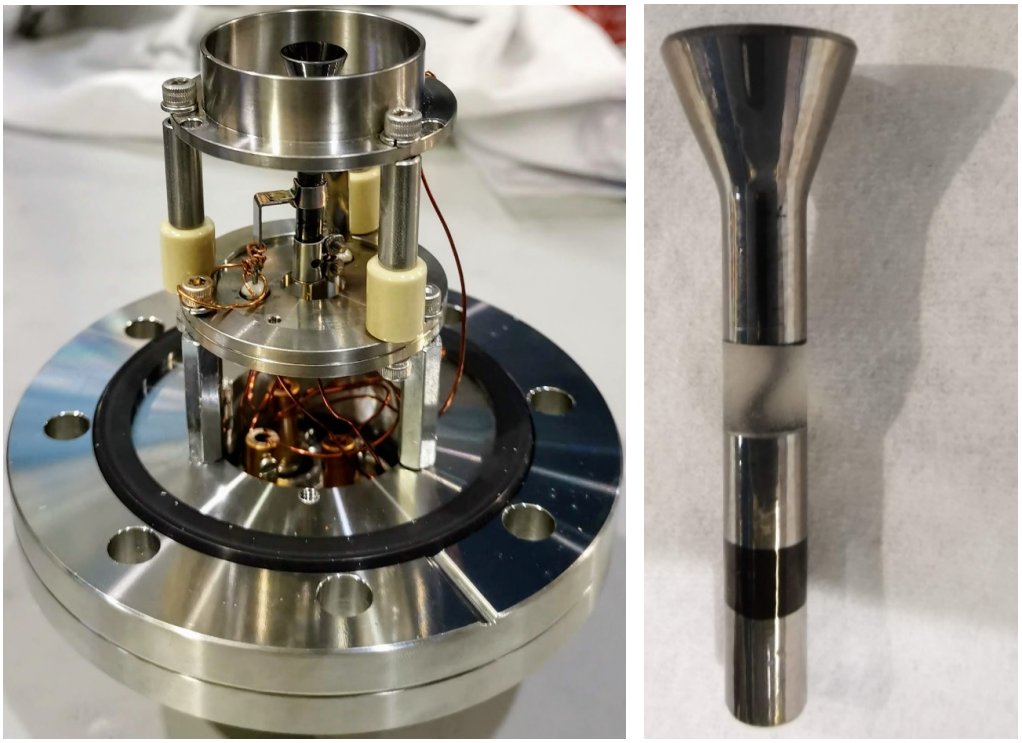

(a) (b)

Figure 5.4: (a) The CEM assembly installed on a 4.5 inch CF flange. (b) The CEM without holder; the larger side of the cone has a diameter of 10 mm.

5.1.3 Tests with ion source and detectors

A simple configuration of the test stand was set up as shown in Figure 5.5 to check the working condition of both the ion source and the ion detectors.

The ion source's 4.62" flange was installed to one of the 6-way cross's flange via an 8" to 4.62" CF reducer. The ion detectors were installed about 400 mm away on the opposite side of the 6-way cross via an 8" to 4.5" CF reducer. The Faraday cup was used with the adapter of a D_a=1.6 mm diameter aperture as shown in Figure 5.5(b). If the ions coming into the Faraday cup were uniformly distributed, then the aperture allows a ratio of

$$\eta_a = \frac{A_a}{A_{FC}} = \frac{\pi(D_a/2)^2}{\pi(D_{FC}/2)^2} = 0.7\% \tag{5.1}$$

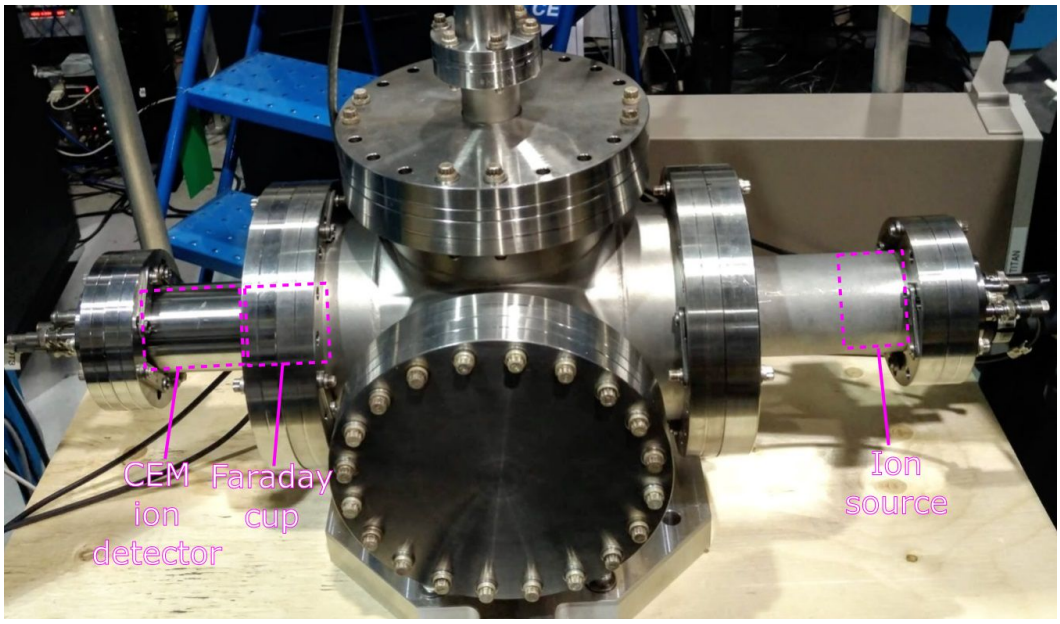

(a)

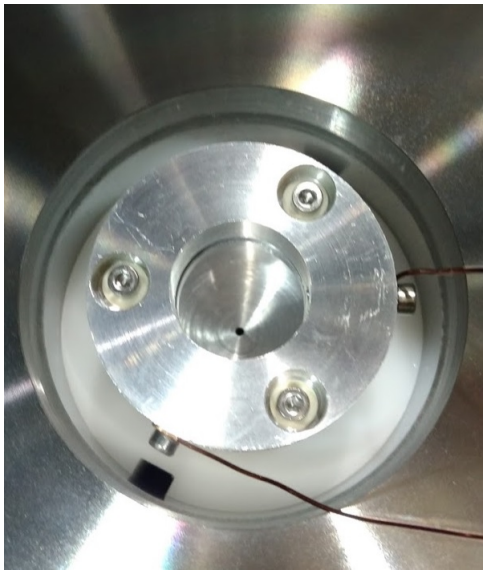

(b) Faraday cup

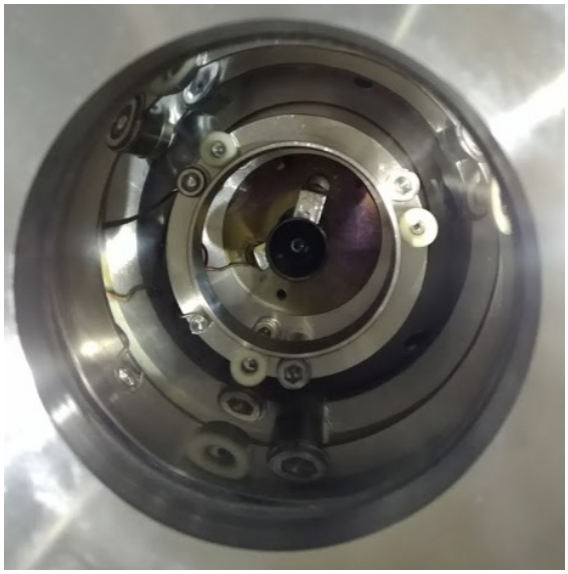

(c) CEM ion detector

Figure 5.5: A configuration of the test stand for testing ion source and detectors. (a) Configuration of the vacuum chambers. The location of the ion source and ion detectors are annotated. (b) The Faraday cup with a 1.6 mm diameter aperture on the bottom. (c) The CEM ion detector positioned behind the Faraday cup.

of ions to pass through, where $D_{FC} = 19.1$ mm is the diameter of the FC's opening.

The Faraday cup was installed inside the tube of the 8" to 4.5" CF reducer and the aperture on the bottom was positioned about 10 mm in front of the CEM ion detector as shown in Figure 5.5.

The ion source was heated to 1.35 A (4.1 W heating power) and given a few hours for it to stabilize. The ion source was floated to a voltage between 0 to 80 V, while the anode voltage was fixed to 0 V. For each ion source floating voltage, a 50 seconds measurement was done to record 100 samples of ion current in the FC. The control of the power supply voltage and the data recording are automated using Labview. The results are plotted in Figure 5.6.

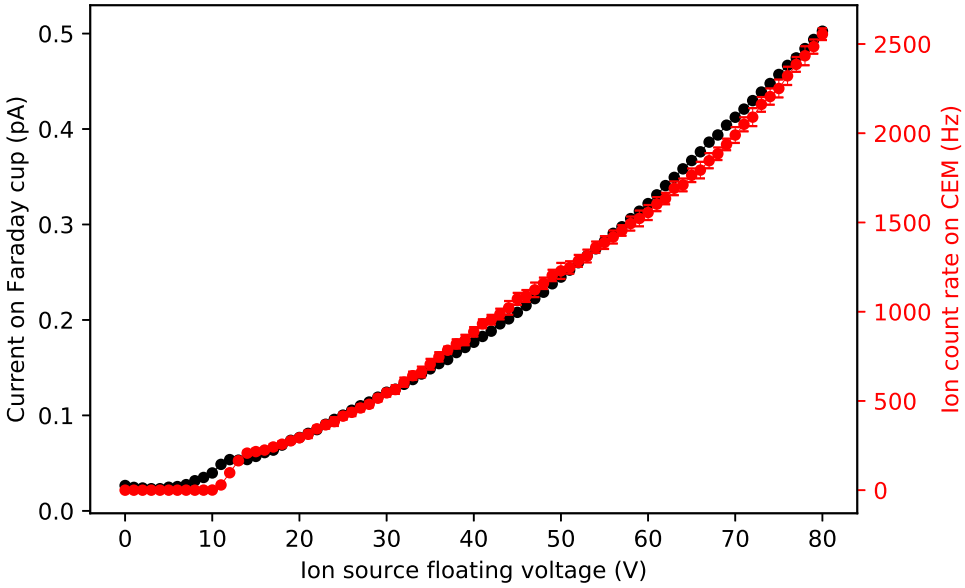

Figure 5.6: Measurement of ion detectors reading at different ion source floating voltages.

The ion current increased along with the increase of the floating voltage, as a result of a stronger electric field gradient around the ion emitting surface [PS78, KSP+10].

The CEM was operated by applying -2.3 kV [1] to the cone where incoming ions are collected. The ion count rate was recorded and also plotted in Figure 5.6. The ion count rate appears to be proportional to the ion current in FC, demonstrating that both ion detectors detect the number of ions in a stable condition. For every 1 pA of uniformly distributed ion current in the Faraday cup, the rate of ions coming out of the aperture is calculated to be

$$R_{cem} = \frac{1 \text{ pA}}{e}\eta_a = 4.37 \times 10^4 \text{Hz}. \tag{5.2}$$

The measured ion count rate on the CEM corresponds to an ion detection efficiency of around 12%.

The ion source and detector tests demonstrated their reliability to be used in experiments with the prototypes in the following sections.

5.2 Quadrupole mass filter prototypes

A few prototypes of the QMF have been built and tested for different purposes.

The first QMF prototype, QMF1, was built to test the practicality of the mechanical design described in Section 4.3 and the mechanical rigidity of the design. The details of the QMF1's manufacturing, installation and preliminary ion transmission tests are described in Appendix A.1.

The tests found that the mechanical design is viable. Low amplitude (10 V) RF voltages were used to operate the QMF1 as an ion guide. The ion transmission properties of the QMF1 were as expected even with its 0.2 mm positional precision of the quadrupole electrodes.

The second QMF prototype, QMF2.1, was designed and built with the aim of achieving better mechanical precision using the available machine shop resources. The details of the QMF2.1's design, manufacturing, installation, ion transmission tests and mass measurements as a QMS are described in Appendix A.2.

The QMF2.1's quadrupole electrodes were found to have 40 µm positional precision, limiting its maximum mass resolving power to be

$$R_{FWHM} = m/\Delta m_{FWHM} \approx 51.$$

[1] This voltage needed was relatively large, probably because the CEM has been heavily used previously and was near the end of its lifetime.

The RF, electronics and automated control and DAQ systems were developed along with the QMF prototypes.

The third QMF prototype, QMF2.2, was built using the same design as QMF2.1. The parts were more carefully machined to aim at higher mechanical precision. The details of QMF2.2 are described in Section 5.2.1.

5.2.1 QMF2.2

The mechanical errors in QMF2.1 mainly come from the mismatch between the electrodes and slightly larger holes in the holder. A new 5/16 inch end mill cutter was purchased and used on the same vertical milling machine to make the holders for QMF2.2. Due to the lack of PEEK material at the time of machining, acetal (a different type of engineering plastic) was used.

The finished holders for QMF2.2 are shown in Figure 5.7(a). The quadrupole electrodes and aperture plates from QMF2.1 were repurposed for QMF2.2.

To define a better electric potential at the aperture plate for adjusting ion energy, each of the aperture plates was overlaid with stainless steel woven mesh as shown in Figure 5.7(b). The mesh has 400 openings per inch and the open area that can allow ions through is

$$\alpha_{mesh} = 31\%. \tag{5.3}$$

The assembled QMF2.2 is shown in Figure 5.7(c).

Mechanical precision of QMF2.2

The fitting between the quadrupole electrode rods and the holes of the holders was extremely tight. Based on the machining precision of the holder's four holes, the positioning of the quadrupole electrodes was within 10 µm. This precision was double checked with measurement of the spacings between the quadrupole electrodes with a digital caliper using the same procedure as described for QMF2.1. The measured spacings were all within 20 µm compared to the expected value except one measured spacing was 0.15 mm too small, which was caused by an electrode's positioning problem as shown in Figure 5.8.

The 0.15 mm gap shown in the figure leads to an inward displacement of one end of that electrode. The electrode's displacement would adversely

(a) Holders for QMF2.2

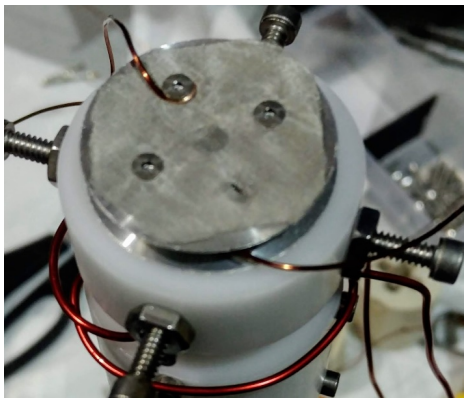

(b) Apertures with mesh

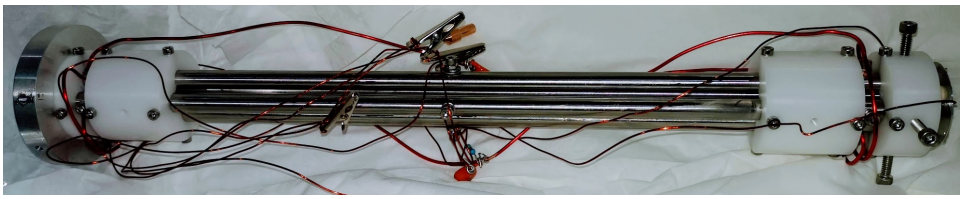

(c) Assembled QMF2.2 with wires and electrical connectors

Figure 5.7: Photos of QMF 2.2. See text for details.

affect the performance of the QMF2.2. The gap is hard to notice and was only found during troubleshooting after the measurements had been completed. The measurements revealed a possible mechanical precision problem of the QMF2.2

Installation of QMF2.2 in test stand

The QMF2.2 was installed into the vacuum chamber of the test stand as shown in Figure 5.9. The Faraday cup was added to measure the ion current in front of the QMF2.2. The bottom of the Faraday cup has a 4 mm diameter aperture to allow a small percent of ions to pass through as shown in Figure 5.9(d).

After sealing the vacuum chamber and starting pumping, the pressure reached 1×10^{-6} mbar in 12 hours. The ultimate pressure after two days of pumping was 4.2×10^{-7} mbar, which is 27% higher than the pressure of

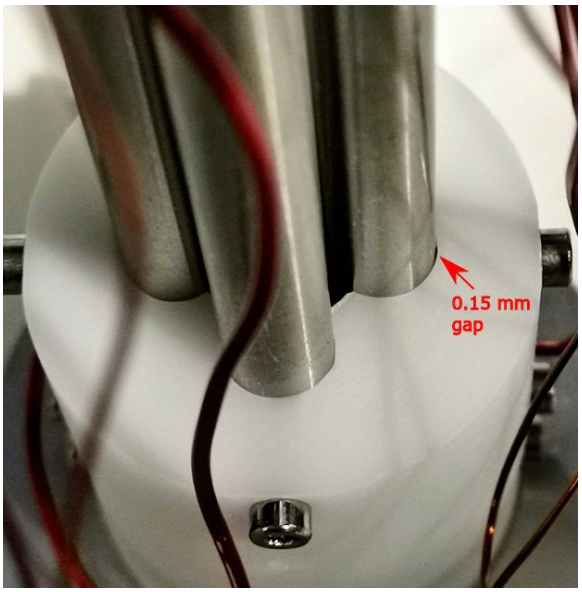

Figure 5.8: Photo of a mechanical precision problem in the QMF2.2 assembly. There was an unexpected 0.15 mm gap between the holder and one of the electrodes.

QMS2.1 and 75% higher than when there is nothing in the vacuum chamber.

The Faraday cup was installed with an adapter also made of acetal as shown in Figure 5.9(d), so there was more acetal material in the vacuum chamber for QMS2.2 than the amount of PEEK for QMS2.1. The acetal is not used as commonly as PEEK in vacuum due to its higher outgassing rate. But it was found that the outgassing rate of acetal is no more than 27% higher than PEEK in the tested setups of this study.

Test of RF amplitude stability and balance

In order for a QMF to operate at a mass resolving power $R = m/\Delta m$, the RF amplitude V needs to be stabilized and balanced to $V/\Delta V = R$ or better.

In order to systematically check the stability of the RF amplitude and the balance between the two channels, the function generator (FG) was configured to have fixed RF amplitude $V_{FG} = 3$ V at both output channels. The RF signals were amplified by the RF amplifier with a fixed gain of

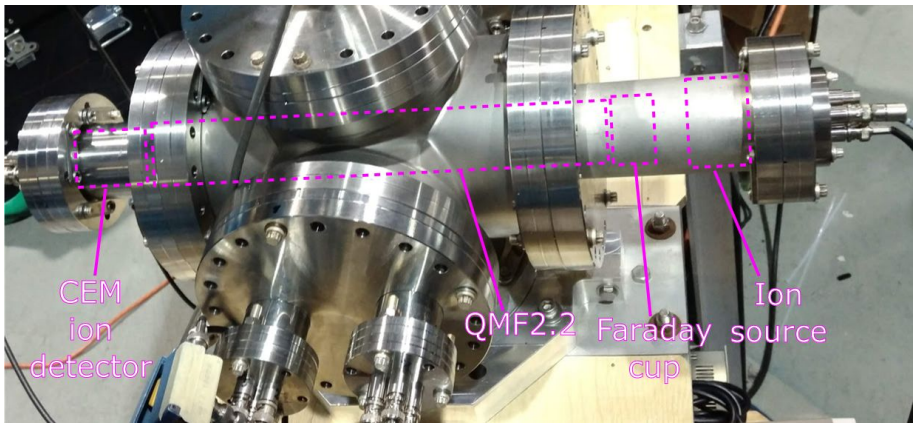

(a) Position of major components in vacuum chamber

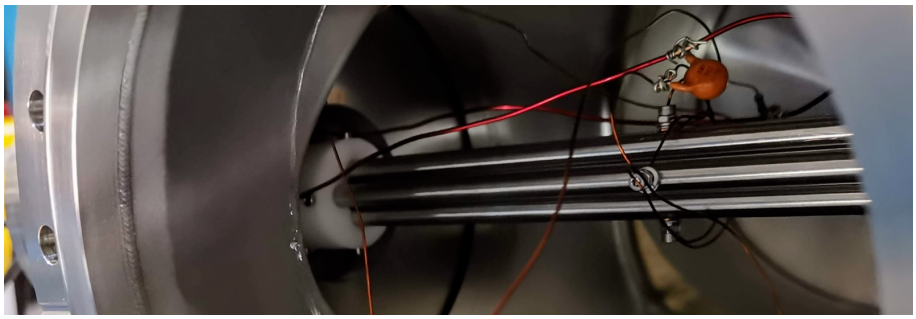

(b) Side view of quadrupole electrodes in vacuum chamber

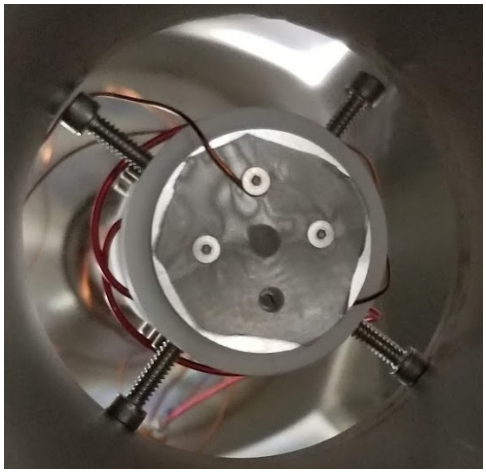

(c) View from ion entrance

(d) View of Faraday cup from ion entrance

Figure 5.9: Photos of QMF2.2 installed in the vacuum chamber of test stand.

30 times for both channels. The amplified signal was then mixed with DC voltages and sent to the quadrupole electrodes; "T" shaped connectors were used to allow for measurements of the voltages using an oscilloscope during the operation of the RFQ.

The Tektronix TDS2024C oscilloscope has an 8-bit ADC and therefore limits the measurement precision to be 0.4%. The measurement precision of the amplified RF amplitudes over the scanned frequency range was around 1% due to the range setting of the voltage measurement; this limited the mass resolving power to $R \approx 100$.

To obtain better mass resolving power with QMF2.2, a PicoScope 5442D with a 16-bit ADC was used. The PicoScope was configured to work at 14-bit with 125 MS/s sampling rate, corresponding to an amplitude measurement precision better than 0.01%.

Measurements were done from 0.1 MHz to 3 MHz. For each frequency, the amplitude of the input signal from the function generator (FG) and the amplified RF voltage was measured and recorded 10 times by the PicoScope. The frequency response of the FG and the gain of the RF amplifier are shown by the results in Figure 5.10.

The stability of the amplified RF voltage is characterized by their standard deviations σ_V, which are plotted as the error bars in the central plot of Figure 5.10. The error bars are too small to be seen because σ_V/V <0.1% for almost all data points.

The difference between the two amplified RF voltages is plotted in the right axis of the central plot in Figure 5.10. The differences at some frequencies are as large as 2%. These differences originate from the independent frequency response of the RF amplifier's dual channels, which are plotted as the gains in the bottom plot of Figure 5.10.

The gain difference between the RF amplifier's dual channels was compensated by RF amplitude balancing. This was done as the following:

1. During the operation of QMF2.2, both channels of the function generator were first set with an initial amplitude, e.g. V_{FG} =3 V.

2. After amplifying both channels and mixing them with the DC voltages, the voltage was measured with an oscilloscope.

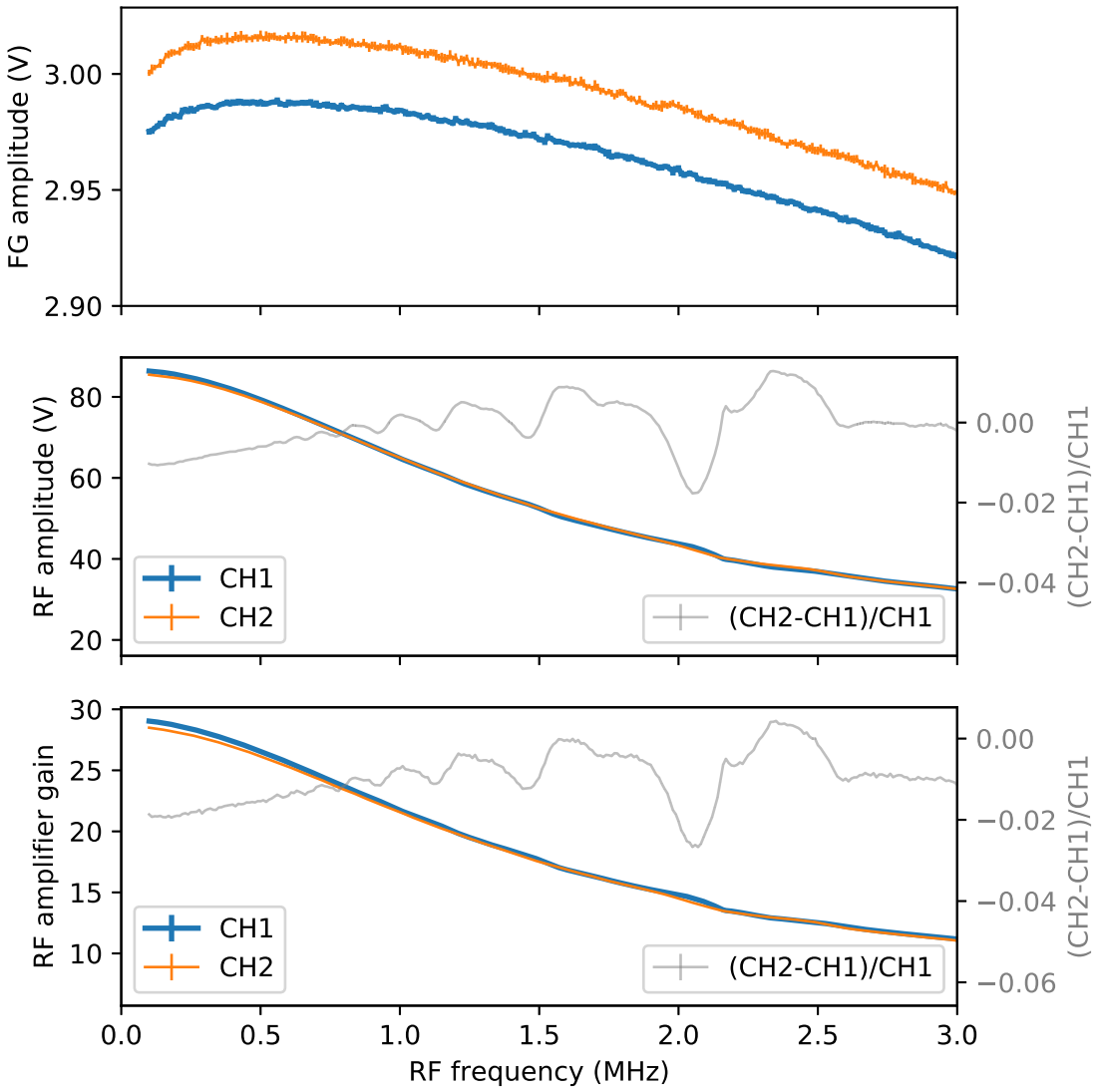

Figure 5.10: Frequency response of the function generator (FG, top plot) and the gain of the RF amplifier (bottom plot). The middle plot shows the amplitude of the amplified RF voltages. The error bars for all lines are too small to be seen.

3. At each scanned RF frequency, the secondary channel of the function generator was fixed with an RF amplitude of $V_{FG_{CH2}}$ =3 V while the amplitude of the main channel was adjusted.

The RF frequency adjustment only needs to be done to the main channel and was synchronized to the secondary channel.

An example of the balanced RF amplitude is shown in Figure 5.11. The top plot shows that channel 1 (CH1) of the function generator's amplitude was adjusted at each frequency to compensate for the gain difference of the RF amplifier's two channels. The middle plot shows the two amplified RF voltages are balanced to within 0.2%. In the middle plot of Figure 5.11, the amplitude of the function generator's CH1 can be seen adjusted at the beginning and each frequency later to compensate the RF amplifier's gain difference. The RF amplifier gain shown in the bottom plot in Figure 5.11 is mostly the same as the one in Figure 5.10, this is expected because of the hardware properties of the RF amplifier.

The gain of the RF amplifier's frequency response was found to only change if the load (capacitance between the RFQ's electrodes) has been changed. If a faster mass scan is needed, the measured RF amplifier's gain can be used as calibration data for RF balancing of each scan.

Ion transmission tests with QMF2.2

The ion source was heated to 1.45 A to produce sufficient ions for the tests with QMF2.2 as the two layers of mesh on the aperture plate at the entrance of QMF2.2 allow 9.6% of ion transmission. The ion source was floated at 10 V; an optimum anode voltage of -120 V was set to produce 18.0 pA of ion current in the Faraday cup.

Mass measurements were done at different DC voltage U corresponding to different mass resolving power. The RF amplitude and the range of frequency scans were set the same as for the measurement of QMF2.1 with the RF amplifier. The RF amplitudes of the dual channels were balanced as described above, but using an 8-bit oscilloscope. The results are shown in Figure 5.12.

The maximum ion count rate was $I_{max} = 85\,000$ Hz when the DC voltage $U = 0$. Assuming the ion current entering the Faraday cup was uniformly

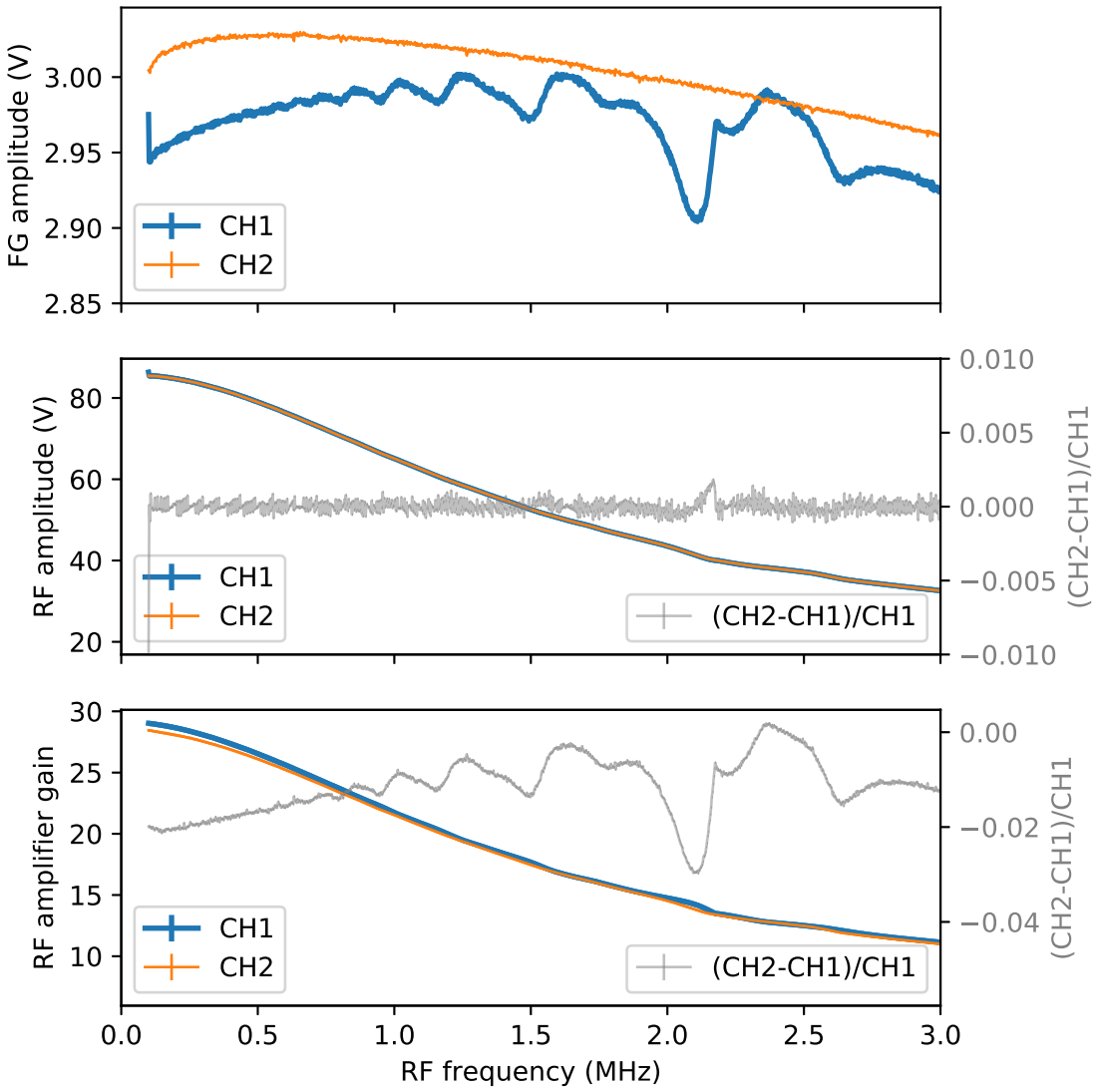

Figure 5.11: Amplitudes of function generator (top) and amplified RF voltages with RF balancing (middle). The amplitude of CH1 in the top plot has a similar shape as the gain difference (CH2-CH1)/CH1 in the bottom plot as a result of the RF balancing. See text for details.

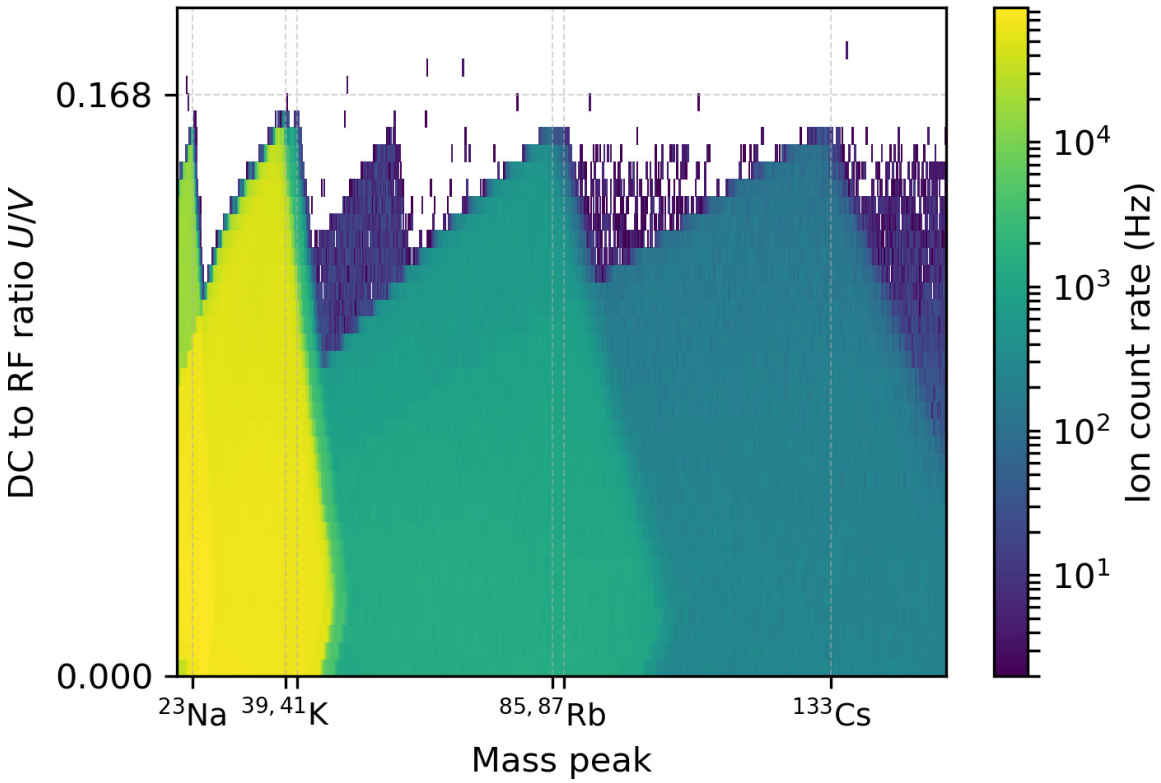

Figure 5.12: Ion mass measurements with QMF2.2 at different U/V values. The cutoffs of the ion stability patterns near the lower right corners are explained in the text.

distributed, the expected ions entering the QMF2.2 is

$$I_{expected} = \frac{18\,\text{pA}}{e}\eta_a\alpha_{mesh}^2 = 119\,000\text{ Hz}, \tag{5.4}$$

where $\eta_a = (\frac{2\text{mm}}{19.05\text{ mm}})^2$ as a result of the second aperture plate's 2 mm diameter opening.

After considering the CEM detector efficiency of $\eta_{CEM} \approx 80\%$ at this range of ion energy, the absolute ion transmission efficiency of QMF2.2 at the maximum ion count rate is preliminarily calculated as

$$\eta_I = \frac{I_{max}}{\eta_{cem}I_{expected}} \approx 89\%. \tag{5.5}$$

The stable region of ions shown in Figure 5.12 has unexpected cutoffs at the lower right corners as compared to Figure 2.13. The cause of the cutoff was found to be an incorrect electrical connection to the entrance and exit Brubaker filters. Two 1 nF capacitors were used to remove the DC voltage and supply the RF only voltages to the Brubaker filters. In this situation, ion deposition on the quadrupole electrodes can create charge buildup and create a parasitic DC potential on these Brubaker filters. This parasitic DC potential also existed with the QMF2.1 but its effect was not noticed. The effect of the parasitic DC potential was found to be more obvious when the ions were at lower kinetic energy.

The parasitic DC potential problem was fixed by adding a DC connection to the Brubaker filters via two 1 MΩ resistors. This also allows the quadrupole electrodes to be floated to any given DC potential. Later the QMF2.2 was always floated to DC potential of $U_f = 15.5$ V. Hence the DC quadrupole potential U applied to the electrodes can be either positive or negative relative to U_f without re-configuring the electrical connection to the power supply. Results of such measurements are shown in Figure 5.13.

Now the stability diagram corresponding to each ion appears symmetric along the $U = 0$ axis and there is no longer cutoff around $U = 0$. During the measurement, the ion source was floated at 16 V and the anode was set at -200 V. The QMF2.2 was floated at $U_f = 15.5$ V, hence the incoming ions have energy around 1 eV.

The smaller ion energy caused fewer ions to enter the QMF2.2. In order to get more ion counts, the Faraday cup was also biased to -200 V. The ion current couldn't be measured in such configuration, hence the absolute ion transmission efficiency was not obtained.

The data used for Figure 5.13 was also used to plot 1D mass spectra. Such a mass spectrum measured at $U/V = 0.16$ is shown in Figure 5.14. The lower two figures show the zoomed-in plots of the mass spectrum for the potassium and rubidium isotope pairs. Least square fittings with empirically chosen Gaussian distribution were done to the measured data and also shown in the plots.

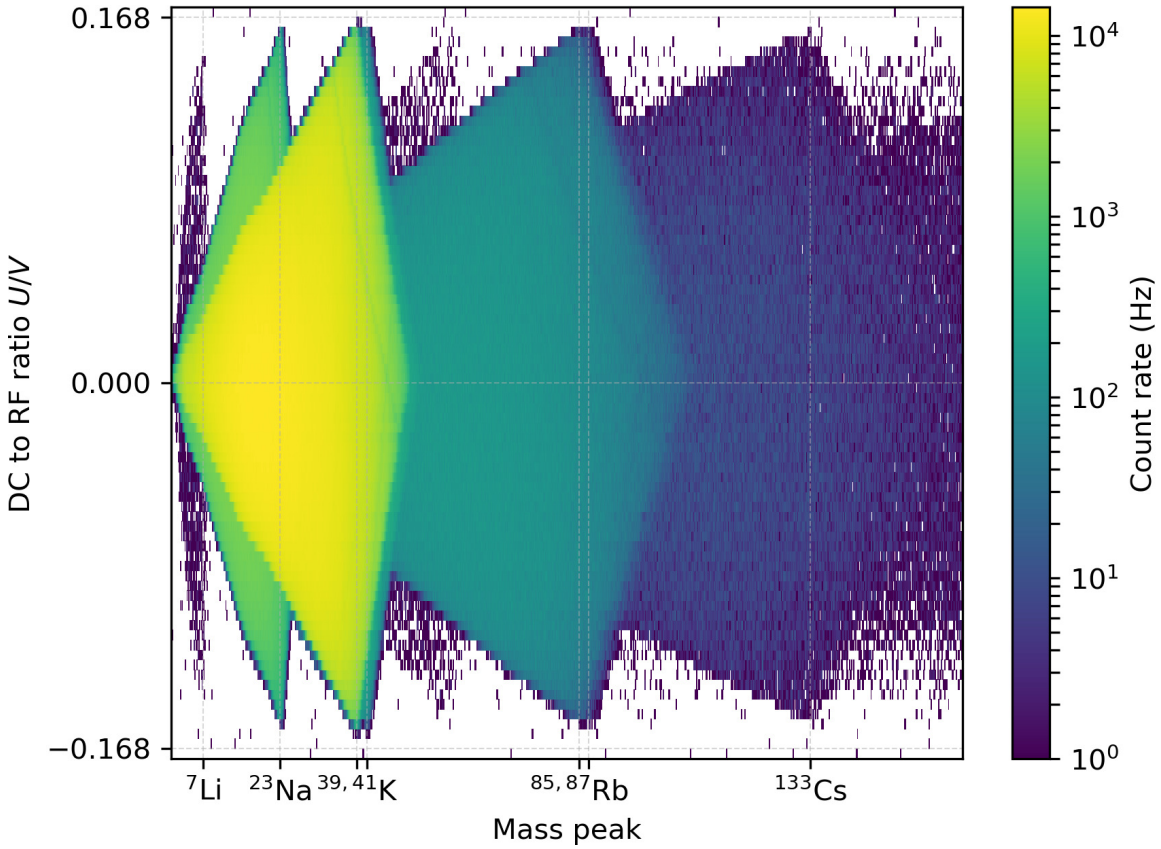

Figure 5.13: Ion mass measurements with QMF2.2 at different U/V values. The cutoff in the ion stability diagram as described in Figure 5.12 has been fixed as explained in the text.

Maximum achievable mass resolving power of QMF2.2

The maximum mass resolving power R_{max} of QMF2.2 was studied by detailed mass measurements focused on the ^{39}K and ^{41}K isotopes after considering the RF amplitude stabilization and balancing. The R_{max} is limited by the RF cycles of the ions flying through the RMF as discussed in Section 2.4.2. For a realistic QMF with a finite and fixed length, the RF cycle is determined by the ion energy.

A few sets of measurements were done with the ion source floating at different voltages; the anode voltage was set to -145 V.

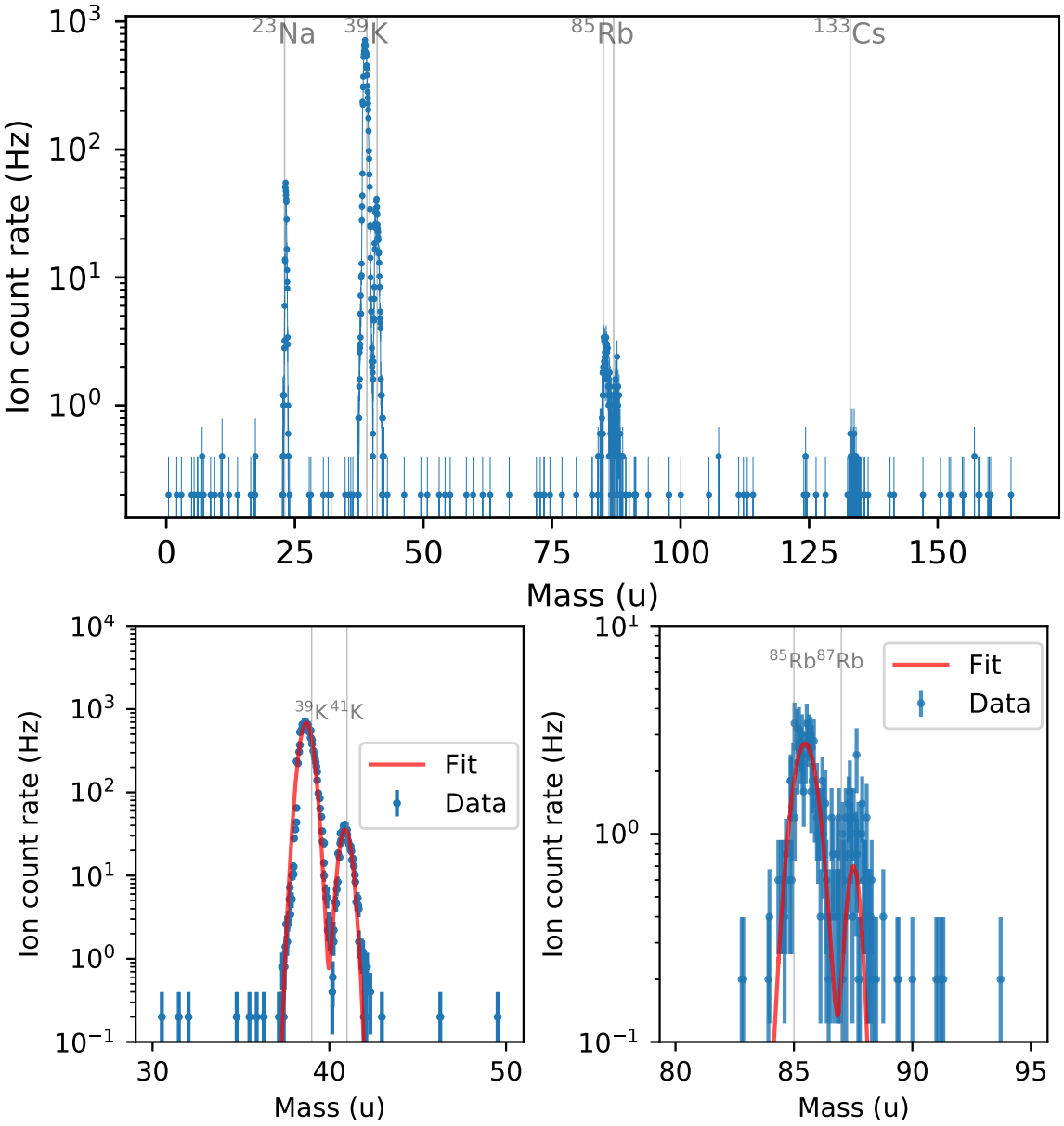

Figure 5.14: Mass spectrometry measurement of QMS V2.2 at $U/V = 0.16$. See text for details.

At first, the ion source was floating at 50 V. The ions entering the QMF have energy around 50 eV and energy spread around 1 eV. The ion velocity in the longitudinal direction is $v_x \approx 15.5\,\mathrm{mm/\mu s}$. The corresponding RF cycle is $n_{RF} \approx 17$ when the ions fly through the QMF. The measurement results are shown in Figure 5.15 along with results from the simulation.

The SIMION simulations were done for ^{39}K ions flying through an electric potential array model of the same geometry and voltages as the QMF2.2. The displacement of one of the electrodes as shown in Figure 5.8 was included modeled in the simulation. The simulation also modeled the 2 mm diameter aperture at the entrance of the QMF2.2.

For every DC to RF voltage U/V in the measured and simulated range of 0.154 to 0.170, the mass spectrum for ^{39}K was fitted as demonstrated in Figure 5.14. The Δm_{FWHM} of the mass spectrum's full-width at half-maximum from the fitting is used to calculate the mass resolving power $R = m_{^{39}K}/\Delta m_{FWHM}$. The R was obtained in this way for both measurement and simulation and shown in the middle plot of Figure 5.15.

The maximum mass resolving power of QMF2.2 for ions of 50 eV was found to be $R_{max} \approx 35$ from measurements. In this case, R_{max} was mainly limited by the number of the RF cycles. The obtained $R_{max} = 35$ corresponds to $h \approx 8$ in $R_n = \frac{n_{RF}^2}{h}$ as discussed in Section 2.4.2. The value of h here for the mass scans with frequency sweep is smaller than the literature value of $h = 20$ which was obtained for mass scans with voltage sweep. The frequency sweep mode of mass scan resulted in a larger R_{max} by a factor of 2.5.

The bottom plot of Figure 5.15 shows the peak of the fitted mass spectrum as a function of U/V for the measurements and simulations. The value of the peaks is proportional to the ion transmission efficiency of the QMF at the different DC to RF voltages U/V and the corresponding mass resolving power R.

For the second set of measurements, the ion source was floated at 5 V. The ions entering the QMF have energy around 5 eV and energy spread around 1 eV. The ion velocity in the longitudinal direction is $v_x \approx 5.0\mathrm{mm/\mu s}$. The corresponding RF cycle is $n_{RF} \approx 53$ when the ions fly through the QMF. The measurement results are shown in Figure 5.16 along with results from the simulation.

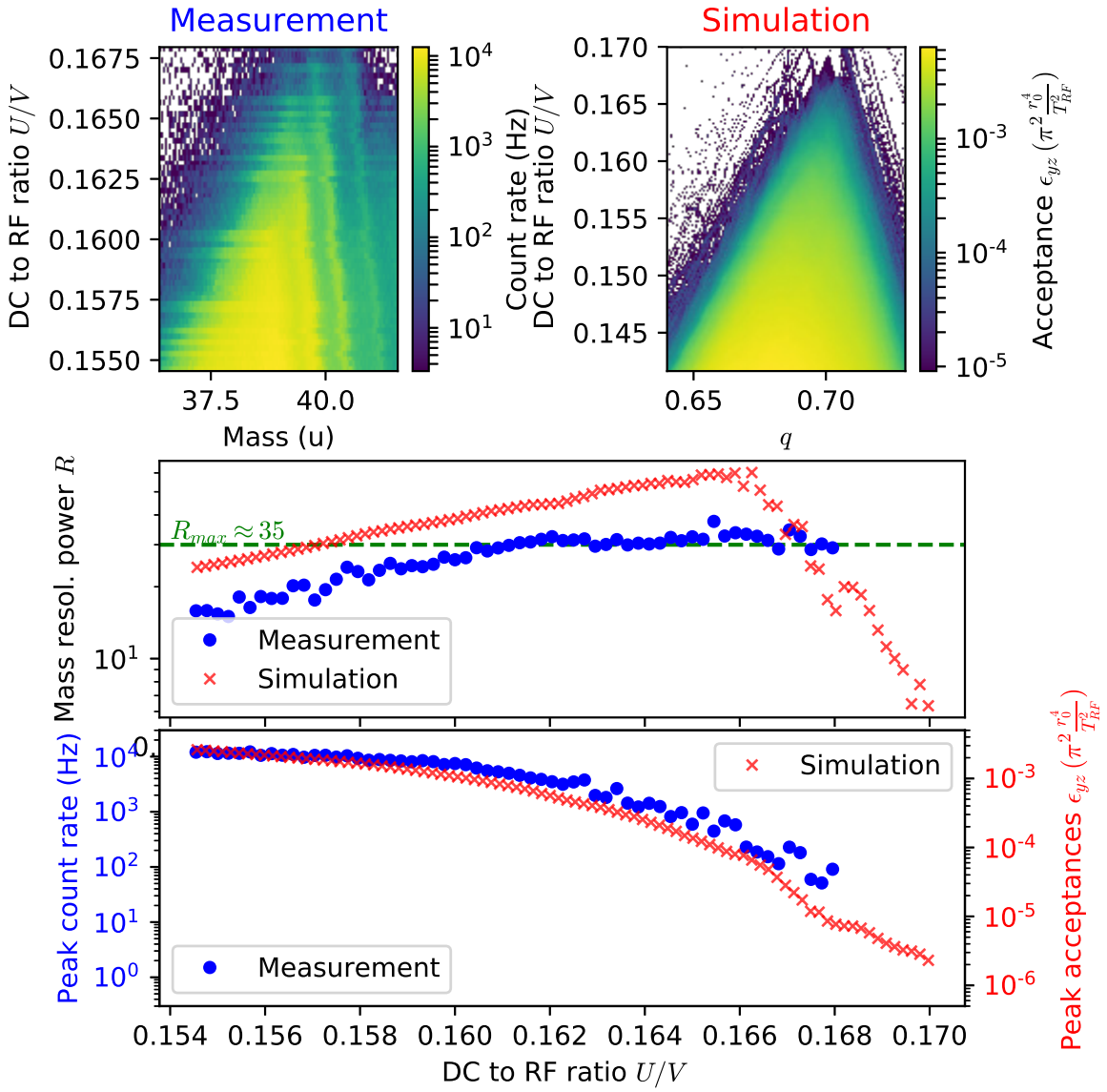

Figure 5.15: Measured and simulated ion transmission at different RF to DC voltages U/V. Ion energy is around 50 eV. See text for details.

The calculated maximum mass resolving power using $h \approx 8$ as obtained above is $R_{max} = 346$. However, the experimentally obtained R_{max} from measurement is $R_{max} \approx 80$. In this case, the R_{max} is most likely limited by the mechanical error of one of the quadrupole electrodes as shown in Figure 5.8.

A final set of measurements was done with the ion source floated at 1 V. The ions entering the QMF have energy around 1 eV and energy spread around 1 eV. The ion velocity in the longitudinal direction is $v_x \approx 2.2\text{mm}/\mu\text{s}$. The corresponding RF cycle is $n_{RF} \approx 120$ when the ions fly through the QMF. The measurement results are shown in Figure 5.17 along with results from the simulation.

The maximum mass resolving power was found to be $R_{max} \approx 140$ for the ions with 1 eV energy. In this case, the R_{max} is still limited by the mechanical error of the QMF2.2 as shown in Figure 5.8. However, $R_{max} \approx 140$ already meets the requirement of $R > 80$ for the purpose of eliminating sufficient contaminant ions from the RF funnel as described in Section 4.1.

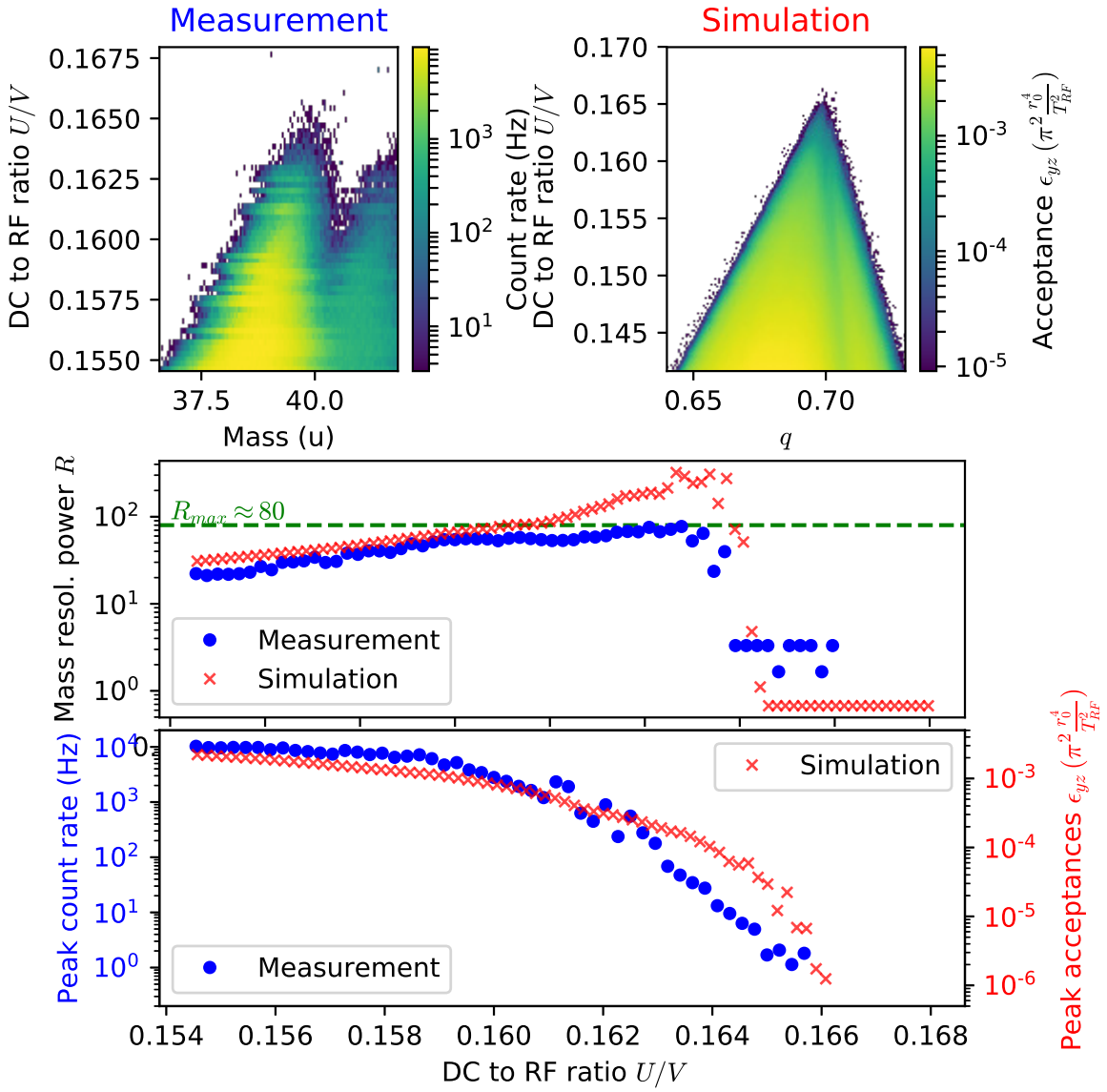

Figure 5.16: Measured and simulated ion transmission at different RF to DC voltages U/V. Ion energy is around 5 eV. See text for details.

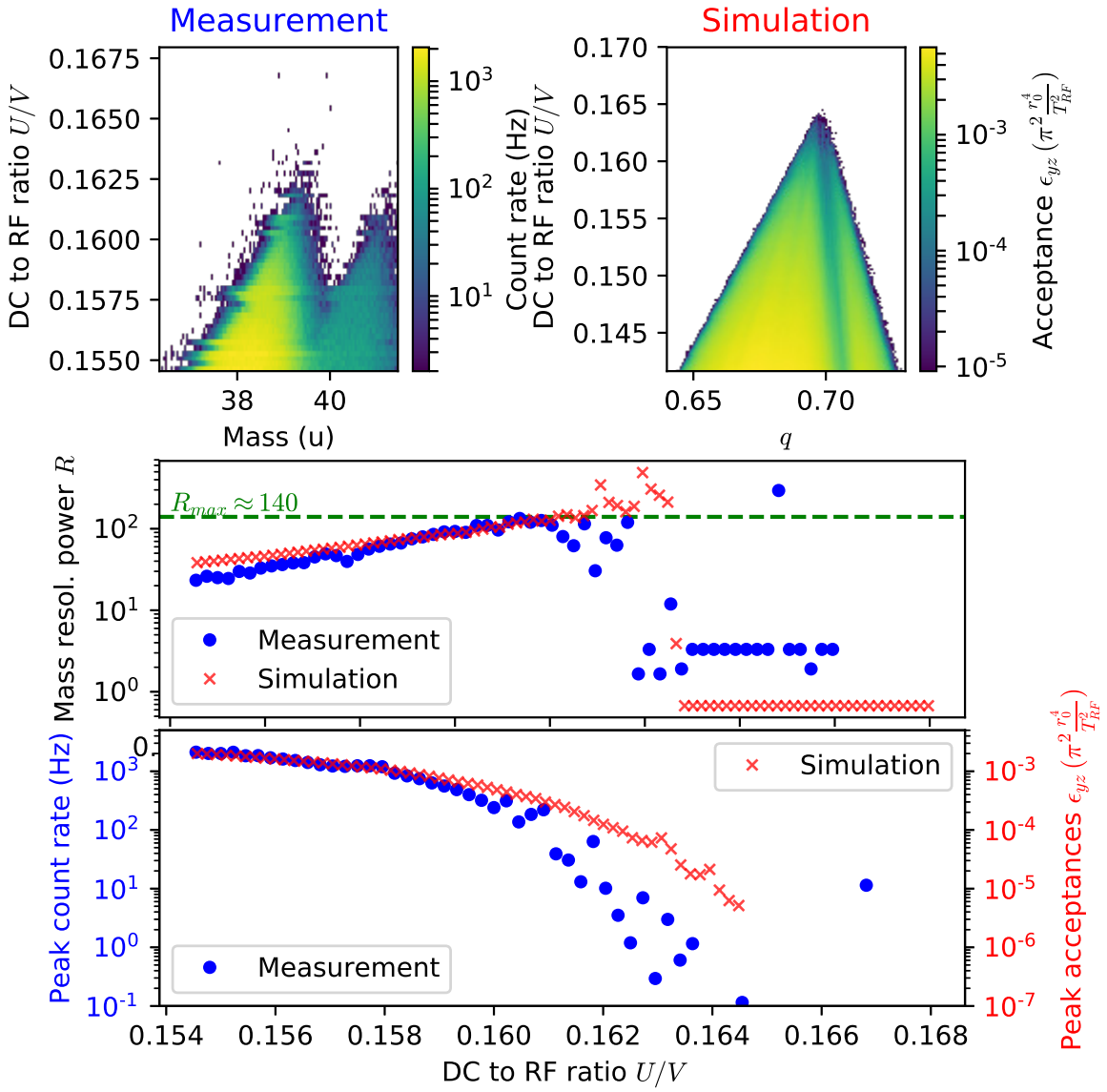

Figure 5.17: Measured and simulated ion transmission at different RF to DC voltages U/V. Ion energy is around 1 eV. See text for details.

5.3 RFQ cooler prototype

A prototype of the RFQ cooler has been built as shown in Figure 5.18 (hereafter referred to as the cooler). The metal tube and the electrodes were machined by the author in the TRIUMF ISAC-II machine shop. The electrode holders have a more complicated structure, so these holders were 3D printed from nylon powder using SLS (selective laser sintering) technique. The 3D printing was done by a commercial company Shapeways [1]. The components for the cooler are shown in Figure 5.18(a). The assembled cooler is shown in Figure 5.18(b), the inset shows the positioning of the quadrupole electrodes.

The machined quadrupole electrodes have a mechanical precision of around 0.2 mm. The 3D printed metal electrodes were also tested. The top quadrupole electrode shown in Figure 5.18(b) was 3D printed using steel fused with bronze material. However, the post-processing required for this material led to a 2 mm shrinkage of the electrode in the longitudinal direction and eventually it was not used.

The lowest quadrupole electrodes shown in Figure 5.18(a) were 3D printed from aluminum powder using the SLM (selective laser melting) technique, also by Shapeways. The 3D printed aluminum electrode has a rough surface and was manually polished with sandpapers. Afterward, the mechanical precision of the electrode is measured and estimated to be around 0.1 mm. The 3D printed electrode was used with the 3 conventionally machined aluminum electrodes in the cooler.

The tapered quadrupole electrodes with width converging from 4 mm at the ion entrance side to 2 mm at the ion exit side are shown in Figure 5.19(a) and (b) before the aperture plates were installed. The aperture plates each have a 2 mm diameter hole in the center for both the ion entrance/exit and the differential pumping of helium gas. The cooler with these aperture plates installed is shown in Figure 5.19(c) and (d). The four extended metal structures were improvised to position that side of the cooler inside the tube of the 8" to 4.5" reducer.

[1] `https://www.shapeways.com/`

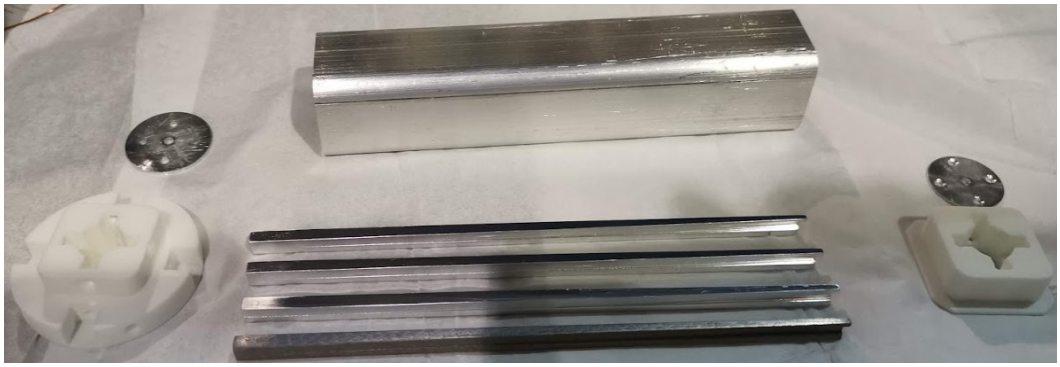

(a) Parts for RFQ cooler prototype

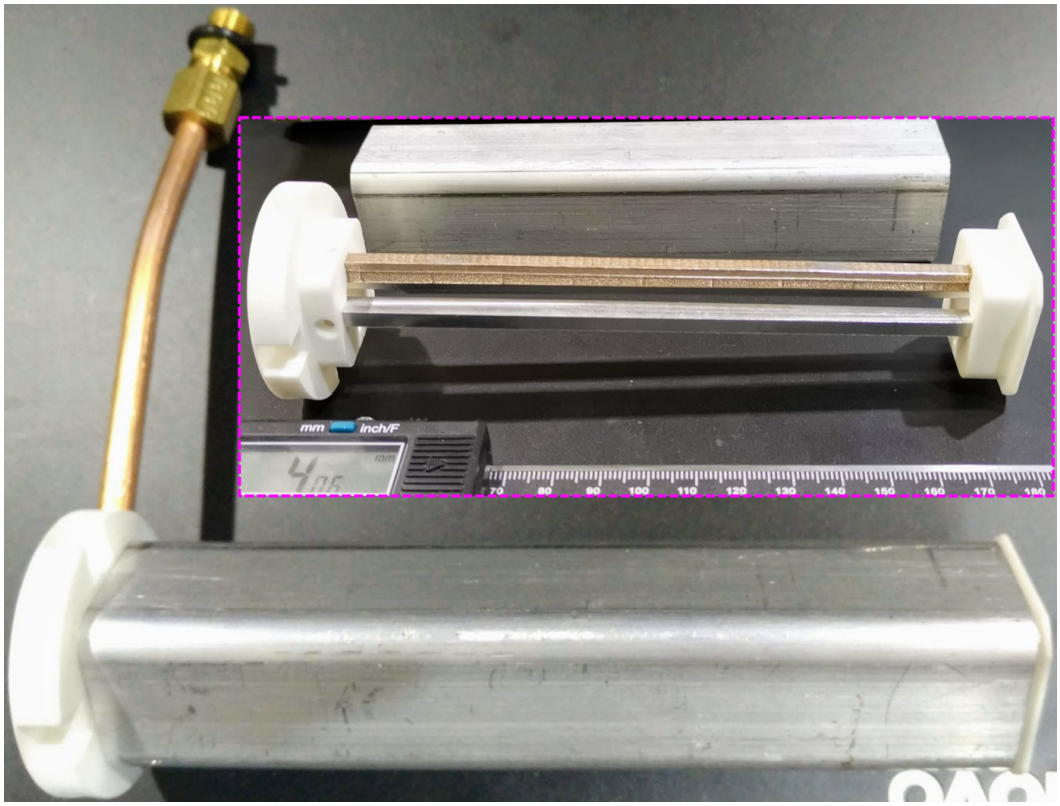

(b) Assembled RFQ cooler prototype

Figure 5.18: Photos of the RFQ ion cooler prototype. See text for details.

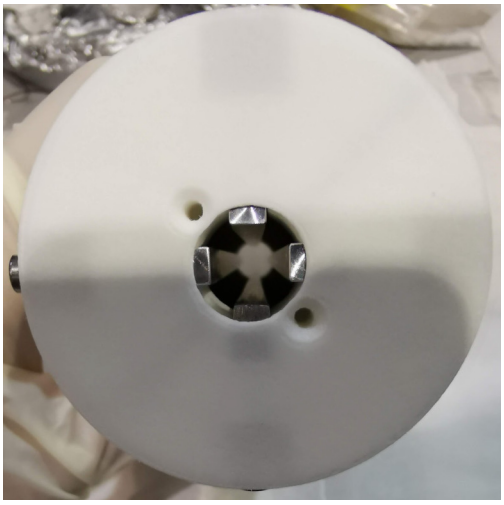

(a) View from ion entrance

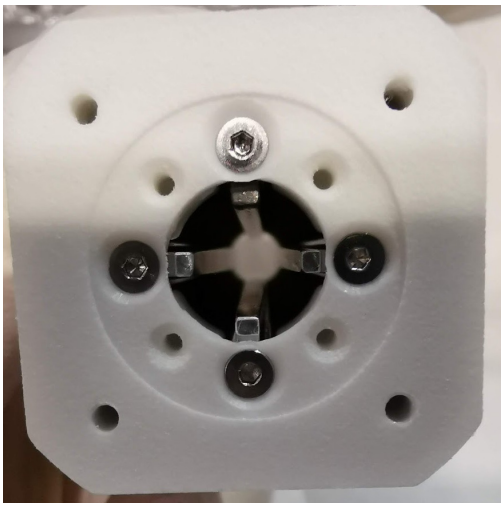

(b) View from ion exit

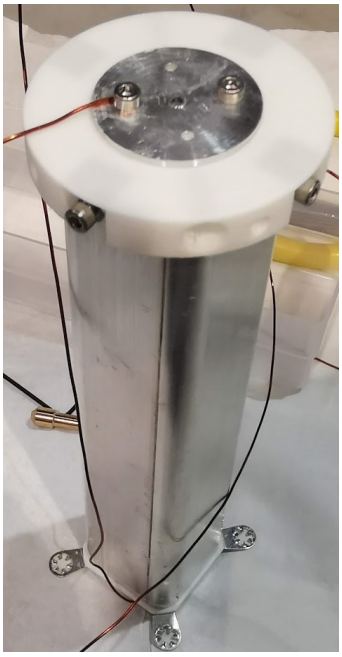

(c) Assembled

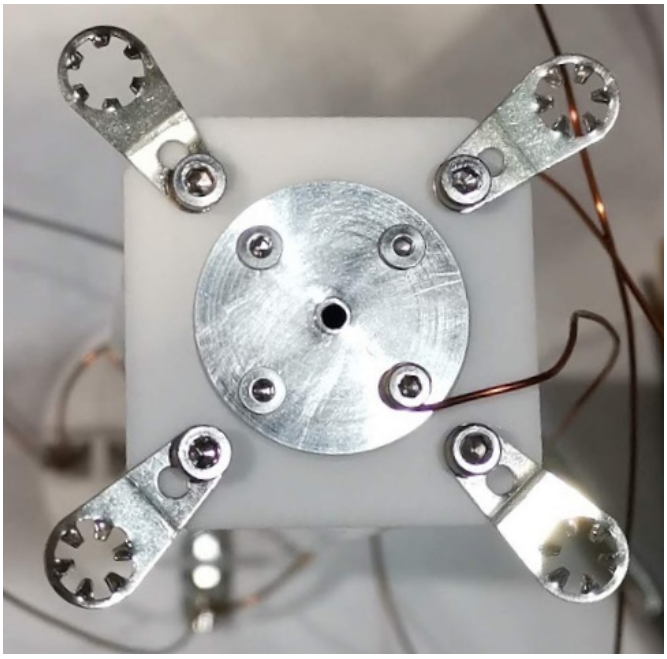

(d) Ion exit with aperture plate

Figure 5.19: Photos of the RFQ ion cooler during (top figures) and after (bottom figures) assembly.

5.3.1 Installation of the cooler prototype in test stand

The cooler was installed in the vacuum chamber of the test stand as shown in Figure 5.20. The paths for helium gas to enter the cooler and for the pressure to be measured by a vacuum gauge are shown in Figure 5.20(b). The position of the cooler relative to the ion source and the ion detector is shown in Figure 5.20(c).

After closing the vacuum chamber, the vacuum pressure reached 1×10^{-6} mbar after pumping for 8 hours. The ultimate pressure after pumping for two days was 4.3×10^{-7} mbar, which is 79% higher than when the vacuum chamber was empty. It demonstrated the outgassing rate of the nylon used for 3D printing for these holders was not significantly higher than acetal and PEEK.

5.3.2 Ion transmission tests with the cooler

The cooler was first tested as a poorly built QMF with non-ideal electrode geometry and bad mechanical precision (0.2 mm) in order to fully validate its electrical connections and its ion transmission properties. These tests would also reveal the cooler's performance as an ion guide in some of the tests when only RF voltage was applied.

The tests were done both with and without helium buffer gas in the cooler to study the vacuum requirement of a QMS and the effect of buffer gas in an RFQ ion guide.

Cooler tests without helium gas

The cooler was first tested without helium buffer gas to check the performance of the flat and tapered quadrupole electrodes.

The ion source was heated to 1.35 A and floated at 50 V, the RFQ cooler was floated at 45.5 V. The energy of incoming ions was around 5 eV.

Ion transmission measurements were done with the cooler at different DC voltage U. The RF voltage of the function generator and the RF amplifier was set to be the same as during the measurements with the QMF prototypes. The RF frequency was scanned from 4.5 MHz to 0.6 MHz for each of the DC voltage U. The results are shown in Figure 5.21. The

(a)

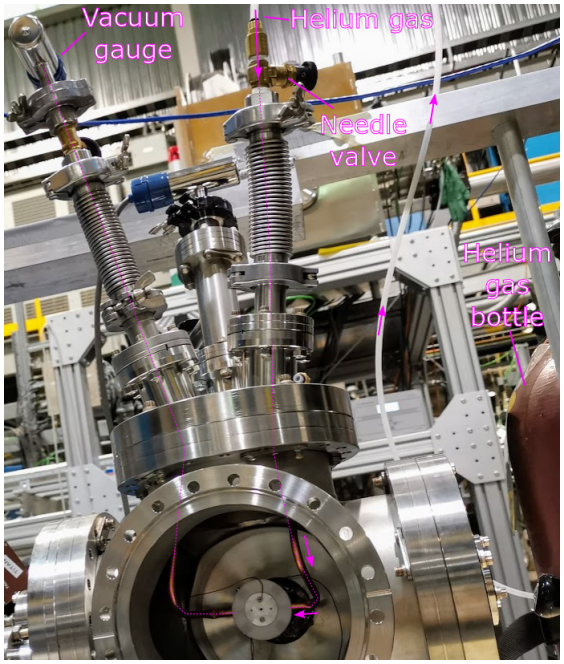

(b)

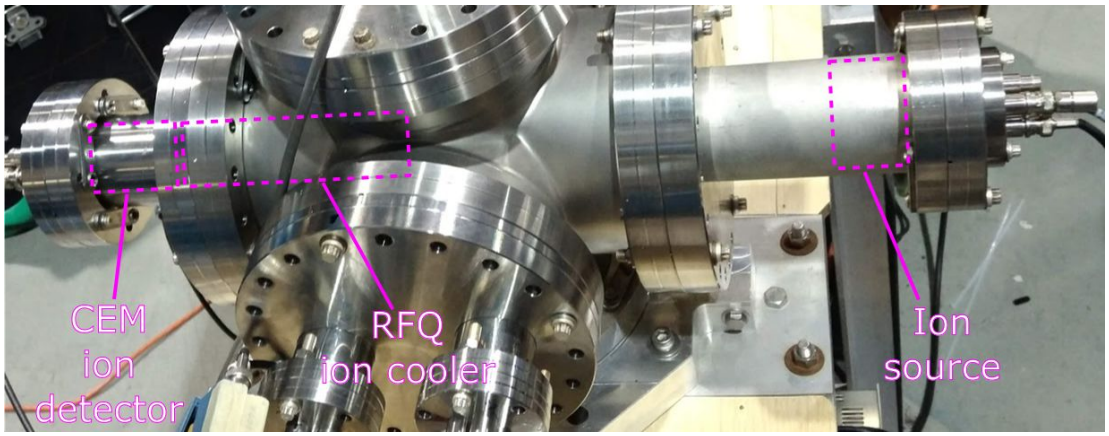

(c) Position of major components in vacuum chamber

Figure 5.20: Installation of the cooler to the test stand's vacuum chamber. See text for details.

patterns of stability diagram can still be recognized for the ^{23}Na, ^{39,41}K and ^{85}Rb ions.

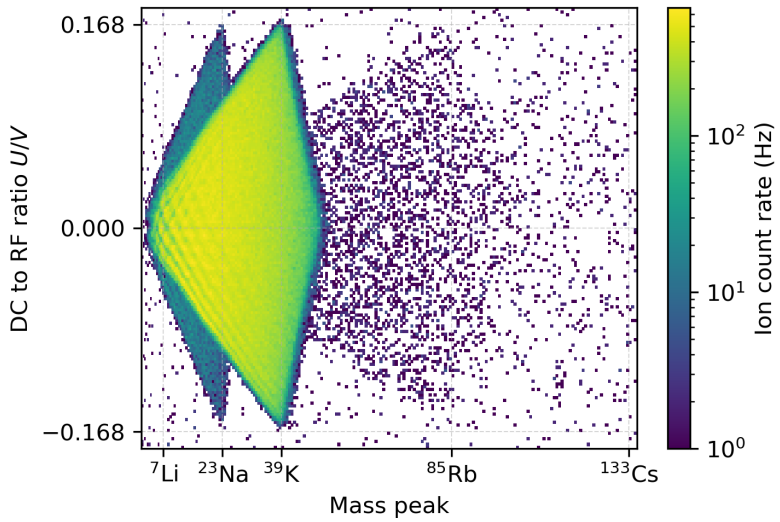

Figure 5.21: Ion transmission measurement with the cooler at different DC voltage U.

Later a different ion source (#2) was used as shown in Figure 5.2(c). This ion source produced $> 99.9\%$ of ^{133}Cs and $< 0.1\%$ of ^{39}K. Similar measurements were done as above and the results are shown in Figure 5.22. As expected, this time there is only a single pattern of the stability diagram for the ^{133}Cs ion. This ion source was used for all later measurements discussed below.

Both measurements shown in Figure 5.21 and Figure 5.22(a) have maximum mass resolving power $R \approx 20$. In this case, the mass resolving power of the cooler was limited by the higher-order spatial harmonics in the electric potential, also by the varying magnitude of the quadrupole term A_2 as a result of the changing width of the electrodes.

Figure 5.22(b) shows the ion transmission of the cooler working as an RFQ ion guide when the DC voltage $U = 0$. The horizontal axis is

$$q = q_t \frac{m_{pk}}{m_{Cs}}, \tag{5.6}$$

where $q_t \approx 0.706$, m_{pk} is the value on the horizontal axis of Figure 5.22(a)

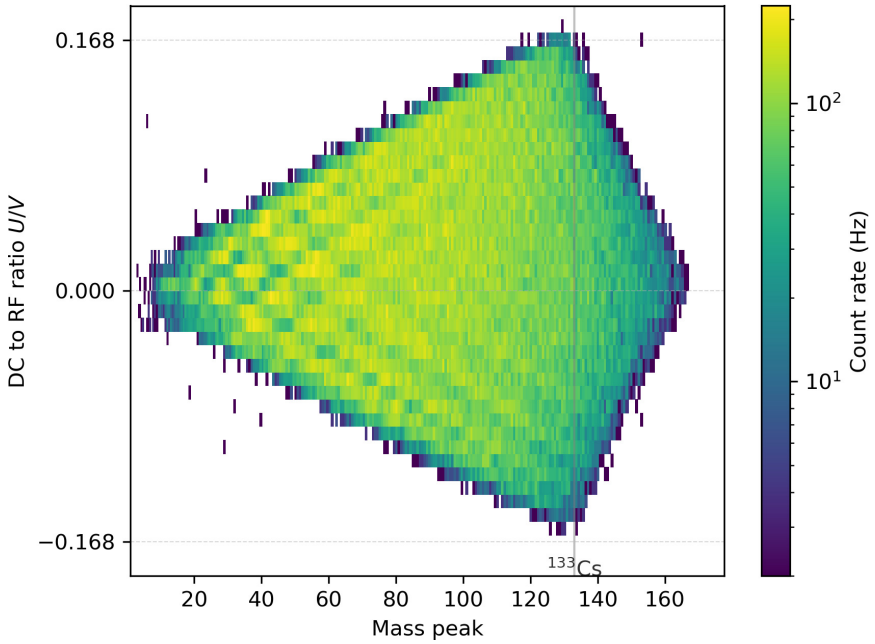

(a) Ion count rate at different U

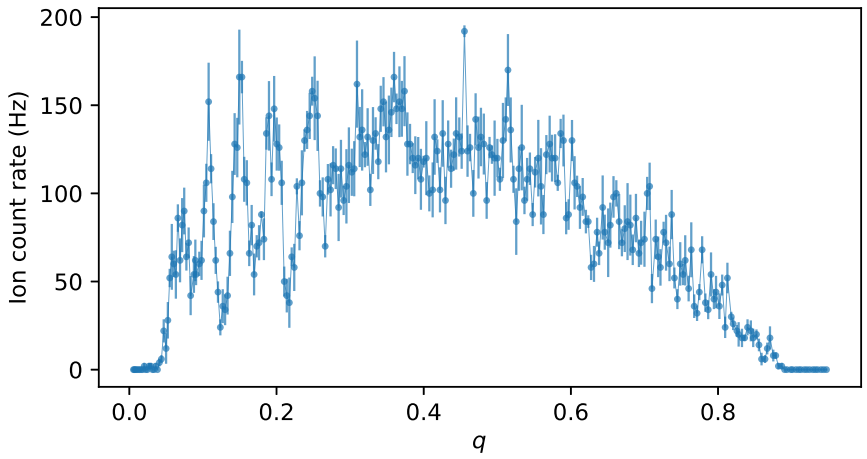

(b) Ion count rate at $U = 0$

Figure 5.22: Ion transmission measurements with the cooler using ions from an almost pure cesium ion source (#2).

and m_{Cs} is the mass of ^{133}Cs. The ^{133}Cs ions were transmitted between $0 < q < 0.908$ as expected in an ion guide. However, there are obvious fluctuations in the ion count rate as a function of q. The fluctuations are probably caused by the non-ideal electric potential inside the cooler. The fluctuations were found to be smaller when the ions flew through the cooler at a smaller velocity.

Ion transmission tests with helium buffer gas

The cooler was filled with some helium gas after slightly opening a needle valve which is connected to a helium gas bottle. The pressure in the vacuum chamber (outside of the cooler) also increased due to helium gas flowing out of the 2 mm diameter apertures on the entrance and exit of the cooler. After a few hours, the pressure in the vacuum chamber stabilized at 4.0×10^{-6} mbar, while the pressure inside the cooler was 5.5×10^{-3} mbar due to the differential pumping as measured by the vacuum gauge shown in Figure 5.20(b).

An ion transmission test was done with the same configuration (ion source voltages and the RF&DC voltages) and the results are shown in Figure 5.23.

The smoother variation of the ion count rate at different RF and DC voltage indicated the ions traveled at a lower velocity through the cooler. The effect of ion velocity on the count rate can be understood by comparing Figure A.15(a) and Figure 5.12. The measurements were done at the same configuration of the ion source voltages, so the only possibility is that the ions were cooled and slowed down by the helium buffer gas.

To further validate the ion cooling effect of the helium buffer gas, a set of measurements was done at higher helium gas pressure of 1.9×10^{-2} mbar; the pressure in the vacuum chamber was 1.3×10^{-5} mbar. The results are shown in Figure 5.24.

The even smoother variation of the ion count rate in Figure 5.24 corresponds to an even smaller ion velocity inside the cooler and validates the helium gas's cooling effect. The ion transmission as indicated by the count rate also increased because of ion cooling. The maximum mass resolving power of the cooler is $R \approx 20$ at both gas pressures.

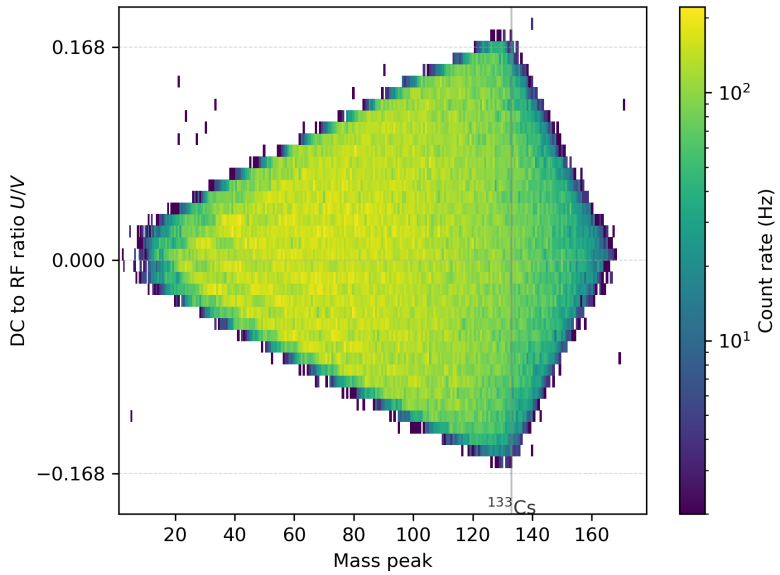

Figure 5.23: Ion transmission measurements of the cooler with helium gas pressure of 5.5×10^{-3} mbar.

The turbo molecular pump and the CEM ion detector are both ideal to work at low gas pressure to ensure a long operation lifetime. So no tests were done at helium gas pressure higher than 1.3×10^{-5} mbar in the vacuum chamber (1.9×10^{-2} mbar in the cooler).

5.3.3 Experiments with ion trapping

The RFQ cooler was tested as a standalone ion trap to validate ion cooling and trapping with the novel tapered quadrupole electrodes. Note that in the final LPT, the ions are intended to be trapped in the laser spectroscopy ion trap following the ion cooler.

The RF voltage applied to the ion cooler's quadrupole electrodes was set to be $V = 71.0$ V and the RF frequency was $f_{RF=}0.8$ MHz. The stability parameter for the $^{133}CS^+$ ions in the cooler is $q = 0.46$. The metal tube was biased to a negative voltage U_{tube} to form the drag field. The quadrupole electrodes in the RFQ cooler were floated at U_f =45.5 V. The cooler was enclosed by an aperture plate with a 2 mm diameter hole where the ions exit. When the aperture plate voltage U_{ap} was set to be higher than U_f, a trapping potential can be formed as shown in solid lines in Figure 5.25. The

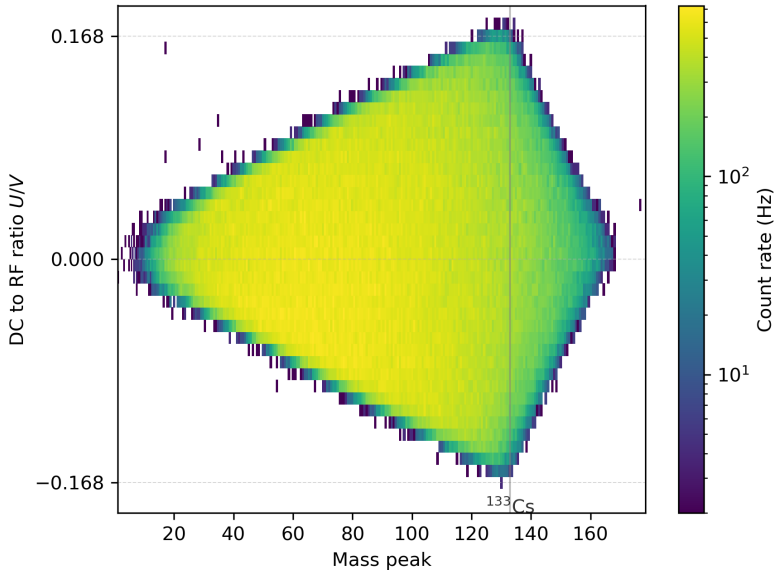

(a) Ion count rate at different DC voltage U

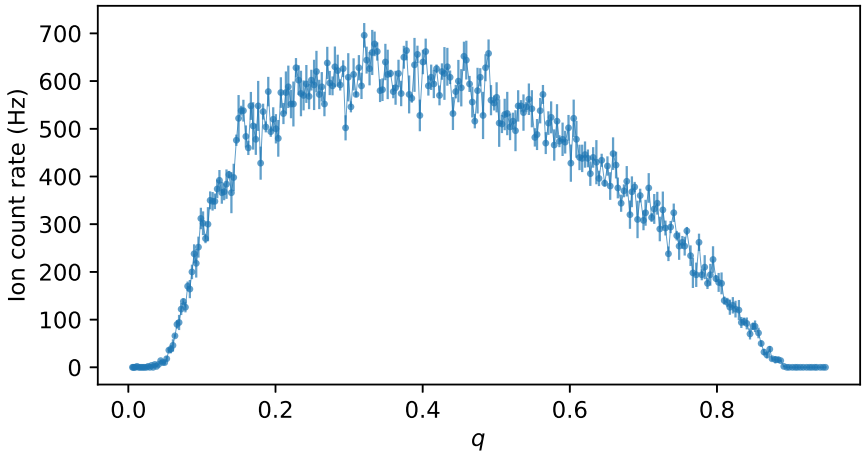

(b) Ion count rate at $U = 0$

Figure 5.24: Ion transmission measurements of the cooler with helium gas pressure of 1.9×10^{-2} mbar.

profile of the trapping potential and the position of the minimum potential is dependent on the aperture voltage.

When the aperture voltage U_{ap} was switched to be lower than U_f, the trapped ions would be ejected out of the RFQ cooler under the electric potential gradient as shown in dashed lines in Figure 5.25. The ejected ions were detected by a CEM ion detector a few millimeters away from the aperture plate.

The ion signal from the CEM detector was amplified by an Ortec VT120 fast timing amplifier. The amplified ion signal was then sent to a LeCroy LRS 621AL discriminator to identify the ion signal with a threshold of -0.25 V. For each ion ejection, the amplified ion signal and the pulses output from the discriminator were recorded by a Siglent SDS1104X-E oscilloscope. The switch voltage was also recorded by the oscilloscope. The data acquisition of the signals was done at 500 MS/s, corresponding to a 2 ns time resolution.

As an example, Figure 5.26 shows the ejection of 11 ions after the aperture voltage was switched to 0V. Before the ejection, the ions were trapped inside the cooler with the aperture set at 240 V. The repetition rate of the ion ejection was 0.25 Hz to allow for 4 seconds of accumulation of cooled ions (due to the low ion rate).

The ejected ions have an average time of flight (ToF) $\overline{t_{ToF}} = 29\,\mu s$. The spread of their ToF is $\sigma_{t_{ToF}} = 11\,\mu s$. There was electronic noise in the ion signal when the aperture voltage was switched. This noise was excluded and not counted as an ion signal in the data processing.

Ion injection energy

The cooling and trapping of ions injected into the cooler was then tested and validated by varying the injection energy E_{inj} of the incoming ions to study the buffer gas's effect on slowing down the ions in the longitudinal direction. For the helium gas pressure of 5.5×10^{-3} mbar inside the cooler, the ion energy was varied by changing the ion source floating voltage U_s in the range from 30 V to 55 V. The results are shown in Figure 5.27.

In the ideal case, in order to achieve the maximum ion trapping efficiency, the ion source floating voltage U_s should be slightly above the floating voltage of the cooler U_f. If U_s is too small, the ions won't have enough

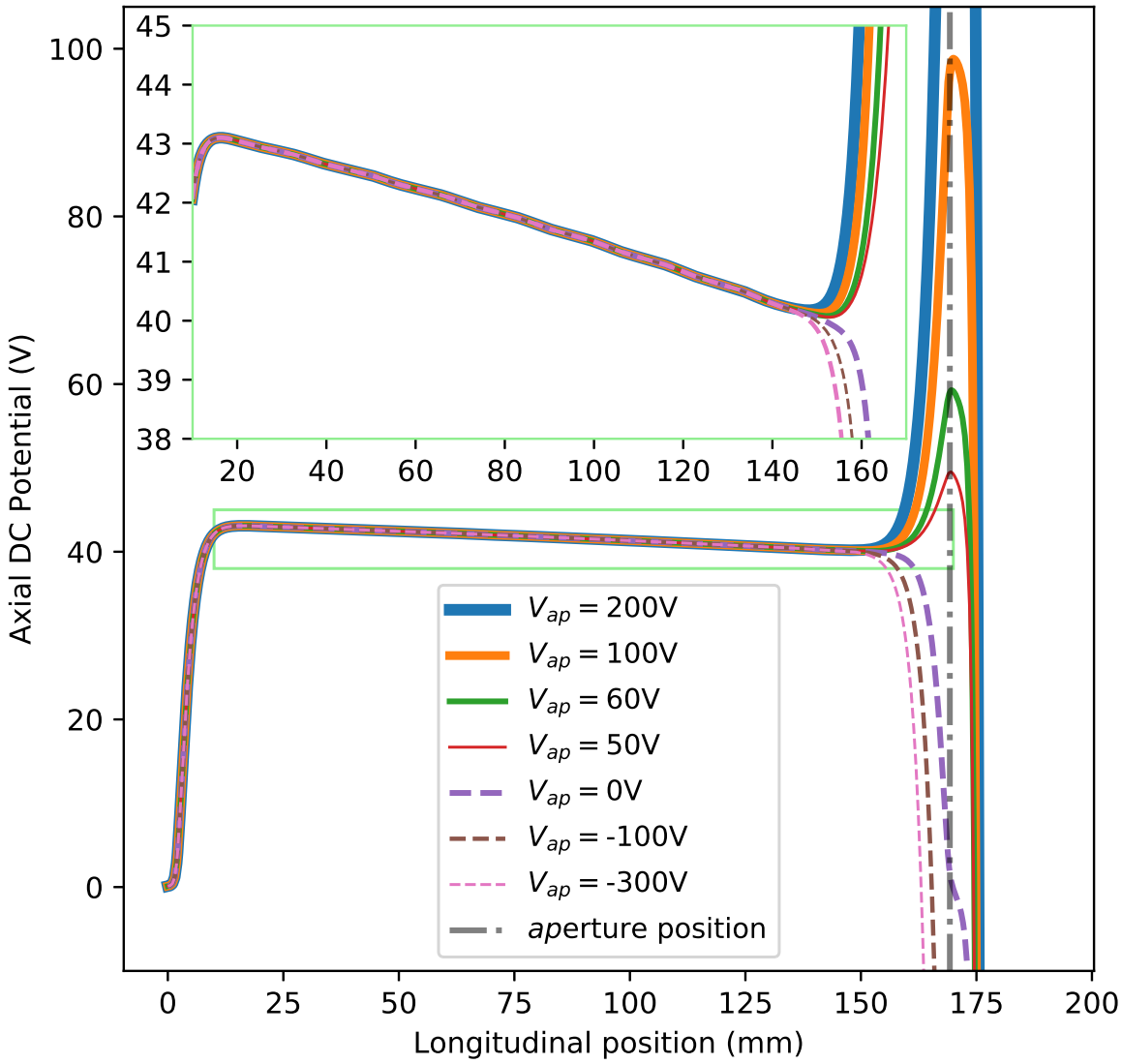

Figure 5.25: Simulated DC potential along the RFQ cooler's central axis for ion trapping and ejection when the metal tube voltage was set at $U_{tube} = -150\,\mathrm{V}$. The inset is a zoomed-in plot.

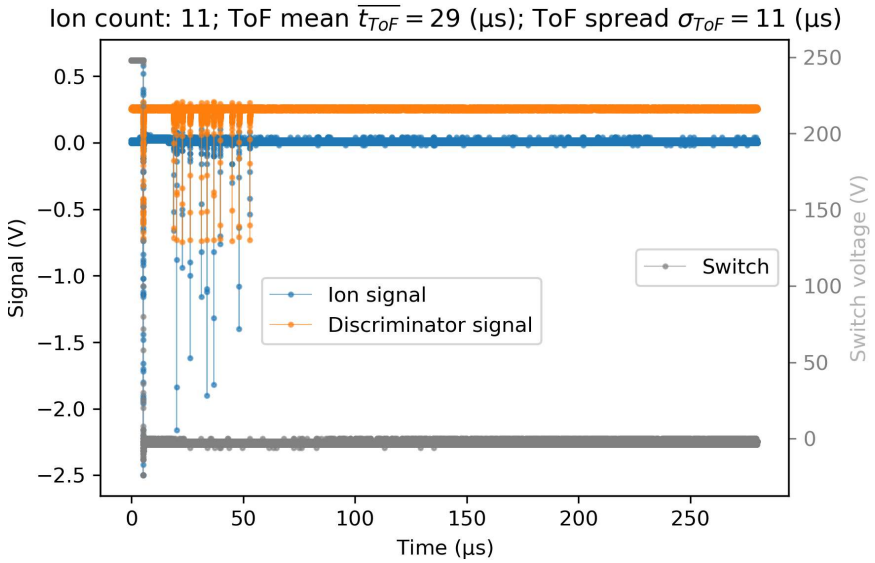

Figure 5.26: An example showing ion signal detected by the CEM ion detector from the ejected ions as a function of time of flight (ToF). The ions were trapped with the aperture voltage of 240 V. After the aperture voltage was switched to 0 V, the ions started to fly out and hit the CEM detector later. The ToF of the ions is obtained from the ion signals.

energy to overcome the electric potential at the entrance of the cooler and will be repelled; if U_s is too large, the ions will have too much energy such that the buffer gas cannot sufficiently cool the ions and the ions will have a round trip inside the cooler and exit through the entrance of the cooler.

However, as shown in Figure 5.27 the setting of the optimum ion source floating voltage to achieve the maximum number of trapped ion was experimentally found to be $U_s \approx 41$ V, which is a few volts lower than the floating voltage of the cooler $U_f = 45.5$ V. This is most likely due to the effect of the RF voltage which is oscillating. As a result, half of the cross-sectional area of the cooler's entrance has an actual electric potential lower than U_f and allows the ions with lower energy to enter the cooler.

The ion injection energy has a full-width of $\Delta E_{inj} \approx 6$ eV at the half-maximum of the ion count per bunch.

Later, the ion injection test was done at the higher helium gas pressure of 1.9×10^{-2} mbar in the cooler. The results are shown in Figure 5.28.

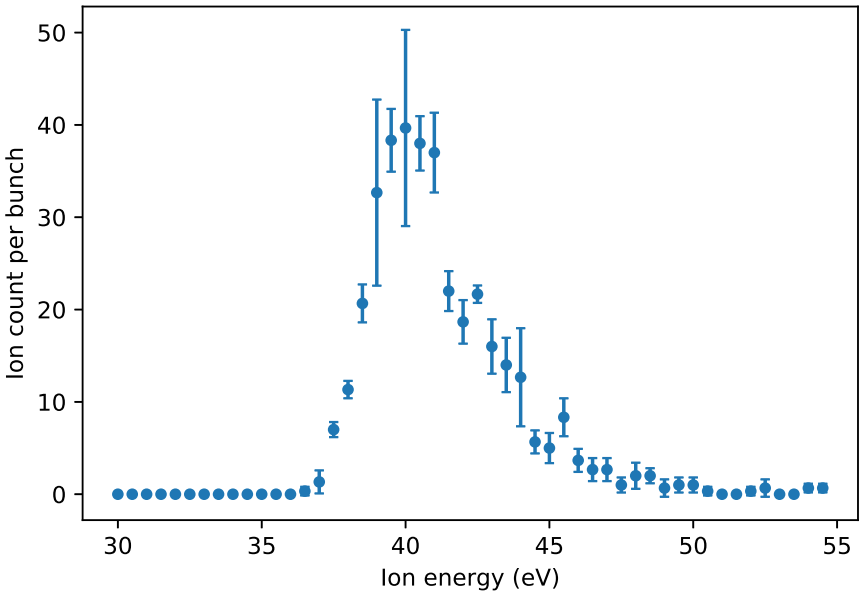

Figure 5.27: Ion count of cooled and ejected ions as a function of injection energy at 5.2×10^{-3} mbar helium buffer gas pressure.

With the higher helium gas pressure inside the cooler, the ion cooling and trapping was more efficient. The optimum ion injection voltage for the maximum ion trapping efficiency is $U_s \approx 50\,\mathrm{V}$. The full-width of the injection energy at the half-maximum ion count per bunch is $\Delta E_{inj} \approx 20\,\mathrm{eV}$.

At these two tested gas pressures, the range of the ion injection energy ΔE_{inj} is proportional to the gas pressure. Therefore, at the designed operating pressure of 0.1 mbar, the cooler can achieve the required cooling of ions with injection energy in the range of $\Delta E_{inj} \approx 100$.

Effects of aperture voltage on ion ToF

The voltage of the aperture plate determines the DC potential near the exit of the cooler for the trapping and ejection of the ions, as shown in Figure 5.25. The aperture plate voltage therefore affects the kinetic energy of the ejected ions, which in turn determine the time of flight (ToF) of the ions as below:

- A higher trapping voltage on the aperture plate would push the position of the potential minimum further away from the aperture plate.

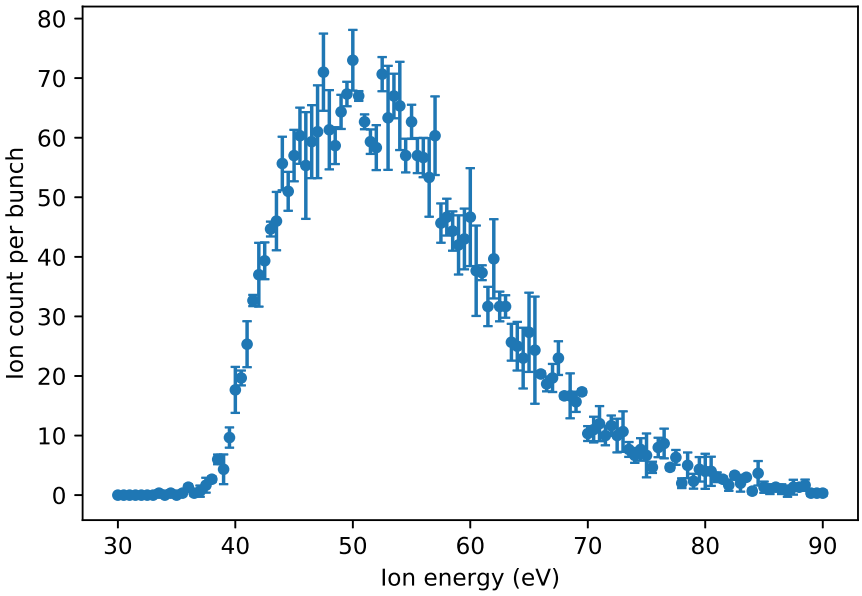

Figure 5.28: Cooling and trapping of ions with different injection energy at 1.9×10^{-2} mbar helium buffer gas pressure.

As a result, the ions will have a longer path from the trapped position to the CEM detector and correspondingly larger ToF.

- A higher ejection voltage [1] on the aperture plate generates a less steep potential gradient for the ions to fly out, hence the ions will experience a smaller kinetic energy gain and have larger ToF to reach the CEM ion detector.

- On the contrary, a smaller trapping or ejection voltage will cause the ion ejection to have a smaller ToF.

Measurements were done with ion ejection at different trapping voltage U_T and ejection voltage U_E of the aperture plate. When the trapping voltage is 110 V or lower, the average of the ion time of flight $\overline{t_{ToF}}$ is a few microseconds, and the ToF spread σt_{ToF} is smaller than 1 microsecond as shown in the results in Figure 5.29.

[1] The aperture voltage for ion ejection here is usually a negative value. So a higher ejection voltage corresponds to a smaller absolute value of the voltage.

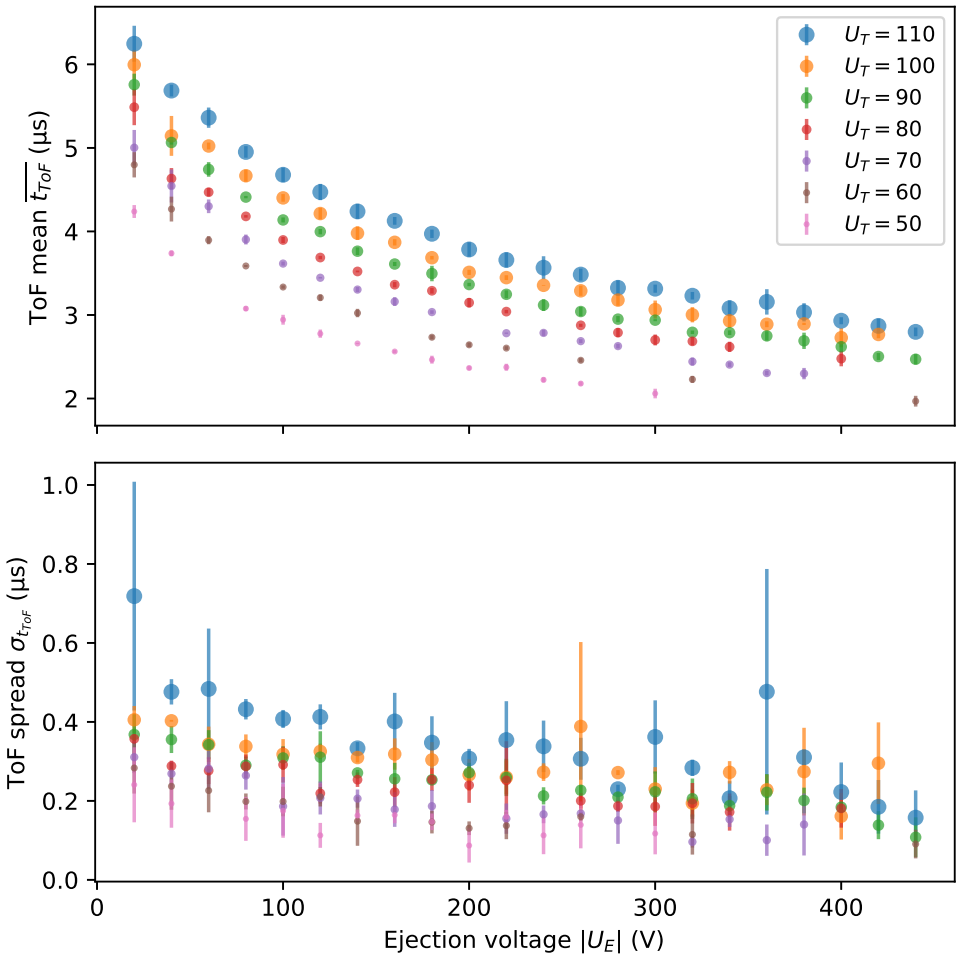

Figure 5.29: Measured ion time of flight (ToF) mean $\overline{t_{ToF}}$ and ToF spread σt_{ToF} as a function of the ejection voltage U_E at trapping voltage U_T from 50 V to 110 V.

When the trapping voltage is 120 V or larger, both $\overline{t_{ToF}}$ (top plot) and σt_{ToF} (bottom plot) are significantly larger as shown by the results in Figure 5.30.

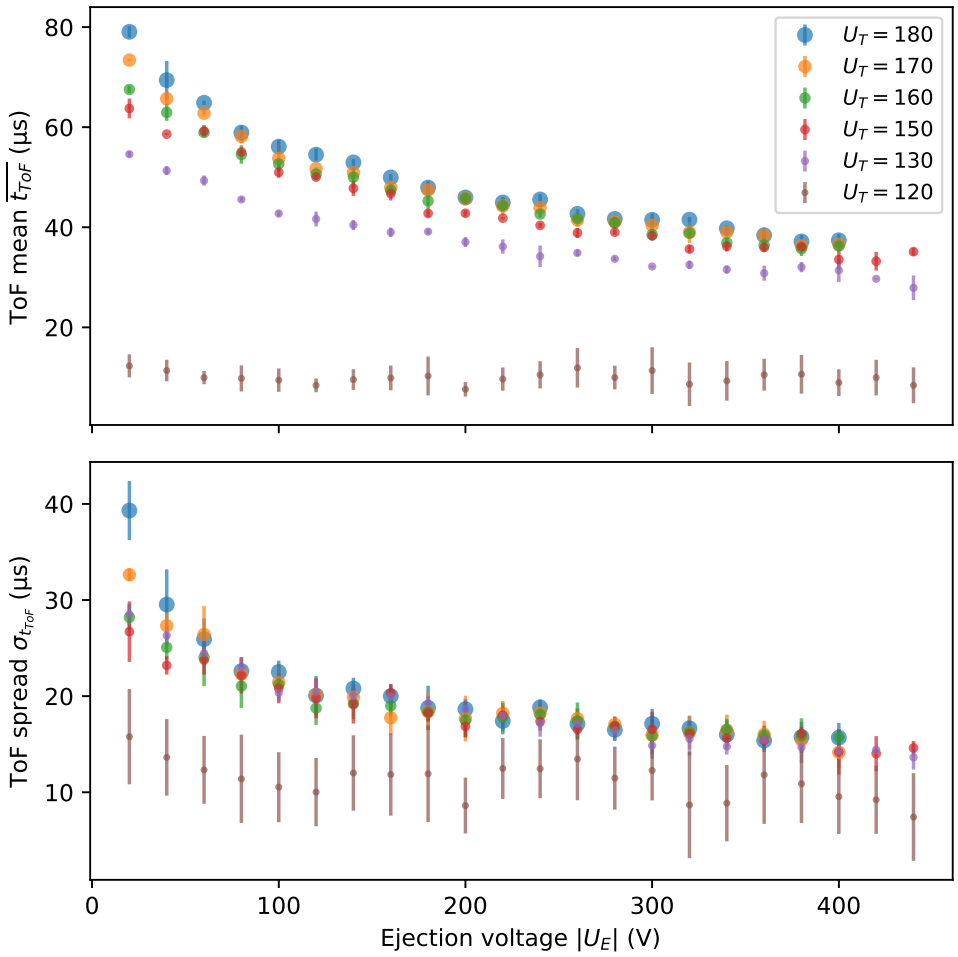

Figure 5.30: Measured ion time of flight (ToF) mean $\overline{t_{ToF}}$ (top plot) and ToF spread σt_{ToF} (bottom plot) as a function of the ejection voltage U_E at larger trapping voltage U_T from 120 V to 180 V.

In order to understand the measured ToF of the ion ejection, SIMION simulations were performed for the cooler for comparison. The simulations started with 1000 ions near the central axis of the cooler and the longitudinal position of the minimum DC potential. The ions were cooled for 2000

microseconds to reach thermal equilibrium with the buffer gas before the ion ejection was simulated. The ion ejection was simulated at these trapping voltages U_T and ejection voltages U_E used in measurements. The results of the simulation are shown in Figure 5.31.

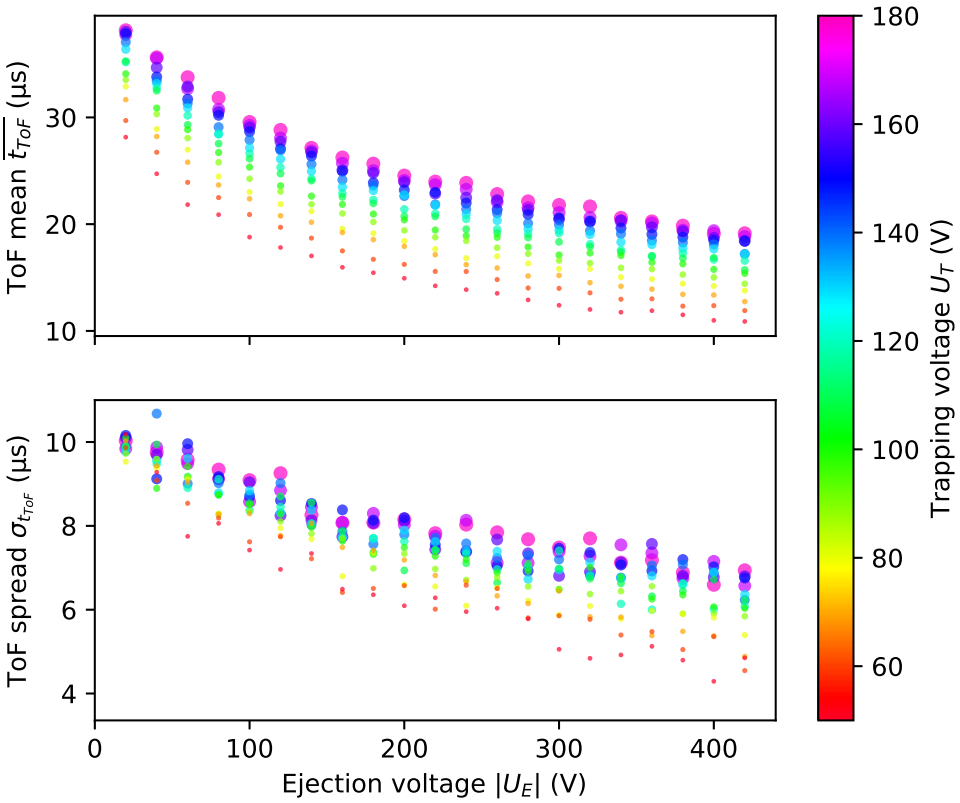

Figure 5.31: Simulation of cooler's ion ejection ToF as a function of the ejection voltage U_E at different trapping voltage U_T. The trapping voltage U_T is from 50 V to 180 V with a 10 V increment as represented by the size of the marker and the colorbar.

For a fixed trapping voltage U_T, the decrease of $\overline{t_{ToF}}$ and σt_{ToF} as a function of the ejection voltage $|U_E|$ follow a similar trend in the simulation and experimental measurement. However, when $U_T \geq 120$ V, the measured $\overline{t_{ToF}}$ and σt_{ToF} are larger than the simulation; when $U_T \leq 110$ V, the measured $\overline{t_{ToF}}$ and σt_{ToF} are smaller than the simulation.

After more careful troubleshooting and ion ejection measurements with

varied parameters, the discrepancy between the measured and simulated ion ToF was found to be caused by charge buildup on the surface of the electrode holder as highlighted in Figure 5.32. The charge buildup was caused by ion deposition on the surface of the insulating material.

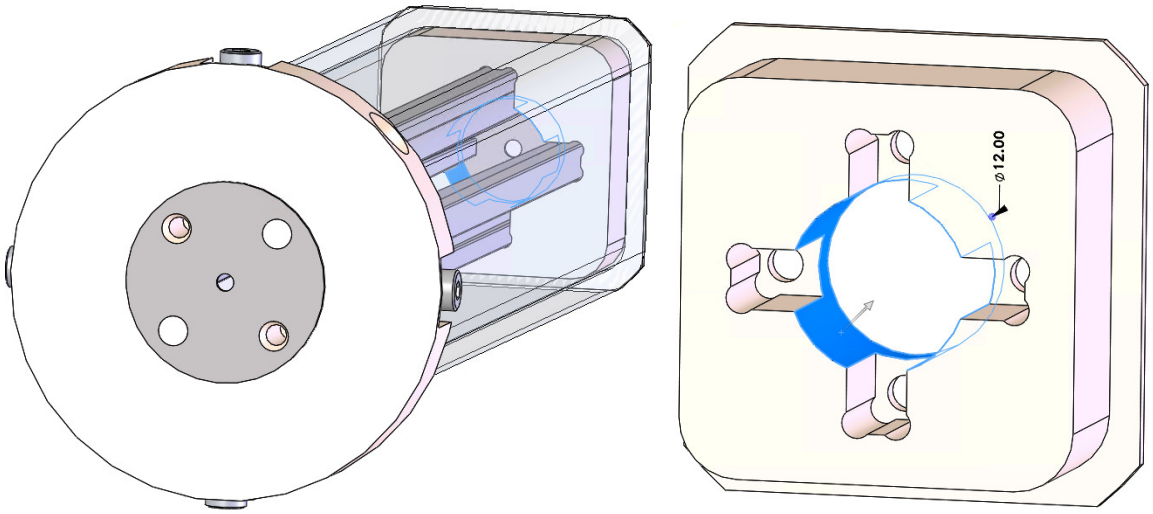

(a) Cooler with the tube set transparent (b) Electrode holder near the exit

Figure 5.32: Charge buildup problem near the exit of the cooler. The charge buildup occurred after lots of ions deposit on the inner surface of the electrode holder (highlighted in blue).

The deposited ions created charge buildup and distorted the potential around where the ions were trapped. The charge buildup has a potential $U_{CB} \approx 120\,\mathrm{V}$ (which is approximately $U_f + V$). So that when the trapping potential $U_T < U_{CB}$, the position of the trapped ions were pushed by the charge buildup to be close to the exit of the cooler and cause the ion ejection to have a smaller ToF. When $U_T > U_{CB}$, the position of the trapped ions were pushed further away from the cooler exit and caused the ion ejection to have a large ToF.

When the trapping potential is about the same as the potential of the charge buildup at 120 V, the ion bunch were observed to be split into two as shown in Figure 5.33.

The ion bunch 1 has an average ToF $\overline{t_{ToF}} = 6.7\,\mu\mathrm{s}$, indicating these ions

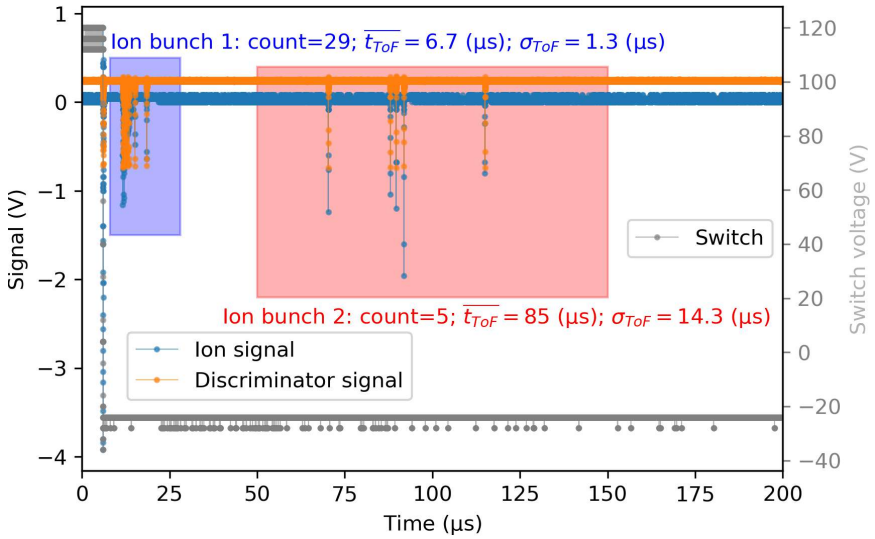

Figure 5.33: Ion cloud split by the charge buildup, resulting in two ion bunches. The ejection voltage used in this measurement was $U_E = -20\,\mathrm{V}$.

were trapped close to the cooler exit, similar to the earlier measurements shown in Figure 5.29. The ion bunch 2 has a much larger average and spread of ToF, indicating these ions were trapped further away from the cooler exit, similar to the measurements shown in Figure 5.30.

The trapping region that corresponds to the ion bunch 1 has very limited volume as the ion bunch 1 was found to have a maximum ion count of around 40. The ion bunch 2 can have up to 1000 ion count at a larger trapping voltage. The effect of the charge buildup was also less obvious at the larger trapping voltages. So, the ion bunch 2 corresponds to a trapping potential similar to the ones shown in Figure 5.25.

The issue of the charge buildup can be resolved by removing as much as possible of the electrode holder's insulating material near the position of the ion trapping as highlighted in Figure 5.32(b). The design of the electrode holder was revised in such a way and shown in the mechanical drawings in Appendix B (drawing number LPT2CC04).

If needed in the future, more detailed experiments with the ion ejection will be done with a retarding field analyzer and a emittance meter.

Ion storage lifetime

The ion storage lifetime is important for the laser spectroscopy identification of the barium ions in the laser spectroscopy ion trap. The ion identification required the ions to be trapped for at least a few seconds. As a first step of studying the storage lifetime of the trapped ions, experiments were done with ions trapped in the cooler.

The ion source was floated to 45 V for 10 seconds for the ions to enter the cooler, then the ion source floating voltage was set to 0 V to prevent further ions from entering the cooler. After a storage time t_s, the ions were ejected from the cooler and detected by a CEM. For each t_s from 1 second to 285 seconds in log scale increment, 10 measurements were repeated and the ion count in every bunch of ejected ions was recorded. The result is shown in Figure 5.34(a).

The count of the ejected ions as a function of the storage time t_s was fitted to an exponential function

$$N = N_0 \exp(-\frac{t_s}{\tau}). \tag{5.7}$$

The fitted initial ion count is $N_0 = 58.3 \pm 0.8$ and the storage lifetime $\tau = 16.9 \pm 0.6$ s.

Another set of measurements was done by fixing the ion storage time $t_s = 1$ s while increasing the ion accumulation time from 0.1 s to 140 s. In this case, the ion count in the ejected ion bunch will be affected by both the rate of ions entering the cooler R_{ion} and the storage lifetime of the ions in the cooler τ. The measured results are shown in Figure 5.34(b) and fitted to a modified exponential function

$$N = R_{ion}\tau(1 - \exp(-\frac{t_a}{\tau})). \tag{5.8}$$

The fitted ion count rate is $R_{ion} = 8.1 \pm 0.1$/s, and the ion storage lifetime is $\tau = 13.5 \pm 0.4$ s.

The shorter ion storage lifetime measured during the accumulation of the ions indicates saturation of ions in the cooler. The ion storage lifetime was also found to be in the range of $7 < \tau < 40$ s depending on the voltage configuration of the cooler and the number of stored ions in the cooler.

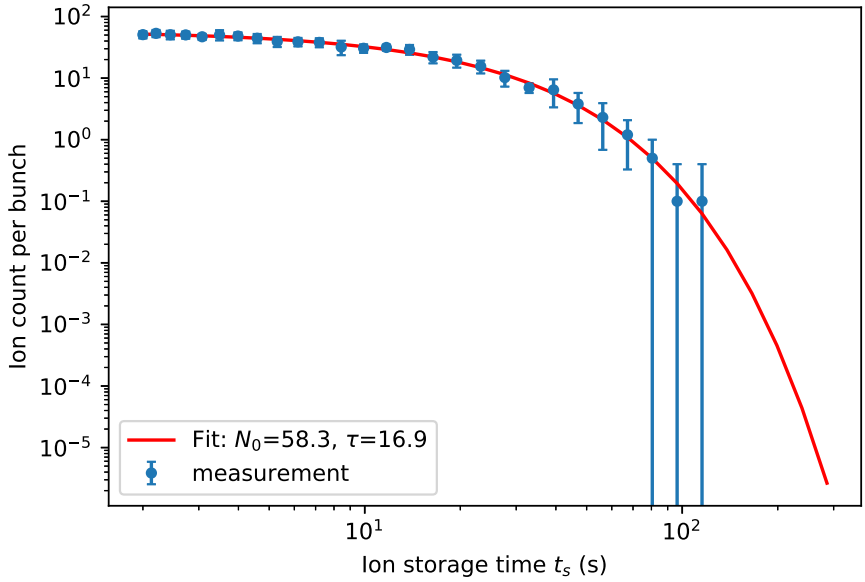

(a) Ion storage in the cooler

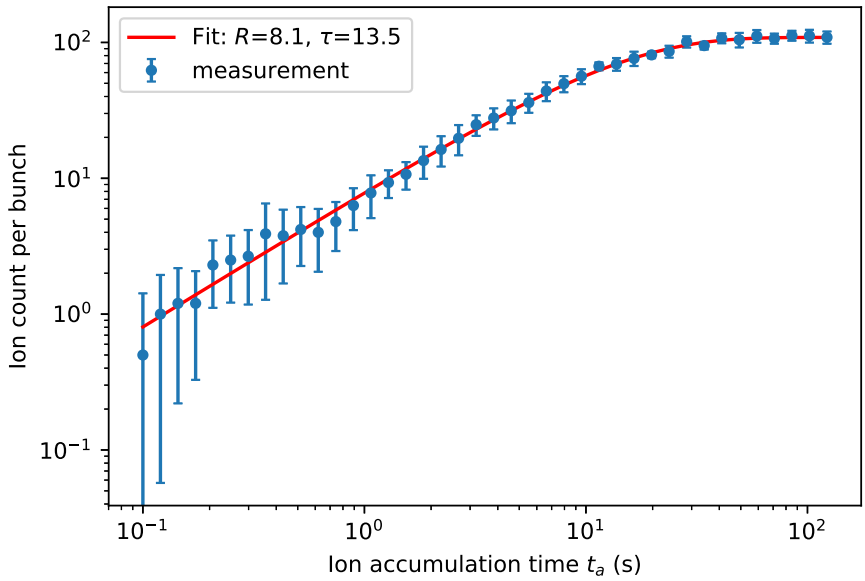

(b) Ion accumulation in the cooler

Figure 5.34: Measurement of ion numbers in the cooler as a function of storage time.

Simulations of ions trapped in the cooler with extended trapping time reveal the ions have stable ion temperature and confinement, no ion loss was caused by the RF heating. The loss of trapped ions in experiments is likely caused by collisions with molecules or ions other than helium. Therefore, the storage lifetime of the ions depends on the vacuum in the system and the impurities in the helium gas. The helium gas used for the experiment in this study has a purity of $P_{purity=}$99.999%. The helium gas purity can be improved by a gas purifier such as a SAES getter to make $P_{impurity} = 1 - P_{purity}$ reach the ppb (parts per billion) level. The increased helium gas purity can improve the storage time of ions in the cooler and the laser spectroscopy ion trap. For reference, barium ions have been observed to have a storage lifetime above 500 seconds in the previous generation of linear Paul trap for barium tagging [GWD$^+$07, Gre10] which had the helium gas purified by a SAES purifier.

The experiments with the ion cooler prototype demonstrated the success of its design with the novel tapered quadrupole electrodes in ion cooling, trapping and ejection.

5.4 Ion temperature in the LPT

The ion time-of-flight (ToF) spread $\sigma_{t_{ToF}}$ is related to the trapped ions' positional spread σ_x and velocity spread σ_{v_x} as described in Section 3.6. The temperature of the trapped ions determines σ_x and σ_{v_x}.

Measurement of ion ejections without the effect of the charge buildup may be obtained from the final setup of the LPT system with the revised electrode holder at the exit of the cooler. In an ideal case, the ion temperature T_x in the longitudinal direction can be derived from the dependence of the ion ToF spread on the ion ejection electric field. Such dependence can be seen in the simulations of the ion buncher in Section 3.6.

In the following, the temperature of trapped $^{136}Ba^+$ ions in the cooler was obtained from simulations as discussed in Section 3.5.3 (the charge buildup problem was not considered in the simulations). The simulation was done at the designed cooler operating parameter of RF frequency $f_{RF} =$ 1 MHz with 0.1 mbar of helium buffer gas. The result is shown in Figure 5.35. The ion temperatures are similar to the simulation results of the ion buncher as shown in Figure 3.31.

The temperature T_y and T_z in the transverse directions of the ions cooled

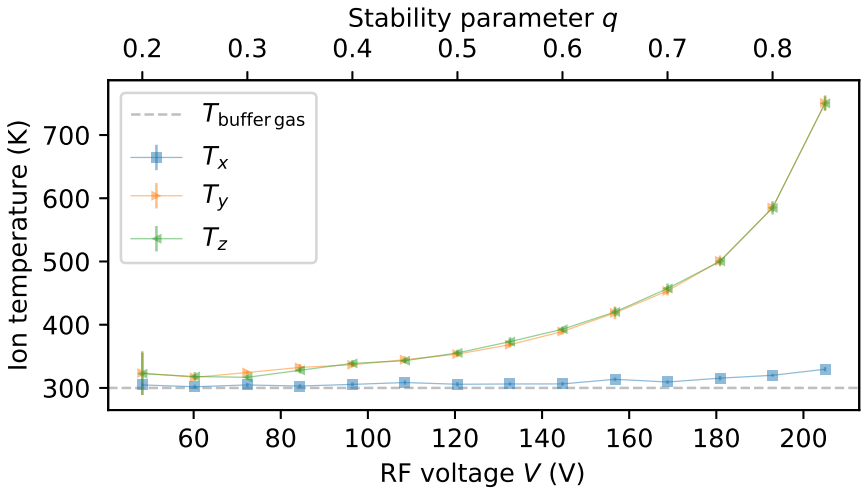

Figure 5.35: Temperature of $^{136}Ba^{+}$ ions trapped in the cooler with different RF voltage obtained from simulation.

and trapped inside the cooler was found to be below 400 K when the RF voltage V is below 150 V. In the longitudinal direction, the ion temperature T_x is always close to the buffer gas temperature. These ion temperatures meet the requirement of the cooler in the LPT system.

5.5 The final LPT system

The machining of the LPT parts was completed as of November 2019. These parts include everything needed for the final LPT system except the cooler and the laser spectroscopy ion trap (LSIT). From the experience of the cooler prototype, the 3D printed parts were found to be good enough for the final LPT in terms of vacuum compatibility and mechanical precision. Therefore we decided to 3D print the parts for the cooler and the LSIT for the final LPT system as well.

The revised design of the electrode holder at the exit of the cooler was used for the final LPT system to mitigate the charge buildup problem as discussed in Section 5.3.3.

The final LPT system has been partially assembled at McGill University. The electronics, control and DAQ system described in this chapter will be used and further improved.

The LPT system will be tested and commissioned as a standalone setup first. Once completed, it will be installed in between the RF el and the MR-TOF mass spectrometer to systematically study the ions extracted from the RF funnel. The lasers and a fluorescent light detector will be installed at a later stage for the barium ion identification. If successful, the LPT can be used as a part of the setup for the barium tagging purpose of nEXO.

Chapter 6

Conclusion and future work

A linear Paul trap (LPT) has been developed for barium tagging in gaseous xenon. The LPT can be used for the nEXO if the barium ions can be successfully extracted from the liquid xenon through a cold probe or a capillary. Through barium tagging, nEXO can identify and consequently reject all non-$\beta\beta$ background, therefore greatly improve the sensitivity in the search for $0\nu\beta\beta$.

For this study, the theory of ion trapping in an ideal radio frequency quadrupole (RFQ) has been derived from first principles. An analytical method was developed to describe the ion confinement and ion acceptance in the ideal RFQ. The mass resolving power and ion transmission efficiency for an ideal quadrupole mass filter (QMF) were solved analytically. The analytical results were also used to validate a simulation method.

The validated simulation method was used to study the effect of the non-ideal electric potential in a realistic RFQ. The impact of the electric potential's higher-order spatial harmonics was studied in detail. These simulations led to the optimum design and operating parameters of an RFQ ion guide, a QMF and an RFQ ion cooler/buncher.

The temperature of trapped ions in an LPT was studied via simulation and was found to be anisotropic. The ion temperature in the longitudinal direction was found to be mostly close to the helium buffer gas temperature. In the transverse directions, the ion temperature is close to the helium gas temperature at a small stability value $q \leq 0.3$; while, when the q value approaches 0.9, the ion temperature increases several fold. The trapping depth, either in the longitudinal or transverse directions, was found to have a small or non-existent effect on the ion temperature. However, the longitudinal trapping potential was found to cause an expelling potential in the transverse direction and can lead to ion loss if too strong. The effect of the expelling potential was observed in simulations and agreed with the theory.

A LPT system was designed based on optimizations in simulations. The designed LPT has phase independent acceptance large enough to capture or transmit at least 99% of ions from the RF funnel.

Practical considerations were taken into account for the mechanical design of the LPT along with its vacuum system. The major components of the LPT consist of a QMF with a specially designed monolithic electrode holder to reduce mechanical error during assembly, a cooler with a novel design of the quadrupole electrode to form the drag field and a laser spectroscopy ion trap which can also work as an ion buncher.

The mechanical drawings of the LPT system were sent for manufacturing at the Physics department machine shop of the Université de Montréal. In the meantime, prototypes of the QMF and the cooler were made to validate the designs and for the development of the electronics, control and DAQ (data acquisition) systems.

Three prototypes of the QMF were built and tested, each of which showed the expected ion transmission properties at the tested RF voltages and frequencies. It was shown that the final prototype of the QMF, the QMF2.2, has the best achievable mass resolving power $R \approx 140$ which exceeds the requirement of $R \approx 80$. When operating in ion guide mode, the absolute ion transmission efficiency was preliminarily measured to be $T \approx 89\%$. The electronics, control and DAQ systems were developed along with the QMF prototypes.

A prototype of the cooler with the novel quadrupole electrodes was manufactured mostly via 3D printed parts. Measurements with the cooler revealed its capability of working as a low-resolution QMF with a maximum mass resolving power $R \approx 20$ at helium gas pressure up to 1.9×10^{-2} mbar. Successful ion cooling, trapping and ejection were demonstrated by the cooler prototype. The cooler can cool down injected ions with energy spread $\Delta E_{inj} \approx 20\,\text{eV}$ at 1.9×10^{-2} mbar helium gas pressure, and $\Delta E_{inj} \approx 100\,\text{eV}$ at 0.1 mbar helium gas pressure.

The ejected ions' time-of-flight (ToF) of the cooler prototype was found to agree with simulations qualitatively. The discrepancies were found to be caused by a charge buildup on the electrode holder at the exit of the cooler. A revised design of the electrode holder was 3D printed for the final setup of the LPT system. After modifications to the design, it is expected that the charge buildup in the final LPT system is eliminated. The ion temperature T_x in the longitudinal direction can be obtained by analyzing the measured and simulated ions' ToF dependence of the electric field.

The ion storage lifetime in the cooler prototype was measured to be $\tau = 16.9\,\mathrm{s}$ which is long enough for the barium ion identification via laser spectroscopy. It is expected that the ion storage lifetime can be significantly increased by purifying the helium gas in the final LPT system.

The final LPT system with improvements based on the prototypes is being set up at McGill University. The LPT will be first tested and commissioned as a standalone system. Then the LPT will be combined with the RF funnel, MR-TOF and the laser spectroscopy setup for a systematic study of barium ion extraction and identification. If successful, the LPT can be a part of the setup for the barium tagging purposes of nEXO.

Bibliography

[AAA+02] QR Ahmad, RC Allen, TC Andersen, JD Anglin, JC Barton, EW Beier, M Bercovitch, J Bigu, SD Biller, RA Black, et al. Direct evidence for neutrino flavor transformation from neutral-current interactions in the Sudbury Neutrino Observatory. *Physical Review Letters*, 89(1):011301, 2002.

[AAA+11] N Ackerman, B Aharmim, M Auger, DJ Auty, PS Barbeau, K Barry, L Bartoszek, E Beauchamp, V Belov, C Benitez-Medina, et al. Observation of Two-Neutrino Double-Beta Decay in Xe 136 with the EXO-200 Detector. *Physical Review Letters*, 107(21):212501, 2011.

[AAA+12] K Abe, N Abgrall, Y Ajima, H Aihara, JB Albert, C Andreopoulos, B Andrieu, MD Anerella, S Aoki, O Araoka, et al. First muon-neutrino disappearance study with an off-axis beam. *Physical Review D*, 85(3):031103, 2012.

[AAA+18a] N Aghanim, Y Akrami, M Ashdown, J Aumont, C Baccigalupi, M Ballardini, AJ Banday, RB Barreiro, N Bartolo, S Basak, et al. Planck 2018 results. VI. Cosmological parameters. *arXiv preprint arXiv:1807.06209*, 2018.

[AAA+18b] JB Albert, G Anton, IJ Arnquist, I Badhrees, P Barbeau, D Beck, V Belov, F Bourque, JP Brodsky, E Brown, et al. Sensitivity and discovery potential of the proposed nEXO experiment to neutrinoless double-β decay. *Physical Review C*, 97(6):065503, 2018.

[AAA+19] M Aker, K Altenmüller, M Arenz, M Babutzka, J Barrett, S Bauer, M Beck, A Beglarian, J Behrens, T Bergmann, et al. Improved upper limit on the neutrino mass from a direct kinematic method by KATRIN. *Physical Review Letters*, 123(22):221802, 2019.

[AAB+12] M Auger, DJ Auty, PS Barbeau, L Bartoszek, E Baussan, E Beauchamp, C Benitez-Medina, M Breidenbach, D Chauhan, B Cleveland, et al. The EXO-200 detector, part I: detector design and construction. *Journal of Instrumentation*, 7(05):P05010, 2012.

[ABB+11] VN Aseev, AI Belesev, AI Berlev, EV Geraskin, AA Golubev, NA Likhovid, VM Lobashev, AA Nozik, VS Pantuev, VI Parfenov, et al. Upper limit on the electron antineutrino mass from the Troitsk experiment. *Physical Review D*, 84(11):112003, 2011.

[ABB+19] G Anton, I Badhrees, PS Barbeau, D Beck, V Belov, T Bhatta, M Breidenbach, T Brunner, GF Cao, WR Cen, et al. Search for Neutrinoless Double-β Decay with the Complete EXO-200 Dataset. *Physical Review Letters*, 123(16):161802, 2019.

[AFG+04] I Podadera Aliseda, T Fritioff, T Giles, A Jokinen, M Lindroos, and F Wenander. Design of a second generation RFQ Ion Cooler and Buncher (RFQCB) for ISOLDE. *Nuclear Physics A*, 746:647–650, 2004.

[AHL76] WE Austin, AE Holme, and JH Leck. The mass filter: Design and performance. In *Quadrupole mass spectrometry and its applications*. Elsevier, 1976.

[AIEE08] Frank T Avignone III, Steven R Elliott, and Jonathan Engel. Double beta decay, Majorana neutrinos, and neutrino mass. *Reviews of Modern Physics*, 80(2):481, 2008.

[Bar14] Bradley Ryan Barquest. *An advanced ion guide for beam cooling and bunching for collinear laser spectroscopy of rare isotopes*. PhD thesis, Michigan State University, 2014.

[Ber14] José Bernabeu. On the history of the PMNS Matrix... with today's perspective. *Nuovo Cimento. C (Print)*, 37(3):145–154, 2014.

[BFV+15] Thomas Brunner, Daniel Fudenberg, Victor Varentsov, Amanda Sabourov, Giorgio Gratta, Jens Dilling, Ralph DeVoe, David Sinclair, W Fairbank, Joshua B Albert, et al. An RF-only ion-funnel for extraction from high-pressure gases.

International Journal of Mass Spectrometry, 379:110–120, 2015.

[BK18] A Baha Balantekin and Boris Kayser. On the properties of neutrinos. *Annual Review of Nuclear and Particle Science*, 68:313–338, 2018.

[BKQW89] R Blümel, C Kappler, W Quint, and H Walther. Chaos and order of laser-cooled ions in a Paul trap. *Physical Review A*, 40(2):808, 1989.

[Bru68] Wilson M Brubaker. An improved quadrupole mass analyzer. *Adv. Mass Spectrom*, 4:293–299, 1968.

[BSB+12] T Brunner, MJ Smith, M Brodeur, S Ettenauer, AT Gallant, Vanessa V Simon, A Chaudhuri, A Lapierre, E Mané, R Ringle, et al. TITAN's digital RFQ ion beam cooler and buncher, operation and performance. *Nuclear Instruments and Methods in Physics Research Section A: Accelerators, Spectrometers, Detectors and Associated Equipment*, 676:32–43, 2012.

[c+14] EXO-200 collaboration et al. Search for Majorana neutrinos with the first two years of EXO-200 data. *Nature*, 510(7504):229–234, 2014.

[Car18] L Cardani. Neutrinoless Double Beta Decay Overview. *SciPost Phys. Proc.*, 1(arXiv: 1810.12828):024, 2018.

[CDDJ+98] Bruce T Cleveland, Timothy Daily, Raymond Davis Jr, James R Distel, Kenneth Lande, CK Lee, Paul S Wildenhain, and Jack Ullman. Measurement of the solar electron neutrino flux with the Homestake chlorine detector. *The Astrophysical Journal*, 496(1):505, 1998.

[CFL+14] F Capozzi, GL Fogli, E Lisi, A Marrone, D Montanino, and A Palazzo. Status of three-neutrino oscillation parameters, circa 2013. *Physical Review D*, 89(9):093018, 2014.

[Cho17] A Cho. The unbearable lightness of neutrinos. *Science (New York, NY)*, 356(6345):1322, 2017.

[CWF+19] C Chambers, T Walton, D Fairbank, A Craycraft, DR Yahne, J Todd, A Iverson, W Fairbank, A Alamre, JB Albert, et al.

Imaging individual barium atoms in solid xenon for barium tagging in nEXO. *Nature*, 569(7755):203–+, 2019.

[D10] D and D Dahl. SIMION 8 3-D electrostatic and charged particle trajectory simulation program. *Idaho National Laboratory, distributed by Scientific Instrument Services Inc., Ringoes, NJ, USA*, 2010.

[Daw75] PH Dawson. The acceptance of the quadrupole mass filter. *International Journal of Mass Spectrometry and Ion Physics*, 17(4):423–445, 1975.

[DDD+00] M Danilov, R DeVoe, A Dolgolenko, G Giannini, G Gratta, P Picchi, A Piepke, F Pietropaolo, P Vogel, JL Vuilleumier, et al. Detection of very small neutrino masses in double-beta decay using laser tagging. *Physics Letters B*, 480(1-2):12–18, 2000.

[Deh68] Hans G Dehmelt. Radiofrequency spectroscopy of stored ions I: Storage. In *Advances in atomic and molecular physics*, volume 3, pages 53–72. Elsevier, 1968.

[DGG+62] Gaillard Danby, JM Gaillard, Konstantin Goulianos, LM Lederman, N Mistry, M Schwartz, and J Steinberger. Observation of high-energy neutrino reactions and the existence of two kinds of neutrinos. *Physical Review Letters*, 9(1):36, 1962.

[DGKS99] DJ Douglas, TA Glebova, NV Konenkov, and M Yu Sudakov. Spatial harmonics of the field in a quadrupole mass filter with circular electrodes. *Technical Physics*, 44(10):1215–1219, 1999.

[Die12] Maria Montero Diez. *Development of a Resonance Ionization Spectroscopy Ion-transport Probe for the Enriched Xenon Observatory*. PhD thesis, Stanford University, 2012.

[DK02] DJ Douglas and NV Konenkov. Influence of the 6th and 10th spatial harmonics on the peak shape of a quadrupole mass filter with round rods. *Rapid communications in mass spectrometry*, 16(15):1425–1431, 2002.

[DK06] L Ding and S Kumashiro. Ion motion in the rectangular wave quadrupole field and digital operation mode of a quadrupole ion trap mass spectrometer. *Rapid Communications in*

Mass Spectrometry: An International Journal Devoted to the Rapid Dissemination of Up-to-the-Minute Research in Mass Spectrometry, 20(1):3–8, 2006.

[DMVV16] Stefano Dell'Oro, Simone Marcocci, Matteo Viel, and Francesco Vissani. Neutrinoless double beta decay: 2015 review. *Advances in High Energy Physics*, 2016.

[Dou09] DJ Douglas. Linear quadrupoles in mass spectrometry. *Mass spectrometry reviews*, 28(6):937–960, 2009.

[DPR19] Michelle J Dolinski, Alan WP Poon, and Werner Rodejohann. Neutrinoless double-beta decay: status and prospects. *Annual Review of Nuclear and Particle Science*, 69:219–251, 2019.

[DSB+04] Li Ding, Michael Sudakov, Francesco L Brancia, Roger Giles, and Sumio Kumashiro. A digital ion trap mass spectrometer coupled with atmospheric pressure ion sources. *Journal of Mass Spectrometry*, 39(5):471–484, 2004.

[EEF+03] KamLAND Eguchi, S Enomoto, K Furuno, J Goldman, H Hanada, H Ikeda, K Ikeda, K Inoue, K Ishihara, W Itoh, et al. First results from KamLAND: evidence for reactor antineutrino disappearance. *Physical Review Letters*, 90(2):021802, 2003.

[FGW+07] B Flatt, M Green, J Wodin, R DeVoe, P Fierlinger, G Gratta, F LePort, M Montero Díez, R Neilson, K O' Sullivan, et al. A linear RFQ ion trap for the Enriched Xenon Observatory. *Nuclear Instruments and Methods in Physics Research Section A: Accelerators, Spectrometers, Detectors and Associated Equipment*, 578(2):399–408, 2007.

[FHI+98a] Y Fukuda, T Hayakawa, E Ichihara, K Inoue, K Ishihara, H Ishino, Y Itow, T Kajita, J Kameda, S Kasuga, et al. Study of the atmospheric neutrino flux in the multi-GeV energy range. *Physics Letters B*, 436(1):33–41, 1998.

[FHI+98b] Y Fukuda, T Hayakawa, E Ichihara, K Inoue, K Ishihara, Hirokazu Ishino, Y Itow, T Kajita, J Kameda, S Kasuga, et al. Evidence for oscillation of atmospheric neutrinos. *Physical Review Letters*, 81(8):1562, 1998.

[Fud15] Daniel Fudenberg. Private Communication, 2015.

[Fud18] Daniel Fudenberg. *Improved discrimination for neutrinoless double beta decay searches with EXO-200 and nEXO.* PhD thesis, Stanford University, 2018.

[Gha96] Dezfuli AM Ghalambor. *Injection, cooling, and extraction of ions from a very large Paul trap.* PhD thesis, McGill University, 1996.

[GP12] Andrea Giuliani and Alfredo Poves. Neutrinoless double-beta decay. *Advances in High Energy Physics*, 2012.

[Gre10] Matthew Piron Green. *On Ion Probes and Traps: Barium Tagging for the EXO Double Beta Decay Detector.* PhD thesis, Stanford University, 2010.

[GT01] John Raymond Gibson and Stephen Taylor. Numerical investigation of the effect of electrode size on the behaviour of quadrupole mass filters. *Rapid Communications in Mass Spectrometry*, 15(20):1960–1964, 2001.

[GWD+07] M Green, J Wodin, R DeVoe, P Fierlinger, B Flatt, G Gratta, F LePort, M Montero Díez, R Neilson, K OSullivan, et al. Observation of single collisionally cooled trapped ions in a buffer gas. *Physical Review A*, 76(2):023404, 2007.

[Hal12] Kendy Hall. *In-situ laser tagging of barium ions in liquid xenon for the EXO experiment.* PhD thesis, Colorado State University, 2012.

[HDK+01] F Herfurth, J Dilling, A Kellerbauer, G Bollen, S Henry, H-J Kluge, Emily Lamour, D Lunney, RB Moore, C Scheidenberger, et al. A linear radiofrequency ion trap for accumulation, bunching, and emittance improvement of radioactive ion beams. *Nuclear Instruments and Methods in Physics Research Section A: Accelerators, Spectrometers, Detectors and Associated Equipment*, 469(2):254–275, 2001.

[Jen04] Shie-Chang Jeng. *New fluorescence technique to search for neutrino masses by identification of double beta decay barium-136 ion daughters in liquid xenon.* PhD thesis, Colorado State University, 2004.

[KAA+18] S Al Kharusi, A Alamre, JB Albert, M Alfaris, G Anton, IJ Arnquist, I Badhrees, PS Barbeau, D Beck, V Belov, et al. nEXO pre-conceptual design report. *arXiv preprint arXiv:1805.11142*, 2018.

[KBB+05] Ch Kraus, B Bornschein, L Bornschein, J Bonn, B Flatt, A Kovalik, B Ostrick, EW Otten, JP Schall, Th Thümmler, et al. Final results from phase II of the Mainz neutrino mass searchin tritium decay. *The European Physical Journal C-Particles and Fields*, 40(4):447–468, 2005.

[KI12] J Kotila and F Iachello. Phase-space factors for double-β decay. *Physical Review C*, 85(3):034316, 2012.

[Kil15] Ryan Scott Killick. Observation of Singly Charged Barium Ions in a Buffer Gas: Towards a Functional Barium-Tagging System for Use in the Enriched Xenon Observatory. Master's thesis, Carleton University, 2015.

[Kim97] Taeman Kim. *Buffer gas cooling of ions in a radio frequency quadrupole ion guide: a study of the cooling process and cooled beam properties*. PhD thesis, McGill University, 1997.

[KP15] Alexander Kuhlicke and Heather Partner. Nano-probes and Nano-particles. `https://www.physik.hu-berlin.de/de/nano/forschung/nanoprobesparticles`, 2015. [Online; accessed 14-July-2017].

[KSP+10] Thomas Kolling, Andreas Schlemmer, Clemens Pietzonka, Bernd Harbrecht, and Karl-Michael Weitzel. Field effects in alkali ion emitters: Transition from Langmuir–Child to Schottky regime. *Journal of Applied Physics*, 107(1):014105, 2010.

[KUA+01] K Kodama, N Ushida, C Andreopoulos, N Saoulidou, G Tzanakos, P Yager, B Baller, D Boehnlein, W Freeman, B Lundberg, et al. Observation of tau neutrino interactions. *Physics Letters B*, 504(3):218–224, 2001.

[Lan18a] Yang Lan. Linear Paul trap design requirement: ion acceptance and mechanical tolerance. Unpublished manuscript, 2018.

[Lan18b] Yang Lan. TRI-DN-17-34 A Linear Paul Trap for Identification of Barium Ions. TRIUMF design note, 2018.

[LBM92] MDN Lunney, F Buchinger, and RB Moore. The Temperature of buffer-gas cooled ions in a Paul trap. *Journal of Modern Optics*, 39(2):349–360, 1992.

[Lun92] Matthew David Norwood Lunney. *The phase space volume of ion clouds in Paul traps*. PhD thesis, McGill University, 1992.

[LW16] Y Lan and CE Waltham. Acoustic Modeling and Optimization of the Xiao. *Acta Acustica united with Acustica*, 102(6):1128–1137, 2016.

[LWY71] GE Lee-Whiting and L Yamazaki. Semi-analytical calculations for circular quadrupoles. *Nuclear Instruments and Methods*, 94(2):319–332, 1971.

[MAA+06] DG Michael, P Adamson, T Alexopoulos, WWM Allison, GJ Alner, K Anderson, C Andreopoulos, M Andrews, R Andrews, KE Arms, et al. Observation of muon neutrino disappearance with the MINOS detectors in the NuMI neutrino beam. *Physical Review Letters*, 97(19):191801, 2006.

[Man07] D Manura. Additional notes on the SIMION hs1 collision model. *Scientific Instrument Services*, 2007.

[McL51] Norman W McLachlan. *Theory and application of Mathieu functions*. Clarendon Press, 1951.

[MCW+15] B Mong, S Cook, T Walton, C Chambers, A Craycraft, C Benitez-Medina, K Hall, W Fairbank Jr, JB Albert, DJ Auty, et al. Spectroscopy of Ba and Ba+ deposits in solid xenon for barium tagging in nEXO. *Physical Review A*, 91(2):022505, 2015.

[MD68] FG Major and HG Dehmelt. Exchange-collision technique for the rf spectroscopy of stored ions. *Physical Review*, 170(1):91, 1968.

[MDCG09] John H Moore, Christopher C Davis, Michael A Coplan, and Sandra C Greer. *Building scientific apparatus*. Cambridge University Press, 2009.

[ME13] MT Mustonen and J Engel. Large-scale calculations of the double-β decay of 76 Ge, 130 Te, 136 Xe, and 150 Nd in the

deformed self-consistent Skyrme quasiparticle random-phase approximation. *Physical Review C*, 87(6):064302, 2013.

[Moe91] MK Moe. Detection of neutrinoless double-beta decay. *Physical Review C*, 44(3):R931, 1991.

[MT05] Raymond E March and John F Todd. *Quadrupole ion trap mass spectrometry*, volume 165. John Wiley & Sons, 2005.

[NHJ+01] A Nieminen, J Huikari, A Jokinen, J Äystö, P Campbell, ECA Cochrane, Exotraps Collaboration, et al. Beam cooler for low-energy radioactive ions. *Nuclear Instruments and Methods in Physics Research Section A: Accelerators, Spectrometers, Detectors and Associated Equipment*, 469(2):244–253, 2001.

[NHTD80] W Neuhauser, M Hohenstatt, PE Toschek, and H Dehmelt. Localized visible Ba+ mono-ion oscillator. *Physical Review A*, 22(3):1137, 1980.

[Pau30] Wolfgang Pauli. Dear radioactive ladies and gentlemen. *Phys. Today*, 31:27, 1930.

[PRVZ58] Wolfgang Paul, HP Reinhard, and U Von Zahn. Das elektrische massenfilter als massenspektrometer und isotopentrenner. *Zeitschrift für Physik*, 152(2):143–182, 1958.

[PS53] Wolfgang Paul and Helmut Steinwedel. Ein neues massenspektrometer ohne magnetfeld. *Zeitschrift für Naturforschung A*, 8(7):448–450, 1953.

[PS78] AN Pargellis and M Seidl. Thermionic emission of alkali ions from zeolites. *Journal of Applied Physics*, 49(9):4933–4938, 1978.

[PWM+91] JD Prestage, A Williams, L Maleki, MJ Djomehri, and E Harabetian. Dynamics of charged particles in a Paul radio-frequency quadrupole trap. *Physical Review Letters*, 66(23):2964, 1991.

[RC56] Frederick Reines and Clyde L Cowan. The neutrino. *Nature*, 178(4531):446–449, 1956.

[RHH73] JA Richards, RM Huey, and J Hiller. A new operating mode for the quadrupole mass filter. *International Journal of Mass Spectrometry and Ion Physics*, 12(4):317–339, 1973.

[Rol11] Etienne Rollin. *Barium Ion Extraction and Identification from Laser Induced Fluorescence in Gas for the Enriched Xenon Observatory*. PhD thesis, Carleton University Ottawa, 2011.

[RSM+96] AJ Reuben, GB Smith, P Moses, AV Vagov, MD Woods, DB Gordon, and RW Munn. Ion trajectories in exactly determined quadrupole fields. *International Journal of Mass Spectrometry and Ion Processes*, 154(1-2):43–59, 1996.

[RZS05] Vladimir L Ryjkov, XianZhen Zhao, and Hans A Schuessler. Simulations of the rf heating rates in a linear quadrupole ion trap. *Physical Review A*, 71(3):033414, 2005.

[SBR+16] S Schwarz, G Bollen, R Ringle, J Savory, and P Schury. The LEBIT ion cooler and buncher. *Nuclear Instruments and Methods in Physics Research Section A: Accelerators, Spectrometers, Detectors and Associated Equipment*, 816:131–141, 2016.

[Sch06] Stefan Schwarz. IonCool - A versitile code to characterize gas-filled ion bunchers and coolers (not only) for nuclear physics applications. *Nuclear Instruments and Methods in Physics Research Section A: Accelerators, Spectrometers, Detectors and Associated Equipment*, 566(2):233–243, 2006.

[SGSP99] Ernst P Sheretov, Victor S Gurov, Michael P Safonov, and Igor W Philippov. Hyperboloid mass spectrometers for space exploration. *International Journal of Mass Spectrometry*, 189(1):9–17, 1999.

[SKHG+03] F Schmidt-Kaler, H Häffner, S Gulde, M Riebe, GPT Lancaster, T Deuschle, C Becher, W Hänsel, J Eschner, CF Roos, et al. How to realize a universal quantum gate with trapped ions. *Applied Physics B*, 77(8):789–796, 2003.

[SM13] Sabin Stoica and Mihail Mirea. New calculations for phase space factors involved in double-β decay. *Physical Review C*, 88(3):037303, 2013.

[Smi05] Mathew Smith. *A square-wave-driven radiofrequency quadrupole cooler and buncher for TITAN*. PhD thesis, University of British Columbia, 2005.

[TKD+14] K Twelker, S Kravitz, M Montero Díez, G Gratta, W Fairbank Jr, JB Albert, DJ Auty, PS Barbeau, D Beck, C Benitez-Medina, et al. An apparatus to manipulate and identify individual Ba ions from bulk liquid Xe. *Review of Scientific Instruments*, 85(9):095114, 2014.

[VM95] LA Viehland and EA Mason. Transport properties of gaseous ions over a wide energy range, IV. *Atomic Data and Nuclear Data Tables*, 60(1):37–95, 1995.

[Wal05] Samuel J Waldman. *Single ion trapping for the Enriched Xenon Observatory*. PhD thesis, Stanford University, 2005.

[Wal16] Josiah Walton. *The search for majoron emission in xenon-136 and two-neutrino double-beta decay of xenon-134 with the Enriched Xenon Observatory*. PhD thesis, University of Illinois at Urbana-Champaign, 2016.

[Wam07a] Kolo Wamba. *Aspects of the R&D for the Enriched Xenon Observatory for double beta decay*. PhD thesis, Stanford University, 2007.

[Wam07b] Kolo Wamba. *Identification of single barium atoms with resonance ionization mass spectroscopy for the nEXO neutrinoless double beta decay experiment*. PhD thesis, Stanford University, 2007.

[Wat19] Jacob Gary Watkins. Background Reduction for Improved Sensitivity at the Enriched Xenon Observatory through advancements in Barium-Tagging Simulations, Prediction and Prevention of High-Voltage Breakdown in Liquid Xenon Time-Projection Chambers, and Event Classification using Ensemble Methods and Machine Learning. Master's thesis, Carleton University, 2019.

[Web20a] WebElements. Collision Model HS1. `https://www.webelements.com/helium/atom_sizes.html`, 2020. [Online; accessed 14-January-2020].

[Web20b] WebElements. Collision Model HS1. `https://www.webelements.com/barium/atom_sizes.html`, 2020. [Online; accessed 14-January-2020].

[Whe74] N Rey Whetten. Macroscopic particle motion in quadrupole fields. *Journal of Vacuum Science and Technology*, 11(2):515–518, 1974.

[WSL59] Ralph F Wuerker, Haywood Shelton, and RV Langmuir. Electrodynamic containment of charged particles. *Journal of Applied Physics*, 30(3):342–349, 1959.

Appendix A

QMF prototypes

A few prototypes of the QMF were built and tested. Other than validating the design of the QMF itself, these prototypes also facilitate the development of the RF, electronics, control and DAQ system for the experimental setup. The manufacturing, installation and tests with the first two prototypes QMF1 and QMF2.1 are described in this appendix. The final prototype QMF2.2 is described in Section 5.2.1.

A.1 Prototype QMF1

The first prototype of the QMF (QMF1) was made mainly to test the machining procedure and the mechanical rigidity of the specially designed monolithic QMF holder. The machining procedure and the rigidity had been a concern about the design, while the machining of such a holder using a CNC milling machine can be time consuming and expensive.

A.1.1 QMF1 machining

An acrylic rod was used to make this prototype to reduce the material cost, also to make the internal structure visible for demonstration purposes. Due to the limitation in tools, 3/8 inch diameter rods were used for making the quadrupole electrodes and the QMF was scaled up by a factor of 6/5 in the radial direction compared to the design in Section 4.3. The machining was done by the author in the UBC Physics and Astronomy student machine shop using a manual vertical milling machine as shown in Figure A.1. The main structure of the holder was formed by cutting the long and deep (29 mm) slots every 90°.

The openings at both ends of the holder were machined on a lathe, and the remaining block of material along the central axis was removed from the openings. The finished QMF holder is shown in Figure A.2(a). The electrodes were machined from commercially available tight-tolerance 3/8 inch

Figure A.1: Machining of the QMF1's monolithic holder.

stainless rods (McMaster-Carr 1255T16) and are shown in Figure A.2(a). The QMF1 after assembly is shown in Figure A.2(b).

The mechanical rigidity of the QMF holder was inspected manually by applying a force to different positions of the holder and observing the deformation. For the magnitude of force corresponding to the weight of the electrodes and force needed during the assembly, no deformation was observed. So the holder for QMF1 is rigid and strong enough for its purpose. In the later manufacturing of the QMF, a more vacuum friendly plastic material PEEK (polyether ether ketone) will be used. PEEK has a larger rigidity than the acrylic, so the design of the QMF meets the mechanical rigidity requirement. The mechanical tolerance of the QMF1 is discussed below.

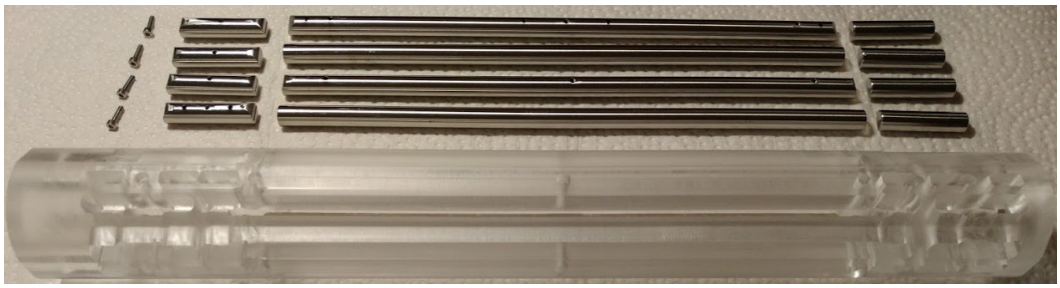

(a) Parts for the QMF1

(b) Assembled QMF1

Figure A.2: The first prototype QMF1 before and after assembly.

A.1.2 QMF1 mechanical precision measurement

Due to the limited performance of tools used for holding the acrylic rod during the machining process as shown in Figure A.1, the mechanical precision of the holder is not expected to be great. A method for measuring the positioning of the quadrupole electrodes in the QMF1 was devised and shown in Figure A.3(a).

The measurement method makes use of the high precision (5 µm) readout of a lathe to measure the position of the electrodes with a homemade probe. The probe is made of a long stainless steel rod with a smooth metal ball of similar diameter soldered to one end of the rod. The probe is installed on the tool holder of the lathe.

All the quadrupole electrodes were electrically connected by wires to one terminal of a multimeter, while the probe was connected to the other terminal. The resistance is measured between the probe and the electrodes. The probe is manually controlled to move along with the lathe's tool holder. Once the protruded metal ball on the probe touches the inner surface of

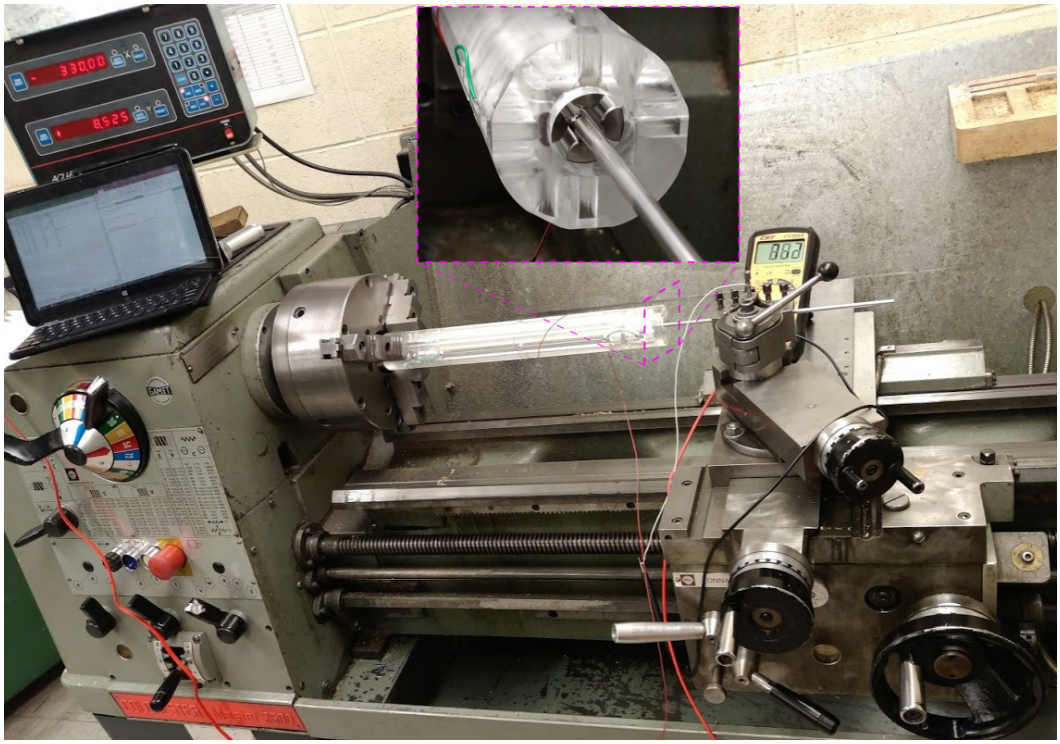

(a) Setup for measurement of quadrupole electrodes position

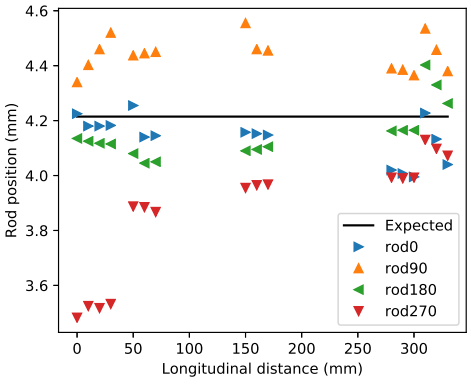

(b)

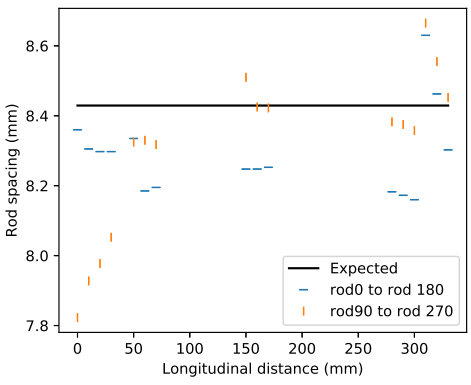

(c)

Figure A.3: A setup for measurement of QMF electrode positioning and mechanical tolerance.

an electrode, the resistance measured by the multimeter would change from infinity to zero and the multimeter would start beeping.

The horizontal coordinates of the electrode x and y are displayed on the digital readout of the lathe and recorded into an electronic spreadsheet. For every three electrodes on the same rotational angle, 16 measurements were done along the longitudinal direction x. The QMF were rotated every 90° to measure the position of all the electrodes. Before starting measurement for each rotation angle, the QMF were rotated slightly and checked with the probe to make sure of the exact alignment.

The measured position of the inner surface of the electrodes is shown in Figure A.3(b). The value of the vertical axis is the distance of the electrode's inner surface to the QMF's central axis. For every segment of the electrode, three or four measurements were made at different longitudinal positions. In the ideal situation, all the measured positions of the electrodes' inner surface should be $r_0^{QMF1} = 4.21$ mm as indicated by the black horizontal line in the same figure.

The measured positions for 7 out of the 12 electrodes appear to be reliable because they each appeared to be along a straight line, also indicating these 5 electrodes are aligned well with the QMF in the longitudinal direction x. If an electrode is not aligned well, the measured position will also reflect the cylindrical surface curvature of the electrodes.

The measured positions of the other 5 electrodes don't all appear to be caused by the misalignment of the electrodes, so human error might have been introduced during the measurement. The probe is easy to deflect once it touches the electrode, so the movement of the probe needs to be carefully and slowly controlled in order to get the exact coordinates of the electrode's inner surface. The measurement shown in Figure A.3(b) took 2 hours to complete. A slower measurement is expected to avoid these human introduced errors.

The distance between each diagonal pair of electrodes is shown in Figure A.3(c). Based on these results, the positioning of the QMF1 electrodes has a mechanical tolerance of about 0.3 mm and cannot meet the requirement as discussed in Section 4.1.3. The mechanical error mostly comes from the QMF holder, which had the mechanical precision limited both by the tools available in the student machine shop and the machining skills of the author. A QMF holder made by a professional machinist using a CNC mill may be able to meet the tolerance requirement.

A.1.3 Installation of QMF1 in test stand

The QMF1 was installed into the 6-way cross vacuum chamber of the test stand as shown in Figure A.4. The ion source and the ion detectors were installed in the same way as shown in Figure 5.5.

Part of the QMF was positioned in the tube of the 8" to 4.62" CF flange reducer as shown in Figure A.4(b) and (c). The positioning of the QMF relative to the vacuum chamber wasadjusted by the bolts attached to the QMF holder.

The configuration is the same as during the ion source and detectors test described in Section 5.1.3, except now the QMF1 is placed in between the ion source and the two detectors. The position of the QMF's exit was a few millimeters in front of the Faraday cup, and the CEM was still positioned a few millimeters behind the aperture on the bottom of the Faraday cup.

After sealing the vacuum chamber and pumping for two days, the vacuum level inside the chamber reached 4.8×10^{-6} mbar. The pressure is 20 times higher than when the vacuum chamber is empty. The increased pressure comes from the larger out-gassing rate of the acrylic material. However, the vacuum level is still suitable for the operation of a CEM ion detector for some ion transmission tests.

A.1.4 Ion transmission test

The ion transmission test was done with the QMF1. Due to its rough mechanical precision, the QMF was operated as an RFQ ion guide by applying only RF voltages.

The tests were done at the early stage of setting up the electronic system for the test stand. A low-cost two-channel signal generator SainSmart MHS5200A was used to directly supply RF voltage of up to 10 V (20 V peak-to-peak) to the QMF. The dual channels were set to have synchronized amplitude and the phases were set to be 180° different.

To make the best use of the signal generator, the RF amplitude was fixed to $V = 10$ V and the frequency f_{RF} were used as a scan parameter.

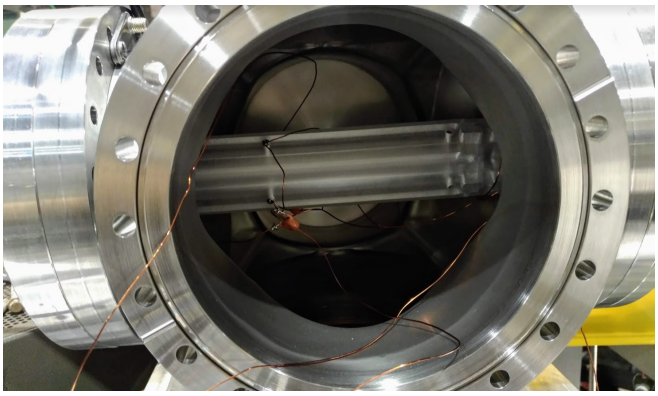

(a) Side view

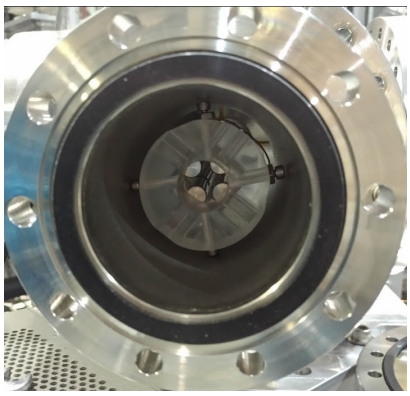

(b) View from ion entrance

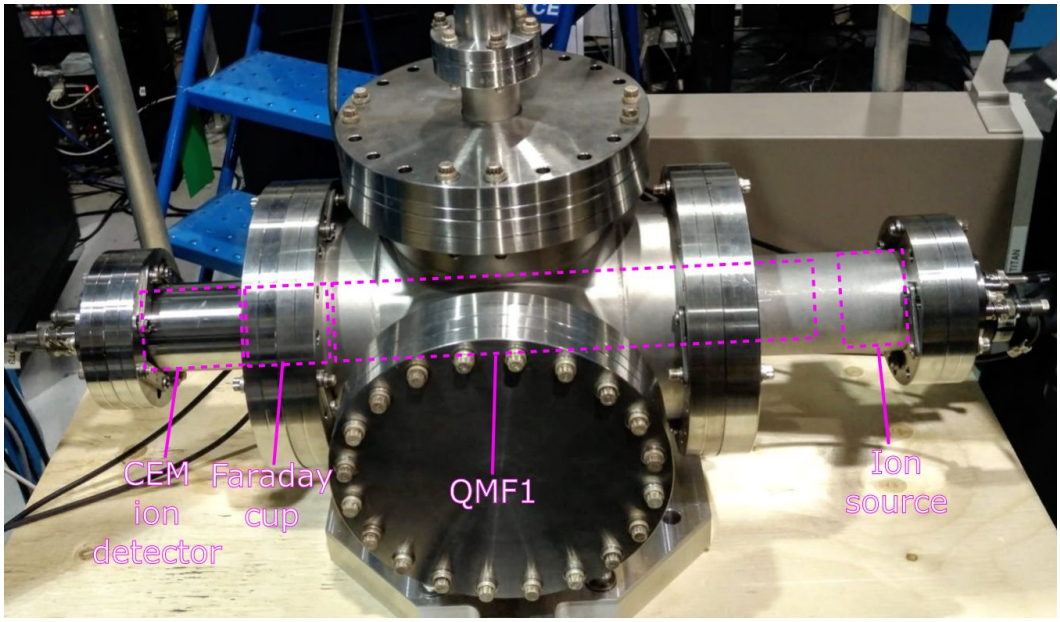

(c) Position of major components in the vacuum chamber

Figure A.4: Photos of the QMF1 installed in the vacuum chamber of the test stand. See text for details.

The RF frequency f_{RF} is related to the stability parameter q and the ion mass as defined in Eq. (2.8). The q value is calculated for the expected alkali ions from the ion source at a few RF frequencies as shown in Table A.1. The values between $0 < q < 0.908$ are emphasized in bold font to indicate that the ion can be transmitted. The maximum ion transmission is around $q = 0.6$ as shown in Figure 3.5.

Table A.1: Stability parameter q for different ions at a few RF frequencies. Values between 0 and 0.908 are emphasized in bold font.

f_{RF} (MHz) / Ion	0.2	0.3	0.4	0.5	1.0	1.1	1.4
^{7}Li	19.6	8.73	4.91	3.14	**0.79**	**0.64**	**0.40**
^{23}Na	6.00	2.66	1.50	0.96	**0.24**	**0.20**	**0.12**
^{39}K	3.54	1.57	**0.88**	**0.57**	**0.14**	**0.12**	**0.07**
^{85}Rb	1.62	**0.72**	**0.40**	**0.26**	**0.06**	**0.05**	**0.03**
^{133}Cs	1.04	**0.46**	**0.26**	**0.17**	**0.04**	**0.03**	**0.02**

The ion source was heated to 1.43 A and floated at 160 V. Ion transmission measurements were done with the RF frequency scanned from 0.1 MHz to 1.4 MHz by manual adjustment through the signal generator (this was before an automated control system had been built). The ion current in the Faraday cup was recorded and the results are shown in Figure A.5.

The Faraday cup was used with the adapter of a 1.6 mm diameter aperture to allow 0.7% of ions passing through to the CEM, the same as described in Section 5.1.3. The output signal from the CEM was amplified and sent to a digital oscilloscope. The ion count rate was displayed on the oscilloscope as the trigger rate of the ion pulse signals. The determined ion count rate is considered only rough estimations with large uncertainties because the oscilloscope trigger rate kept fluctuating. The result is also plotted in Figure A.5.

The results indicate that ion transmission occurred between the RF frequencies from 0.4 MHz to 1.1 MHz. Judging by the q value of ions in this frequency range, the ions transmitted are mainly ^{39}K. A smaller percentage of the other ions may also have been transmitted. There is no significant amount of ^{7}Li or ^{133}Cs ions because their presence would result in ion signals above 1.4 MHz or below 0.4 MHz.

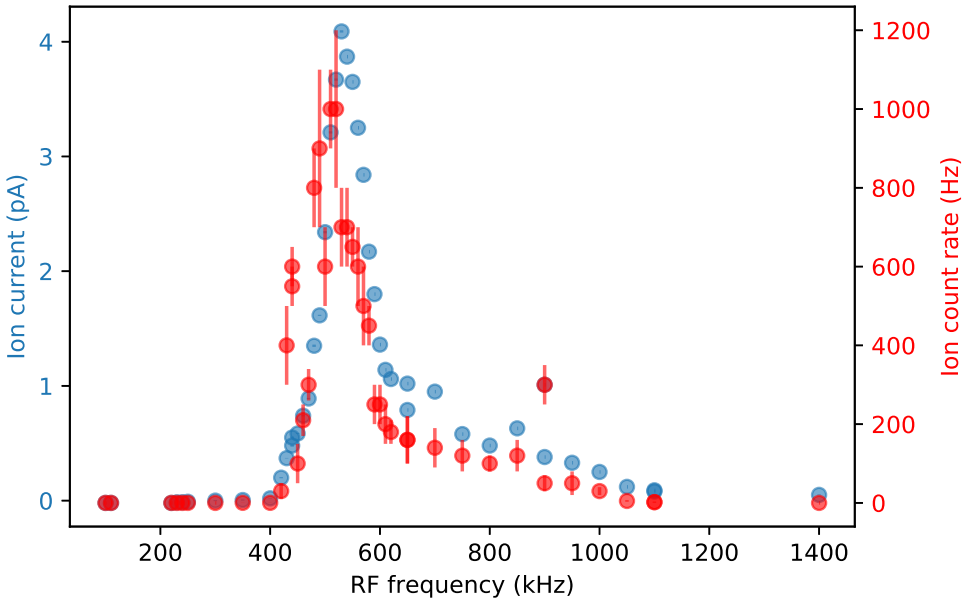

Figure A.5: Ion transmission test of QMSV1 with RF frequency scan.

A.1.5 Summary for QMF1

The mechanical rigidity and stability of the assembled QMF1 proved that the mechanical design for the QMF is viable. The design and drawings of the QMF were sent to the machine shop in the Physics department of the Universityé De Montréal for manufacturing.

The ion transmission tests proved that the QMF1 can be operated as an RFQ ion guide even with its electrode's positional mechanical precision of 0.3 mm. Even though the QMF1 was operating at a low RF voltage (10 V), ion transmissions were observed at the expected frequencies and q values. Ion source #1 was identified as mainly emitting ^{39}K ions.

These ion transmission tests were done in a preliminary manner during an early stage of setting up the electronics, signal processing and data acquisition (DAQ) for the development of the LPT system. The control and DAQ system for the test stand was developed along with other prototypes later, as described in the next sections.

A.2 QMF V2.1

The next QMF prototype, QMF2.1, was built with the aim of a better mechanical precision to reduce the electric potential distortion inside the quadrupole electrodes. It also had exactly the same quadrupole electrode geometry as the formal design, as described in Section 4.3.

A.2.1 QMF2.1 design and machining

From the author's experience of machining the QMF holder for QMF1, higher mechanical precision is difficult to achieve for the design using a manual milling machine with the limited tools. So, a different design was made for the next QMF prototypes. The holding structure of these prototypes consist of separate parts and each of them is easier to machine. This design also leads to a reduced amount of material for the holders. So the vacuum friendly plastic PEEK was used as the material for these holders.

Machining of the parts for QMF2.1 was done by the author in the TRIUMF ISAC-II machine shop. The machining procedure for one of the holders using a vertical milling machine is shown in Figure A.6. The four round holes used for holding the electrodes were formed with a standard 5/16 inch diameter end mill cutter. The position of these four holes was precisely determined by moving the holder along with the milling machine's bed. The horizontal coordinates x and y were displayed on a digital readout with a resolution of 0.0002 inch (5 µm). The position readings are repeatable and hence, reliable according to multiple calibrations done to the edge of the holder. The position of the holes is estimated to have precision within 10 µm.

The holders were then machined on a lathe to have the material along the central axis removed. As much as possible of the material was removed to expose the surface of the electrode while making sure the holder can still hold the electrodes accurately. The purpose is to make the holders have a large distance to the central axis where ions pass through, because such insulating materials are known to get charge buildup from ion deposition which distorts the electric potential in the center of the quadrupole electrodes.

The finished holders were shown in Figure A.7(a) along with the elec-

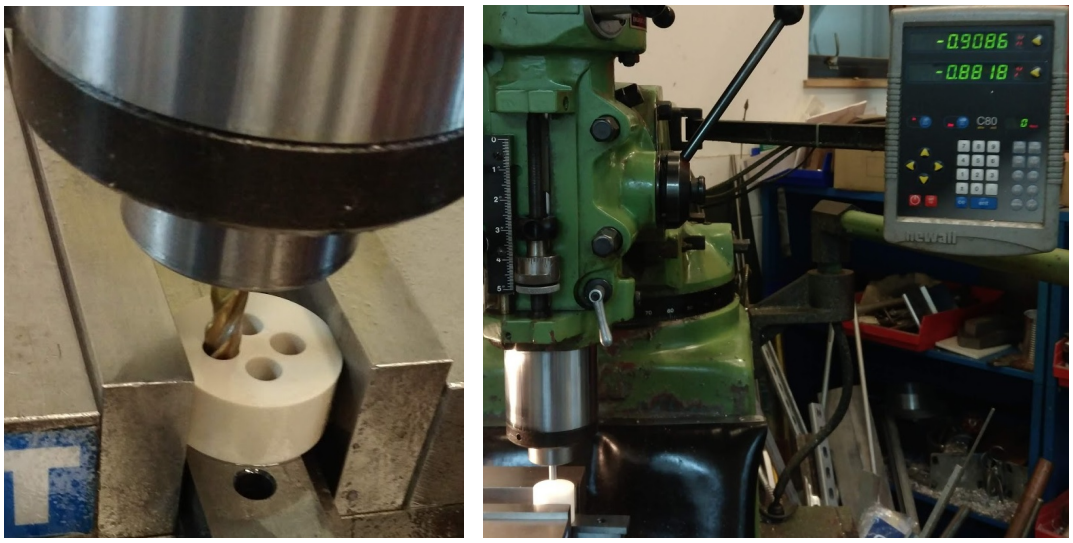

(a) (b)

Figure A.6: Maching of the holders for QMFV2.1.

trodes and two aperture plates. The two aperture plates with the hole diameter of 4 mm and 2 mm each will be installed on the entrance of the QMF with a 5 mm gap in between, similar to the design in Section 4.3.

The assembled QMF2.1 with the electrical connections is shown in Figure A.7(b).

A.2.2 QMF2.1 mechanical precision measurement

The mechanical precision of the assembled QMF2.1 was measured by the spacing between the quadrupole electrodes with a digital caliper. The spacings between the inner surface of two diagonal rods were measured at the two ends of the QMF2.1 and compared to

$$d_{inner} = 2r_0^{QMF2.1} = 7.02 \text{ mm}; \tag{A.1}$$

the distance between the outer surface of the electrodes was also measured at positions in between the holders and compared to

$$d_{out} = 2r_0^{QMF2.1} + 4r_e^{QMF2.1} = 22.90 \text{ mm}. \tag{A.2}$$

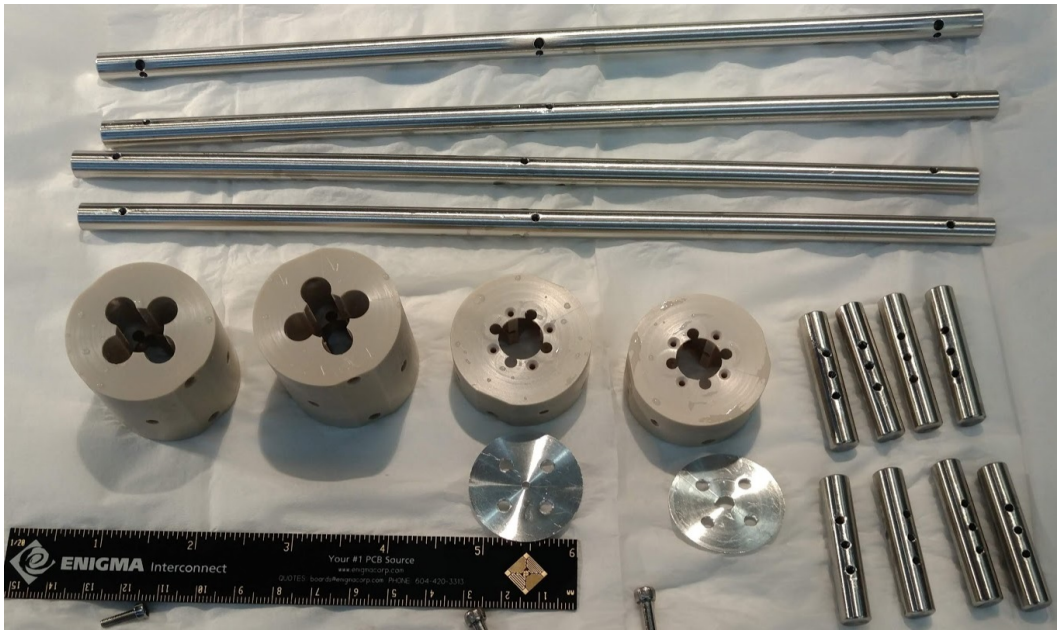

(a) Parts machined for QMF2.1

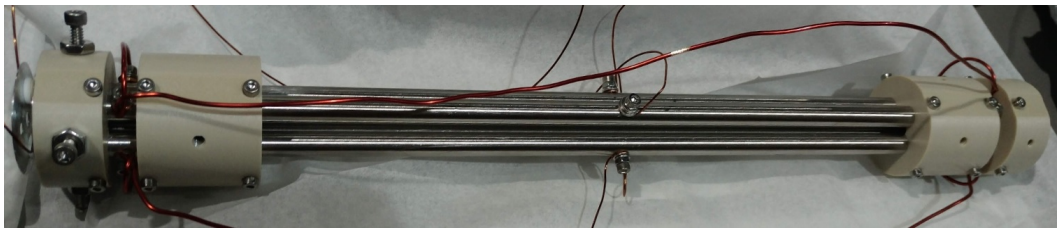

(b) Assembled QMF2.1

Figure A.7: The QMF2.1 prototype before and after assembly.

The mechanical precision of QMF2.1's quadrupole electrode positions was determined to be 40 µm according to the maximum measured mechanical error. A more comprehensive measurement of the QMF2.1's mechanical precision can be done as described in Section A.1.2 but was not done because the lathe in the TRIUMF ISAC-II machine shop doesn't have a digital readout of the positional coordinates.

The mechanical errors mainly come from the imperfect positioning of the electrodes in the circular shaped holes. The four holes were found to be slightly larger than the rods, hence human errors can be introduced during the assembling process.

A.2.3 Installation of QMF2.1 in test stand

The QMF2.1 was installed in the vacuum chamber of the test stand as shown in Figure A.8. The setup was similar to the QMF1 except the Faraday cup was no longer used. Part of the QMF2.1 was positioned inside the 8" to 4.5" CF flange reducer tube as shown in Figure A.8(b), so that the ions exit the QMF2.1 right in front of the CEM ion detector.

After sealing the vacuum flanges and starting pumping, the pressure reached 1×10^{-6} mbar in 5 hours. After two days, the ultimate pressure stabilized at 3.3×10^{-7} mbar, which is only 37% higher than when the vacuum chamber is empty. Compared to the acrylic used in QMF1, the PEEK used for QMF2.1 showed much lower out-gassing rate.

A.2.4 Ion transmission test

The ion source was heated with 1.3 A of current and floated to 60 V. Ion transmission measurements were done for QMF2.1 at low RF amplitude supplied by another low-cost two-channel signal generator FeelTech FY6600 because the SainSmart MHS5200A had been repurposed as a counter to measure the ion count rate as described in Section 5.1.3.

The two outputs from the signal generator were set to both have the amplitude of $V = 10$ V while the phases are 180° different. The RF frequency was scanned from 4.5 M Hz to 0.25 MHz . An ion transmission measurement was first done with the RF-only voltage and shown in Figure A.9(a).

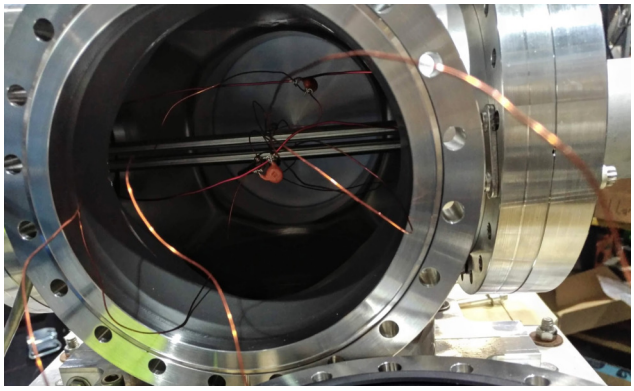

(a) Side view of quadrupole electrodes in vacuum chamber

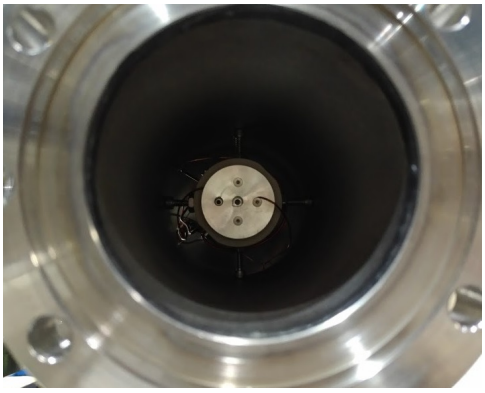

(b) View from ion entrance

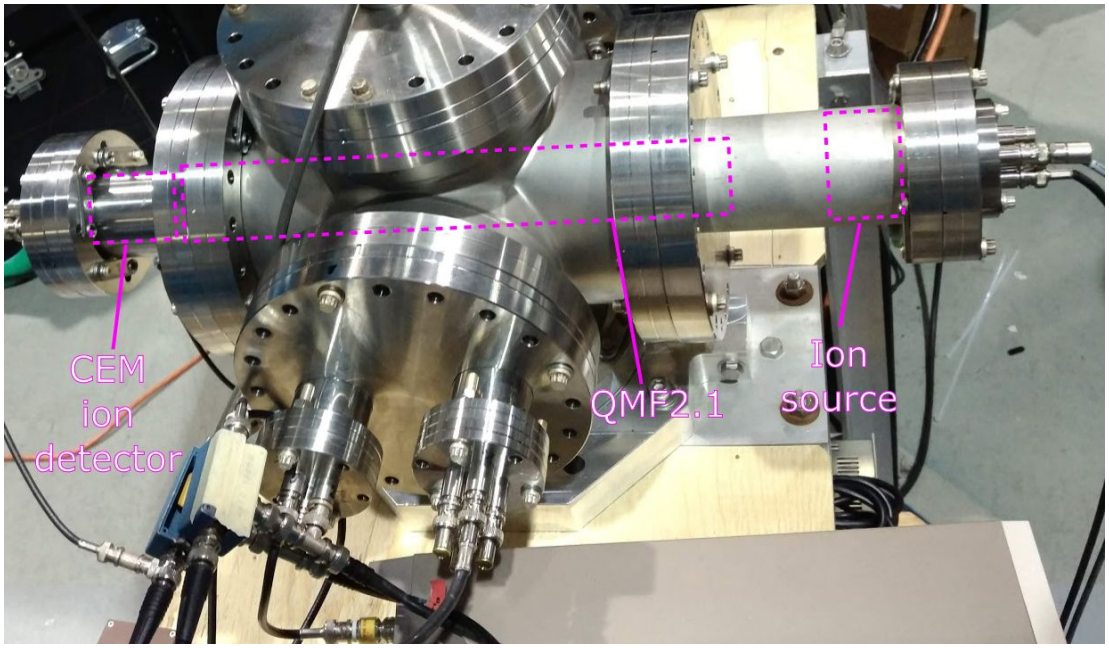

(c) Position of major components in vacuum chamber

Figure A.8: QMF2.1 installed in the vacuum chamber of the test stand.

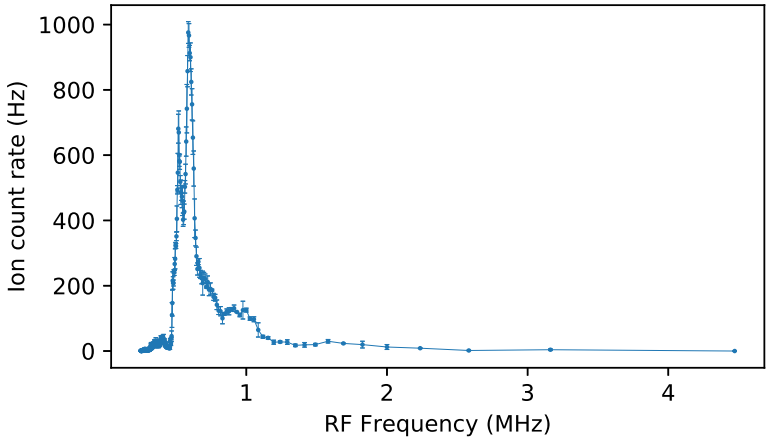

(a)

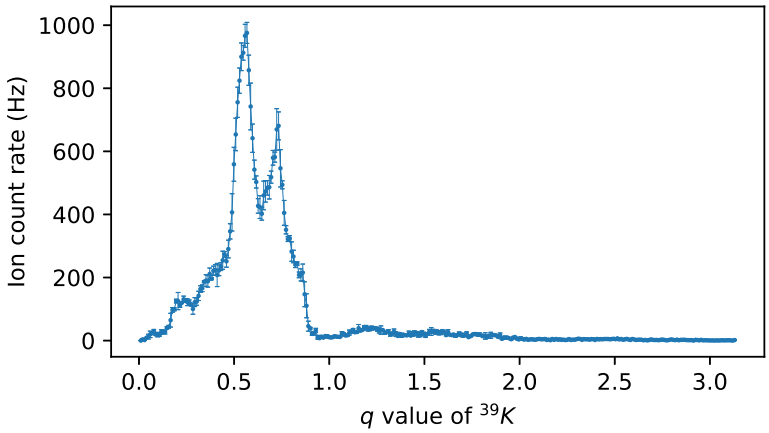

(b)

Figure A.9: (a) Ion transmission test of QMF2.1 with frequency scan. (b) Same measurement re-plotted with the horizontal axis as the q value of ^{39}K.

The q_K value for each of the RF frequencies were calculated for ^{39}K ions using Eq. (2.8), and the ion count rate is also shown as a function of q_K in Figure A.9(b). The ion transmission occurring at $q_K > 0.908$ indicates the presence of heavier ions such as Rb.

A.2.5 QMF2.1 for mass measurement as a QMS

The QMF2.1 was then tested with DC voltages also applied to the quadrupole electrodes to make it work as a quadrupole mass spectrometer (QMS). At first, the DC offset function of the signal generator FY6600 was used. Some preliminary measurement results revealed that the DC voltages were noisy and unstable for this purpose. So, a dedicated two-channel DC power supply Korad KA3303P was used later. The RF&DC mixing was done using a $C_{mix} = 10$ nF capacitor and a $R_{mix} = 1$ MΩ resistor for each channel as shown in Figure A.10. The RF&DC mixing was done at the vacuum chamber's feedthrough as shown in Figure A.8(c). The mixed voltage was monitored by an oscilloscope with a ×10 probe.

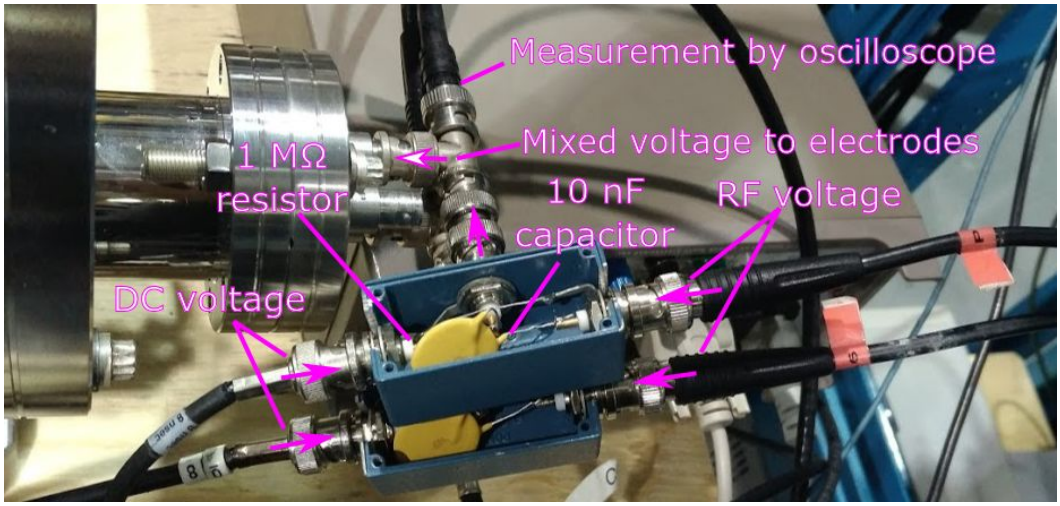

Figure A.10: Photo of the RF&DC mixing boxes with the electronics annotated.

Measurements were done by scanning the RF frequency from 4.5 MHz to 0.25 MHz (corresponding to ions of smaller mass to larger mass) at different DC voltage U. The results are shown in Figure A.11(a) as a 2D plot.

Four distinctive stability diagram patterns can be recognized from the 2D scan result shown in Figure A.11(a) corresponding to ^{23}Na, ^{39}K, ^{85}Rb and ^{133}Cs. Note that the shape of the stability diagrams' boundary is different as compared to Figure 2.13 because the U/V was used in the vertical axis instead of a.

The DC voltage U was obtained from the set value U_{PS} in the power supply KA3303A:

$$U = \eta_{DC} * U_{PS}, \tag{A.3}$$

where

$$\eta_{DC} = \frac{R_{scope}}{R_{DC} + R_{scope}} = \frac{10}{11} \tag{A.4}$$

is a correction factor as the DC voltage was divided between the RF&DC mixing resistor $R_{mix} = 1$ MΩ and the load impedance $R_{scope} = 10$ MΩ of the oscilloscope Tektronix TDC2024C (with ×10 probes).

The DC voltage corresponding to the upper tip of the stability diagram for the mass scan is obtained as $U/V = s_t$, where

$$s_t = \frac{a_t}{2q_t} \approx 0.168. \tag{A.5}$$

The exact values of $q_t \approx 0.706$ and $a_t \approx 0.237$ are given previously in Eq. (2.43). The value of s_t is plotted as a horizontal dashed line in Figure A.11(a) and its location matches the upper tips of the four ions' stability diagrams.

The mass values of the measurements were calculated from

$$m = \eta_C \frac{1}{\Omega^2} \cdot \frac{4eV}{r_0^2 q_t}, \tag{A.6}$$

where η_C is a calibration parameter. In the ideal situation of an RFQ with perfect mechanical precision and perfectly measured voltages,

$$\eta_C^{ideal} = A_2^2, \tag{A.7}$$

where $A_2 = 1.002$ is the coefficient of the quadrupole term in the electric potential in the center of the RFQ with round electrodes of $r_e/r_0 = 1.13$. In the real world, η_C is determined experimentally to compensate for the actual values of the QMF geometry and the voltages. In mass spectrometry,

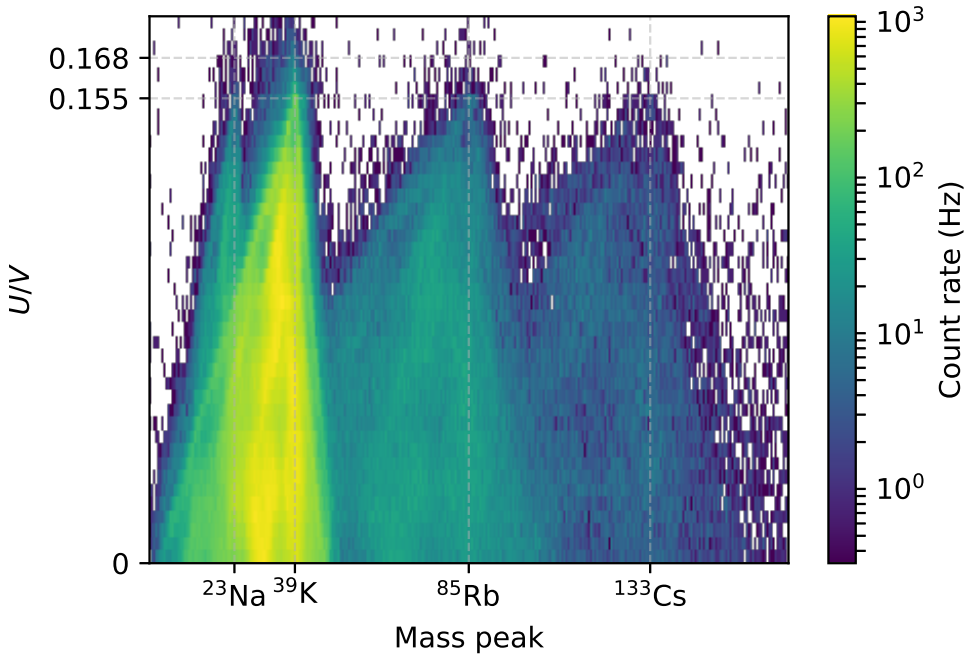

(a) Mass spectrum at different U values

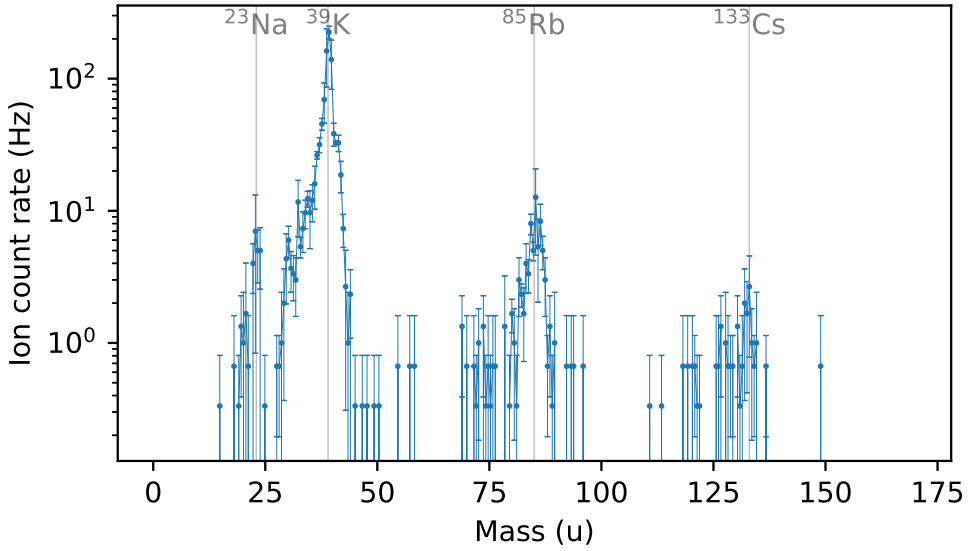

(b) Mass spectrum at $U/V = 0.155$

Figure A.11: Mass measurement using QMF2.1 as a quadrupole mass spectrometer.

this process is usually done by calibration using the known mass of one or more ions.

The above measurements for QMF2.1 were calibrated with a one-point calibration to match the second tip in Figure A.11(a) to the actual mass of ^{39}K. The calibration parameter $\eta_C = 0.925$ was obtained and used to calculate the mass values shown in the horizontal axes of both Figure A.11(a) and (b). The relatively large deviation of η_C from 1 are likely to be caused by the limited accuracy of the RF voltage measured by the oscilloscope, which is specified to be 3%.

The measurement with $U/V = 1.55$ near the upper tip of the stability diagram is shown in Figure A.11(b) as a mass spectrum. Besides ^{39}K which was used for the calibration, the other peaks in the measured mass spectrum match well with the actual mass of these corresponding ions annotated in the figure.

A.2.6 Mass measurement with square wave RF signal

In all the ion transmission tests described above, the RF signal used was sinusoidal. Square wave RF signal is an alternative and has been successfully used in ion traps [SGSP99, DSB$^+$04] and RFQ cooler/buncher [BSB$^+$12]. Such square wave RF signals can be generated by switching the output between preset voltages; it has the advantage of wide frequency range with a relatively high amplitude. In comparison, analog sinusoidal RF signals are more limited by the maximum power and the frequency range of the RF amplifier.

The ion motion in a square wave driven RFQ was found to still have stable and unstable regions in the (q, a) parameter space [RHH73], the first stable region is similar to the sinusoidal case except the q values are smaller. For example, when $a = 0$, the ion motion is stable in a smaller range $0 < q < 0.7125$ [DK06].

Measurements were done with the QMF2.1 using square wave voltages from the signal generator FY6600. The purpose is to test the functionality and performance of the QMF for a possible square wave RF generator to be permanently used in the future.

The maximum RF amplitude of $V = 10.2$ V was configured for the

square wave from the function generator FY6600. The same frequency range of 0.25 MHz to 4.5 MHz was used for the mass scan. The results are shown in Figure A.12. In this case, the tip of the stability diagram for mass scan corresponds to $U/V = 0.214$.

The mass values shown in the horizontal axes of Figure A.12 are calculated from

$$m = \eta_C \frac{1}{\Omega^2} \cdot \frac{4eV}{r_0^2 q_t^s}, \tag{A.8}$$

where $q_t^s \approx 0.554$ is the q value at the upper tip of the ion's stability diagram for a square wave. The same value of $\eta_C = 0.925$ obtained in the above measurement with sinusoidal wave was used here. The mass spectrum measured with $U/V = 0.200$ is shown in Figure A.12(b) and all the peaks agree well with the actual mass of these ions.

A.2.7 Mass measurement at higher RF amplitude

The mass measurements described above have a maximum mass resolving power at FWHM (full-width at half-maximum) $R_{FWHM} = m/\Delta m_{FWHM} \approx 20$, which is mainly limited by the relatively low RF amplitude $V \approx 10$ V of the signal generator. The low RF amplitude corresponds to a small RF frequency, hence reduced RF cycles when the ions travel through the QMS. A low RF frequency also leads to a smaller ion acceptance. For these reasons, a higher RF amplitude is better suited for the QMS operation when the RF frequency sweeping is used, as described in this study.

An RF amplifier Aigtek ATG2022H was acquired for this work. The amplifier has dual channels; each channel can deliver up to 200 Vp-p with a maximum power of 50 W. The -3dB frequency bandwidth is DC to 1 MHz.

From this point forward the RF signals from the function generator FY6600 are amplified by the ATG2022H before being mixed with the DC voltages and sent to the quadrupole electrodes. The voltage gain of the amplification is set to 30 times for both channels. The frequency-dependence of the gain was tested in the following way: the function generator output was set to 1 V and the amplified signal was measured by an oscilloscope. The measured RF voltage and the gain are shown in Figure A.14. The gain is close to the set value of 30 only at low frequency. At higher RF frequency, the gain started to drop and reached 21.2 ($30/\sqrt{2}$) around 1 MHz. This is

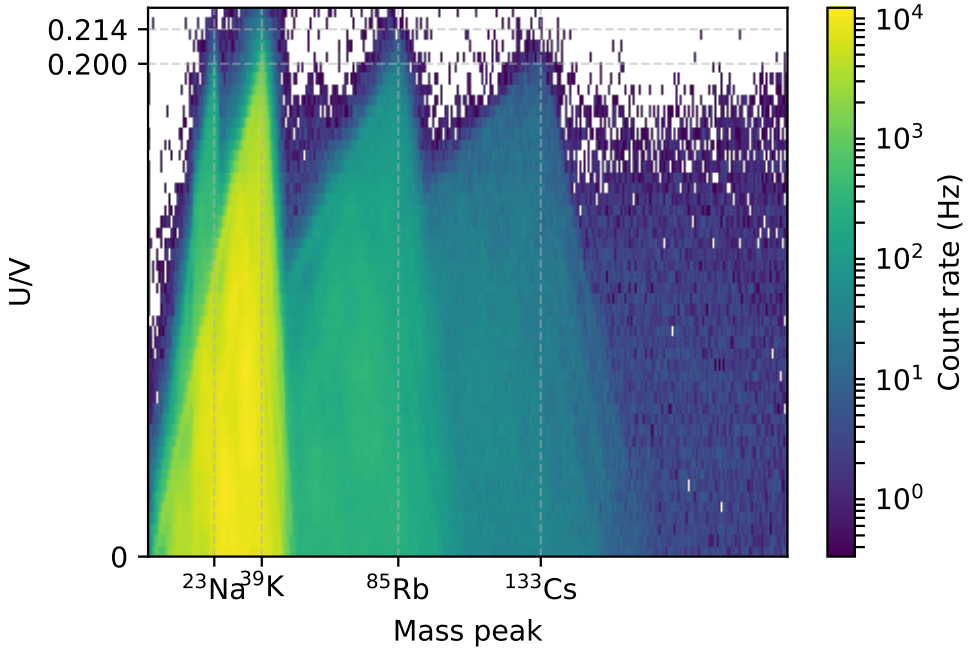

(a) Mass spectrum at different U/V values

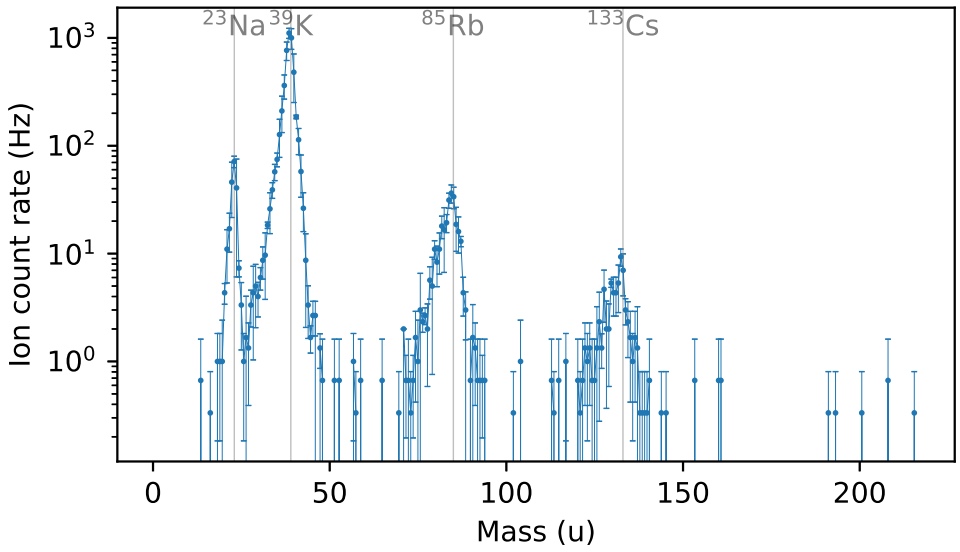

(b) Mass spectrum at $U/V = 0.207$

Figure A.12: Mass measurement using QMF2.1 as a QMS with square wave RF signal.

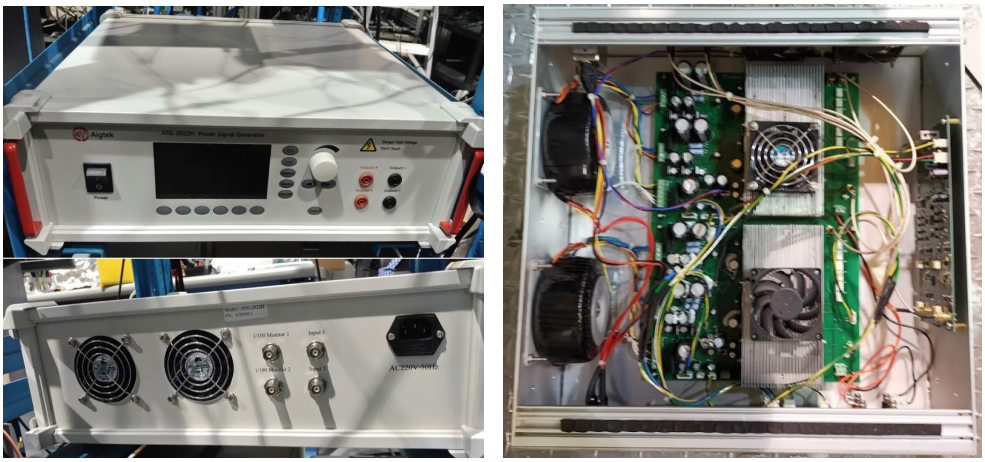

(a) Front and back view (b) Internal view

Figure A.13: Photos of the RF amplifier Aigtek ATG2022H.

expected for a -3dB frequency band of the amplifier.

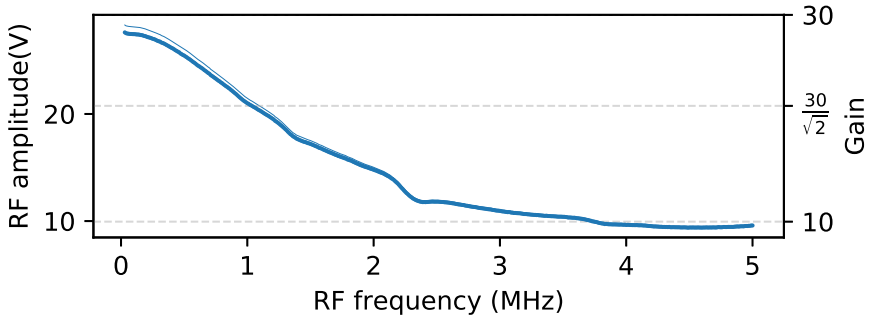

Figure A.14: RF amplitude (and gain) of the RF amplifier at 1 V input from 0.01 to 5 MHz.

The gain of the RF amplifier was found to be not a simple mathematical function of the frequency. Therefore it was decided to measure the RF amplitude while operating the QMS.

A set of measurements was done with QMF2.1 at higher RF amplitude using the RF amplifier. The RF amplitudes of the function generator were set to be $V_{FG} = 4$ V for both channels. The RF voltage was amplified by

a set gain of 30 times. The RF frequency was scanned from 1.8 MHz to 0.8 MHz.

The ion source was still heated to 1.3 A but floated at a lower voltage of 24 V so that the ions would have smaller velocity while flying through the QMF and experience more RF cycles. The anode voltage of the ion source was set to -170 V to obtain a maximum ion count rate. The measured results are shown in Figure A.15.

The mass values of the transmitted ions, as identified on the horizontal axes of the plots of Figure A.15 are calculated using Eq. (A.6) and the measured RF voltage V at each RF frequency. The calibration parameter $\eta_C = 1.052$ was found using the mass of ^{39}K using one-point calibration. The difference in the value of η_C compared to the above measurements with low RF voltage most likely originates from the measurement of the RF amplitude. These low voltage RF were measured at the output of the function generator, which is slightly higher than the amplitude after RF&DC mixing at the electrical feedthrough.

A mass spectrum measured at $U/V = 0.164$ is shown in Figure A.15(b). The mass peaks for potassium isotopes ^{39}K and ^{41}K were identified; the height of these two peaks matches their natural abundance of 93% and 7%. The rubidium isotopes ^{85}Rb and ^{87}Rb can also be identified; the ratio of their peaks also matches their natural abundance of 72% and 28%.

The maximum mass resolving power is found to be

$$R_{FWHM} = m/\Delta m_{FWHM} \approx 51$$

according to the ^{39}K peak. The mass resolving power was likely limited by the QMF2.1's mechanical precision of 40 µm. The next prototype QMF2.2 was built with the aim of better mechanical precision.

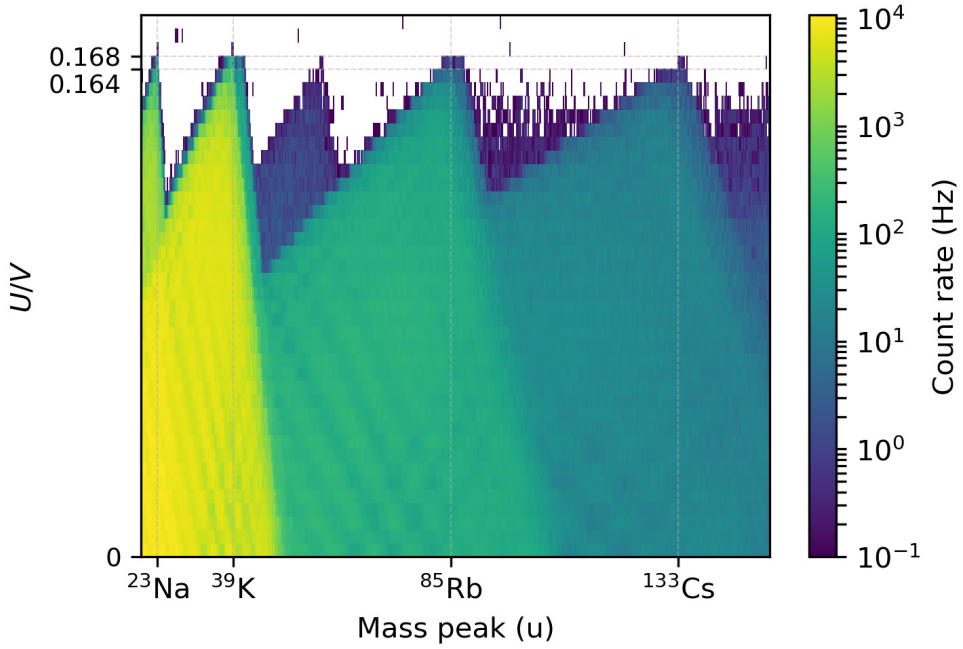

(a) Mass spectrum at different U values

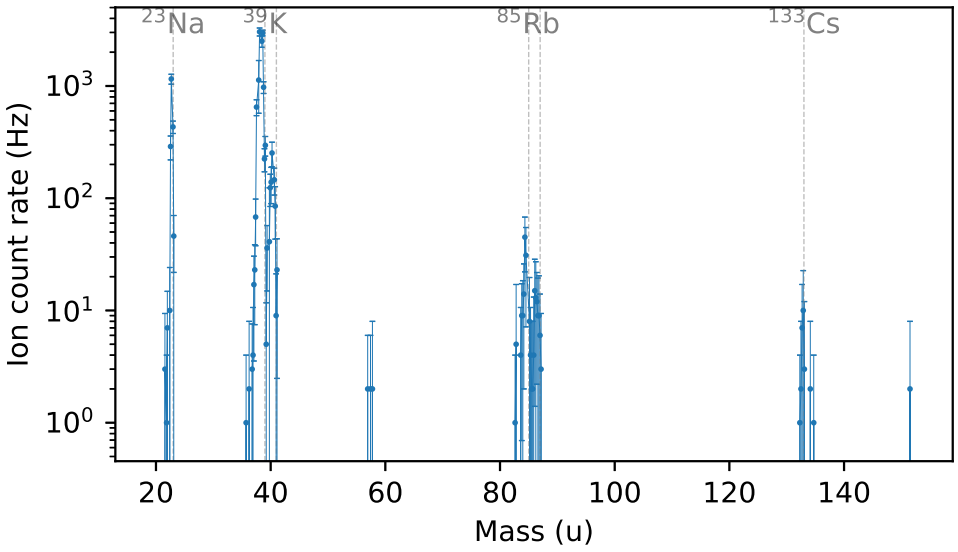

(b) Mass spectrum at U/V=0.164

Figure A.15: Mass measurement with QMF2.1 at higher RF amplitude.

Appendix B

Mechanical drawings of the LPT

The mechanical drawings of the linear Paul trap designed in Chapter 4 are shown here. Note that all the drawings have been scaled from their original size to 11 inch $\times$8.5 inch. The drawings were made by X. Shang at McGill University based on the 3D Solidworks models of this study. A few changes and many improvements have also been contributed by Shang in the 3D models and the drawings.

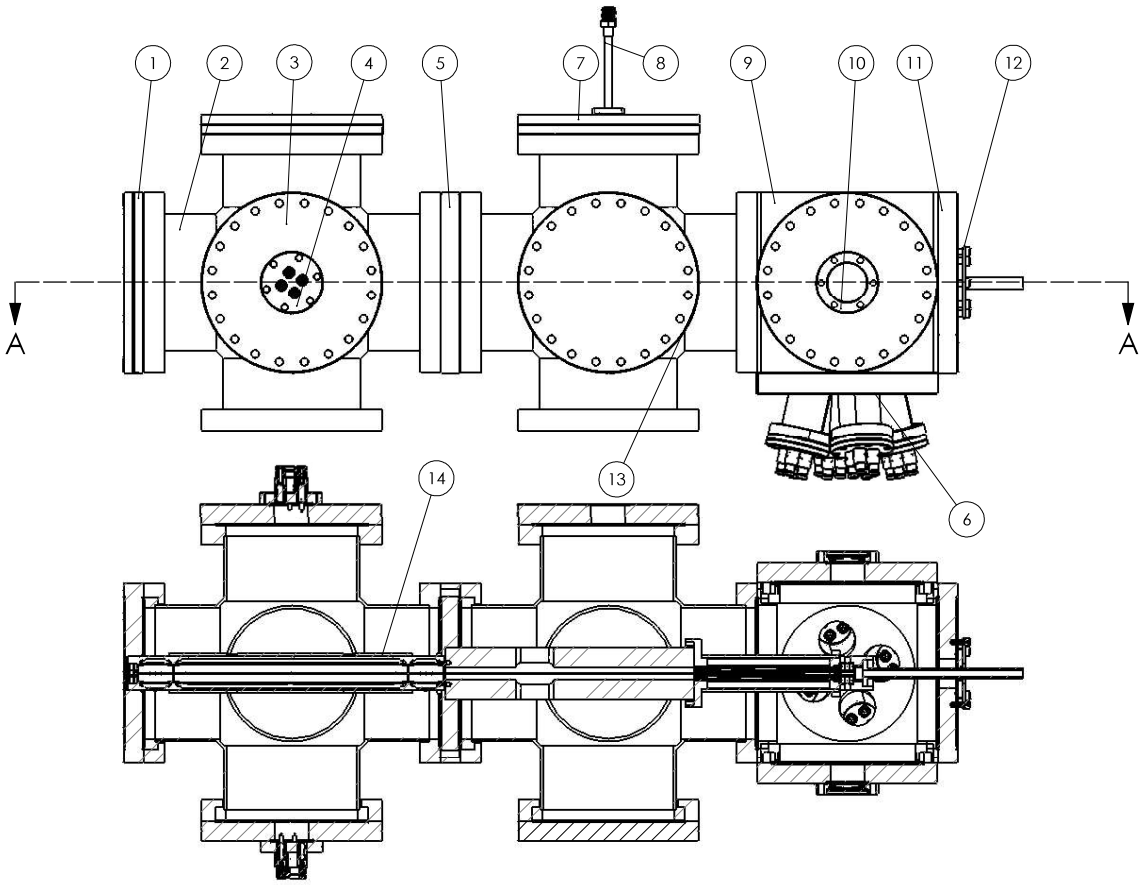

SECTION A-A
SCALE 1 : 4

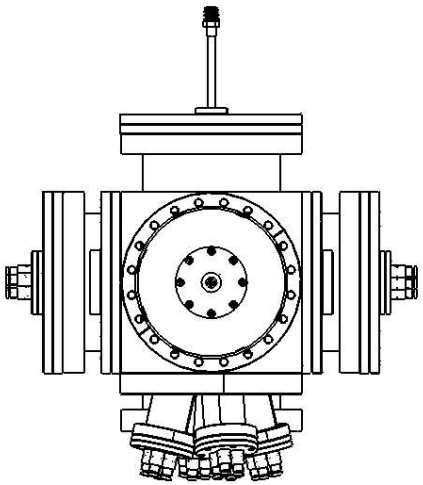

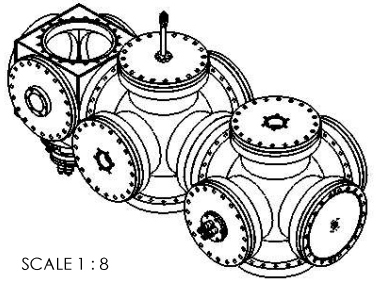

SCALE 1 : 8

ITEM NO.	PART NUMBER	DESCRIPTION	QTY.
1	LPT1Q001	QMF Entrance Flange	1
2	LPT1Q002	QMF and CLB Chambers	2
3	rf800x275	CF8 to CF2.75 0L Reducer	6
4	LPT1Q004	CF2.75 Feed Thru	6
5	LPT1C001	CLB Entrance Flange	1
6	LPT1C002	CF8" Cluster Flange	1
7	LPT1C003	CF8 to CF1.33 0L Reducer	1
8	LPT1C004	MDC FluidFT, 1.33"x1/4"VCR, 1Tube	1
9	LPT1C005	MDC 6-WayCube, 8"	1
10	LPT1C006	VPZL-275DUC2 CF2.75 Viewport	2
11	LPT1C007	CLB End Flange	1
12	LPT1C008	CLB Exit Holder Clamp	1
13	LPT1C009	CF8 Blank Flange	1
14	LPT2	Inner Assembly	1

UNLESS OTHERWISE SPECIFIED: DIMENSIONS ARE IN MILLIMETERS SURFACE FINISH: TOLERANCES: LINEAR: Two place decimal: ±0.25 Three place decimal: ±0.127 ANGULAR: MACH ±0.1

FINISH:

DEBURR AND BREAK SHARP EDGES

DO NOT SCALE DRAWING

REVISION 10

	NAME	SIGNATURE	DATE
Revision	XS		14/02/2020
CHK'D			
APPV'D			
MFG			
Q.A			

MATERIAL:

QUANTITY: 1

Linear Paul Trap - TRIUMF

TITLE: Linear Paul Trap assembly

DWG NO. LPT

A2

SCALE:1:4

SHEET 1 OF 39

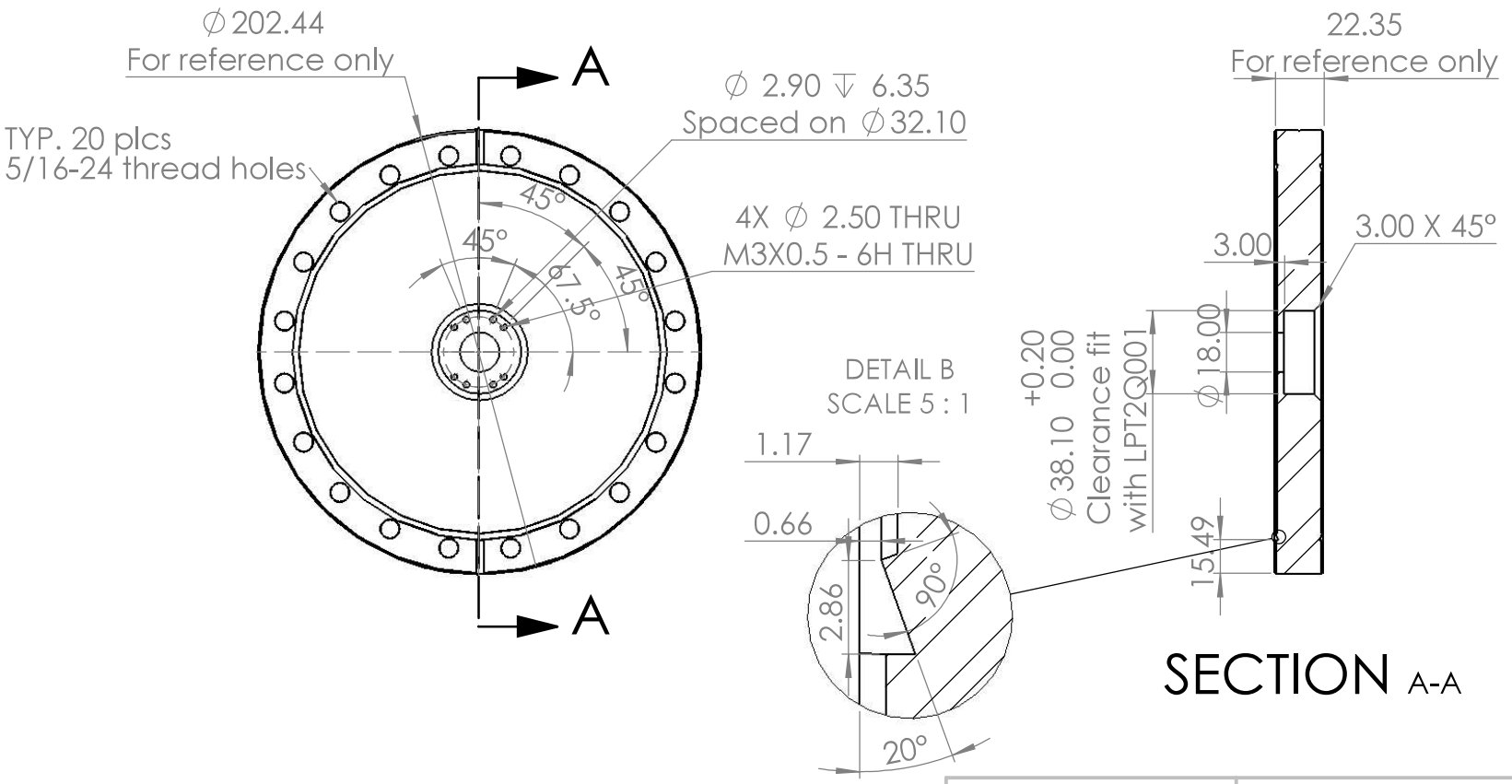

NOTE: Single sided flange with tapped hole is ordered by McGill. The knife edge on the other side of the flange is to be machined.

Same for LPT1C001.

UNLESS OTHERWISE SPECIFIED: DIMENSIONS ARE IN MILLIMETERS SURFACE FINISH: TOLERANCES: LINEAR: Two place decimal: ±0.25, Three place decimal: ±0.127 ANGULAR: MACH ±0.1	DO NOT SCALE DRAWING	REVISION 10
	Linear Paul Trap - TRIUMF	
NAME / DATE	TITLE: QMF Entrance Flange	
DRAWN: XS 14/02/2020		
CHK'D		
APPV'D		
REV'D		
MATERIAL: 304ss Available From Lesker F0800X000NT	DWG NO. LPT1Q001	A4
QUANTITY: 1	SCALE: 1:3	SHEET 2 OF 39

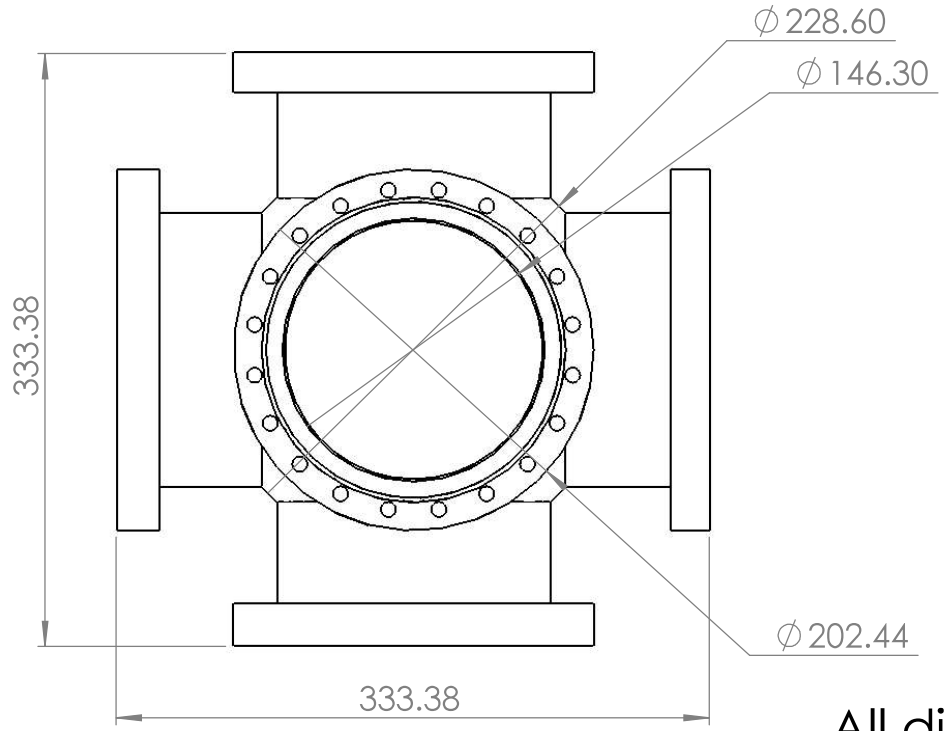

All dimensions are for reference only.

UNLESS OTHERWISE SPECIFIED: DIMENSIONS ARE IN MILLIMETERS SURFACE FINISH: TOLERANCES: LINEAR: Two place decimal: ±0.25 Three place decimal: ±0.127 ANGULAR: MACH ±0.1	DO NOT SCALE DRAWING	REVISION 10
	Linear Paul Trap - TRIUMF	
NAME / DATE DRAWN XS 14/02/2020 CHK'D APPV'D REV'D	TITLE: MDC 6-WayCross, 9"Sphere	
MATERIAL: 304ss Available From MDC Part# 407008	DWG NO. LPT1Q002	A4
QUANTITY: 2	SCALE: 1:4	SHEET 3 OF 39

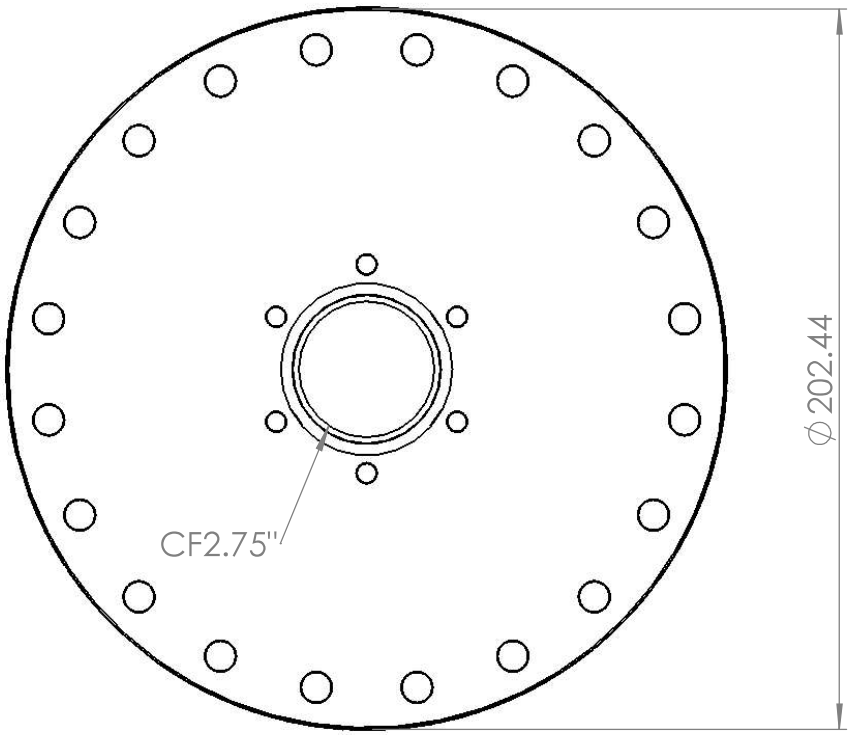

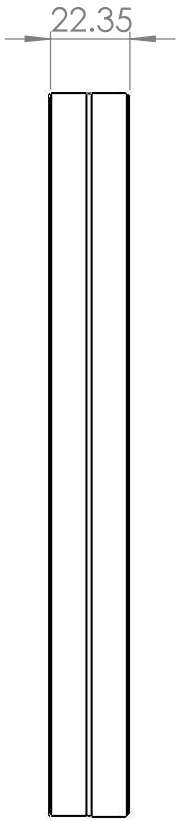

All dimensions are for reference only.

UNLESS OTHERWISE SPECIFIED: DIMENSIONS ARE IN MILLIMETERS SURFACE FINISH: TOLERANCES: LINEAR: ±0.127 ANGULAR: MACH ±0.1	DO NOT SCALE DRAWING	REVISION 10
	Linear Paul Trap - TRIUMF	
NAME / DATE DRAWN XS 14/02/2020 CHK'D APPV'D REV'D	TITLE: CF8 to CF2.75 0L Reducer	
MATERIAL: Lesker #RF800X275	DWG NO. LPT1Q003	A4
QUANTITY: 6	SCALE: 1:2	SHEET 4 OF 39

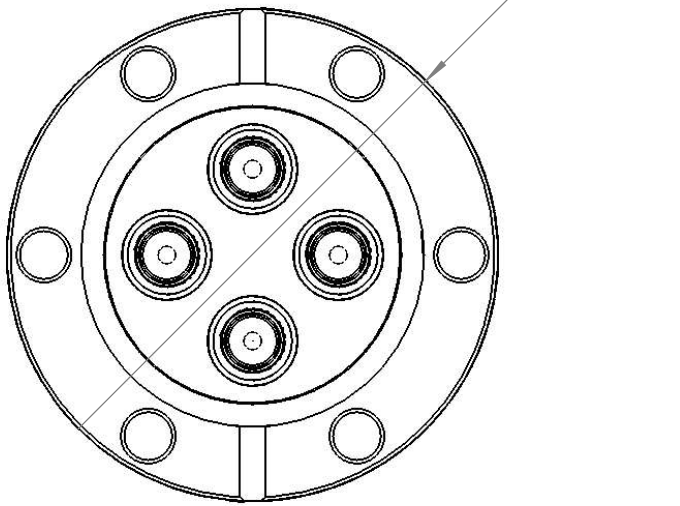

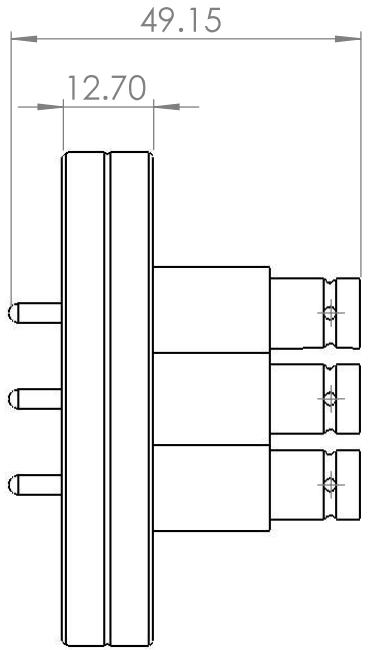

All dimensions are for reference only.

UNLESS OTHERWISE SPECIFIED: DIMENSIONS ARE IN MILLIMETERS SURFACE FINISH: TOLERANCES: LINEAR: ±0.127 ANGULAR: MACH ±0.1	DO NOT SCALE DRAWING	REVISION 10
	Linear Paul Trap - TRIUMF	
NAME / DATE DRAWN XS 14/02/2020 CHK'D APPV'D REV'D	TITLE: CF2.75 Feed Thru	
MATERIAL: Lesker #IFTSG041033	DWG NO. LPT1Q004	A4
QUANTITY: 6	SCALE: 1:1	SHEET 5 OF 39

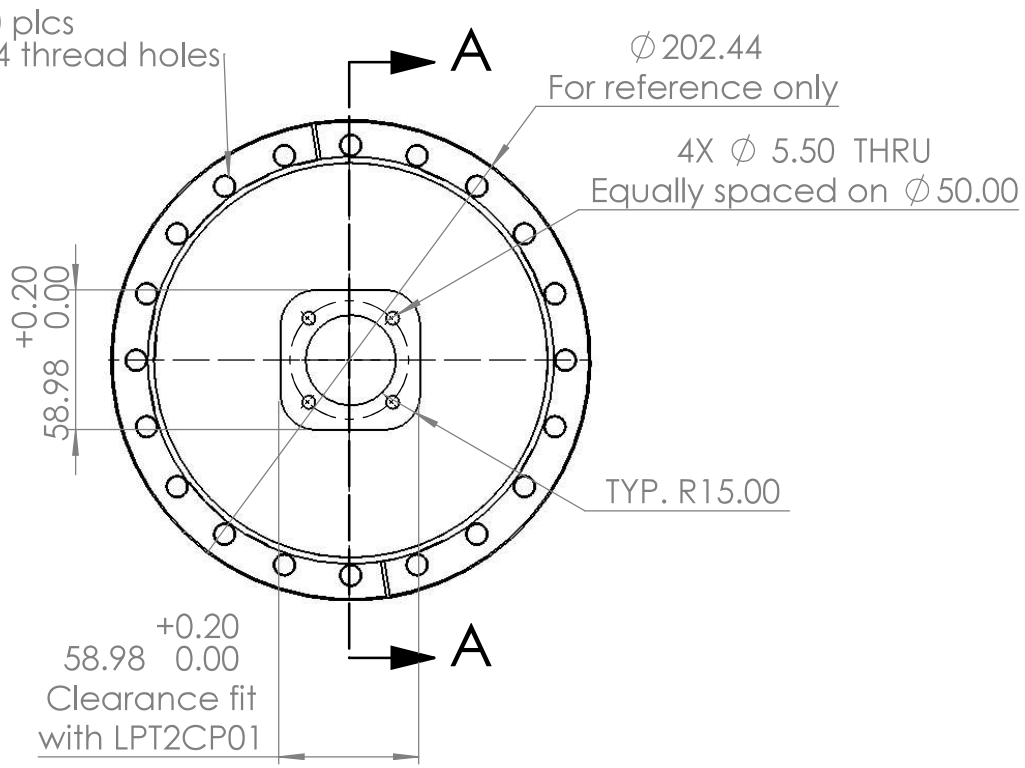

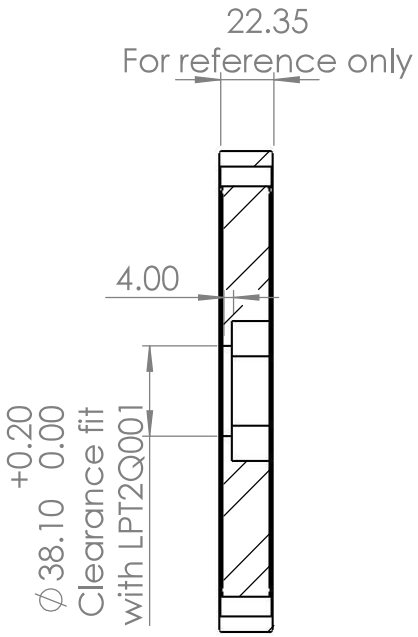

SECTION A-A

SCALE 1 : 3

NOTE: Single sided flange with tapped hole will be ordered by McGill. The knife edge on the other side of the flange is to be machined.

See LPT1Q001 for knife edge details.

UNLESS OTHERWISE SPECIFIED: DIMENSIONS ARE IN MILLIMETERS SURFACE FINISH: TOLERANCES: LINEAR: Two place decimal: ±0.25 Three place decimal: ±0.127 ANGULAR: MACH ±0.1	DO NOT SCALE DRAWING	REVISION 10
	Linear Paul Trap - TRIUMF	
NAME / DATE DRAWN XS 14/02/2020 CHK'D APPV'D REV'D	TITLE: CLB Entrance Flange	
MATERIAL: 304ss Flange Available From MDC Part# 140030	DWG NO. LPT1C001	A4
QUANTITY: 1	SCALE: 1:3	SHEET 6 OF 39

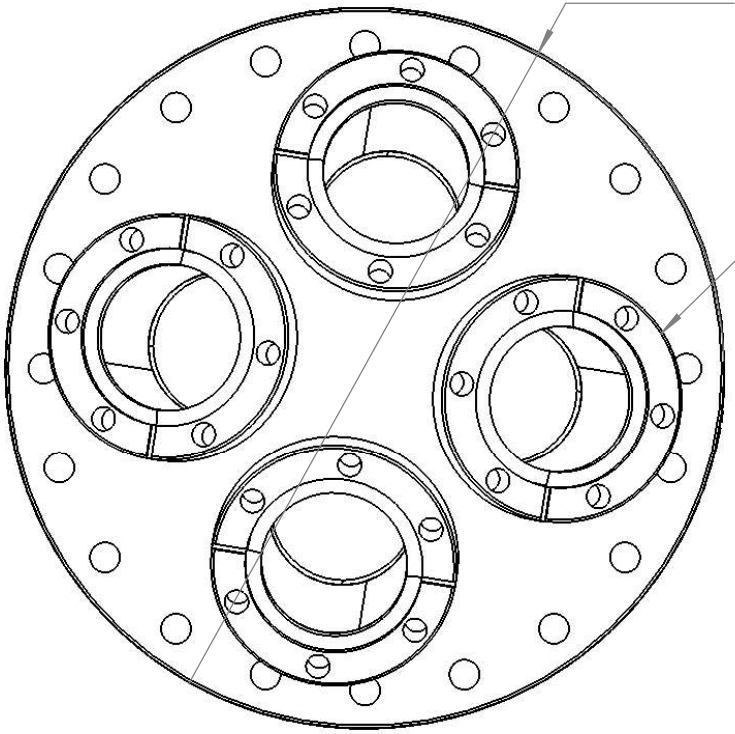

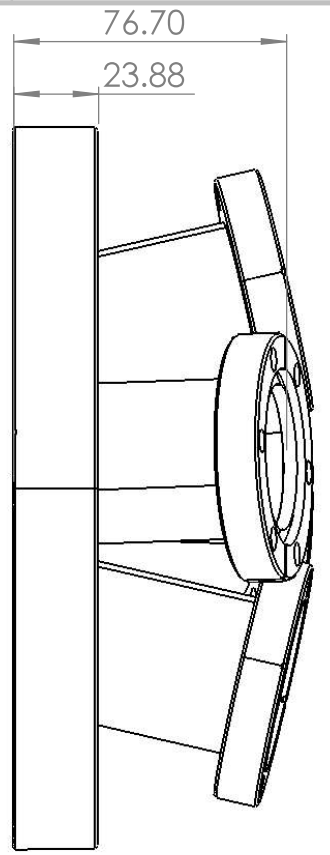

All dimensions are for reference only.

UNLESS OTHERWISE SPECIFIED: DIMENSIONS ARE IN MILLIMETERS SURFACE FINISH: TOLERANCES: LINEAR: ±0.127 ANGULAR: MACH ±0.1	DO NOT SCALE DRAWING	REVISION 10
	Linear Paul Trap - TRIUMF	
NAME / DATE DRAWN XS 14/02/2020 CHK'D APPV'D REV'D	TITLE: CF8" Cluster Flange	
MATERIAL: MDC #409008	DWG NO. LPT1C002	A4
QUANTITY: 1	SCALE: 1:2	SHEET 7 OF 39

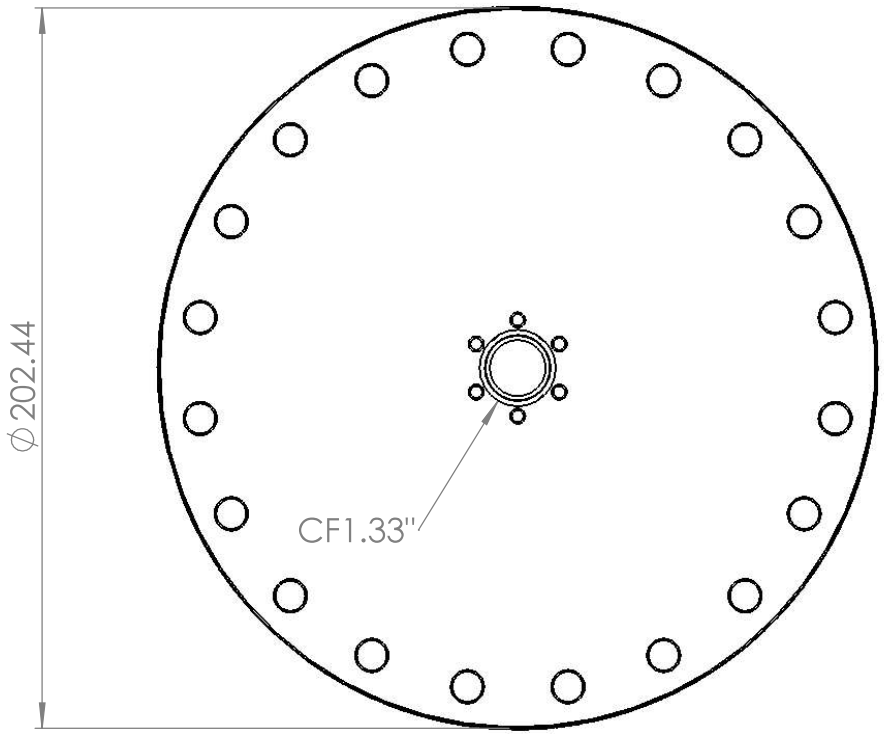

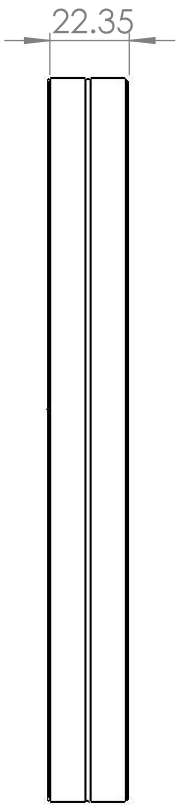

All dimensions are for reference only.

UNLESS OTHERWISE SPECIFIED: DIMENSIONS ARE IN MILLIMETERS SURFACE FINISH: TOLERANCES: LINEAR: Two place decimal: ±0.25 Three place decimal: ±0.127 ANGULAR: MACH ±0.1	DO NOT SCALE DRAWING	REVISION 10
	Linear Paul Trap - TRIUMF	
NAME / DATE	TITLE: CF8 to CF1.33 0L Reducer	
DRAWN XS 14/02/2020		
CHK'D		
APPV'D		
REV'D		
MATERIAL: Lesker #RF800X133	DWG NO. LPT1C003	A4
QUANTITY: 1	SCALE: 1:2	SHEET 8 OF 39

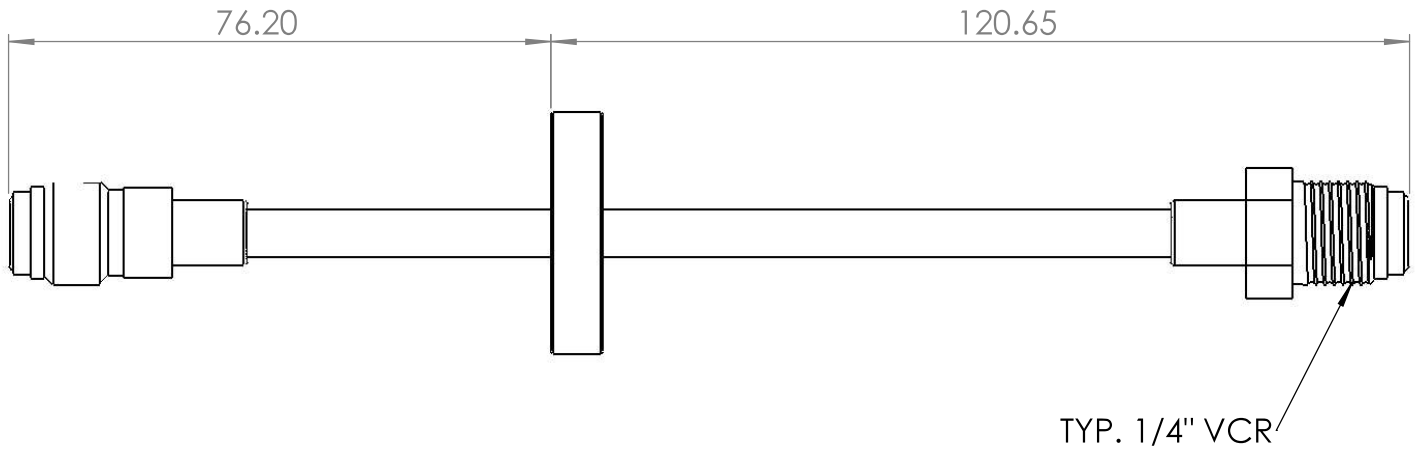

All dimensions are for reference only.

UNLESS OTHERWISE SPECIFIED: DIMENSIONS ARE IN MILLIMETERS SURFACE FINISH: TOLERANCES: LINEAR: Two place decimal: ±0.25 Three place decimal: ±0.127 ANGULAR: MACH ±0.1	DO NOT SCALE DRAWING	REVISION 10
	Linear Paul Trap - TRIUMF	
NAME / DATE DRAWN XS 14/02/2020 CHK'D APPV'D REV'D	TITLE: FluidFT, 1.33"x1/4"VCR	
MATERIAL: Flange and Tubes: 304ss Connectors: 316ss Available from MDC part# 610003	DWG NO. LPT1C004	A4
QUANTITY: 1	SCALE: 1:1	SHEET 9 OF 39

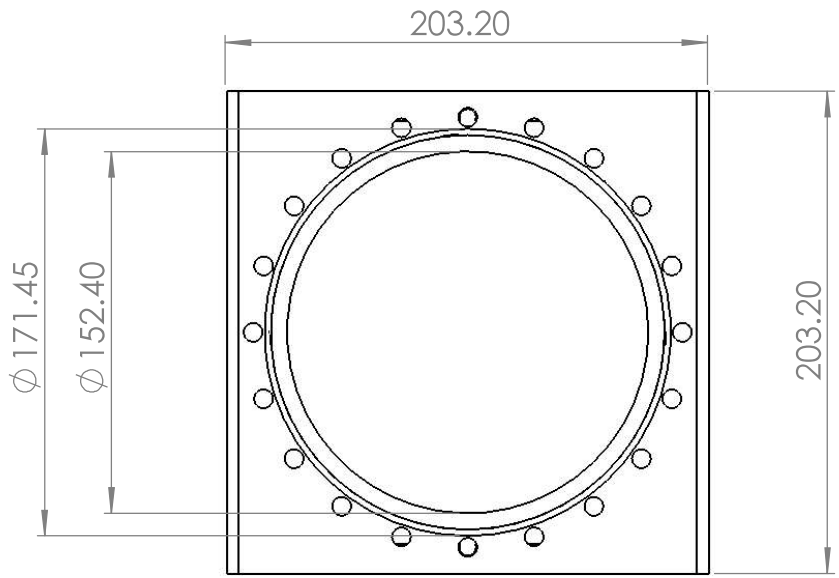

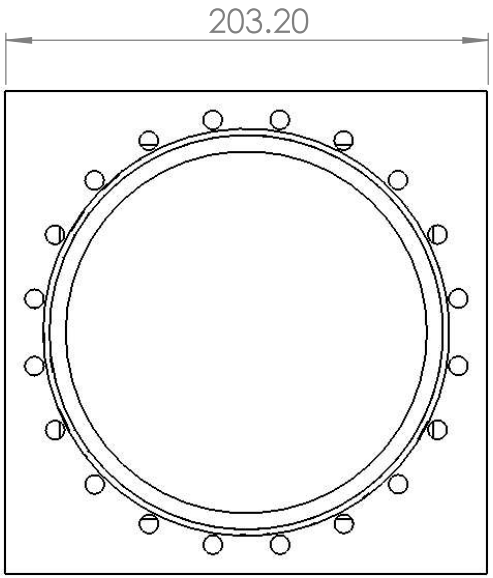

All dimensions are for reference only.

UNLESS OTHERWISE SPECIFIED: DIMENSIONS ARE IN MILLIMETERS SURFACE FINISH: TOLERANCES: LINEAR: Two place decimal: ±0.25 Three place decimal: ±0.127 ANGULAR: MACH ±0.1	DO NOT SCALE DRAWING	REVISION 10
	Linear Paul Trap - TRIUMF	
NAME / DATE DRAWN XS 14/02/2020 CHK'D APPV'D REV'D	TITLE: MDC 6-WAY CUBE, 8"	
MATERIAL: 304ss Available from MDC part# 408005	DWG NO. LPT1C005	A4
QUANTITY: 1	SCALE: 1:3	SHEET 10 OF 39

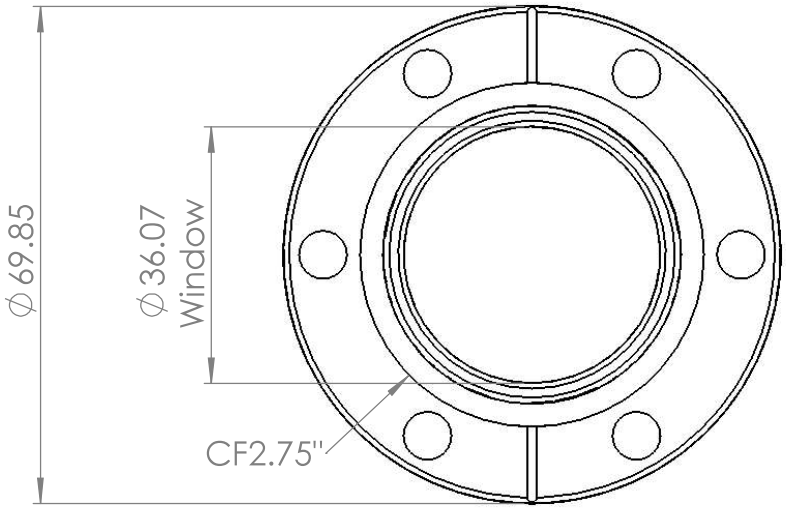

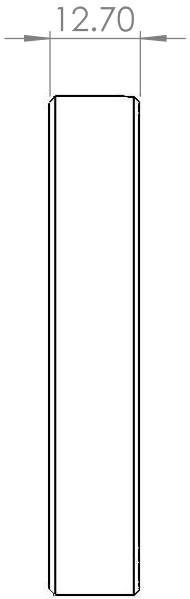

All dimensions are for reference only.

UNLESS OTHERWISE SPECIFIED: DIMENSIONS ARE IN MILLIMETERS SURFACE FINISH: TOLERANCES: LINEAR: Two place decimal: ±0.25 Three place decimal: ±0.127 ANGULAR: MACH ±0.1	DO NOT SCALE DRAWING	REVISION 10
	Linear Paul Trap - TRIUMF	
NAME / DATE DRAWN XS 14/02/2020 CHK'D APPV'D REV'D	TITLE: VPZL-275DUC2 CF2.75 Viewport	
MATERIAL: 304ss Lesker part# VPZL-275DUC2	DWG NO. LPT1C006	A4
QUANTITY: 2	SCALE 1:1	SHEET 11 OF 39

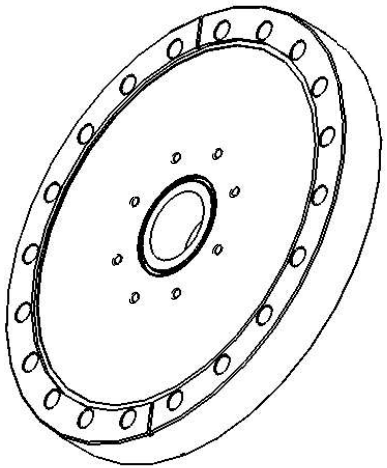

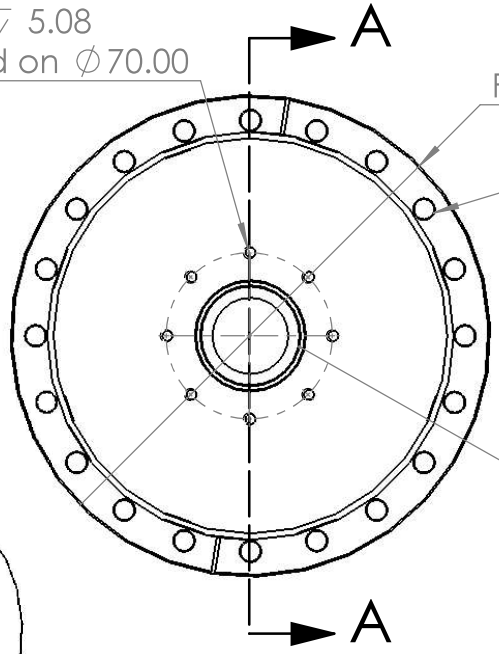

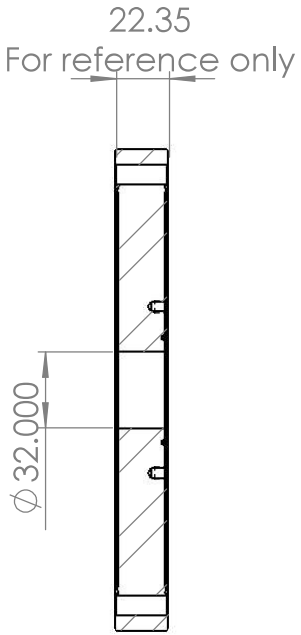

SECTION A-A

SCALE 1 : 3

UNLESS OTHERWISE SPECIFIED: DIMENSIONS ARE IN MILLIMETERS SURFACE FINISH: TOLERANCES: LINEAR: Two place decimal: ±0.25 Three place decimal: ±0.127 ANGULAR: MACH ±0.1	DO NOT SCALE DRAWING	REVISION 10
	Linear Paul Trap - TRIUMF	
NAME / DATE DRAWN XS 14/02/2020 CHK'D APPV'D REV'D	TITLE: CLB End Flange	
MATERIAL: 304ss Available From MDC Part# 140030	DWG NO. LPT1C007	A4
QUANTITY: 1	SCALE: 1:3	SHEET 12 OF 39

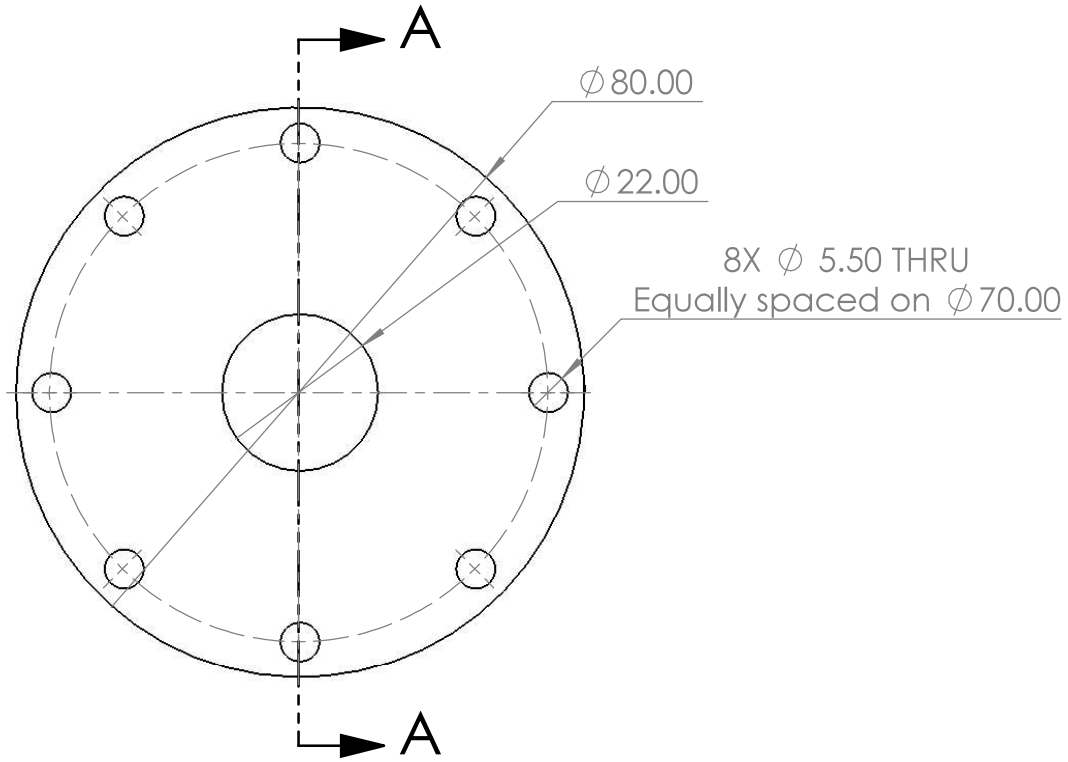

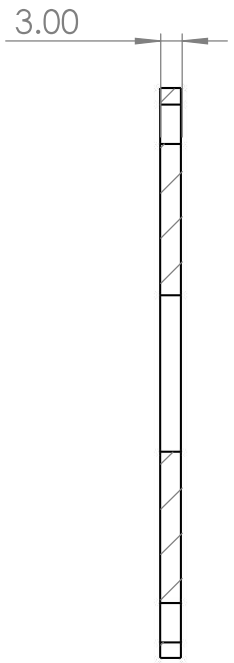

SECTION A-A

SCALE 1 : 1

UNLESS OTHERWISE SPECIFIED: DIMENSIONS ARE IN MILLIMETERS SURFACE FINISH: TOLERANCES: LINEAR: Two place decimal: ±0.25 Three place decimal: ±0.127 ANGULAR: MACH ±0.1	DO NOT SCALE DRAWING	REVISION 10
	Linear Paul Trap - TRIUMF	
NAME / DATE DRAWN XS 14/02/2020 CHK'D APPV'D REV'D	TITLE: CLB Exit Holder Clamp	
MATERIAL: Aluminium 6061	DWG NO. LPT1C008	A4
QUANTITY: 1	SCALE: 1:1	SHEET 13 OF 39

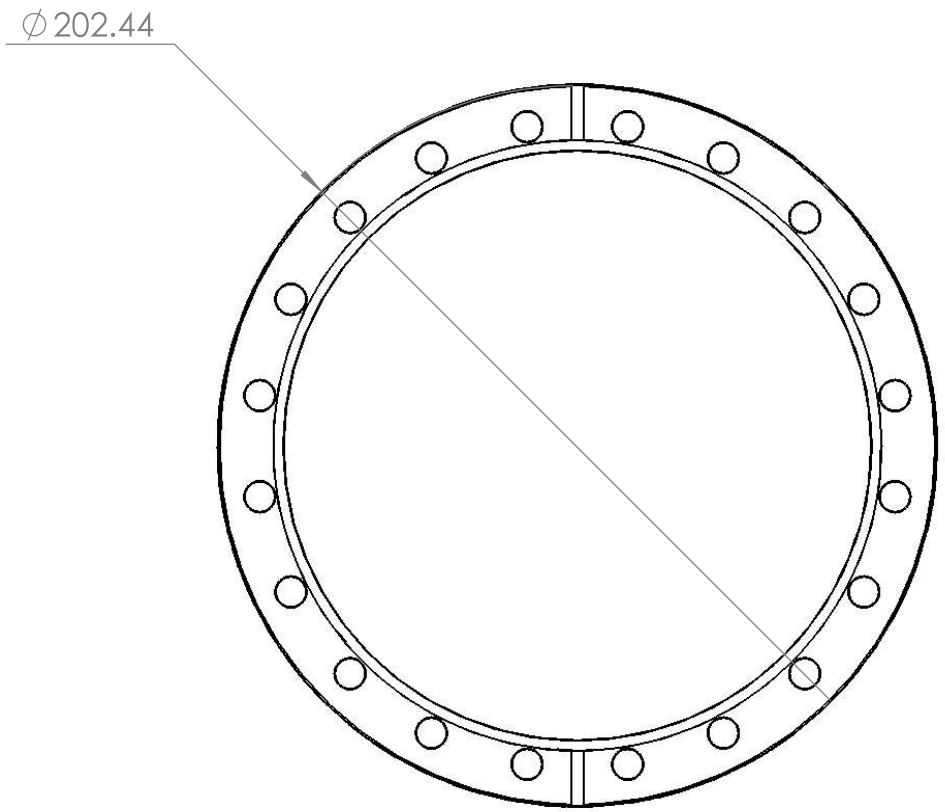

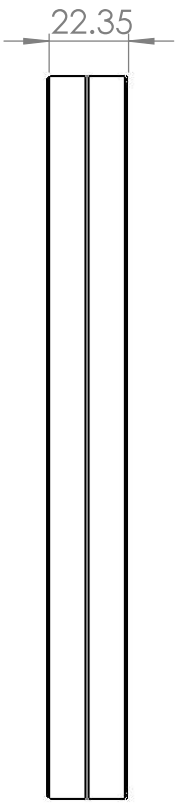

All dimensions are for reference only.

UNLESS OTHERWISE SPECIFIED: DIMENSIONS ARE IN MILLIMETERS SURFACE FINISH: TOLERANCES: LINEAR: ±0.127 ANGULAR: MACH ±0.1	DO NOT SCALE DRAWING	REVISION 10
	Linear Paul Trap - TRIUMF	
NAME / DATE DRAWN XS 14/02/2020 CHK'D APPV'D REV'D	TITLE: CF8 Blank Flange	
MATERIAL: Lesker #F0800X000N	DWG NO. LPT1C009	A4
QUANTITY: 1	SCALE: 1:2	SHEET 14 OF 39

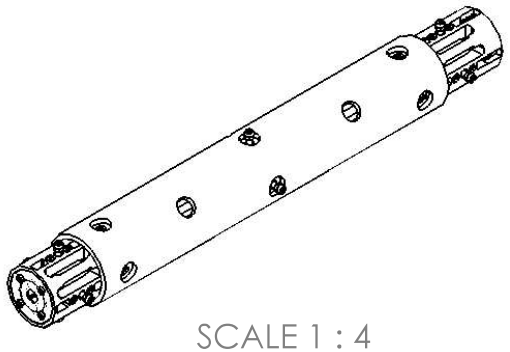

SCALE 1 : 4

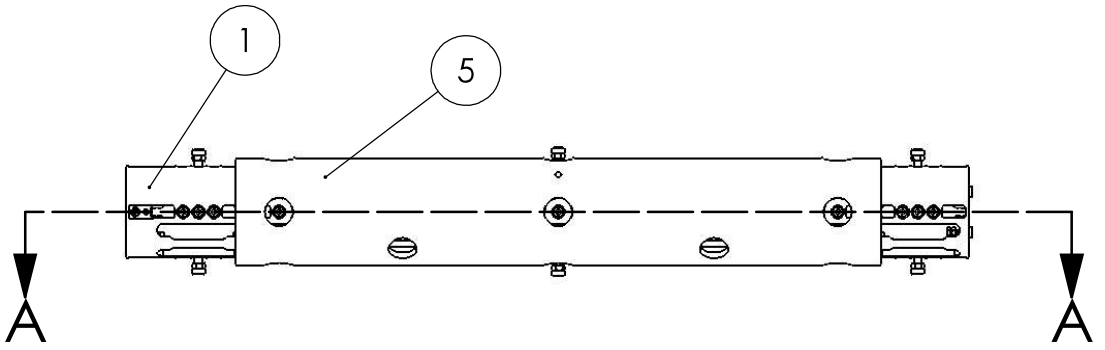

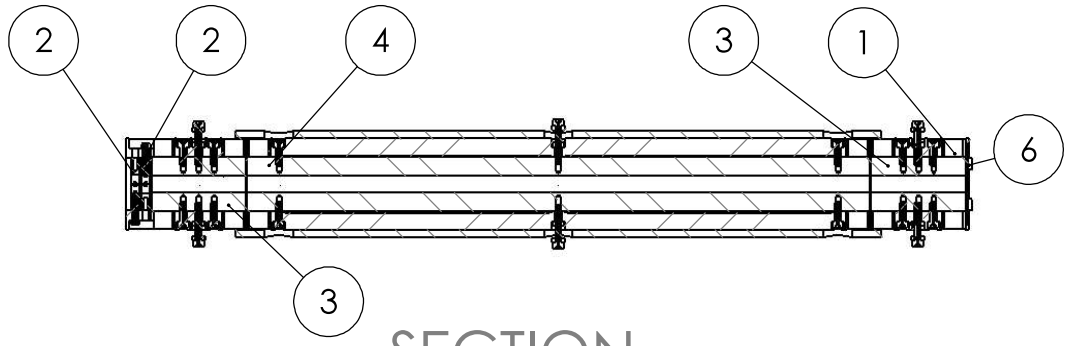

SECTION A-A

SCALE 1 : 3

ITEM NO.	PART NUMBER	DESCRIPTION	QTY.
1	LPT2Q001	QMF Quad Electrodes Holder	1
2	LPT2Q002, LPT2Q003	Aperture Lens at QMF Entrance	2
3	LPT2Q004, LPT2Q007	1st and 3rd Quad Electrodes for QMF	8
4	LPT2Q005	2nd Quad Electrode for QMF	4
5	LPT2Q006	QMF Holder Outside Tube	1
6	LPT2Q008	Aperture Lens at QMF Exit	1

UNLESS OTHERWISE SPECIFIED:
DIMENSIONS ARE IN MILLIMETERS
SURFACE FINISH:
TOLERANCES:
LINEAR: Two place decimal: ±0.25
Three place decimal: ±0.127
ANGULAR: MACH ±0.1

DO NOT SCALE DRAWING | REVISION 10

Linear Paul Trap - TRIUMF

	NAME	DATE
DRAWN	XS	14/02/2020
CHK'D		
APPV'D		
REV'D		

TITLE:

QMF Inner Assembly

MATERIAL: -

DWG NO. LPT2Q

A4

QUANTITY: 1 | SCALE: 1:6 | SHEET 15 OF 39

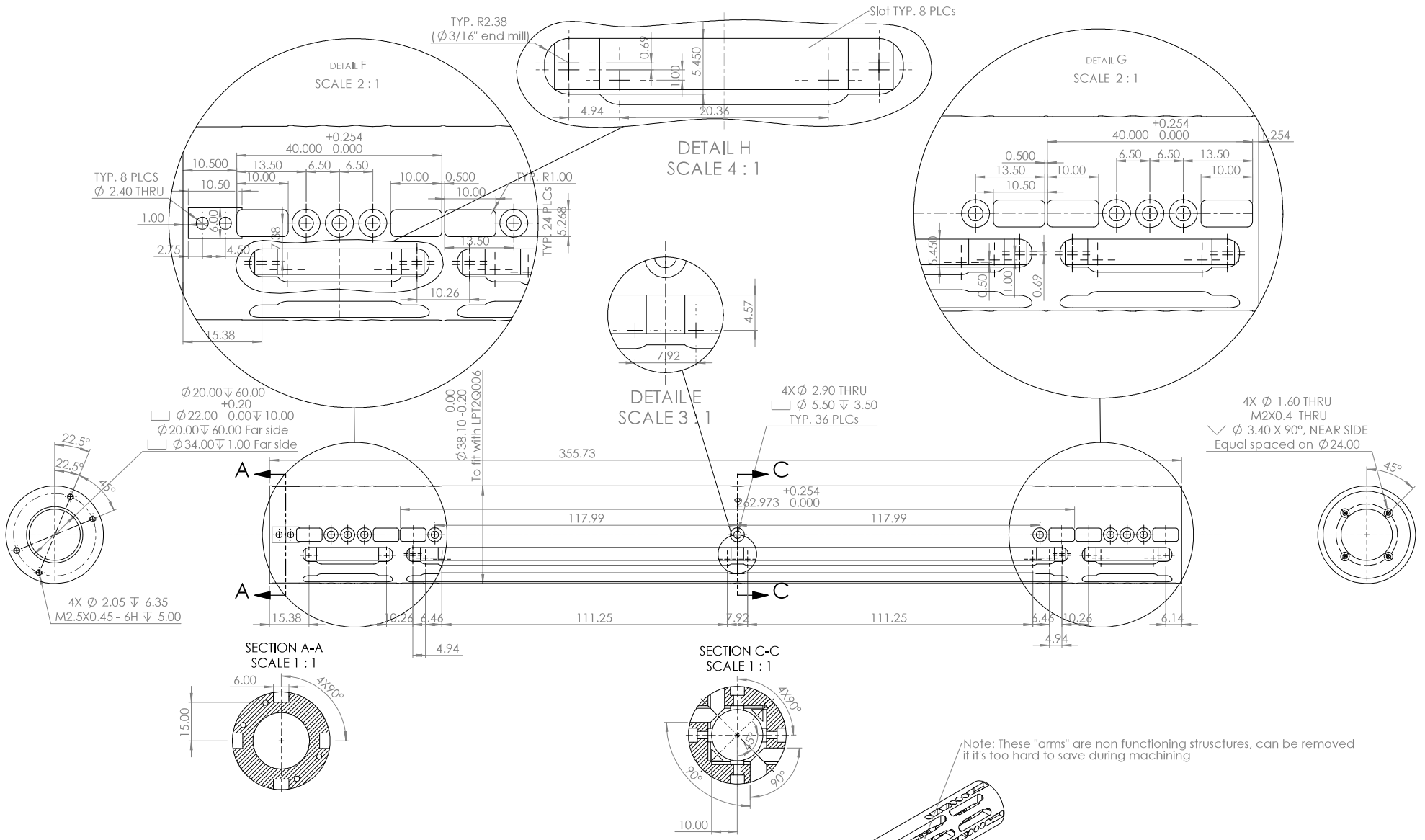

Qty	Description
1	QMF electrodes holder.

UNLESS OTHERWISE SPECIFIED:
DIMENSIONS ARE IN MILLIMETERS
SURFACE FINISH:
TOLERANCES:
LINEAR: Two place decimal: ±0.25
Three place decimal: ±0.127
ANGULAR: MACH ±0.1

FINISH: | DEBURR AND BREAK SHARP EDGES

	NAME	SIGNATURE	DATE
DRAWN	XS		
REVD	XS		20190814
APPV'D			
MFG			
Q.A			

MATERIAL: PEEK

Quality: 1

DO NOT SCALE DRAWING | REVISION 2 | 10

TITLE: Linear Paul Trap - TRIUMF

QMF Quad Electrodes holder

DWG NO. LPT2Q001 | A2

SCALE:1:2 | SHEET 16 OF 39

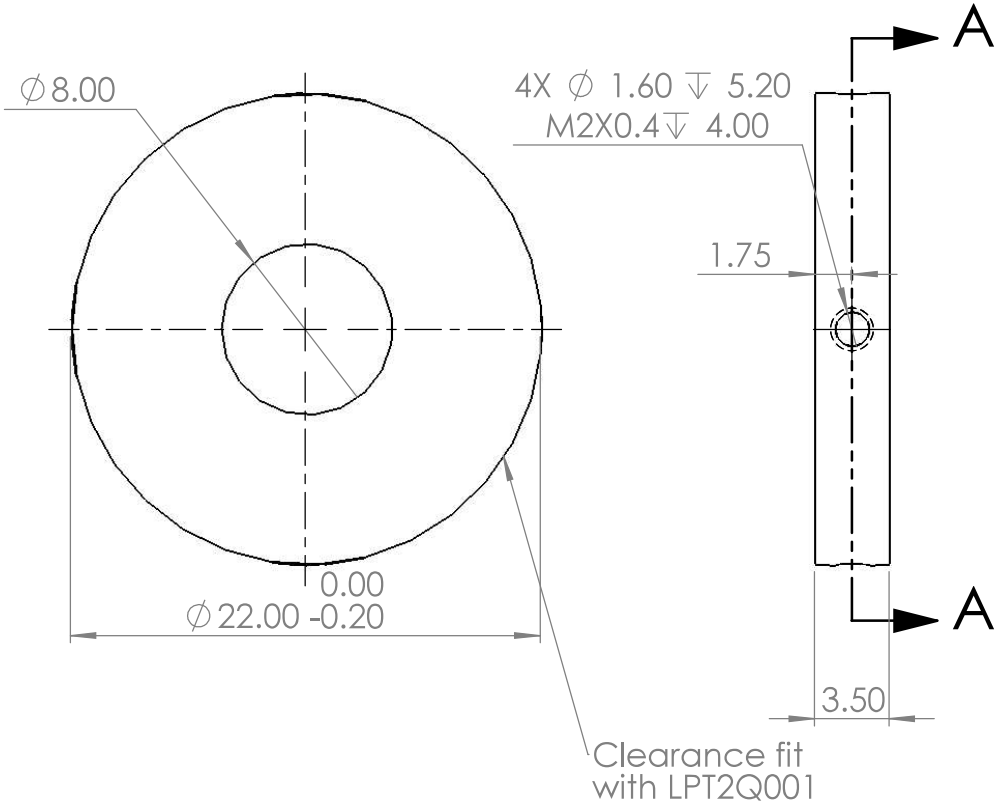

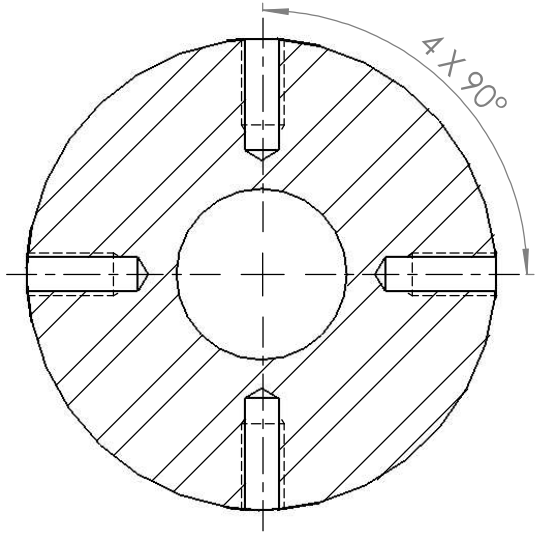

SECTION A-A

SCALE 3 : 1

UNLESS OTHERWISE SPECIFIED: DIMENSIONS ARE IN MILLIMETERS SURFACE FINISH: TOLERANCES: LINEAR: Two place decimal: ±0.25 Three place decimal: ±0.127 ANGULAR: MACH ±0.1	DO NOT SCALE DRAWING	REVISION 10
	Linear Paul Trap - TRIUMF	
NAME / DATE DRAWN XS 14/02/2020 CHK'D APPV'D REV'D	TITLE: Aperture lens at entrance of QMF	
MATERIAL: 304 Stainless Steel	DWG NO. LPT2Q002, LPT2Q003	A4
QUANTITY: 2	SCALE: 3:1	SHEET 17 OF 39

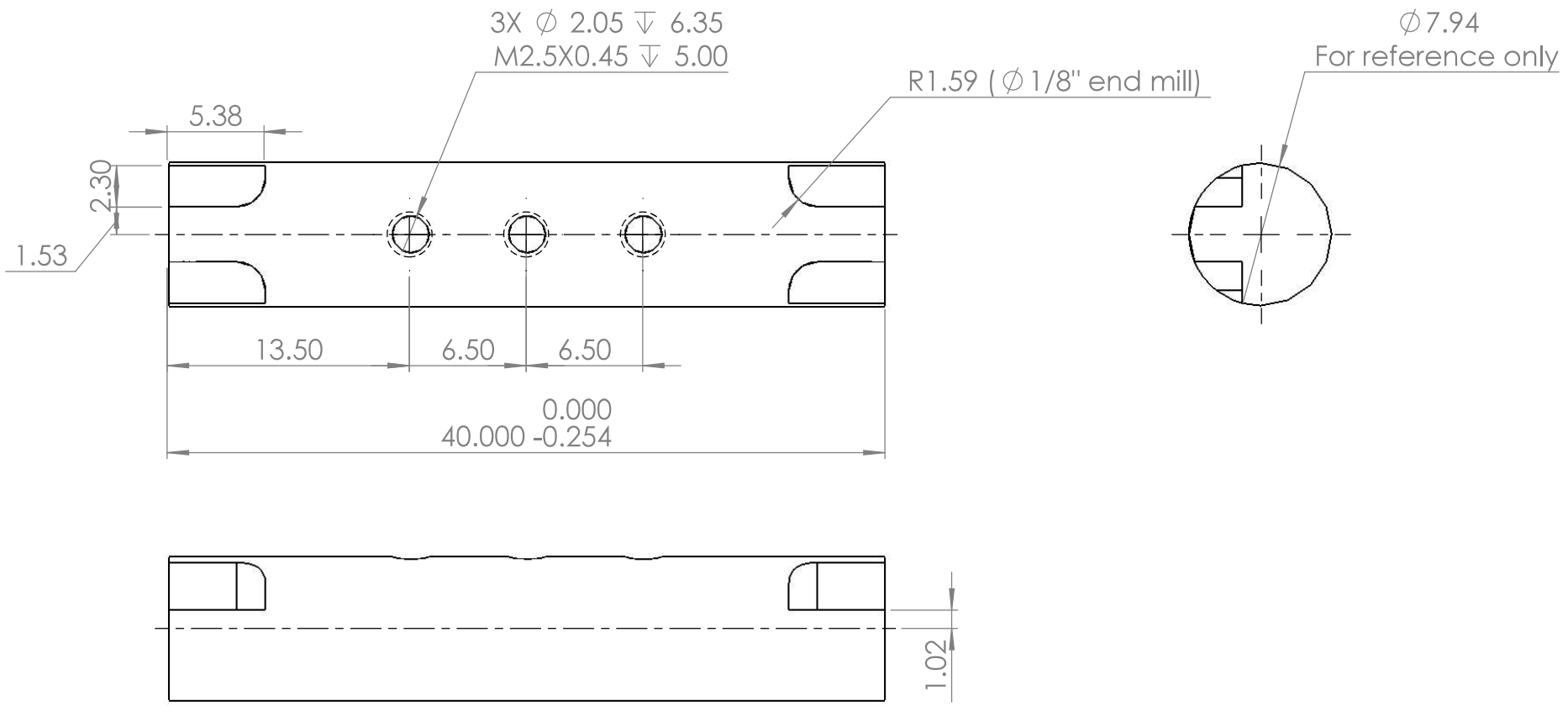

UNLESS OTHERWISE SPECIFIED: DIMENSIONS ARE IN MILLIMETERS SURFACE FINISH: TOLERANCES: LINEAR: Two place decimal: ±0.25 Three place decimal: ±0.127 ANGULAR: MACH ±0.1	DO NOT SCALE DRAWING	REVISION 10
	Linear Paul Trap - TRIUMF	
NAME / DATE DRAWN XS 14/02/2020 CHK'D APPV'D REV'D	TITLE: 1st & 3rd quad electrode for QMF	
MATERIAL: 304ss Available From McMaster Carr Part# 1255T15	DWG NO. LPT2Q004, LPT2Q007	A4
QUANTITY: 8	SCALE: 3:1	SHEET 18 OF 39

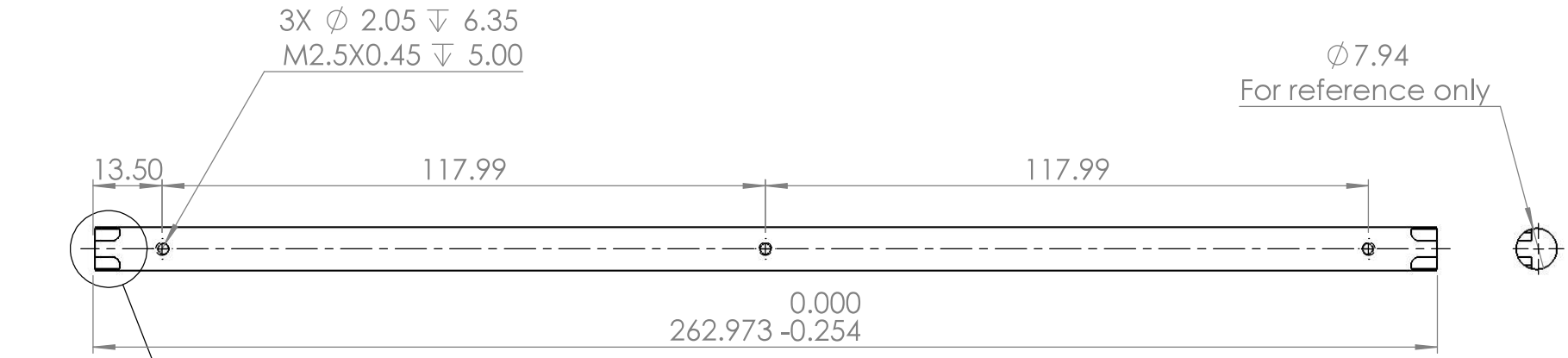

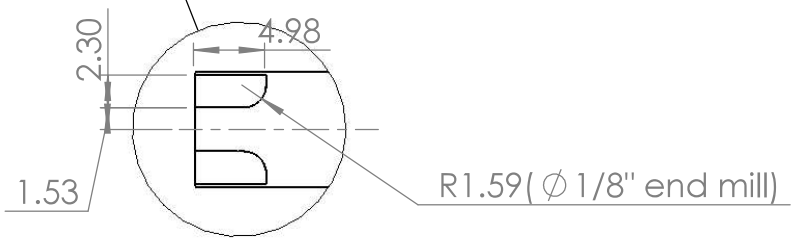

DETAIL A
SCALE 2 : 1

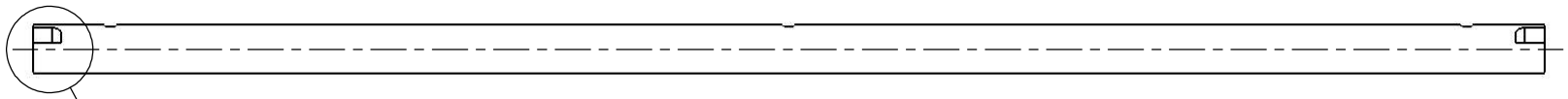

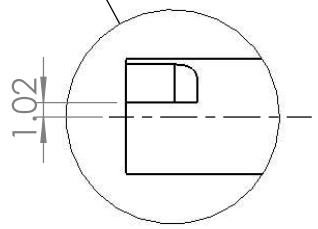

DETAIL B
SCALE 2 : 1

UNLESS OTHERWISE SPECIFIED: DIMENSIONS ARE IN MILLIMETERS SURFACE FINISH: TOLERANCES: LINEAR: Two place decimal: ±0.25 Three place decimal: ±0.127 ANGULAR: MACH ±0.1	DO NOT SCALE DRAWING	REVISION 10
	Linear Paul Trap - TRIUMF	
NAME / DATE	TITLE: 2nd quad electrode for QMF	
DRAWN XS 14/02/2020		
CHK'D		
APPV'D		
REV'D		
MATERIAL: 304ss Available From McMaster Carr Part# 1255T15	DWG NO. LPT2Q005	A4
QUANTITY: 4	SCALE: 5:6	SHEET 19 OF 39

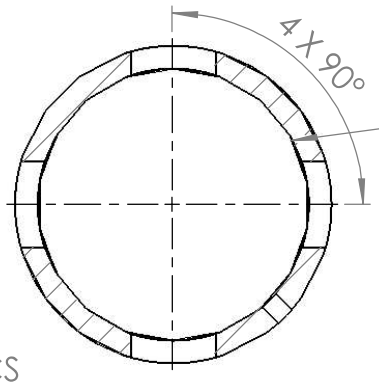

Clearace fit with LPT2Q001

TYP. 16 PLCS
∅ 12.00 THRU

SECTION A-A
SCALE 1 : 1

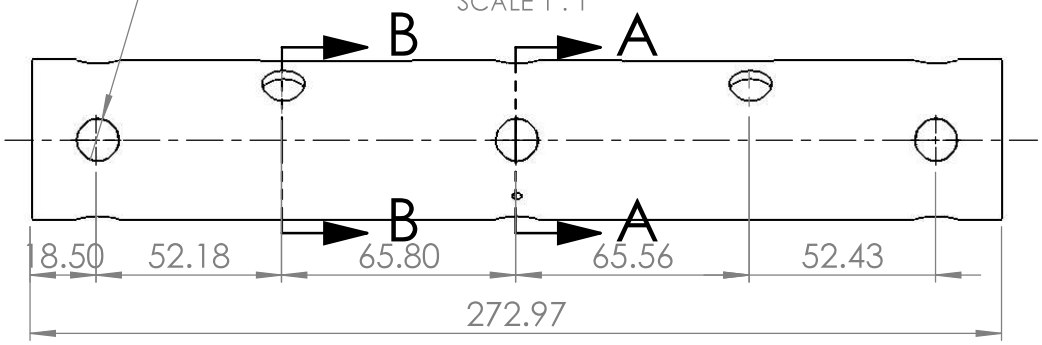

∅ 44.45
For reference only

+0.2
∅ 38.1 0.0
For reference only
Fit with LPT2Q001

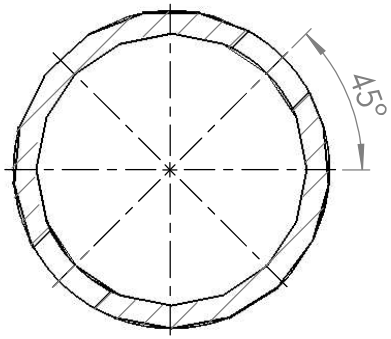

SECTION B-B
SCALE 1 : 1

ISOMETRIC VIEW

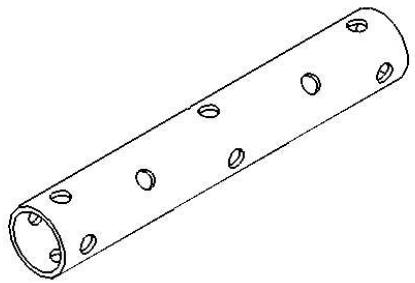

UNLESS OTHERWISE SPECIFIED: DIMENSIONS ARE IN MILLIMETERS SURFACE FINISH: TOLERANCES: LINEAR: Two place decimal: ±0.25 Three place decimal: ±0.127 ANGULAR: MACH ±0.1	DO NOT SCALE DRAWING	REVISION 10
	Linear Paul Trap - TRIUMF	
NAME / DATE	TITLE: QMF Holder Outside Tube	
DRAWN XS 14/02/2020		
CHK'D		
APPV'D		
REV'D		
MATERIAL: Aluminium 6061 Available from McMaster Carr part # 9056K39	DWG NO. LPT2Q006	A4
QUANTITY: 1	SCALE: 1:2	SHEET 20 OF 39

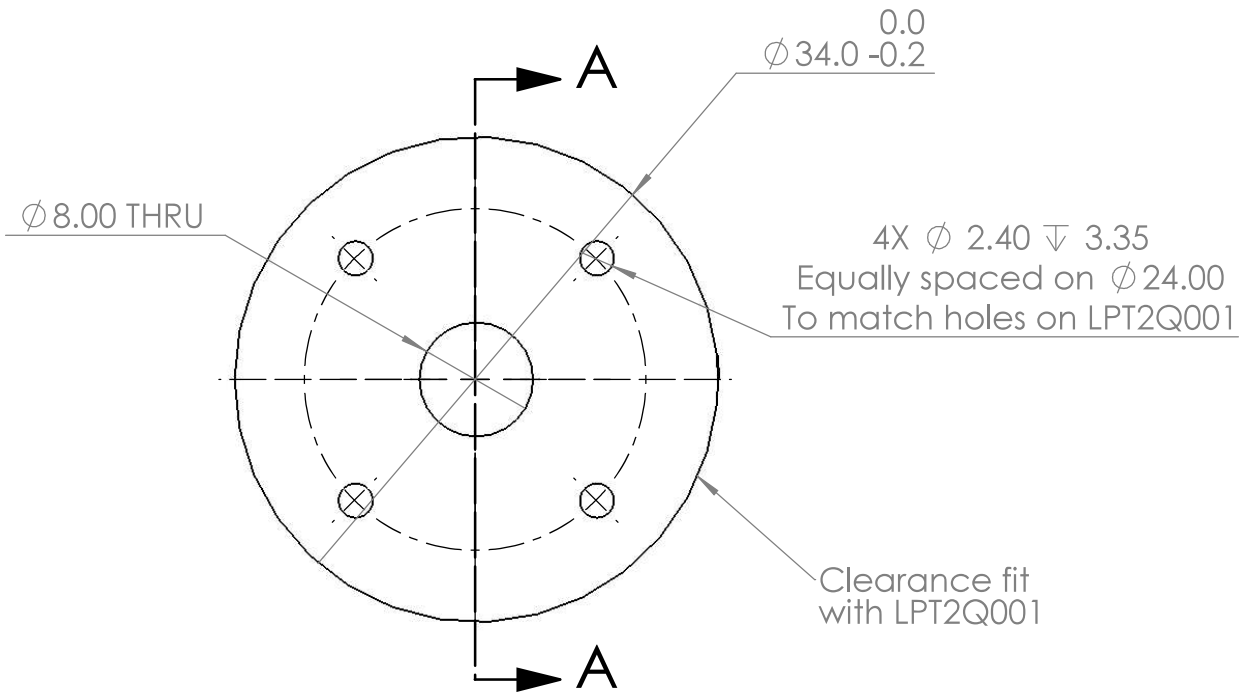

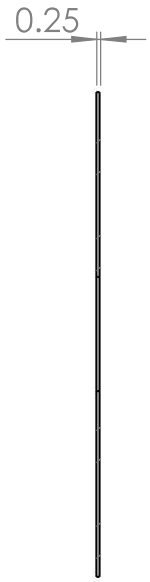

SECTION A-A

SCALE 2 : 1

UNLESS OTHERWISE SPECIFIED: DIMENSIONS ARE IN MILLIMETERS SURFACE FINISH: TOLERANCES: LINEAR: Two place decimal: ±0.25 Three place decimal: ±0.127 ANGULAR: MACH ±0.1	DO NOT SCALE DRAWING	REVISION 10
	Linear Paul Trap - TRIUMF	
NAME / DATE DRAWN XS 14/02/2020 CHK'D APPV'D REV'D	TITLE: Aperture lens at exit of QMF	
MATERIAL: 304 Stainless Steel	DWG NO. LPT2Q008	A4
QUANTITY: 1	SCALE: 2:1	SHEET 21 OF 39

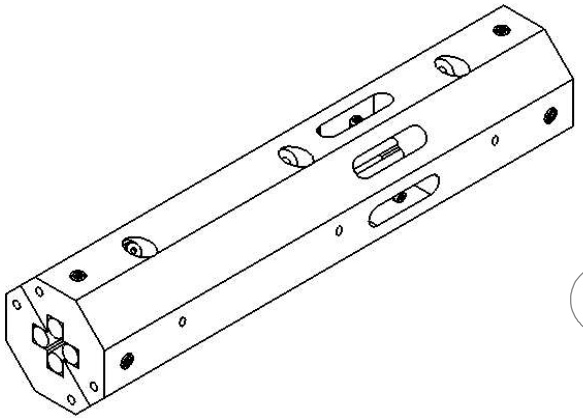

Isometric view
SCALE 1 : 3

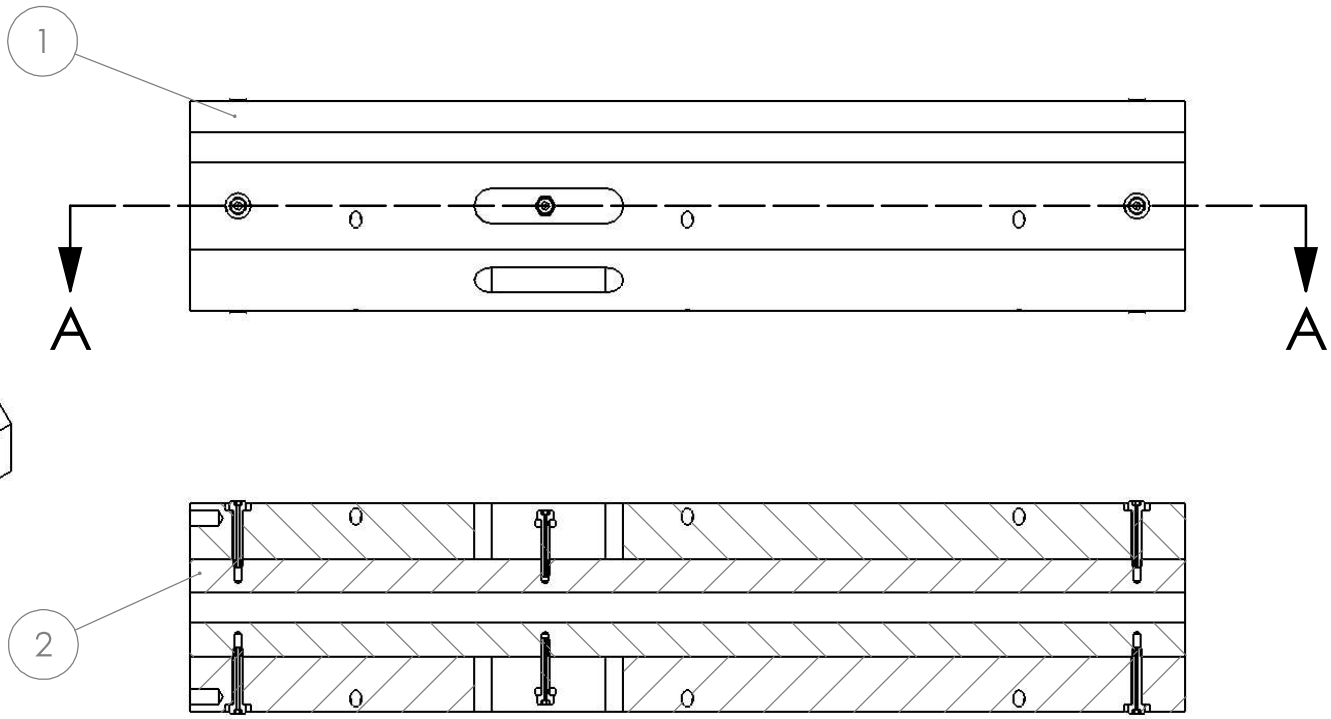

SECTION A-A
SCALE 1 : 2

ITEM NO.	PART NUMBER	DESCRIPTION	QTY.
1	precooler_holder	Pre-cooler Holder	2
2	LPT2CP02	Quad electrode for pre-cooler	4

UNLESS OTHERWISE SPECIFIED:
DIMENSIONS ARE IN MILLIMETERS
SURFACE FINISH:
TOLERANCES:
LINEAR: Two place decimal: ±0.25
Three place decimal: ±0.127
ANGULAR: MACH ±0.1

DO NOT SCALE DRAWING | REVISION 10

Linear Paul Trap - TRIUMF

	NAME	DATE
DRAWN	XS	14/02/2020
CHK'D		
APPV'D		
REV'D		

TITLE: Pre-cooler Assembly

MATERIAL: -

DWG NO. LPT2CP

A4

QUANTITY: 1 | SCALE: 1:2 | SHEET 22 OF 39

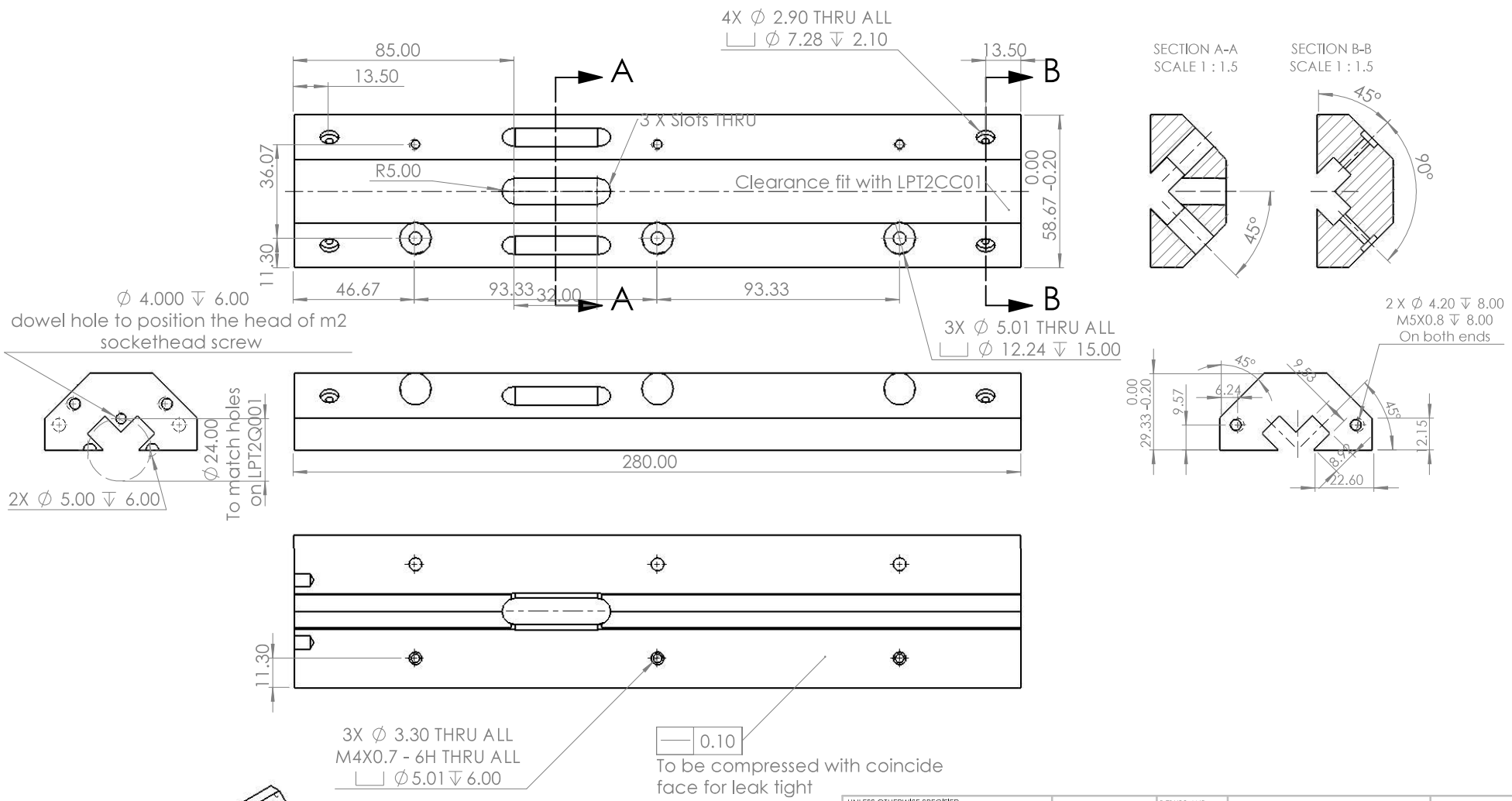

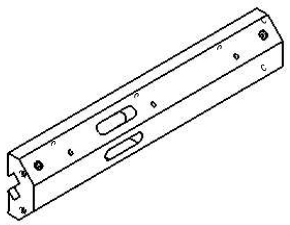

UNLESS OTHERWISE SPECIFIED: DIMENSIONS ARE IN MILLIMETERS SURFACE FINISH: TOLERANCES: LINEAR: Two place decimal: ±0.25 Three place decimal: ±0.127 ANGULAR: MACH ±0.1			FINISH:	DEBURR AND BREAK SHARP EDGES	DO NOT SCALE DRAWING	REVISION 10
					LinearPaulTrap-TRIUMF	
	NAME	SIGNATURE	DATE		TITLE: Linear Paul Trap assembly	
DRAWN	XS					
CHK'D						
APP'V'D						
MFG						
Q.A				MATERIAL: Material <not specified>	DWG NO. LPT2CP01	A3
				WEIGHT:	SCALE:1:12	SHEET 23 OF 39

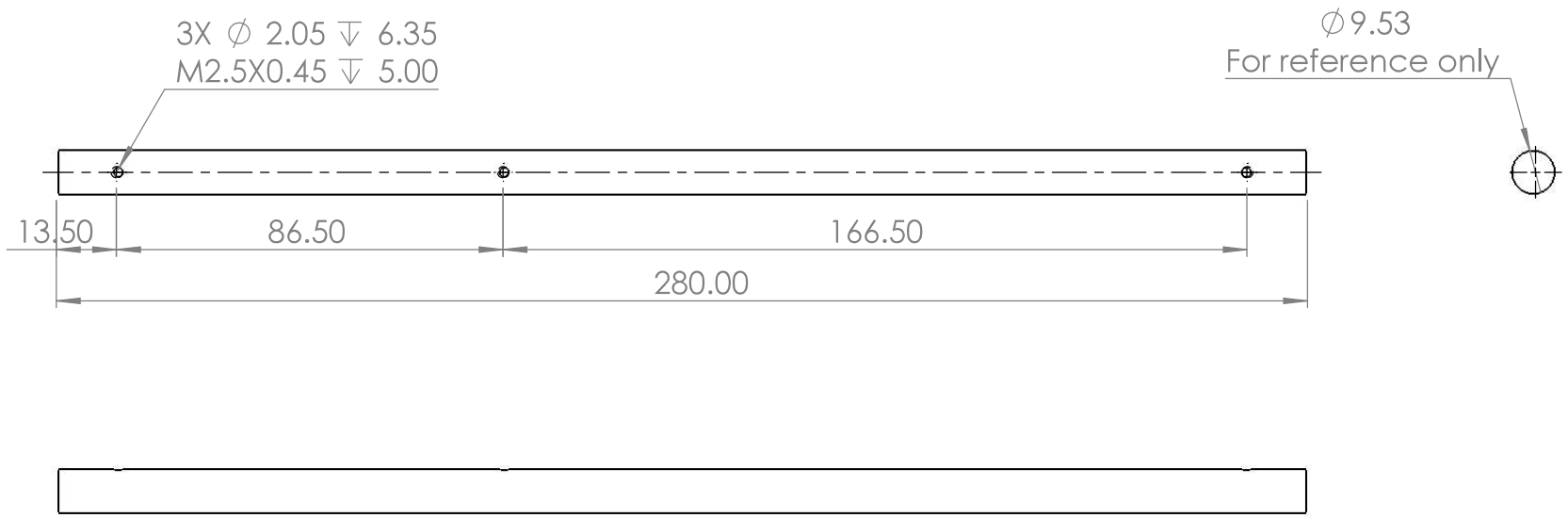

UNLESS OTHERWISE SPECIFIED: DIMENSIONS ARE IN MILLIMETERS SURFACE FINISH: TOLERANCES: LINEAR: Two place decimal: ±0.25 Three place decimal: ±0.127 ANGULAR: MACH ±0.1	DO NOT SCALE DRAWING	REVISION 10
	Linear Paul Trap - TRIUMF	
NAME / DATE DRAWN XS 14/02/2020 CHK'D APPV'D REV'D	TITLE: Pre-cooler Quad Electrode	
MATERIAL: 304ss Available From McMaster Carr Part# 1255T16	DWG NO. LPT2CP02	A4
QUANTITY: 4	SCALE: 2:3	SHEET 24 OF 39

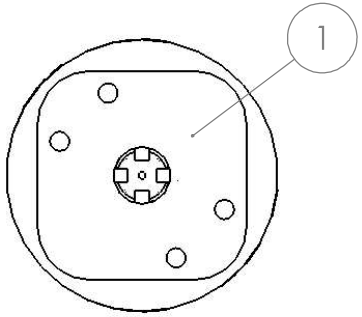

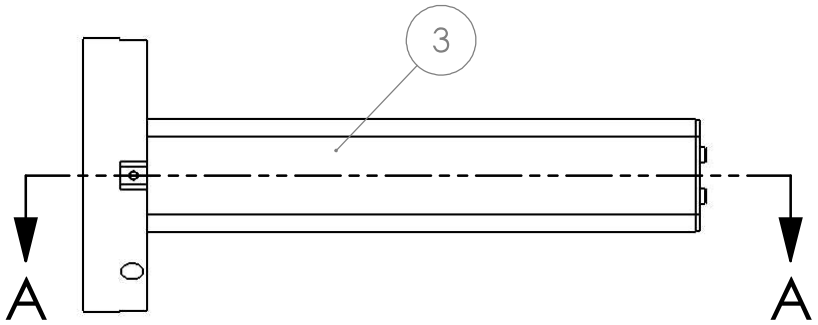

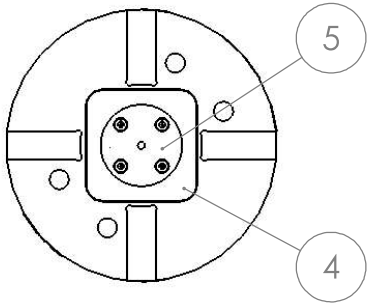

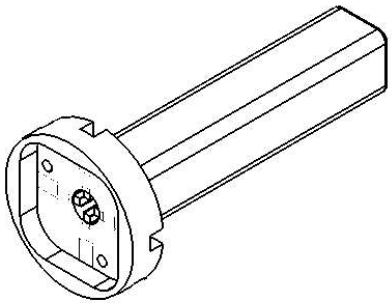

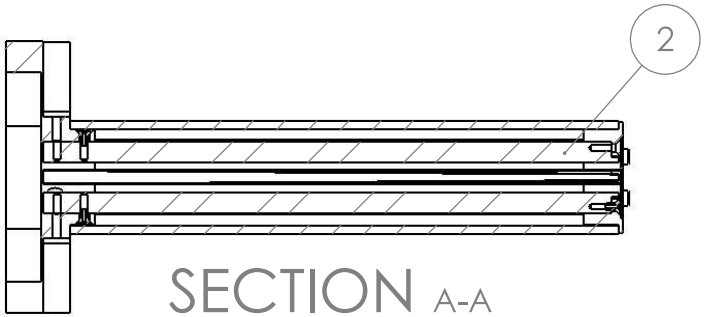

SECTION A-A

SCALE 1 : 2

ITEM NO.	PART NUMBER	DESCRIPTION	QTY.
1	LPT2CC01	Peek holder between precooler and cooler	1
2	LPT2CC02	Cooler quad electrode	4
3	LPT2CC03	Cooler Tube	1
4	LPT2CC05	Cooler exit aperture lens	1

UNLESS OTHERWISE SPECIFIED:
DIMENSIONS ARE IN MILLIMETERS
SURFACE FINISH:
TOLERANCES:
LINEAR: Two place decimal: ±0.25
Three place decimal: ±0.127
ANGULAR: MACH ±0.1

DO NOT SCALE DRAWING | REVISION 10

Linear Paul Trap - TRIUMF

	NAME	DATE
DRAWN	XS	14/02/2020
CHK'D		
APPV'D		
REV'D		

TITLE: Cooler Assembly

MATERIAL: -

DWG NO. LPT2CC

A4

QUANTITY: 1 | SCALE: 1:2 | SHEET 25 OF 39

This Part will be made at TRIUMF

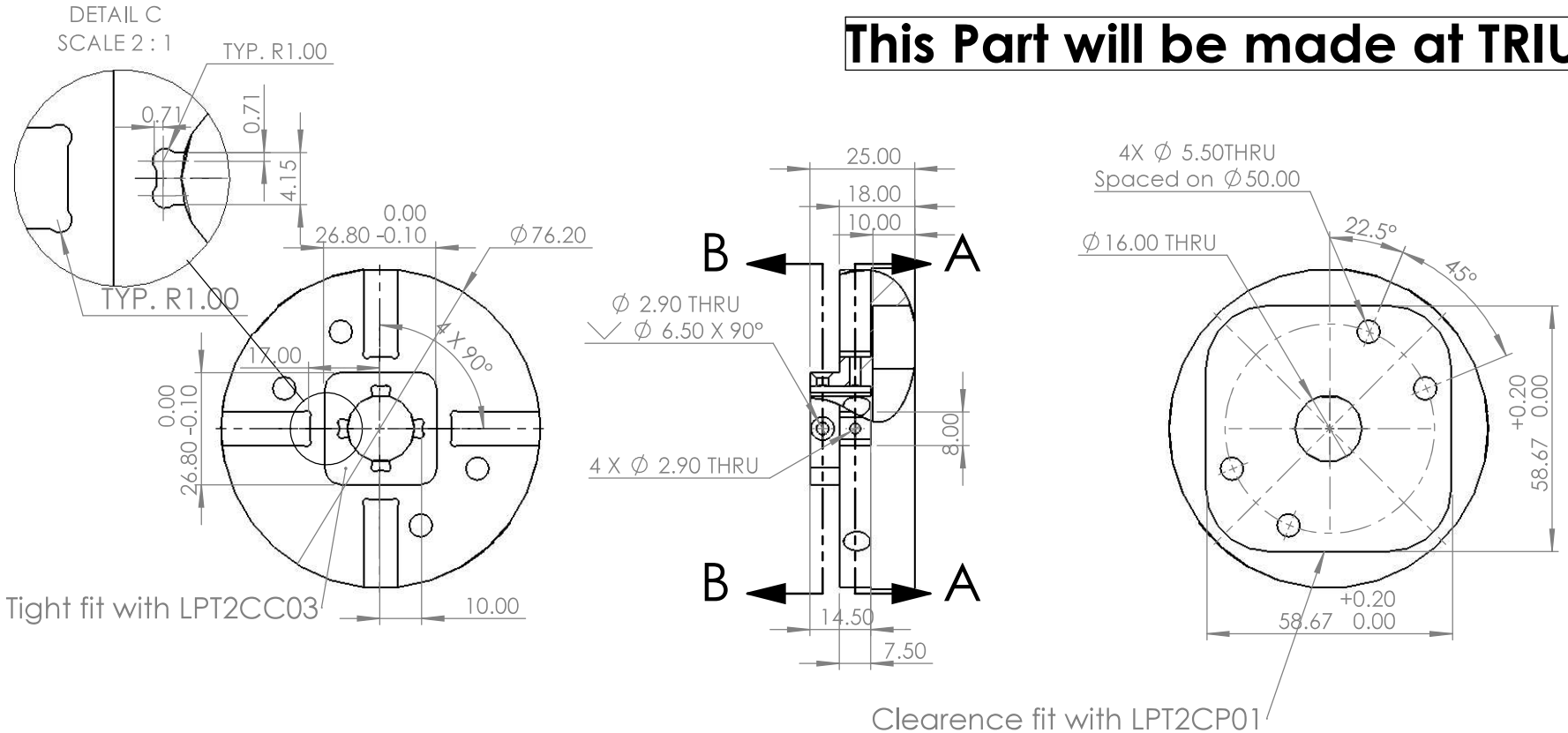

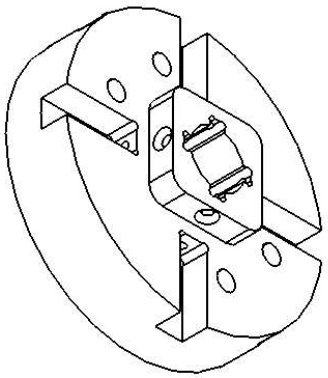

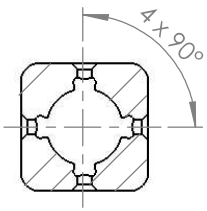

SECTION B-B
SCALE 1 : 1.5

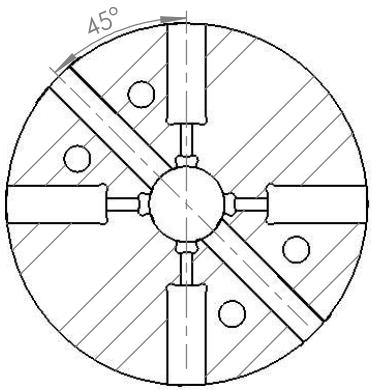

SECTION A-A
SCALE 1 : 1.5

UNLESS OTHERWISE SPECIFIED: DIMENSIONS ARE IN MILLIMETERS SURFACE FINISH: TOLERANCES: LINEAR: Two place decimal: ±0.25 Three place decimal: ±0.127 ANGULAR: MACH ±0.1	DO NOT SCALE DRAWING	REVISION 10
	Linear Paul Trap - TRIUMF	
NAME / DATE DRAWN XS 14/02/2020 CHK'D APPV'D REV'D	TITLE: Peek holder between precooler and cooler	
MATERIAL: PEEK	DWG NO. LPT2CC01	A4
QUANTITY: 1	SCALE: 2:3	SHEET 26 OF 39

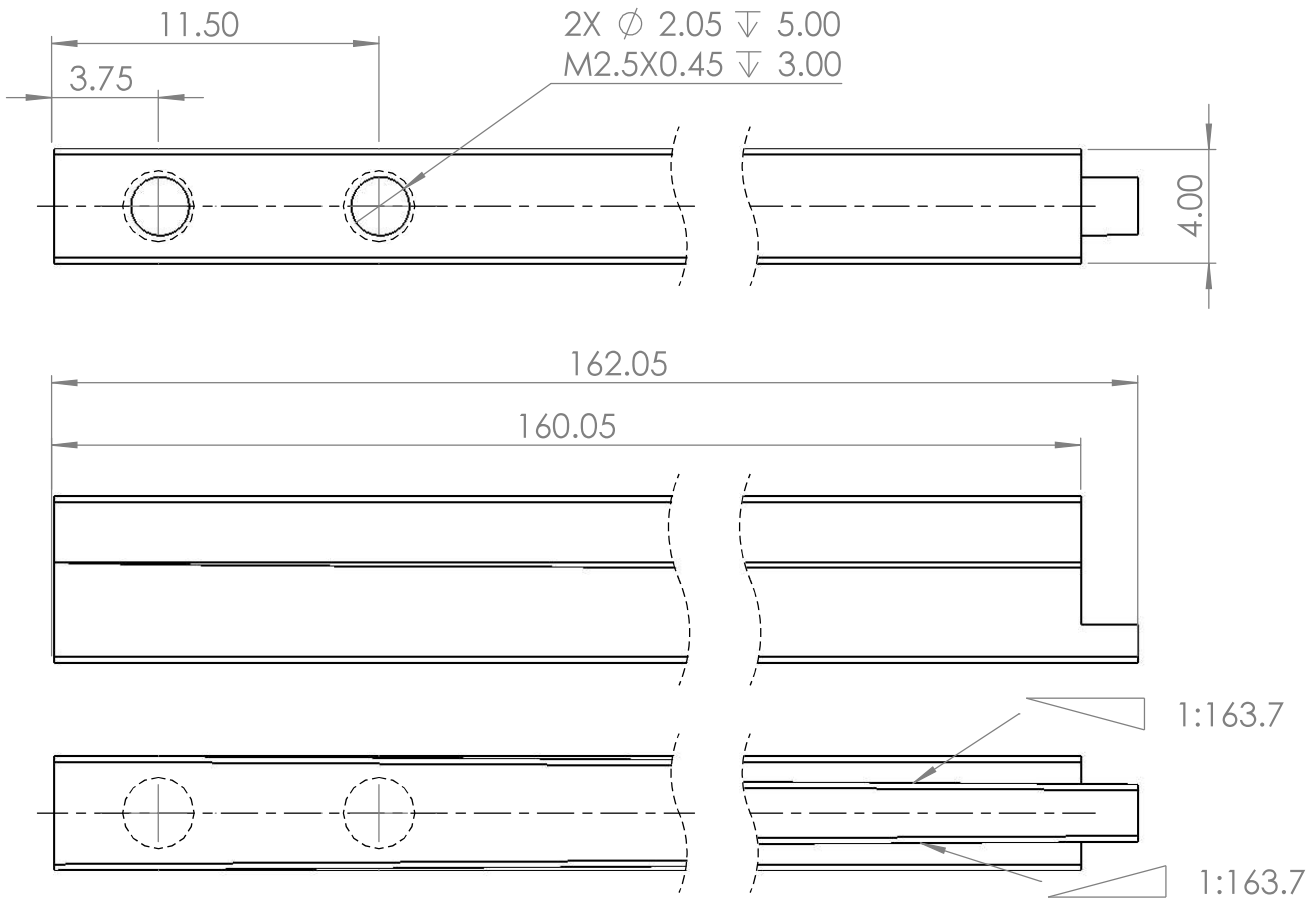

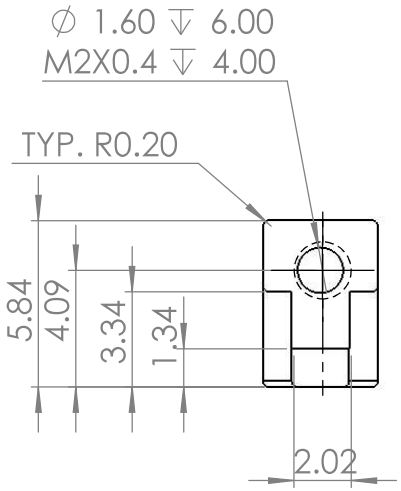

This Part will be made at TRIUMF

UNLESS OTHERWISE SPECIFIED: DIMENSIONS ARE IN MILLIMETERS SURFACE FINISH: TOLERANCES: LINEAR: Two place decimal: ±0.25 Three place decimal: ±0.127 ANGULAR: MACH ±0.1	DO NOT SCALE DRAWING	REVISION 10
	Linear Paul Trap - TRIUMF	
NAME / DATE	TITLE: Cooler quad electrode	
DRAWN XS 14/02/2020		
CHK'D		
APPV'D		
REV'D		
MATERIAL: 304 Stainless Steel	DWG NO. LPT2CC02	A4
QUANTITY: 4	SCALE: 4:1	SHEET 27 OF 39

This Part will be made at TRIUMF

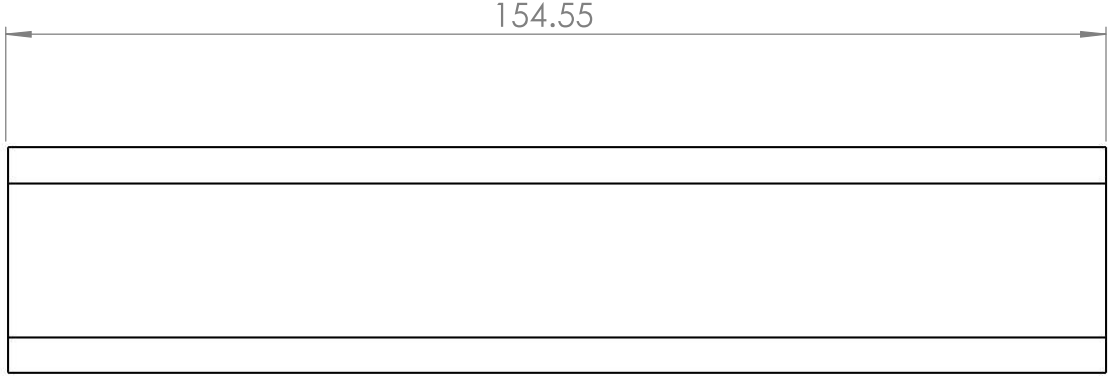

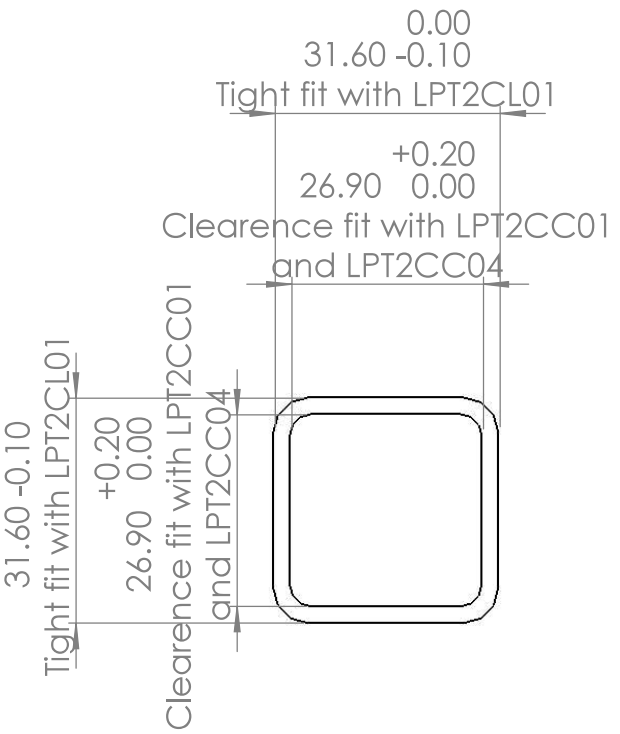

UNLESS OTHERWISE SPECIFIED: DIMENSIONS ARE IN MILLIMETERS SURFACE FINISH: TOLERANCES: LINEAR: Two place decimal: ±0.25 Three place decimal: ±0.127 ANGULAR: MACH ±0.1	DO NOT SCALE DRAWING	REVISION 10
	Linear Paul Trap - TRIUMF	
NAME / DATE	TITLE: Cooler Tube	
DRAWN: XS 14/02/2020		
CHK'D		
APPV'D		
REV'D		
MATERIAL: Aluminium 6061	DWG NO. LPT2CC03	A4
QUANTITY: 1	SCALE: 1:1	SHEET 28 OF 39

This Part will be made at TRIUMF

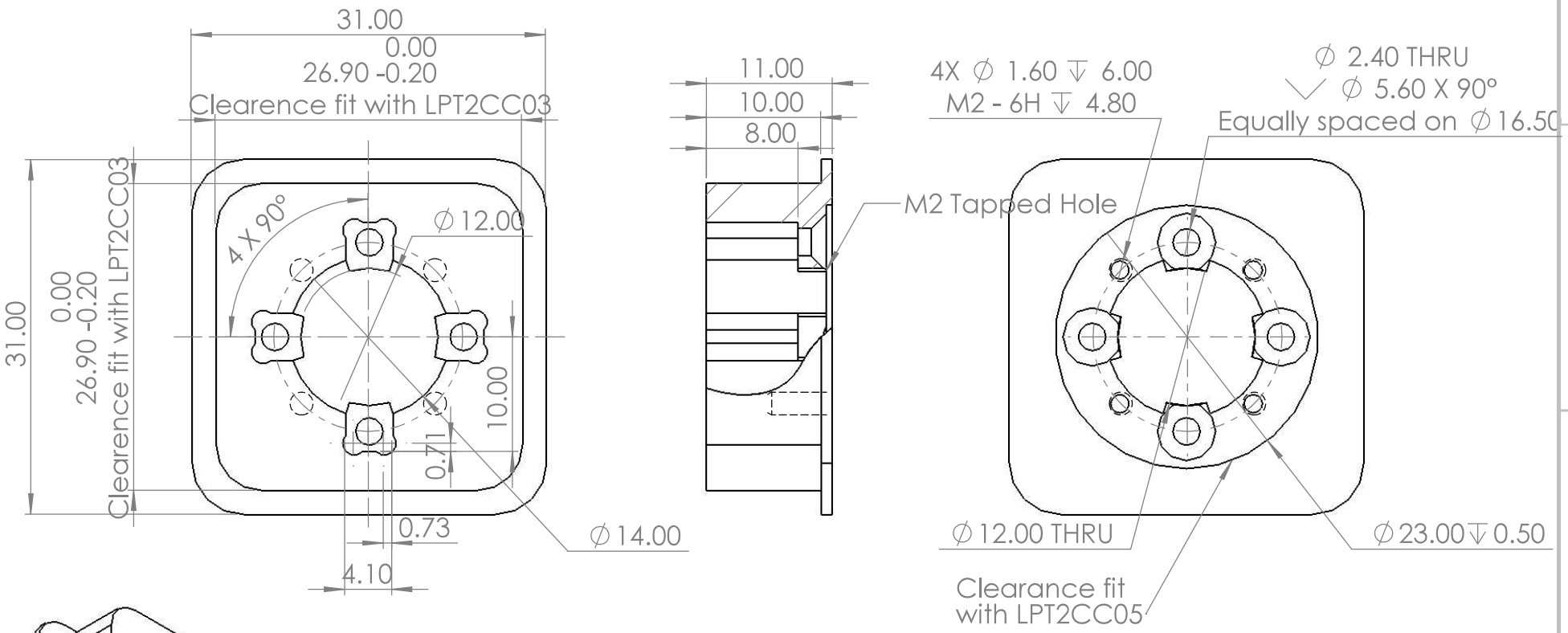

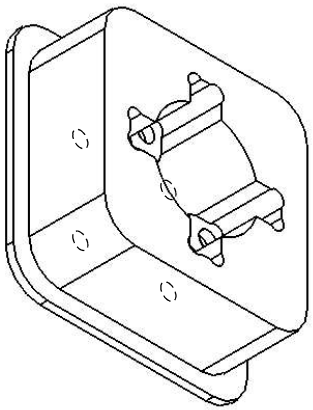

UNLESS OTHERWISE SPECIFIED: DIMENSIONS ARE IN MILLIMETERS SURFACE FINISH: TOLERANCES: LINEAR: Two place decimal: ±0.25 Three place decimal: ±0.127 ANGULAR: MACH ±0.1	DO NOT SCALE DRAWING	REVISION 10
	Linear Paul Trap - TRIUMF	
NAME / DATE DRAWN XS 14/02/2020 CHK'D APPV'D REV'D	TITLE: Cooler Exit PEEK Holder	
MATERIAL: PEEK	DWG NO. LPT2CC04	A4
QUANTITY: 1	SCALE: 3:1	SHEET 29 OF 39

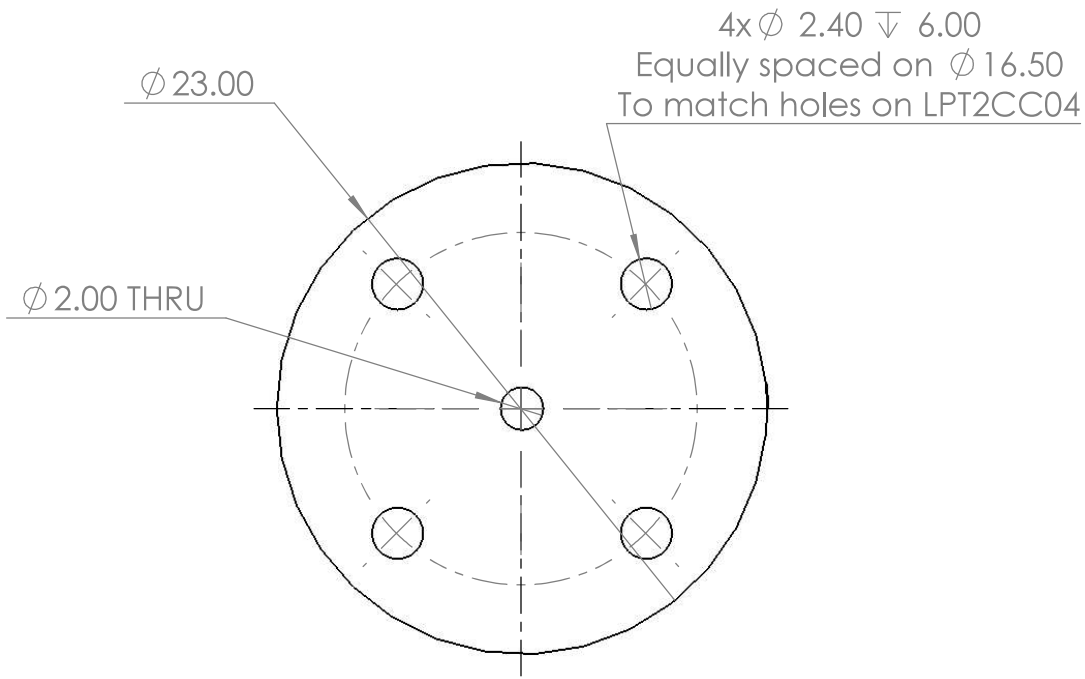

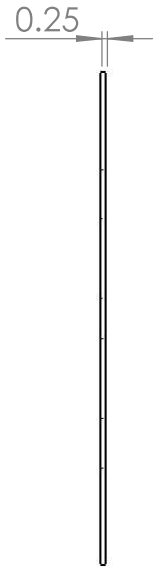

UNLESS OTHERWISE SPECIFIED: DIMENSIONS ARE IN MILLIMETERS SURFACE FINISH: TOLERANCES: LINEAR: Two place decimal: ±0.25 Three place decimal: ±0.127 ANGULAR: MACH ±0.1	DO NOT SCALE DRAWING	REVISION 10
	Linear Paul Trap - TRIUMF	
NAME / DATE DRAWN XS 14/02/2020 CHK'D APPV'D REV'D	TITLE: Cooler Exit Aperture Lens	
MATERIAL: 304 Stainless Steel	DWG NO. LPT2CC05	A4
QUANTITY: 3	SCALE: 1:6	SHEET 30 OF 39

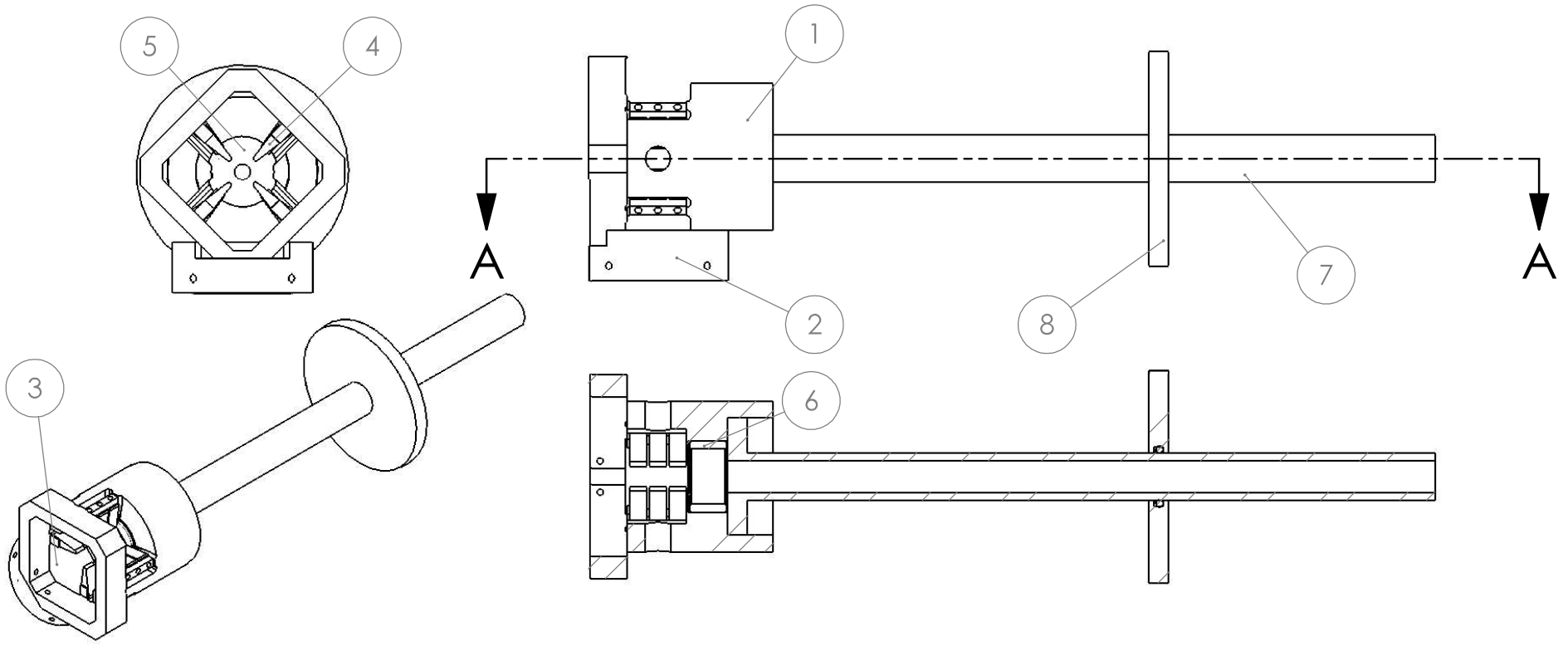

ITEM NO.	PART NUMBER	DESCRIPTION	QTY.
1	LPT2CL01	Electrodes Holder	1
2	LPT2CL02	Spherical Mirror Holder	1
3	LPT2CL03	THORLABS Ø1" Dielectric-Coated Concave Mirror	1
4	LPT2CL04	Quad Electrode	12
5	LPT2CL05	Buncher Entrance Aperture Lens	1
6	LPT2CL06	Insulating Spacer	1
7	LPT2CL07	Buncher Aperture Lens	1
8	LPT2CL08	CLB Exit Holder	1

SECTION A-A

SCALE 2 : 3

UNLESS OTHERWISE SPECIFIED:
DIMENSIONS ARE IN MILLIMETERS
SURFACE FINISH:
TOLERANCES:
LINEAR: Two place decimal: ±0.25
Three place decimal: ±0.127
ANGULAR: MACH ±0.1

DO NOT SCALE DRAWING | REVISION 10

Linear Paul Trap - TRIUMF

	NAME	DATE
DRAWN	XS	14/02/2020
CHK'D		
APPV'D		
REV'D		

TITLE:

Laser Spectroscopy and Buncher Assembly

MATERIAL: -

DWG NO. LPT2CL

A4

QUANTITY: 1 | SCALE: 1:1 | SHEET 31 OF 39

This Part will be made at TRIUMF

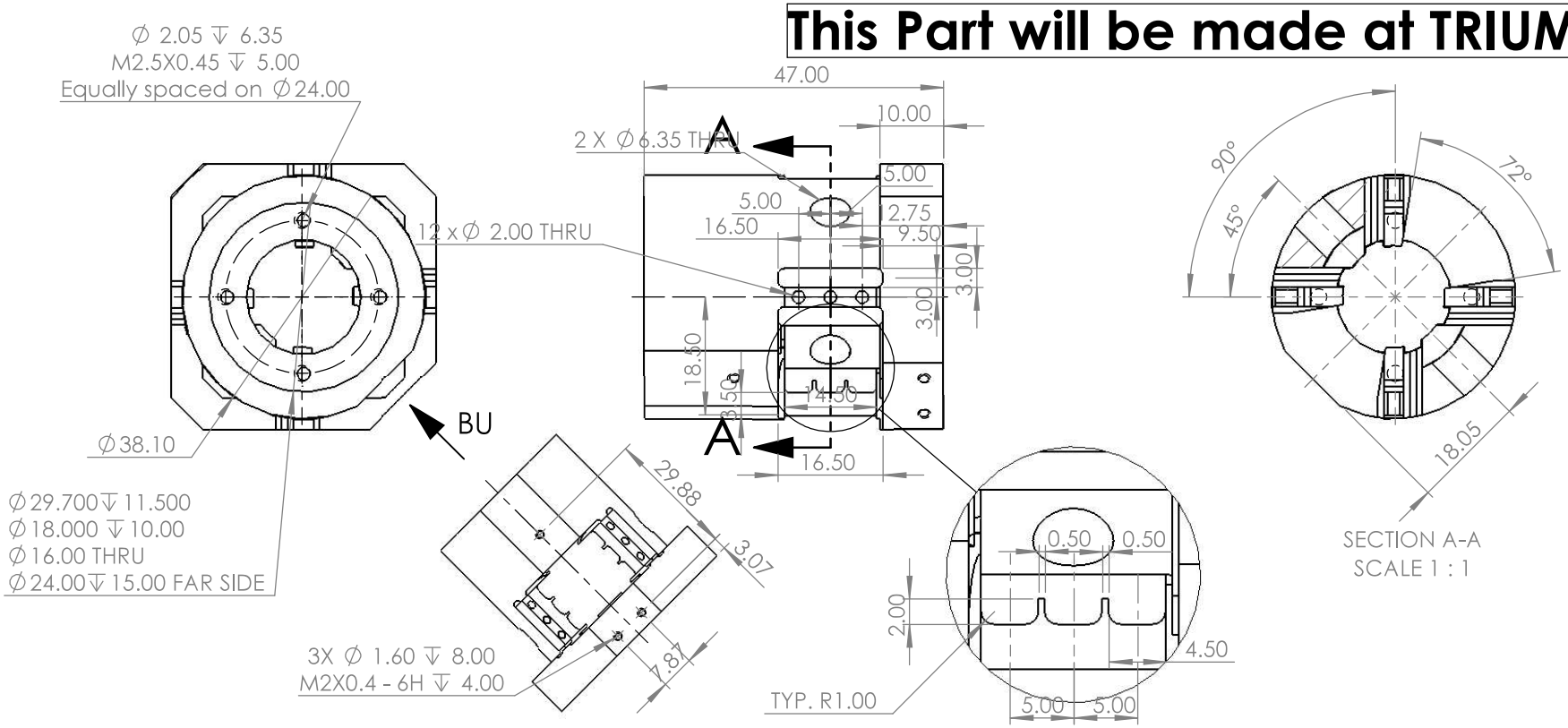

SECTION A-A
SCALE 1 : 1

VIEW BU
SCALE 1 : 1.5

DETAIL C
SCALE 2 : 1

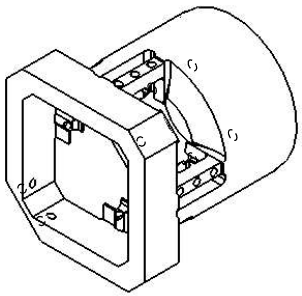

UNLESS OTHERWISE SPECIFIED: DIMENSIONS ARE IN MILLIMETERS SURFACE FINISH: TOLERANCES: LINEAR: Two place decimal: ±0.25 Three place decimal: ±0.127 ANGULAR: MACH ±0.1	DO NOT SCALE DRAWING	REVISION 10
	Linear Paul Trap - TRIUMF	
NAME / DATE	TITLE: Electrodes Holder	
DRAWN: XS 14/02/2020		
CHK'D		
APPV'D		
REV'D		
MATERIAL: PEEK	DWG NO. LPT2CL01	A4
QUANTITY: 1	SCALE: 1:1	SHEET 32 OF 39

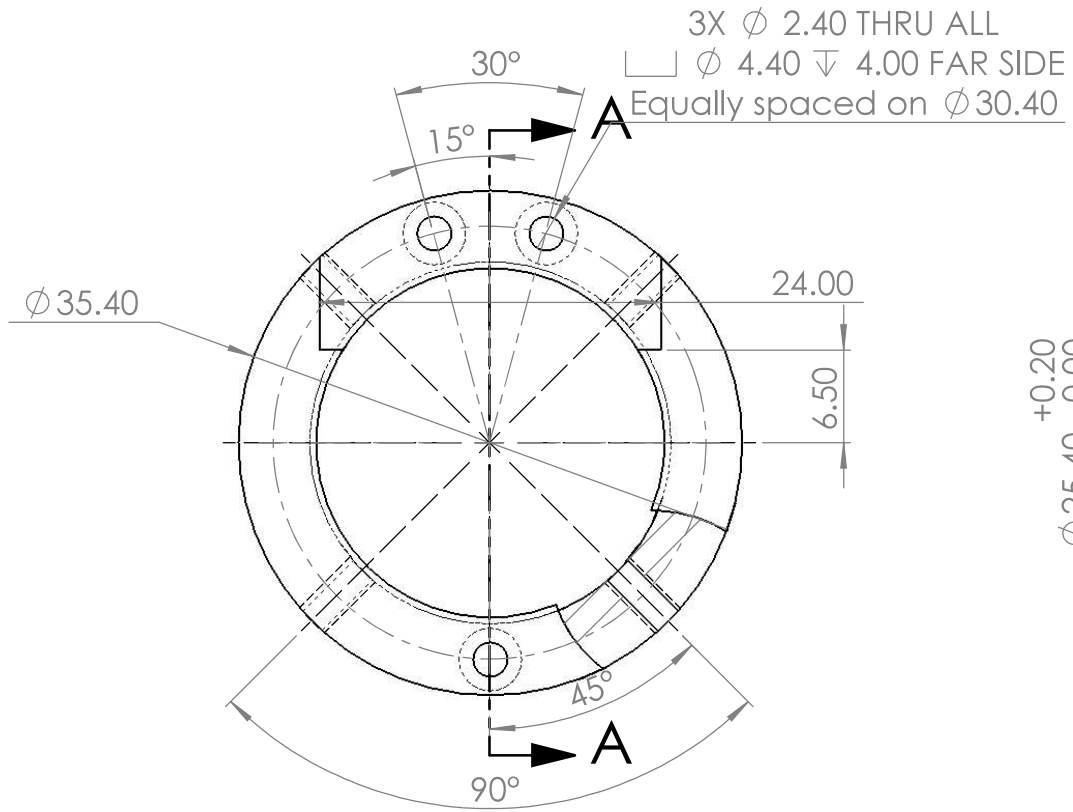

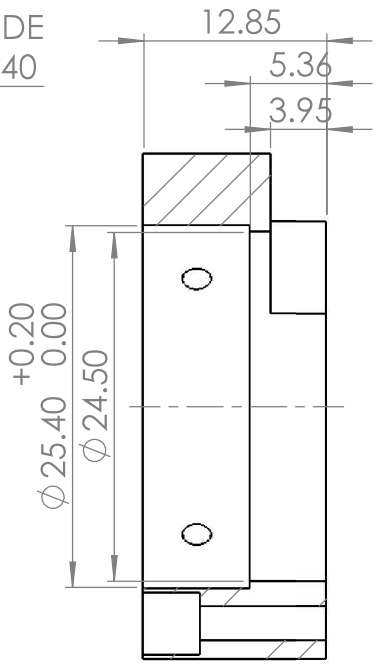

SECTION A-A

SCALE 2 : 1

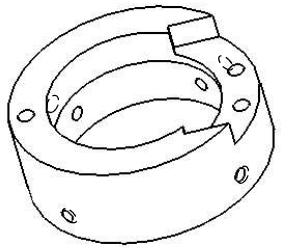

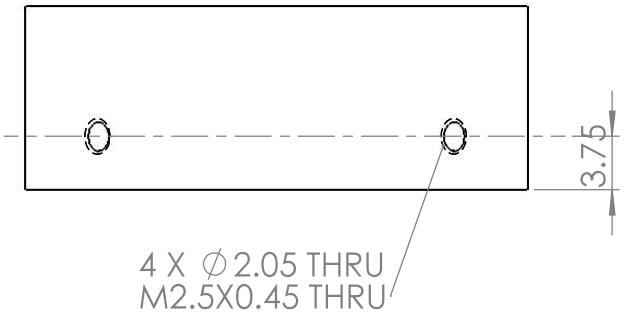

UNLESS OTHERWISE SPECIFIED: DIMENSIONS ARE IN MILLIMETERS SURFACE FINISH: TOLERANCES: LINEAR: Two place decimal: ±0.25 Three place decimal: ±0.127 ANGULAR: MACH ±0.1	DO NOT SCALE DRAWING	REVISION 10
	Linear Paul Trap - TRIUMF	
NAME / DATE	TITLE: Spherical Mirror Holder	
DRAWN XS 14/02/2020		
CHK'D		
APPV'D		
REV'D		
MATERIAL: PEEK	DWG NO. LPT2CL02	A4
QUANTITY: 1	SCALE: 2:1	SHEET 33 OF 39

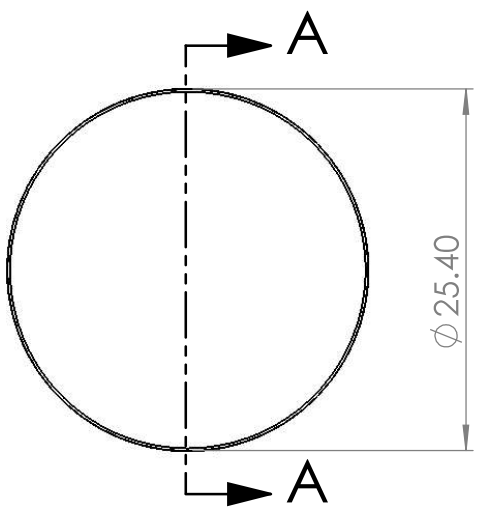

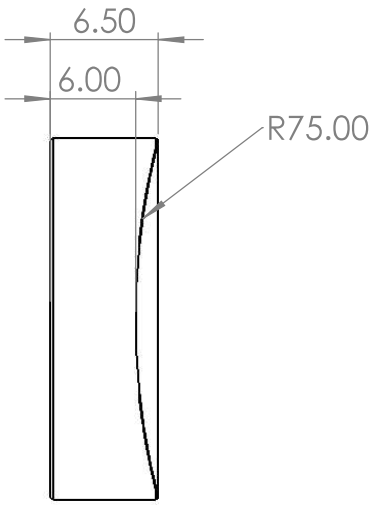

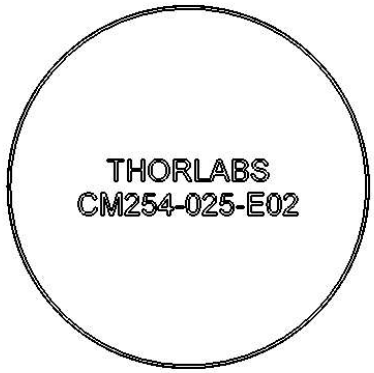

SECTION A-A

SCALE 2 : 1

All dimensions are for reference only

UNLESS OTHERWISE SPECIFIED: DIMENSIONS ARE IN MILLIMETERS SURFACE FINISH: TOLERANCES: LINEAR: Two place decimal: ±0.25 Three place decimal: ±0.127 ANGULAR: MACH ±0.1	DO NOT SCALE DRAWING	REVISION 10
	Linear Paul Trap - TRIUMF	
NAME / DATE	TITLE: Spherical Mirror	
DRAWN XS 14/02/2020		
CHK'D		
APPV'D		
REV'D		
MATERIAL: THORLABS Part# CM254-075-E03	DWG NO. LPT2CL03	A4
QUANTITY: 1	SCALE: 1:6	SHEET 34 OF 39

This Part will be made at TRIUMF

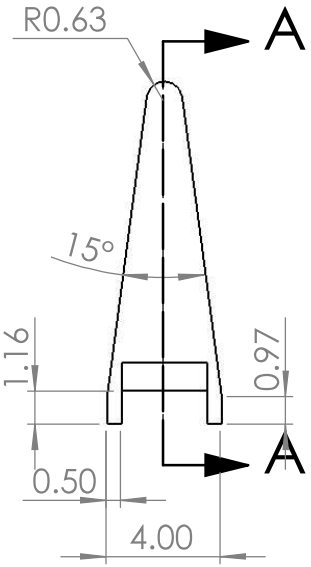

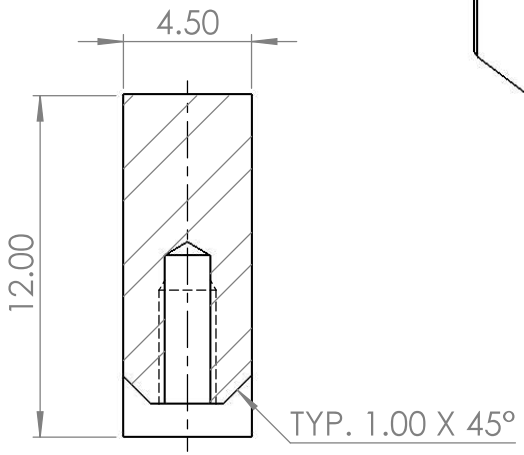

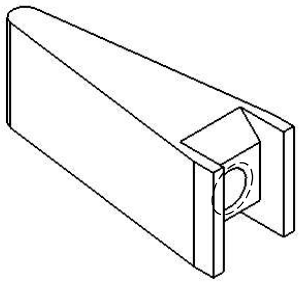

SECTION A-A

SCALE 4 : 1

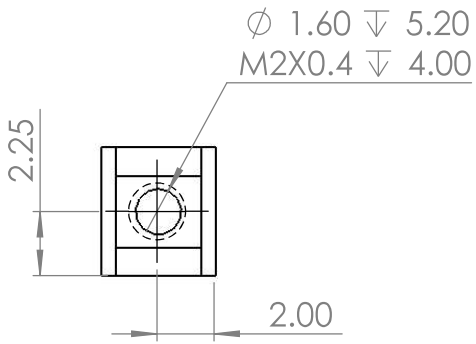

UNLESS OTHERWISE SPECIFIED: DIMENSIONS ARE IN MILLIMETERS SURFACE FINISH: TOLERANCES: LINEAR: Two place decimal: ±0.25 Three place decimal: ±0.127 ANGULAR: MACH ±0.1	DO NOT SCALE DRAWING	REVISION 10
	Linear Paul Trap - TRIUMF	
NAME / DATE	TITLE: Quad Electrode	
DRAWN: XS 14/02/2020		
CHK'D		
APPV'D		
REV'D		
MATERIAL: 304 Stainless Steel	DWG NO. LPT2CL04	A4
QUANTITY: 12	SCALE: 1:6	SHEET 35 OF 39

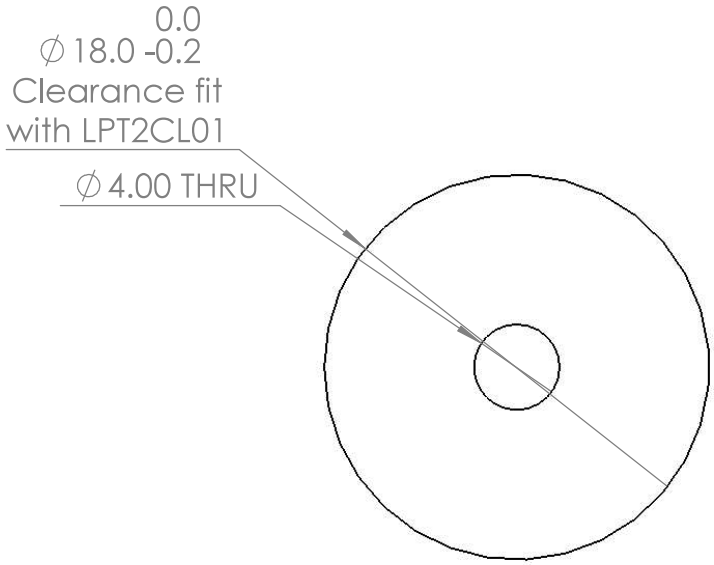

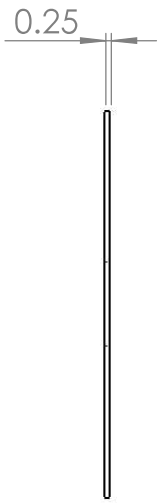

UNLESS OTHERWISE SPECIFIED: DIMENSIONS ARE IN MILLIMETERS SURFACE FINISH: TOLERANCES: LINEAR: Two place decimal: ±0.25 Three place decimal: ±0.127 ANGULAR: MACH ±0.1	DO NOT SCALE DRAWING	REVISION 10
	Linear Paul Trap - TRIUMF	
NAME / DATE DRAWN XS 14/02/2020 CHK'D APPV'D REV'D	TITLE: Buncher Entrance Aperture Lens	
MATERIAL: 304 Stainless Steel	DWG NO. LPT2CL05	A4
QUANTITY: 1	SCALE: 3:1	SHEET 36 OF 39

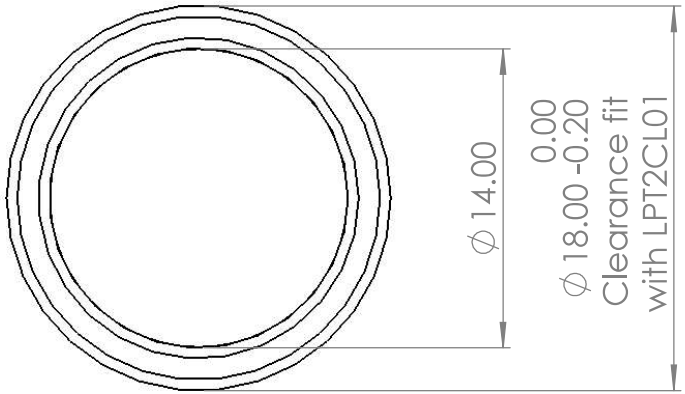

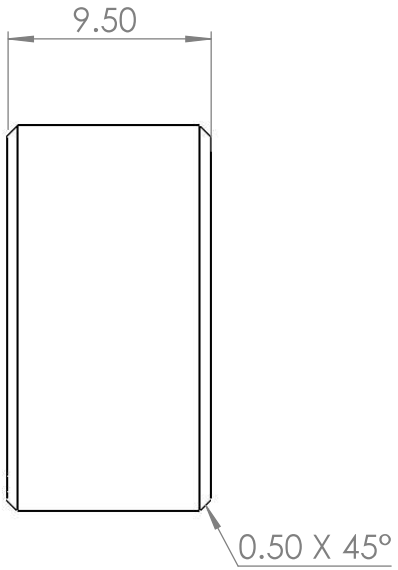

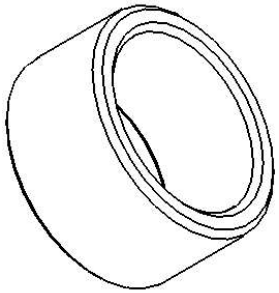

UNLESS OTHERWISE SPECIFIED: DIMENSIONS ARE IN MILLIMETERS SURFACE FINISH: TOLERANCES: LINEAR: Two place decimal: ±0.25 Three place decimal: ±0.127 ANGULAR: MACH ±0.1	DO NOT SCALE DRAWING	REVISION 10
	Linear Paul Trap - TRIUMF	
NAME / DATE DRAWN: XS 14/02/2020 CHK'D: APPV'D: REV'D:	TITLE: Insulating Spacer	
MATERIAL: PEEK	DWG NO. LPT2CL06	A4
QUANTITY: 1	SCALE: 3:1	SHEET 37 OF 39

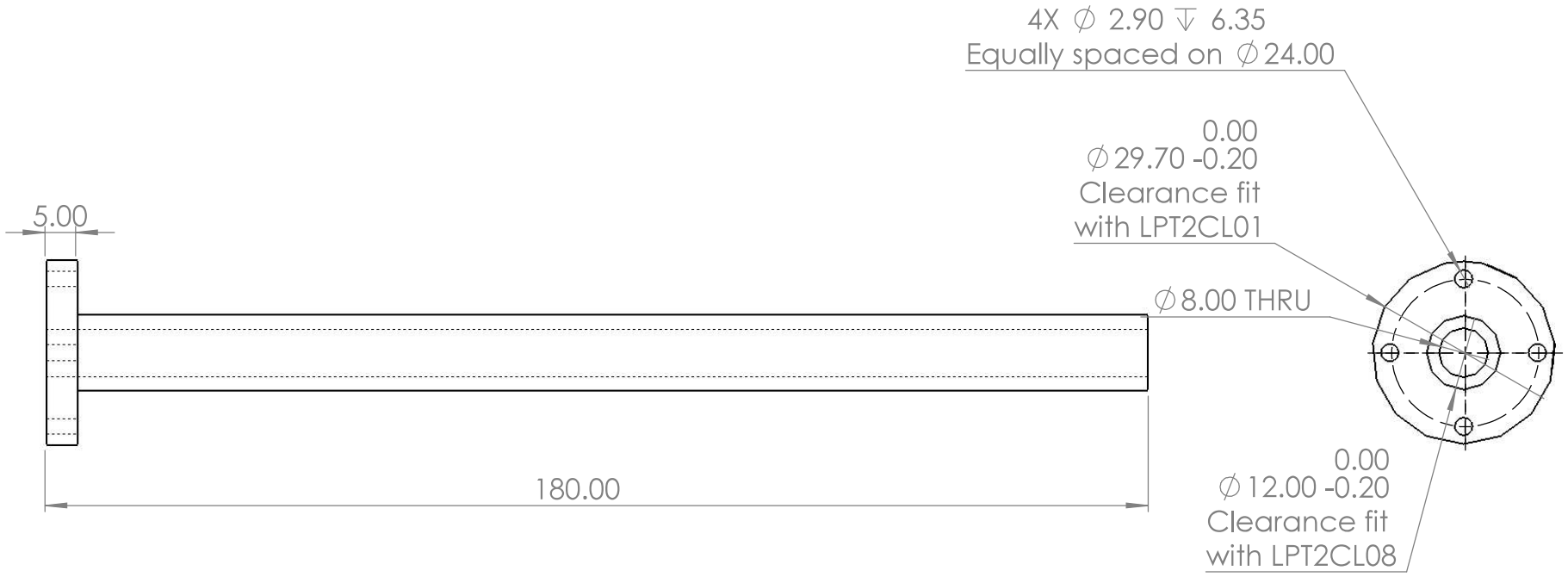

UNLESS OTHERWISE SPECIFIED: DIMENSIONS ARE IN MILLIMETERS SURFACE FINISH: TOLERANCES: LINEAR: Two place decimal: ±0.25 Three place decimal: ±0.127 ANGULAR: MACH ±0.1	DO NOT SCALE DRAWING	REVISION 10
	Linear Paul Trap - TRIUMF	
NAME / DATE DRAWN XS 14/02/2020 CHK'D APPV'D REV'D	TITLE: Buncher Aperture Lens	
MATERIAL: 304 Stainless Steel	DWG NO. LPT2CL07	A4
QUANTITY: 1	SCALE: 3:2	SHEET 38 OF 39

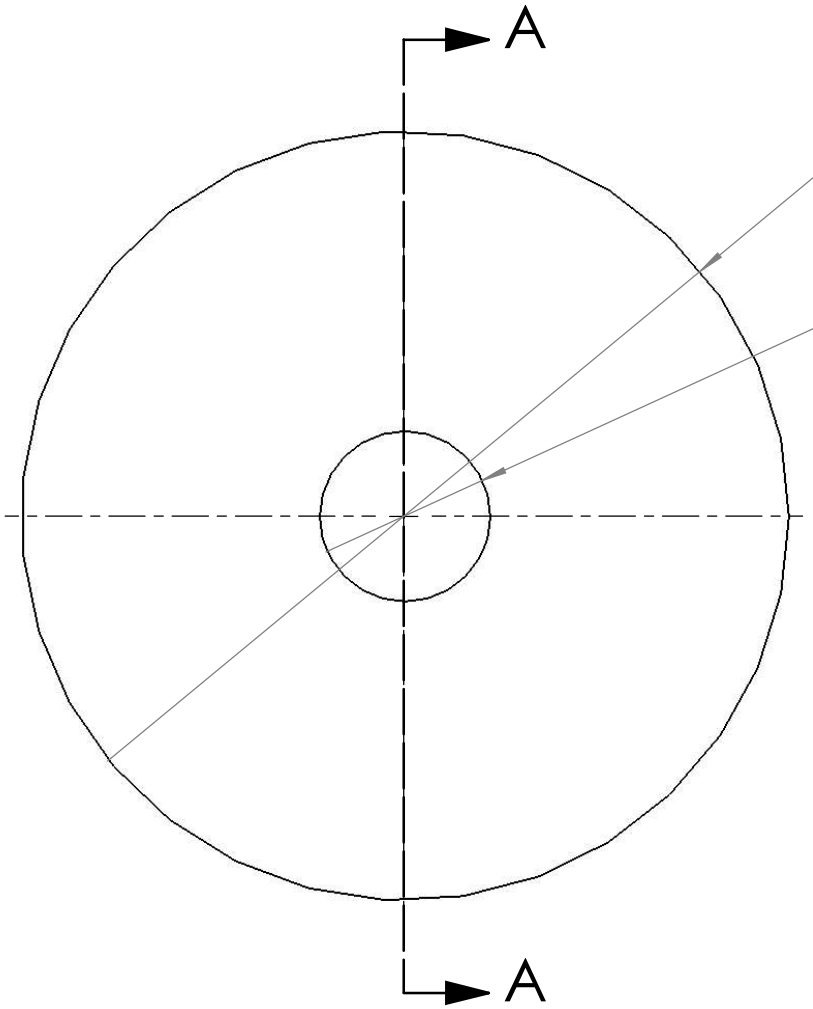

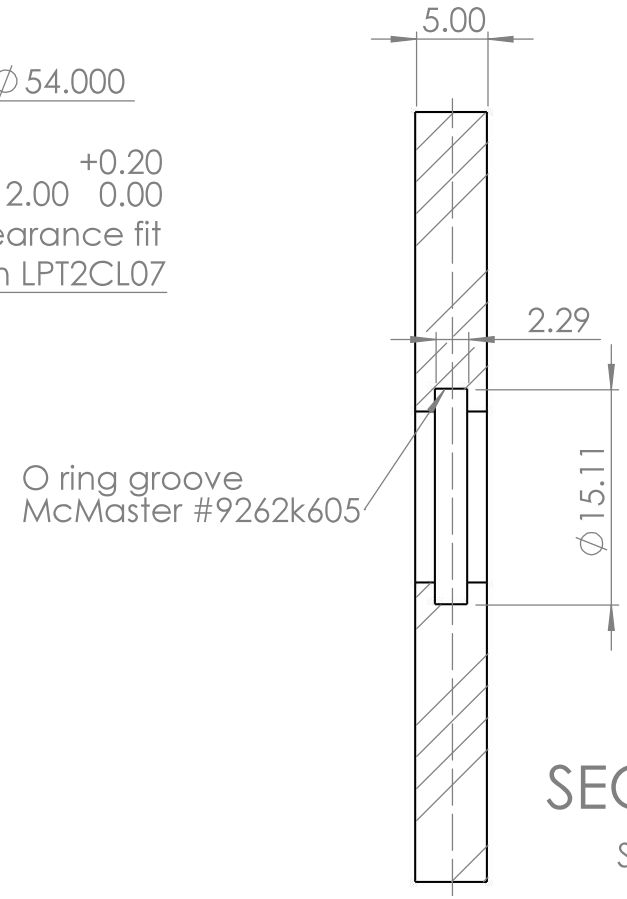

SECTION A-A
SCALE 2 : 1

UNLESS OTHERWISE SPECIFIED: DIMENSIONS ARE IN MILLIMETERS SURFACE FINISH: TOLERANCES: LINEAR: Two place decimal: ±0.25 Three place decimal: ±0.127 ANGULAR: MACH ±0.1	DO NOT SCALE DRAWING	REVISION 10
	Linear Paul Trap - TRIUMF	
NAME / DATE DRAWN XS 14/02/2020 CHK'D APPV'D REV'D	TITLE: CLB Exit Holder	
MATERIAL: PEEK	DWG NO. LPT2CL08	A4
QUANTITY: 1	SCALE: 1:6	SHEET 39 OF 39